DMRG studies of Chebychev-expanded spectral functions and quantum impurity models

Andreas Michael Holzner

München 2011

DMRG studies of Chebychev-expanded spectral functions and quantum impurity models

Andreas Michael Holzner

Dissertation
an der Fakultät für Physik
der Ludwig–Maximilians–Universität
München

vorgelegt von
Andreas Michael Holzner
aus München

München, den 09.12.2011

Erstgutachter: Prof. Dr. Jan von Delft
Zweitgutachter: Prof. Dr. Ulrich Schollwöck
Tag der mündlichen Prüfung: 27.01.2012

Abstract

This thesis is concerned with two main topics: first, the advancement of the density matrix renormalization group (DMRG) and, second, its applications. In the first project of this thesis we exploit the common mathematical structure of the numerical renormalization group and the DMRG, namely, matrix product states (MPS), to implement an efficient numerical treatment of a two-lead, multi-level Anderson impurity model. By adopting a star-like geometry, where each species (spin and lead) of conduction electrons is described by its own so-called Wilson chain, instead of a single Wilson chain we achieve a very significant reduction in the numerical resources required to obtain reliable results. Moreover, we show that it is possible to find an "optimal" chain basis, in which chain degrees of freedom of different Wilson chains become effectively decoupled from each other further out on the Wilson chains. This basis turns out to also diagonalize the model's chain-to-chain scattering matrix.

In the second project we show that Chebyshev expansions offer numerically efficient representations for calculating spectral functions of one-dimensional lattice models using MPS methods. The main features of this Chebychev matrix product state (CheMPS) approach are: (i) it achieves uniform resolution over the spectral function's entire spectral width; (ii) it offers a well-controlled broadening scheme; (iii) it is based on using MPS tools to recursively calculate a succession of Chebychev vectors, (iv) whose entanglement entropies were found to remain bounded with increasing recursion order for all cases analyzed here. We present CheMPS results for the structure factor of spin-$1/2$ antiferromagnetic Heisenberg chains and perform a detailed finite-size analysis. Making comparisons to benchmark methods, we find that CheMPS yields results comparable in quality to those of correction vector DMRG, at dramatically reduced numerical cost and agrees well with Bethe Ansatz results for an infinite system, within the limitations expected for numerics on finite systems.

Following these technologically focussed projects we study the so-called Kondo cloud by means of the DMRG in the third project. The Kondo cloud describes the effect of spatially extended spin-spin correlations of a magnetic moment and the conduction electrons which screen the magnetic moment through the Kondo effect at low temperatures. We focus on the question whether the Kondo screening length, typically assumed to be proportional to the inverse Kondo temperature, can be extracted from the spin-spin correlations. We investigate how perturbations which destroy the Kondo effect, like an applied gate potential or a magnetic field, affect the formation of the screening cloud.

In a forth project we address the impact of Quantum (anti-)Zeno physics resulting from repeated single-site resolved observations on the many-body dynamics. We use time-dependent DMRG to obtain the time evolution of the full many-body wave function that is then periodically projected in order to simulate realizations of stroboscopic measurements. For the example of a 1-D lattice of spin-polarized fermions with nearest-neighbor interactions, we find regimes for which many-particle configurations are stabilized and destabilized depending on the interaction strength and the time between observations.

Zusammenfassung

Diese Arbeit behandelt zwei Themenbereiche, zum einen methodische Fortschritte im Bereich der Dichtematrix-Renormierungsgruppe (DMRG) und zum anderen Anwendungen der DMRG. Im ersten Projekt werden Matrixproduktzustände (MPS), die den gemeinsamen mathematischen Unterbau für die numerische Renormierungsgruppe und DMRG bilden, genutzt, um ein Anderson-Störstellenmodell mit zwei Bändern und mehreren Niveaus numerisch effizient zu beschreiben. Indem jede Art (pro Band und Spin) von Leitungselektronen durch eine eigene sogenannte Wilson-Kette in einer sternförmigen Anordnung anstelle einer einzigen Wilson-Kette repräsentiert wird, lässt dich der numerische Aufwand für eine zuverlässige Beschreibung deutlich reduzieren. Wir zeigen zusätzlich, dass sich eine "optimale" Kettenbasis finden lässt, in der die Kettenfreiheitsgrade verschiedener Ketten ab einem gewissen Abstand zum Zentrum effektiv entkoppelt sind. Diese Basis diagonalisiert auch die Streumatrix bezüglich der Wilson-Ketten.

Im zweiten Projekt nutzen wir im Rahmen von MPS-Methoden Tschebytscheff-Entwicklungen zur effizienten numerischen Berechnung von Spektralfunktionen für eindimensionale Gittermodelle. Diese neu entwickelte Tschebytscheff-Matrixproduktzustandsmethode (CheMPS) zeichnet sich durch folgende Eigenschaften aus: (i) gleichmäßige Auflösung über den gesamte Spektralbereich hinweg, (ii) gut kontrollierbares Verbreiterungsschema, (iii) Rekursionsvorschrift, die auf MPS-Werkzeugen basiert, zur Berechnung einer Folge von Tschebytscheff-Vektoren, (iv) deren Verschränkungsentropie für alle hier betrachteten Fälle mit wachsender Entwicklungordnung nach oben beschränkt ist. Wir berechnen den Strukturfaktor von Spin-$1/2$ Heisenberg-Antiferromagnetketten einschließlich einer detailierten Untersuchung von Systemgrößeneffekten. Im Vergleich zu Referenzmethoden zeigt sich, dass CheMPS der "correction-vector" DMRG bei signifikant verringerten numerischen Kosten qualitativ ebenbürtig ist und mit den Bethe-Ansatz Ergebnissen für unendlich große Systeme im Rahmen der Einschränkungen, die man für endliche Systeme erwartet, übereinstimmt.

Nach diesen methodisch orientierten Kapiteln folgt eine DMRG-Studie der sogenannten Kondo-Wolke. Die Kondo-Wolke entsteht durch räumlich ausgedehnte Spin-Spin-Korrelationen eines magnetischem Moments mit den Leitungselektronen, die das magnetische Moment durch den Kondo-Effekt bei niedrigen Temperaturen abschirmen. Das Hauptaugenmerk dieses Kapitels liegt auf der Frage, ob die Kondo-Abschirmlänge, die in der Regel als umgekehrt proportional zur Kondo-Temperatur angenommen wird, aus den Spin-Spin-Korrelationen berechnet werden kann. Wir untersuchen auch wie Gatespannung und

Magnetfeld als Störeinflüsse auf den Kondo-Effekt die Bildung der Abschirmwolke beeinflussen.

Im vierten Projekt analysieren wir die Auswirkunden des Quanten-(Anti)-Zeno-Effekts, der durch wiederholte Messungen mit einer Genauigkeit von einem Gitterplatz entsteht, auf die Vielteilchendynamik eines Systems. Mit Hilfe der zeitabhängigen DMRG berechnen wir die Zeitentwicklung der vollen Vielteilchenwellenfunktion, die zur Simulation von stroboskopischen Messungen periodisch ausprojiziert wird. Im Beispiels eines eindimensionalen Gitters spinpolarisierter Fermionen mit nächster-Nachbar-Wechselwirkungen zeigen sich Parameterbereiche, in denen Vielteilchenkonfigurationen in Abhängigkeit von Wechselwirkungsstärke und Messfrequenz entweder stabilisiert oder destabilisiert werden.

Contents

List of Publications

During the work for this thesis the following articles have been published or made available as preprints.

1. *Kondo screening cloud in the single-impurity Anderson model: A density matrix renormalization group study*
   A. Holzner, I. P. McCulloch, U. Schollwöck, J. von Delft, F. Heidrich-Meisner
   Phys. Rev. B **80**, 205114 (2009)

2. *Matrix product state approach for a two-lead, multi-level Anderson impurity model*
   A. Holzner, A. Weichselbaum, J. von Delft
   Phys. Rev. B **81**, 125126 (2010)

3. *Correlation density matrices for 1- dimensional quantum chains based on the density matrix renormalization group*
   W. Münder , A. Weichselbaum , A. Holzner , J .von Delft and C. L. Henley
   New J. Phys. **12**, 075027 (2010)

4. *Chebyshev matrix product state approach for spectral functions*
   A. Holzner, A. Weichselbaum, I. P. McCulloch, U. Schollwöck, J. von Delft
   Phys. Rev. B **83**, 195115 (2011)

5. *Stroboscopic observation of quantum many-body dynamics*
   S. Kessler, A. Holzner, I. P. McCulloch, J. von Delft, F. Marquardt
   arXiv:1102.1605

Chapter 1

Introduction

The numerical simulation of quantum systems in general suffers from the fact that the Hilbert space for such systems grows exponentially with the system size. This makes an exact numerical treatment for systems of only moderate size virtually impossible and the use of approximate methods becomes mandatory. For strongly correlated systems where interactions play a dominant role, analytical methods typically cease to work. For special cases or within certain boundaries, however, analytical methods work well and provide deep insights, yet it is advisable to control their approximations with numerical methods.

In this thesis, we consider the more special case of one-dimensional strongly correlated quantum systems at low temperatures. For these systems quantum Monte Carlo approaches usually suffer from the fermionic sign problem [1] and cannot be applied in an efficient manner. Quantum impurity models are a subclass of strongly correlated quantum systems where a small interacting region is coupled to a much larger non-interacting reservoir. Nevertheless, quantum many-body effects play an important role and the whole systems needs to be treated quantum mechanically. For this subclass of quantum impurity models K. G. Wilson developed the numerical renormalization group (NRG) [2] in the early 1970s. The NRG is based on a logarithmic energy discretization and decimates the Hilbert space be keeping only the low-energy eigenstates as the simulated system is increased iteratively. This scheme is tailor-made for impurity systems and works extremely well for these. However, it fails completely for real-space models for fundamental reasons which are related to its Hilbert space truncation based on energy [3].

In 1992 S. R. White introduced the density matrix renormalization group (DMRG) [4, 5] which succeeds in the numerical simulation of one-dimensional strongly correlated quantum systems. One key difference compared to NRG which is responsible for this achievement is the Hilbert space truncation scheme which keeps the most important states, i. e. the states with the biggest weight, according to a reduced density matrix. In its original formulation the DMRG was capable of calculating static properties of ground states and low-lying eigenstates. It has been extended to the calculation of dynamic properties [6–8] and also towards the time-evolution of quantum systems [9–13] and simulations at finite temperature [14, 15]; DMRG can be regarded as a standard numerical method for this class of systems. The foundation of the success of DMRG were the only moderate

numerical resources required by DMRG for the description of most systems with very high precision. The exponentially large Hilbert space of quantum systems is truncated by DMRG in a controlled and effective way which makes the numerical treatment of systems with several hundred lattice sites possible. The deeper physical reason thereof lies in the slow entanglement growth of one-dimensional quantum systems [16]. The stronger growth in two dimensions limits the applicability of DMRG there to rather small systems.

Comparatively long after DMRG was established it was recognized that the states produced by DMRG can be expressed in terms of so-called matrix product states (MPS) [17, 18] which themselves were discovered independently [19, 20]. The same was also found to be true for NRG [21]. The recognition of MPS as building blocks of DMRG opened up a connection into the field of quantum information. Several extensions of DMRG where prompted by the different perspective of quantum information theory.

An ongoing interest in DMRG (and NRG) besides the pure algorithmically triggered interest has been generated by experimental advances in the past. There are in particular two classes of systems that stand out as they can be controlled very precisely: quantum dots [22] and ultracold atoms in optical lattices [23].

Quantum dots are mesoscopic semiconductor structures in which electrons are spatially confined. These structures can be coupled to several reservoirs (called leads) allowing for transport processes into and off the quantum dot. Due to the small size of the quantum dot the Coulomb interaction between electrons in the dot becomes a very important effect as opposed to the leads where interaction effects usually can be neglected. Such devices can be manufactured with high precision allowing to control all relevant physical parameters of quantum dots. Quantum dots can be made so small that single electrons within the dot can be detected and quantization effects are directly observable, e. g. in transport measurements [24]. This allows to study basic physical effects experimentally: in particular, the Kondo effect which was first experimentally observed in 1934 [25] as a resistance anomaly of metals at very low temperatures. It was theoretically explained by J. Kondo in 1964 [26] as a many-body effect where localized impurities with a magnetic moment interact with the spin-$1/2$ conduction electrons. This spin-spin interaction includes spin-flip scattering processes which become dominant at low temperatures. The temperature, or equivalently the energy scale, where the spin-flip processes start to dominate is called the Kondo temperature T_K. A theoretical description of the temperature regime below T_K can only be achieved with sophisticated methods like the NRG. As opposed to the magnetic impurities in the original experimental setup where the Kondo effect was discovered, quantum dots allow accurate control over single electrons. This allows direct experimental access to Kondo systems under full control [27] which, in turn, renewed the interest in the Kondo effect [28].

The field of ultracold atoms is relatively young and emerged 1995 with the first realizations of a Bose–Einstein condensation of dilute atomic gases [29–31]. Such ultracold quantum gases can be loaded into optical lattices [23] yielding periodic systems of arbitrary dimension where the tunneling and interaction parameters are under almost perfect control. With such good control over a optical lattice systems a big class of lattice Hamilton operators can be implemented experimentally. In addition, almost arbitrary many-body states can be prepared to study their time-evolution. Thus optical lattices can be used to

simulate the dynamics of a huge class of Hamilton operators [32]. This idea of a universal quantum simulators was proposed by Feynman [33] almost three decades ago and describes the use of a controllable quantum system to simulate another (more complex) local quantum system. Using a classical computer instead would lead to an exponential slowdown when performing an exact simulation of a quantum system.

The physics of one-dimensional systems is fundamentally different from that of systems of higher dimensions as interaction effects become more important. This makes one-dimensional systems a very interesting subject. The DMRG is well adapted to the numerical simulation of such one-dimensional strongly interacting quantum systems. In particular, the time-evolution capabilities of DMRG allow for the direct simulation of experimental setups as they are realized in optical lattice experiments.

In the following, we summarize the contents of this thesis, divided into two main topics: the evolution of DMRG techniques and applications of the DMRG. In order to establish a common basis for all further discussions we begin with an introduction of DMRG in Chapter 2. We start from first principles and use solely the language of MPS and the corresponding graphical representation in favor of the original representation in terms of block states. The notion of matrix product operators (MPOs), the equivalent to MPS for operators, is introduced and all necessary operations for DMRG calculations, including the calculation of dynamic properties and time-evolutions, are shown.

In Chapter 3, the DMRG is applied to a two-lead, multi-level Anderson impurity model, a model which is typically analyzed with NRG. In NRG the numerical representation would consist of a single chain. Using DMRG instead, this NRG chain can be split into four chains that are connected in a "star-like" geometry. That way a significant reduction of numerical resources can be achieved. Furthermore, the new geometry allows to choose a numerically optimal basis for lead degrees of freedom which turns out to also diagonalize the model's chain-to-chain scattering matrix.

The calculation of dynamic properties with the standard DMRG correction-vector approach is much more expensive numerically than ground state calculations. We develop a novel approach for calculating spectral functions in Chapter 4 based on Chebyshev polynomials, called Chebyshev matrix product state approach (CheMPS). CheMPS achieves a competitive accuracy compared with the correction-vector approach at significantly reduced costs. Also the properties of the underlying Chebyshev polynomials carry over advantageously, most notably, the numerically stable recursion relation, almost uniform spectral resolution and a broadening scheme that is well controlled. Since time-evolution is related to the calculation of spectral functions by the means of Fourier transformation the Chebyshev approach can also be used for time-evolution (tCheMPS).

After these studies focussing on aspects of the method DMRG itself, we apply the DMRG to the single impurity Anderson model in Chapter 5 to study the Kondo screening cloud. The Kondo effect originates in spin-flip processes and these manifest themselves in spatially extended spin-spin correlations, the so called Kondo screening cloud, whose extension is inverse proportional to the Kondo temperature. The standard choice of numerical methods for Kondo systems would be the NRG and in fact the NRG has been extended to study the Kondo cloud [34]. However, with current NRG techniques the Kondo screening

cloud cannot be directly studied for e. g. double quantum dots or interacting leads. Such more complex models can be treated with DMRG and the Kondo screening cloud can be measured directly since DMRG works on real-space models. On the other hand, DMRG is limited in its capability to reach very low Kondo temperatures as the necessary energy resolution would require very large system sizes. To explore the potential of DMRG for Kondo screening cloud calculations we investigate how the Kondo screening length can be extracted from spin-spin correlation data and which Kondo temperatures can be reached with reasonable numerical effort. We also study how the Kondo screening cloud is affected when a gate voltage and magnetic field are applied to the quantum dot.

For the last project of this thesis presented in Chapter 6, we turn towards ultracold atoms in optical lattices. We study the effects of repeated single-site resolved measurements on the time-evolution of one-dimensional systems of interacting spin-polarized fermions by the means of time-dependent DMRG. Such repeated (stroboscopic) measurements affect the stability of many-body configurations and can have both stabilizing and destabilizing effects depending on the interaction strength and measurement interval length.

Chapter 2

The density matrix renormalization group

Parts of this chapter have been published in New Journal of Physics:
W. Münder, A. Weichselbaum, A. Holzner, J. von Delft, C. L. Henley, New J. Phys. **12**, 075027 (2010), Appendix.

In this technical introductory chapter, we offer a tutorial guide to the DMRG using the MPS formalism. We will not discuss the classical representation of DMRG nor try to be exhaustive on other applications and variants of DMRG than presented in this work since both can be found in the literature with the reviews [35, 36] serving as an excellent starting points.

After a short overview of the method, we introduce MPS as the fundamental building block for DMRG. We point out all the important properties of the MPS and explain how to perform basic quantum calculations such as evaluating scalar products and constructing a reduced density matrix. The concept of MPS can be extended from states to operators leading to MPOs and we demonstrate how to operate with MPOs such as applying MPOs on MPSs and calculating expectation values. With these representations for states and operators at hand, we explain the process of "sweeping" that is most prominently used to find a good approximation for the ground states in an iterative fashion. This idea of iteratively optimizing a MPS for a certain goal is also used for calculating spectral functions and for finding optimal representations of certain states.

2.1 Introduction

Quantum many-body systems deal with very large Hilbert spaces even for relatively small system sizes. For example, a one-dimensional quantum chain of N spin-$1/2$ particles forms a Hilbert space of dimension 2^N, which is exponential in system size. For quantum lattice models in 1D a very efficient numerical method is the DMRG, introduced by Steven R. White [4, 5]. The problem of large Hilbert space dimension is avoided by an efficient

description of the ground state, which discards those parts of the Hilbert space which have negligible weight in the ground state. In this manner the state space dimension of the effective description becomes tractable, and it has been shown that this produces excellent results in many quasi one-dimensional systems. In the meantime, the method has been extended to dynamic quantities [6–8] and to time-dependence and various time-dependent Hamiltonian operators have been studied [9–13].

The original DMRG formulation did not rely on MPS but used "block states" to represent the effective Hilbert spaces of one or more targeted states. The notion of MPS was introduced independent of DMRG [19, 37–40] before it was realized that the algebraic structure of the ground state for one-dimensional systems calculated with DMRG can be described in terms of position-dependent MPS [17, 18, 38, 41–45]. The MPS based formulation of DMRG has proven to be very enlightening and fruitful, in particular the observation that DMRG is in essence a variational method [41] opened up rich connections to quantum information theory: some new fields of application arose like periodic systems [41] and finite temperature calculations through purification of the density operator [14, 15]. Recently a new approach for finite temperature using minimally entangled typical thermal states has been introduced [46, 47] promising improved efficiency.

The origin of the MPS structure underlying the DMRG approach can be understood as follows (a detailed description will follow later): pick any specific site of the quantum lattice model, say site k, representing a local degree of freedom whose possible values are labeled by an index σ_k (e.g., for a chain of spinless fermions, $\sigma_k = 0$ or 1 would represent an empty or occupied site). Any many-body state $|\psi\rangle$ of the full chain can be expressed in the form

$$|\psi\rangle = \sum_{l_k r_k \sigma_k} A^{[\sigma_k]}_{l_k r_k} |l_k\rangle |\sigma_k\rangle |r_k\rangle \,, \tag{2.1}$$

where $|l_k\rangle$ and $|r_k\rangle$ are sets of states (say N_l and N_r in number) describing the parts of the chain to the left and right of current site k, respectively, and for each σ_k, $A^{[\sigma_k]}$ is a matrix with matrix elements $A^{[\sigma_k]}_{l_k r_k}$ and dimension $N_l \times N_r$. Since such a description is possible for any site k, the state $|\psi\rangle$ can be specified in terms of the set of all matrices $A^{[\sigma_k]}$, resulting in a *matrix product state* of the form

$$|\psi\rangle = \sum_{\sigma_1 \ldots \sigma_N} A^{[\sigma_1]} \ldots A^{[\sigma_N]} |\sigma_1\rangle \ldots |\sigma_N\rangle \,, \tag{2.2}$$

where the matrices $A^{[\sigma_1]}$ and $A^{[\sigma_N]}$ at the ends have row- and column-vector shape, respectively, to account for open boundary conditions.[1]

One may now seek to approximate a certain state or expression (most prominent example being the ground state) within the space of all MPS by treating the matrix elements of the A-matrices as variational parameters. This is done by locally updating one A-matrix

[1] In this work, we deal only with open boundary conditions. In principle, a MPS can also be written down for periodic boundary conditions by conserving 2D-matrix shape for the first and last A-matrix and tracing over the open indices at the end.

at a time (while keeping the other matrices fixed) in a sequential ordering and a manner according to the approximation task at hand. One series of local updates of every A-matrix is called a *sweep*. In the case of a ground state calculation the local update aims for minimizing the expectation value $\langle\psi|H|\psi\rangle$ and the corresponding sweeps are repeated until sufficient convergence has been achieved. The resulting procedure is equivalent to a strictly variational minimization of the ground state energy within the space of all MPS of the form of Eq. (2.2) [17, 18, 38, 41, 44]. If instead the local update is performed for two adjacent matrices at a time, the resulting (quasi-variational) procedure is equivalent to White's original formulation of DMRG [17, 18, 38, 41, 44].

In general, such an approach works for both bosonic and fermionic systems. However, to be efficient the method needs a local Hilbert space with finite and small dimension, limiting its applicability to cases where the local Hilbert space is finite dimensional a priori (e.g. fermions or hard-core bosons) or effectively reduced to a finite dimension, e.g. by interactions. For example, such a reduction is possible if there is a large repulsion between bosons on the same site such that only a few states with small occupation number will actually take part in the ground state. For fermions, on the other hand, the fermionic sign must be properly taken care of. This problem can be simplified by either correctly accounting of the particle number as (in most cases) conserved quantity or by applying a Jordan-Wigner transformation [48] that creates new operators obeying bosonic commutation relations.

DMRG performs well for 1D systems, a fact that has been put on a firm theoretical footing in recent years [16, 49–55]. The numerical effort of a DMRG calculation depends strongly on the entanglement of the wave function and how the entanglement scales with system size. For ground states the scaling of entanglement obeys an area law [56–61] and thus does not grow with the system size in 1D (with logarithmic corrections for critical systems) [62–64]. This reasoning applies only for ground states and cannot be expected to hold for arbitrary states. Indeed, the time-evolution of DMRG is limited to small timescales as the entanglement of the time-evolved state increases [65, 66] and exponential resources would be necessary to describe the state properly for longer times. Although there have been 2D DMRG studies [67, 68], in general DMRG works poorly in 2D as MPS cannot produce the correct entanglement scaling efficiently [60, 69]. Various classes of ansatz states have been suggested [70–74] for 2D, among them "projected entangled pair states" (PEPS) [75] as a straightforward generalization of MPS and the field of quantum simulation in 2D is actively investigated.

The following introduction to DMRG is organized from a technical point of view. We begin with a presentation of MPSs and MPOs as the fundamental building blocks of DMRG in Sec. 2.2 and Sec. 2.3. The key concepts of DMRG, namely, the Hilbert space truncation (see Sec. 2.2.9) and the above-mentioned optimization scheme (see Sec. 2.4) follow. As an application of the so far laid out techniques we discuss the principles of adaptive time evolution (tDMRG) in Sec. 2.6.

2.2 Matrix product states

2.2.1 Construction of matrix product states

We consider a chain with open boundary conditions consisting of N equal sites with a local Hilbert space dimension of d. A state $|\psi\rangle$ is described by

$$|\psi\rangle = \sum_{\sigma_1 \ldots \sigma_N} \psi_{\sigma_1,\ldots,\sigma_N} |\sigma_1\rangle \ldots |\sigma_N\rangle \,, \tag{2.3}$$

where $\sigma_i = 1, \ldots, d$ labels the local basis states of site i. In general, the size of the coefficient space ψ scales with $\mathcal{O}(d^N)$. This can be rewritten in a matrix decomposition of the form of Eq. (2.2) with a set of N times d matrices $A^{[\sigma_k]}$ (see Sec. 2.2.5 for details). Formally, this decomposition has two open indices, namely the first index of $A^{[\sigma_1]}$ and the second index of $A^{[\sigma_N]}$, as $A^{[\sigma_1]}$ and $A^{[\sigma_N]}$ are not multiplied onto a matrix to the left and to the right, respectively. However, these two indices range only over one value as $A^{[\sigma_1]}$ and $A^{[\sigma_N]}$ are of row- and column-vector shape, respectively. As a consequence the matrix product of Eq. (2.2) gives a scalar.

If these A-matrices are sufficiently large this decomposition is formally exact, but since that would require A-matrices of exponentially large size, such an exact description is of academic interest only. The reason why the A-matrices are introduced is that they offer a very intuitive strategy for reducing the numerical resources needed to describe a given quantum state. This strategy involves limiting the dimensions of these matrices by systematically using singular-value decomposition (SVD) and retaining only the set of largest singular values. The A-matrices can be chosen much smaller while still giving a very good approximation of the state $|\psi\rangle$.

Selecting a certain site k, the state can be rewritten in the form of Eq. (2.1). The effective 'left' basis $|l_k\rangle = \sum_{\sigma_1 \ldots \sigma_{k-1}} A^{[\sigma_1]} \ldots A^{[\sigma_{k-1}]} |\sigma_1\rangle \ldots |\sigma_{k-1}\rangle$ describes the sites $j = 1, \ldots, k-1$, the effective 'right' basis $|r_k\rangle$ similarly describes the sites $j = k+1, \ldots, N$. Site k is called the *current* site, as the description of the state makes explicit only the A-matrix of this site (see Fig. 2.1).

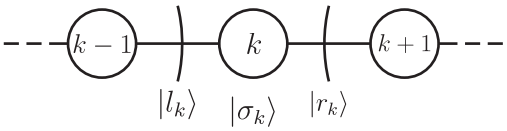

Figure 2.1: Current site with effective basis sets.

So far Eqs. (2.3) and (2.1) are equivalent, but now we have a representation of the state which allows a convenient truncation of the total Hilbert space, used for the description of a MPS. For example, if we truncate all effective Hilbert spaces of all sites to the fixed dimension D, each $A^{[\sigma_k]}$-matrix has at most the dimension $D \times D$. This reduces the resources used to describe a state from $\mathcal{O}(d^N)$ for the full many-body Hilbert space down to $\mathcal{O}(ND^2d)$. This is linear in the system size, assuming that the size required for D

to accurately describe the state grows significantly slower than linearly in N. This, in fact, turns out to be the case for ground state calculations [49]. Details of this truncation procedure and estimates of the resulting error are described in Sec. 2.2.9.

2.2.2 Global view and local view

Matrix product states can be viewed in two alternative ways: a global view and a local view. Both views are equivalent and both have their applications. In the global view the state is expressed as in Eq. (2.2), i.e. the effective Hilbert spaces have been used 'only' to reduce resources. The state is stored in the A-matrices, and no site is treated special as *current* site. In this case, the state is *formally* represented in terms of the product of the local Hilbert spaces $|\sigma_1\rangle \dots |\sigma_N\rangle$, however, this contraction of the A-matrices is never carried out due to exponential numerical costs. In the local view the state is expressed as in Eq. (2.1). It is called local because there is one special site, the *current* site, and all other sites are combined in effective orthonormalized basis sets. Usually, the local view is used iteratively for every site. In this perception, we need effective descriptions of operators contributing to the Hamiltonian operator acting on other sites than the current site (see Sec. 2.3.4).

2.2.3 Center matrix view

All operations on MPS that are performed by sweeping share the concept of *local updates*, i. e. one or two A-matrices[2] are modified at a time while the others remain fixed. One-site and two-site sweeps (see Sec. 2.2.9) differ slightly in their convergence properties and variational nature. Apart from that, we can provide an unified description for both one- and two-site processes through a slightly adapted local view description, the *center view* description [45] that also simplifies the handling of effective matrix elements for operators.

To that end, we rewrite Eq. (2.2) by inserting a center matrix C next to the *current* site such that the overall state $|\psi\rangle$ is not changed. For the example of a one-site update with k being the *current* site we insert C between $A^{[\sigma_k]}$ and $A^{[\sigma_{k+1}]}$

$$|\psi\rangle = \sum_{\sigma_1 \dots \sigma_N} A^{[\sigma_1]} \dots A^{[\sigma_{k-1}]} \tilde{A}^{[\sigma_k]} C A^{[\sigma_{k+1}]} \dots A^{[\sigma_N]} |\sigma_1\rangle \dots |\sigma_N\rangle \,, \tag{2.4}$$

where $\tilde{A}^{[\sigma_k]}_{ij} = \delta_{id+\sigma_k,j}$, $C_{jl} = A^{[\sigma_k]}_{il}$ and $j = id + \sigma_k$ running over Dd states. That way, we obtained a local description of $|\psi\rangle$ through the $dD \times D$ center matrix C

$$|\psi\rangle = C_{l_c r_c} |l_c\rangle |r_c\rangle, \tag{2.5}$$

with $|r_c\rangle = |r_k\rangle$ and the *expanded* left basis

$$|l_c\rangle = \tilde{A}^{[\sigma_k]} |l_k\rangle |\sigma_k\rangle \tag{2.6}$$

[2] In principle, this can be generalized to changing more A-matrices at once, but this increases the numerical costs and offers no relevant improvement.

which has dimension Dd and is just the tensor product of $|l_k\rangle$ and $|\sigma_k\rangle$. Since $\tilde{A}^{[\sigma_k]}_{ij} C_{jl} = A^{[\sigma_k]}_{il}$ holds, the state $|\psi\rangle$ is not changed. The right basis can be expanded in complete analogy. If both the left and right basis are expanded at the same time both generated C-matrices are multiplied together to form a $Dd \times Dd$ C-matrix holding the information of two neighboring A-matrices. Thus an update of this C-matrix is equivalent to one step in a two-site sweep. With the *center matrix* view of Fig. 2.2(c) we achieved an easy local description suitable for both one-site and two-site sweeps. In order to adopt to useful notion of the *current* site also for the center matrix representation we call the site left to C the *current* site.

2.2.4 Graphical representation

Matrix product states can be depicted in a convenient graphical representation (see Fig. 2.2). In this representation, A-matrices are displayed as boxes and $A^{[\sigma_k]}$ is replaced by A_k for brevity. Indices correspond to links from the boxes. The left link connects to the effective left basis, the right link to the right one, and the link at the bottom to the local basis. Sometimes indices are explicitly written on the links to emphasize the structure of the sketch. Connected links denote a summation over the indices (also called contraction) of the corresponding $A^{[\sigma]}$-matrices. As this representation contains the complete information

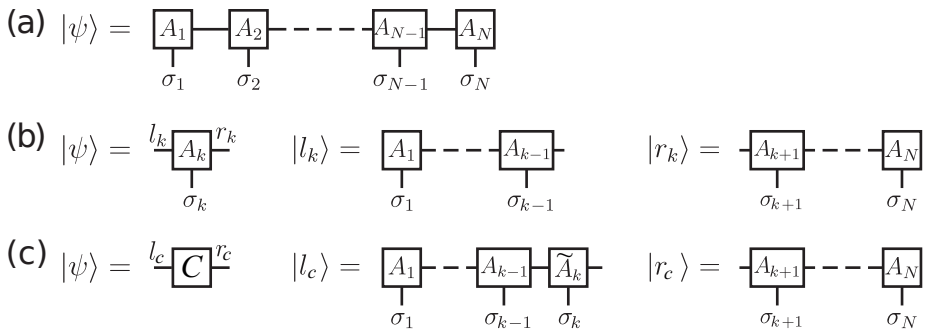

Figure 2.2: Graphical representation of a matrix product state in the (a) global view, (b) local view and (c) center matrix view with the left basis expanded.

on the state (or even MPS/ MPO expression) depicted it is a rigorous way of denoting MPSs, yet with greatly improved readability compared to ordinary equations.

2.2.5 Details of the A-matrices

The A-matrices have some useful properties that hold independently of the truncation scheme used to limit the effective Hilbert spaces. First of all, we notice that by construction $dim(\mathcal{H}^{r_{k-1}}) \equiv dim(\mathcal{H}^{l_k})$, otherwise the matrix products in Eq. (2.2) would be ill defined. Based on this, we can find another interpretation of the A-matrices in the local view. The

part of the chain to the left of site k (where k is far from the ends for simplicity) is described by the effective basis $|l_k\rangle$, which is built of truncated A-matrices:

$$\begin{aligned}|l_k\rangle &= \sum_{\sigma_1,\ldots,\sigma_{k-1}} \left(A^{[\sigma_1]}\ldots A^{[\sigma_{k-1}]}\right)_{l_k} |\sigma_1\rangle\ldots|\sigma_{k-1}\rangle \\ &= \sum_{\sigma_{k-1}}\sum_{l_{k-1}} \underbrace{\sum_{\sigma_1,\ldots,\sigma_{k-2}} \left(A^{[\sigma_1]}\ldots A^{[\sigma_{k-2}]}\right)_{l_{k-1}} |\sigma_1\rangle\ldots|\sigma_{k-2}\rangle}_{|l_{k-1}\rangle} A^{[\sigma_{k-1}]}_{l_{k-1},l_k}|\sigma_{k-1}\rangle \\ &= \sum_{\sigma_{k-1},l_{k-1}} A^{[\sigma_{k-1}]}_{l_{k-1}l_k}|l_{k-1}\rangle|\sigma_{k-1}\rangle\,.\end{aligned} \tag{2.7}$$

The $A^{[\sigma_{k-1}]}$-matrix maps the effective left basis $|l_{k-1}\rangle$ together with the local $|\sigma_{k-1}\rangle$ basis onto the effective left basis $|l_k\rangle$! The same argument applied on the effective right basis of site k leads to the transformation of $|r_{k+1}\rangle$ and $|\sigma_{k+1}\rangle$ onto $|r_k\rangle$ via the $A^{[\sigma_{k+1}]}$-matrix:

$$|r_k\rangle = \sum_{\sigma_{k+1},r_{k+1}} A^{[\sigma_{k+1}]}_{r_k r_{k+1}}|\sigma_{k+1}\rangle|r_{k+1}\rangle\,. \tag{2.8}$$

So far, this may be any transformation, but in order to deal with properly orthonormal basis sets, we may impose unitarity on the transformation (see below).

The A-matrices towards the ends of the chain have to be discussed separately. The use of open boundary conditions implies that we have a one-dimensional effective state space to the left of site one and the right of site N, respectively, both representing the empty state. This implies that $\dim(\mathcal{H}^{l_1}) = 1 = \dim(\mathcal{H}^{r_N})$. Moving inwards from the ends of the chain, the effective Hilbert spaces acquire dimension $d^1, d^2, \ldots$ until they become larger than D and need to be truncated. Correspondingly, the dimension of matrix $A^{[\sigma_k]}$ is $D_{k-1}\times D_k$, where $D_k = \min(d^k, d^{N-k}, D)$. There is no truncation needed if $\dim(\mathcal{H}^{l_k})\cdot d = \dim(\mathcal{H}^{r_k})$ or $\dim(\mathcal{H}^{r_k})\cdot d = \dim(\mathcal{H}^{l_k})$.

Summarizing, the A-matrices have two functions. If site i is the current site in Eq. (2.1), the $A^{[\sigma_i]}$-matrices represent the state, i.e. its coefficients specify the linear combination of basis states $|l_k\rangle$, $|\sigma_k\rangle$ and $|r_k\rangle$. In the center matrix representation this information on the state is moved to the center matrix C in Eq. (2.5)(c) and $A^{[\sigma_i]} \equiv \tilde{A}^{[\sigma_i]}$ provides the expanded basis for C as in Eq. (2.6). On the other hand, if not the current site, the A-matrices are used as a mapping to build the effective orthonormal basis for the current/center site, as we describe next:

Orthonormal basis sets

In the center view, the whole system is described by the C-matrix of the current site k in the effective left basis and the effective right basis, where at least one of the effective basis sets is expanded according to Eq. (2.6). A priori, the basis states form an orthonormal set

only for the local basis set, but we may ask for the effective basis sets $|l\rangle$ and $|r\rangle$[3] to be orthonormal, too, i. e. require them to obey:

$$\begin{aligned} \langle l'|l\rangle &= \delta_{l'l}\,, \\ \langle r'|r\rangle &= \delta_{r'r}\,. \end{aligned} \tag{2.9}$$

This immediately implies the following condition on the $A^{[\sigma_j]}$-matrices, using Eq. (2.7) and Eq. (2.8) (for a derivation, see Sec. A.1):

$$\begin{aligned} \sum_{\sigma_j} {A^{[\sigma_j]}}^\dagger A^{[\sigma_j]} &= \mathbb{1} \qquad \text{for } j <= k\,, \\ \sum_{\sigma_j} A^{[\sigma_j]} {A^{[\sigma_j]}}^\dagger &= \mathbb{1} \qquad \text{for } j > k\,. \end{aligned} \tag{2.10}$$

The orthonormality Eq. (2.9) for both the left- *and* right basis states holds only for the current site. For the other sites there is always only one orthonormal effective basis.

2.2.6 Orthonormalization of effective basis states

We now describe how an arbitrary MPS state can be rewritten into a form where its local view with respect to a given site has orthonormal left- and right basis states. It should be emphasized that this really just amounts to a reshuffling of information among the state's A-matrices without changing the state itself, by exploiting the freedom that we always can insert any $X^{-1}X = \mathbb{1}$ at any position in the matrix product state without altering it.

Assume site k to be the current site and assume that it has an orthonormal left basis (the latter is automatically fulfilled for $k = 1$). We need a procedure to ensure that, when the current site is switched to site $k+1$, this site, too, will have an orthonormal left basis. (This is required for the orthonormality properties used in the proof in Sec. A.1. A similar procedure can be used to ensure that site $k-1$ has an orthonormal right basis provided k has such a basis.) For this purpose we use the singular value decomposition (SVD, see Sec. A.2) for which we have to rewrite $A^{[\sigma_k]}_{l_k r_k}$ by *fusing* the indices l_k and σ_k:

$$A^{[\sigma_k]}_{l_k r_k} \widehat{=} A_{(l_k\sigma_k) r_k} = \sum_{m,n} u_{(l_k\sigma_k)m} s_{mn} \left(v^\dagger\right)_{nr_k} \widehat{=} \sum_{m} u^{[\sigma_k]}_{l_k m} \left(sv^\dagger\right)_{mr_k}\,, \tag{2.11}$$

where m, n and r_k have the same index range (see Fig. 2.3). Specifically, u fulfills

$$\mathbb{1} = u^\dagger u = \sum_{(l_k\sigma_k)} u^*_{(l_k\sigma_k),m'} u_{(l_k\sigma_k),m}\,, \tag{2.12}$$

which is equivalent to the orthonormality condition Eq. (2.10) for the $A^{[\sigma_k]}$-matrices.

[3] From now on the indices k or c are only displayed when several sites are involved. For the central site or in the case when only one A-matrix is considered the index will be dropped.

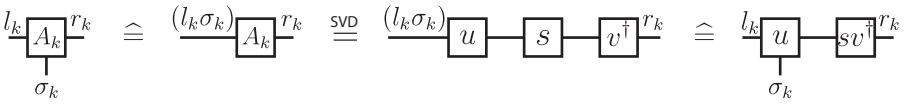

Figure 2.3: Singular value decomposition of the A-matrices

As u replaces $A^{[\sigma_k]}$ and $sv^\dagger$ is contracted onto $A^{[\sigma_{k+1}]}$, this leaves the overall state unchanged (for a graphical depiction see Fig. 2.4):

$$\begin{aligned} A^{[\sigma_k]}A^{[\sigma_{k+1}]} &= \sum_{(r_k=l_{k+1})} A^{[\sigma_k]}_{l_k r_k} A^{[\sigma_{k+1}]}_{l_{k+1} r_{k+1}} &&= \sum_{(r_k=l_{k+1})} \sum_m u^{[\sigma_k]}_{l_k m} \left(sv^\dagger\right)_{m r_k} A^{[\sigma_{k+1}]}_{l_{k+1} r_{k+1}} \\ &= u^{[\sigma_k]} \left(sv^\dagger A_{k+1}\right)^{[\sigma_{k+1}]} &&\equiv \tilde{A}^{[\sigma_k]} \tilde{A}^{[\sigma_{k+1}]} \,. \end{aligned} \tag{2.13}$$

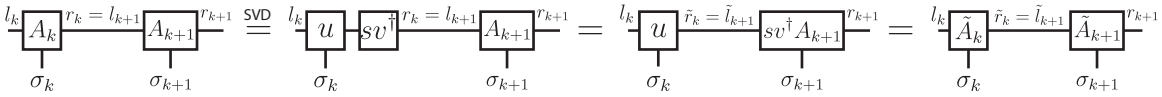

Figure 2.4: Rearrangement of the A-matrices to switch the current site from site k to $k+1$.

Site $k+1$ now has an orthonormal effective left basis. A similar procedure works for the effective right basis, see Fig. 2.5. To obtain an orthonormal effective left basis for the

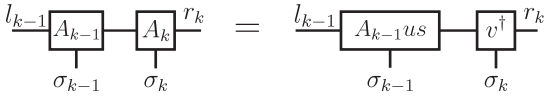

Figure 2.5: Orthonormal effective right basis for site $k-1$.

current site k, we start with the first site, update $A^{[\sigma_1]}$ and $A^{[\sigma_2]}$, move to the next site, update $A^{[\sigma_2]}$ and $A^{[\sigma_3]}$, and so on until site $k-1$. For an orthonormal effective right basis, we start from site N and apply an analogous procedure in the other direction.

If the state $|\psi\rangle$ is in the local description of site k with orthonormal basis sets $|l_k\rangle$, $|\sigma_k\rangle$ and $|r_k\rangle$, it is now very easy to change the current site to site $k\pm1$, with corresponding new orthonormal basis sets $|l_{k\pm1}\rangle$, $|\sigma_{k\pm1}\rangle$, $|r_{k\pm1}\rangle$. Suppose we want to change the current site from site k to site $k+1$. Following the procedure described above, site $k+1$ already has an orthonormal right basis and all sites left of site k fulfill the orthonormality condition. All that is left to do, is to update site k and $k+1$ to obtain an orthonormal left basis for site $k+1$. This is called a *switch* of the current site from site k to $k+1$. The switch from site k to site $k-1$ is done analogously.

2.2.7 Scalar product

The scalar product of two states $|\psi\rangle$ and $|\psi'\rangle$ is one of the simplest operations we can perform with matrix product states.[4] It is calculated most conveniently in the global view because then we do not need to care about orthonormalization of the A-matrices:

$$\begin{aligned}\langle\psi'|\psi\rangle &= \langle\sigma'_1|\dots\langle\sigma'_N| \sum_{\sigma'_1\dots\sigma'_N} \left(A'^{[\sigma'_1]}\dots A'^{[\sigma'_N]}\right)^* \sum_{\sigma_1\dots\sigma_N} \left(A^{[\sigma_1]}\dots A^{[\sigma_N]}\right)|\sigma_1\rangle\dots|\sigma_N\rangle \\ &= \sum_{\sigma_1\dots\sigma_N} \left(A'^{[\sigma_1]}\dots A'^{[\sigma_N]}\right)^* \left(A^{[\sigma_1]}\dots A^{[\sigma_N]}\right),\end{aligned} \tag{2.14}$$

using the orthonormality of the local basis $\langle\sigma'_k|\sigma_l\rangle = \delta_{kl}\delta_{\sigma'_k\sigma_k}$. In principle the order in which these contractions are carried out is irrelevant, but in practice it is possible to choose an order in which this summation over the full Hilbert space is carried out very efficiently by exploiting the one-dimensional structure of the matrix product state (see Fig. 2.6 for a graphical explanation). For details on the numerical costs, see Sec. A.3. In method (a), after contracting all A-matrices of $|\psi\rangle$ and $|\psi'\rangle$, we have to perform a contraction over the full Hilbert space, i.e. a $1 \times d^N$ matrix is multiplied with a $d^N \times 1$ matrix. This contraction is of order $\mathcal{O}\left(d^N\right)$, which is completely unfeasible for practical purposes. In method (b) the most 'expensive' contraction is in the middle of the chain, say at site k, and it is of order $\mathcal{O}\left(dD^3\right)$. Here the A-matrices are viewed as three-index objects $A_{l_k r_k \sigma_k}$ with dimension $D \times D \times d$. All sites left of site k are represented by a $D \times D$ matrix, say $L^{l_k}_{l'_k}$. Contracting this with the matrix at site k yields the object $\sum_{l_k} L^{l_k}_{l'_k} A_{l_k r_k \sigma_k}$, which has dimensions $D \times D \times d$, and since the sum contains D terms, the overall cost is $\mathcal{O}\left(dD^3\right)$ leading to a total cost of $\mathcal{O}(dD^3N)$ for the complete scalar product. Thus, in practice, method (b) is rather efficient and renders such calculations feasible in practice.

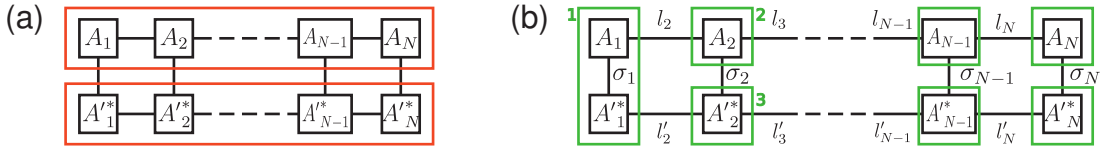

Figure 2.6: Scalar product, computed in two different orders. (a) First all A-matrices of $|\psi\rangle$ and $|\psi'\rangle$ are contracted and then contraction over the local indices is carried out. b) First, for site one, we contract over the local indices of A_1 and A'_1. Then we contract over the effective index between A_1 and A_2 and afterwards over the indices between the resulting object and $(A'_2)^*$. Proceeding over the whole chain yields the scalar product.

[4] Within the classical DMRG formulation using block states the scalar product of two distinct states can not be calculated in a straightforward way as, in general, the system and environment basis states are not identical for both states.

Partial product

Sometimes it is required to calculate a product over only a part of the matrix product state. This is done the same way as the scalar product

$$\left(P^{[L_k]}\right)_{l_k l'_k} \equiv \sum_{\sigma_1 \dots \sigma_{k-1}} \left(A^{[\sigma_1]} \dots A^{[\sigma_{k-1}]}\right)^*_{l'_k} \left(A^{[\sigma_1]} \dots A^{[\sigma_{k-1}]}\right)_{l_k} , \tag{2.15}$$

$$\left(P^{[R_k]}\right)_{r_k r'_k} \equiv \sum_{\sigma_{k+1} \dots \sigma_N} \left(A^{[\sigma_{k+1}]} \dots A^{[\sigma_N]}\right)^*_{r'_k} \left(A^{[\sigma_{k+1}]} \dots A^{[\sigma_N]}\right)_{r_k} , \tag{2.16}$$

$$\left(P^{[kk']}\right)_{r_k r'_k, l_{k'} l'_{k'}} \equiv \sum_{\sigma_{k+1} \dots \sigma_{k'-1}} \left(A^{[\sigma_{k+1}]} \dots A^{[\sigma_{k'-1}]}\right)^*_{r'_k\, l'_{k'}} \left(A^{[\sigma_{k+1}]} \dots A^{[\sigma_{k'-1}]}\right)_{r_k\, l_{k'}} . \tag{2.17}$$

Notice that $P^{[L_k]}$ and $P^{[R_k]}$ are matrices in the indices l_k and r_k, respectively (see Fig. 2.7). In fact, they correspond to the overlap matrices $\langle l'_k | l_k \rangle$ and $\langle r'_k | r_k \rangle$, respectively.

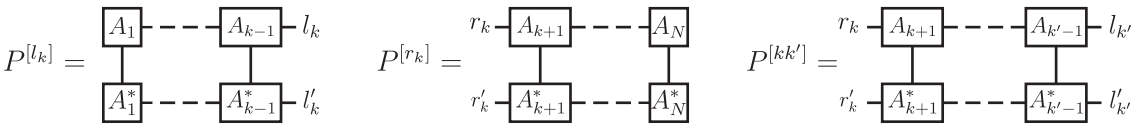

Figure 2.7: Partial products associated with site k.

2.2.8 Reduced density matrix

The pure density matrix given by the matrix product state $|\psi\rangle$ is defined as $\rho = |\psi\rangle\langle\psi|$. To describe only a part of the system, we need to calculate the reduced density matrix. Let I be a set of sites and $\sigma_\mathrm{s} = \{\sigma_{k\in I}\}$ a fused index for their local states. Tracing out all other sites with combined index $\sigma_\mathrm{b} = \{\sigma_{k\notin I}\}$ we obtain

$$\rho_I = \sum_{\sigma_1 \dots \sigma_N \sigma'_1 \dots \sigma'_N} \delta_{\sigma_\mathrm{b} \sigma'_\mathrm{b}} \left(A^{[\sigma'_1]} \dots A^{[\sigma'_N]}\right)^* \left(A^{[\sigma_1]} \dots A^{[\sigma_N]}\right) |\sigma_\mathrm{s}\rangle\langle\sigma'_s| . \tag{2.18}$$

This is a completely general expression, but in the cases where $I = \{k\}$ or $I = \{k, k'\}$ it reduces to (see Fig. 2.8)

$$\rho_{\{k\}} = P^{[L_k]} \left(A^{[\sigma_k]} \otimes A^{[\sigma'_k]^*}\right) P^{[R_k]} |\sigma_k\rangle\langle\sigma'_k| , \tag{2.19}$$

$$\rho_{\{kk'\}} = P^{[L_k]} \left(A^{[\sigma_k]} \otimes A^{[\sigma'_k]^*}\right) P^{[kk']} \left(A^{[\sigma_{k'}]} \otimes A^{[\sigma'_{k'}]^*}\right) P^{[R_{k'}]} |\sigma_k\rangle\langle\sigma'_k||\sigma_{k'}\rangle\langle\sigma'_{k'}| . \tag{2.20}$$

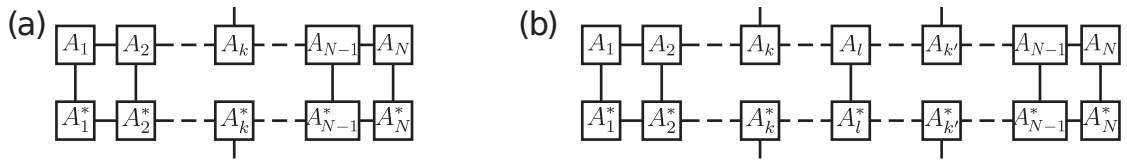

Figure 2.8: Reduced density matrix (a) $\rho_{\{k\}}$ for site k, (b) $\rho_{\{kk'\}}$ for sites k and k', where $k < l < k'$.

2.2.9 Hilbert space truncation

A central ingredient of DMRG is the truncation of the effective Hilbert spaces associated with a given A-matrix. The strategy for truncating the effective Hilbert spaces when using a MPS-based formulation is completely analogous to the original DMRG formulation [18]. The DMRG truncation scheme is based on discarding that part of the Hilbert space on which a certain density matrix has sufficiently small weight. There are two ways, how the Hilbert space truncation can manifest itself: as an explicit truncation of an appropriate reduced density matrix in two-site DMRG [4, 5, 35] and in an implicit way in one-site DMRG [35]. The main difference between the two is the size of the effective Hilbert space that is used at each step, which is reflected in the dimensions of the center matrix C and leads to slightly different properties of both variants. Originally, DMRG has been introduced as a method for calculating the ground state of a Hamiltonian by two-site sweeping through the state and performing local updates. Depending on what local updates are performed, different goals can be reached through sweeping and the sweeping is independent whether one or two sites are considered at a time. Sweeping details will be covered in Sec. 2.4 while here we will illustrate the differences between the one- and two-site algorithm, that mainly occur in the truncation of the effective Hilbert space.

One-site DMRG

One-site DMRG arises when variationally optimizing one site at a time, i. e. the center matrix being subject to the local updates has only *one* attributed expanded basis. In contrast to two-site DMRG, one-site DMRG does not easily allow for dynamical truncation during the calculation. (It is possible in principle to implement the latter, but if one decides to use dynamical truncation, it would be advisable to do so using two-site DMRG.) The truncation is fixed by the initial choice of D, but it is still possible to determine an estimate on the error of this truncation by analyzing the reduced density matrix. Starting from an expression for the full density matrix in the center matrix view (current site k, left basis expanded, C-matrix between sites k and $k+1$ has dimension $Dd \times D$)

$$\rho = |\psi\rangle\langle\psi| = \left(\sum_{lr} C_{lr}|l\rangle|r\rangle\right)\left(\sum_{l'r'} C^*_{l'r'}\langle l'|\langle r'|\right) = \sum_{lrl'r'} C_{lr}C^*_{l'r'}|l\rangle\langle l'||r\rangle\langle r'|\,. \tag{2.21}$$

We trace out the effective right basis and obtain a reduced density matrix for the left part of the system (including site k):

$$\rho^{[l_c]} = \sum_{lrl'} C_{lr} C^*_{l'r} |l\rangle\langle l'| = \sum_{lrl'} C_{lr} \left(C^\dagger\right)_{rl} |l\rangle\langle l'| = \sum_{ll'} \left(CC^\dagger\right)_{ll'} |l\rangle\langle l'| \,. \tag{2.22}$$

This reduced density matrix carries the label l_c because it corresponds precisely to the density matrix $|l_c\rangle\langle l'_c|$ of the expanded left basis $|l_c\rangle$.

In a pure one-site process we do not need to diagonalize the coefficient matrix $CC^\dagger$ to obtain the largest weights in the density matrix, because we get its eigenvalues as a byproduct of the following manipulations anyway [35]. To switch the current site we need to apply a singular value decomposition and obtain $C = usv^\dagger$. Now u gets contracted onto $A^{[\sigma_k]}$ and $sv^\dagger$ onto $A^{[\sigma_{k+1}]}$ (in close analogy to Sec. 2.2.6). Since the left basis is expanded $A^{[\sigma_k]} = \delta_{(l\sigma),r}$ and $A^{[\sigma_k]}$ is simply replaced by u in its index splitted form $u^{[\sigma_k]}$ also the new left basis of site $k+1$ gets expanded and a new center matrix gets constructed (for a graphical description see Fig. 2.9):

$$\begin{aligned} A^{[\sigma_k]} C A^{[\sigma_{k+1}]} A^{[\sigma_{k+2}]} &= \sum_{l_c l_{k+1} r_c r_{k+1}} \delta_{(l_k\sigma_k),l_c} u_{l_c l_{k+1}} \left(sv^\dagger\right)_{l_{k+1} r_c} A^{[\sigma_{k+1}]}_{r_c r_{k+1}} A^{[\sigma_{k+2}]}_{r_{k+1} r_{k+2}} \\ &= \sum_{l_{k+1} r_{k+1}} u_{(l_k\sigma_k),l_{k+1}} \left(sv^\dagger A_{k+1}\right)^{[\sigma_{k+1}]}_{l_{k+1} r_{k+1}} A^{[\sigma_{k+2}]}_{r_{k+1} r_{k+2}} \\ &= \sum_{l_{k+1} l_c r_c} u^{[\sigma_k]}_{l_k l_{k+1}} \delta_{(l_{k+1}\sigma_{k+1}),l_c} \left(sv^\dagger A_{k+1}\right)_{l_c r_c} A^{[\sigma_{k+2}]}_{r_c r_{k+2}} \\ &\equiv \tilde{A}^{[\sigma_k]} \tilde{A}^{[\sigma_{k+1}]} \tilde{C} A^{[\sigma_{k+2}]} \,. \end{aligned} \tag{2.23}$$

Having the SVD of C yields directly $CC^\dagger = usv^\dagger vsu^\dagger = us^2u^\dagger$, which corresponds to the diagonalization of $\rho^{[l_c]}$, implying that the weights of the density matrix are equal to s^2. Of course this works also for the right effective basis. With such an expression, we can check whether the effective Hilbert space dimension D of $\mathcal{H}^{l_{k+1}}$ is too small or not. For example, we could ask for the smallest singular value s_D to be at least n orders of magnitude smaller than the largest one s_1, i.e. the respective weights in the density matrix would be $2n$ orders of magnitude apart. If the singular values do not decrease that rapidly, we have to choose a greater D.

The above described procedure for moving the current site does not change the overall state and thus permits a strictly variational sweeping scheme. However, this pure one-site algorithm shows only slow convergence because no explicit truncation is performed and the number of singular values is bounded by D at every step. This can be improved by adding a small perturbation to the reduced density matrix $\rho^{[l_c]}$ [76] of the form

$$\rho^{[l_c]} \mapsto \rho^{[l_c]} + \epsilon \sum_\alpha B^\alpha \rho^{[l_c]} B^{\alpha\dagger} \,, \tag{2.24}$$

where B^α are usually parts of the Hamiltonian than couple the left and right part of the system (see [45, 76] for details) and ϵ is a small parameter typically chosen between

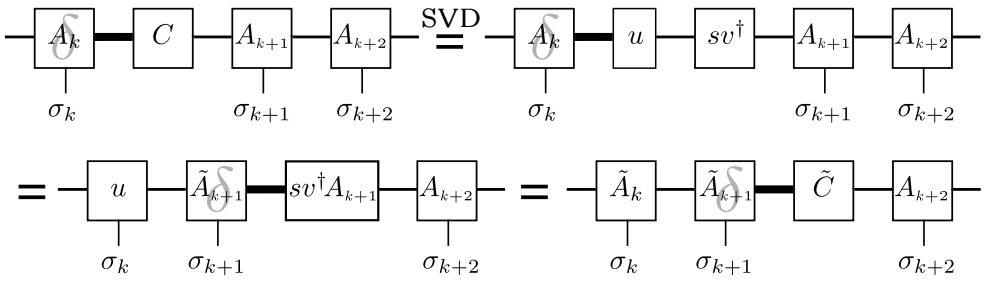

Figure 2.9: Procedure for switching the current site within one-site DMRG. Truncation requires a density matrix perturbation as in Eq. (2.24). Thick bonds indicate indices of dimension Dd instead of D. The gray δ inside a box indicates an A-matrix that provides an expanded basis according to Eq. (2.6).

$\mathcal{O}(10^{-2})$ and $\mathcal{O}(10^{-6})$. The price of this approach is that it is necessary to calculate the reduced density matrix $\rho^{[l_c]}$ explicitly and to diagonalize the perturbed density matrix $\rho' = UE^2U^\dagger \equiv C'C'^\dagger$ in order to obtain the new $C' = UE$, where E is a diagonal matrix containing the square root of the eigenvalues of the positive-semidefinite ρ'. C' has now dimension $Dd \times Dd$ instead of $Dd \times D$ as before thus we need to explicit truncate C'. This is achieved by keeping only the D biggest eigenvalues of ρ', i. e. keeping the first D columns of U and the first D entries on the diagonal of E. The truncated $Dd \times D$ C' is now treated exactly as in Eq. (2.23) for switching the current site only with $sv^\dagger$ replaced by the truncated $D \times D$ E and u by U. The added perturbation makes an part of the Hilbert space not reached by the local update accessible and allows for a controlled explicit Hilbert space truncation rendering this method no longer strictly variational. The truncated weight of ρ' can be analyzed like in the two-site case (see below). The parameter ϵ mediates between convergence speed (grows with ϵ) and final accuracy (decreases with ϵ).

Two-site DMRG

Two-site DMRG arises when variationally optimizing two sites at a time. We consider two current sites, say k and $k+1$, and we may choose the cutoff dimension site-dependent: $D \to D_k \equiv dim(\mathcal{H}^{l_k})$. Following Secs. 2.2.6 and 2.2.3, we assume site k to have an orthonormal left basis and site $k+1$ to have an orthonormal right basis and both the left and right basis of the center matrix expanded, yielding

$$\tilde{A}^{[\sigma_k]}_{l_k l_c} = \delta_{(l_k \sigma_k), l_c}\,, \quad \tilde{A}^{[\sigma_{k+1}]}_{r_c r_{k+1}} = \delta_{r_c, (\sigma_{k+1} r_{k+1})} \tag{2.25}$$

and the center matrix

$$C_{l_c r_c} = \sum_m (A_k)_{l_c = (l_k \sigma_k), m} \, (A_{k+1})_{m, r_c = (\sigma_{k+1} r_{k+1})}\,. \tag{2.26}$$

In this description we may perform the local updates (see Sec. 2.4) on the $Dd \times Dd$ matrix C. Afterwards, we need to move the center matrix view one site further. The reduced

density matrix of the left part of the system is given by Eq. (2.22), the only difference to the one-site case is the different size of C. Thus we can follow the steps of Eq. (2.23) very closely, while adding an explicit truncation of the Dd singular values and also expanding the new effective right basis of the next center matrix (see also Fig. 2.10 for a graphical description):

$$\begin{aligned}
A^{[\sigma_k]}CA^{[\sigma_{k+1}]}A^{[\sigma_{k+2}]} &\overset{\text{SVD}}{=} \sum_{l_c r_c r_{k+1}} \sum_{l_{k+1},m=1}^{Dd} \delta_{(l_k\sigma_k),l_c} u_{l_c l_{k+1}} s_{l_{k+1}m} \left(v^\dagger\right)_{mr_c} A^{[\sigma_{k+1}]}_{r_c r_{k+1}} A^{[\sigma_{k+2}]}_{r_{k+1}r_{k+2}} \\
&\overset{\text{trunc.}}{\approx} \sum_{l_c r_c r_{k+1}} \sum_{l_{k+1},m=1}^{D} \delta_{(l_k\sigma_k),l_c} u_{l_c l_{k+1}} s_{l_{k+1}m} \left(v^\dagger\right)_{mr_c} A^{[\sigma_{k+1}]}_{r_c r_{k+1}} A^{[\sigma_{k+2}]}_{r_{k+1}r_{k+2}} \\
&= \sum_{l_{k+1}r_{k+1}r_c} u_{(l_k\sigma),l_{k+1}} \left(sv^\dagger A_{k+1}\right)^{[\sigma_{k+1}]}_{l_{k+1}r_{k+1}} \left(A_{k+2}\right)_{r_{k+1}r_c} \delta_{r_c,(\sigma_{k+2}r_{k+2})} \\
&= \sum_{l_{k+1}l_c r_c} u^{[\sigma_k]}_{l_k l_{k+1}} \delta_{(l_{k+1}\sigma_{k+1}),l_c} \left(sv^\dagger A_{k+1}A_{k+2}\right)_{l_c r_c} \delta_{r_c,(\sigma_{k+2}r_{k+2})} \\
&\equiv \tilde{A}^{[\sigma_k]}\tilde{A}^{[\sigma_{k+1}]}\tilde{C}\tilde{A}^{[\sigma_{k+2}]} .
\end{aligned} \tag{2.27}$$

For simplicity, we have denoted the truncation in Eq. (2.27) from Dd states back to D states. As the truncation in the two-site case operates on both the expanded left and right basis states we are free to adapt D_k at every site. A common protocol is e. g. to

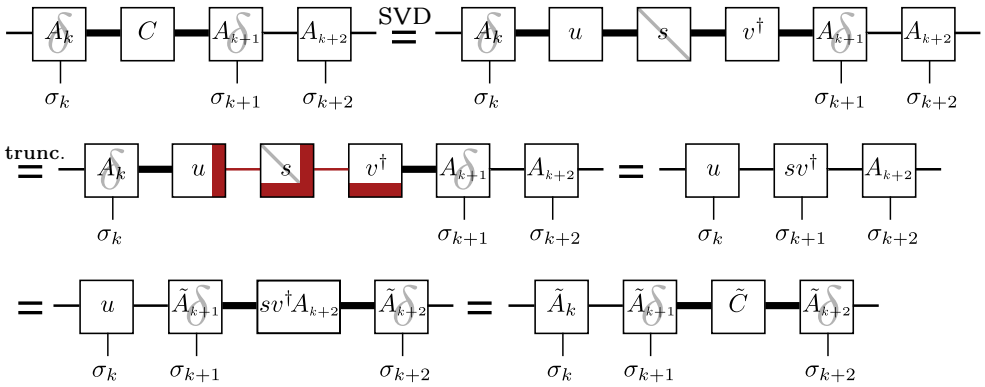

Figure 2.10: Procedure for switching the current site and truncation within two-site DMRG. Thick bonds indicate indices of dimension Dd instead of D. Truncation is shown in red. The gray δ inside a box indicates an A-matrix that provides an expanded basis according to Eq. (2.6) and the gray line under the s indicates that s is the diagonal matrix of singular values.

keep all singular values bigger than some threshold while setting a maximum number of states to keep. The error introduced by discarding some singular values at one site is called truncation error per site τ and is given by

$$\tau = \sum_{i>D} s_i^2 . \tag{2.28}$$

This step makes the method not strictly variational, since we discard some part of the Hilbert space, which could increase the energy. It turns out that this potential increase of energy is negligible and outbalanced by the advantages of having an explicit truncation and using an bigger Hilbert space for the local updates in practice. We can obtain a measure for the information lost due to truncation by using the von Neumann entropy $S = -\operatorname{tr}(\rho \ln \rho)$, given by

$$\varepsilon \equiv -\sum_{i>D} s_i^2 \ln\left(s_i^2\right) , \tag{2.29}$$

where $\sum s_i^2 = 1$ due to the normalization of $|\psi\rangle$.

State truncation

It is often desirable to truncate a given MPS $|\psi\rangle$ further so that the truncated state $|\psi'\rangle$ has smaller dimensions D'. One way of obtaining $|\psi'\rangle$ is to move the current size once through the whole state using the two-site DMRG description from above, but truncating down to $D' < D$. A more preferable way is to determine $|\psi'\rangle$ through *fitting sweeps* (see Sec. 2.4.4) thereby finding the $|\psi'\rangle$ with dimension D' that optimally represents $|\psi\rangle$.

2.2.10 Adding MPS

Another useful operator on MPS is the addition $|\psi\rangle = |\phi\rangle + |\chi\rangle$ which can be performed directly in the global view without caring for orthonormalization of the states and is exact. The A-matrices of $|\psi\rangle$ are given by the direct sum $A_\psi^{[\sigma_k]} = A_\phi^{[\sigma_k]} \oplus A_\chi^{[\sigma_k]}$ and can easily be written in block form in terms of the A-matrices of $|\phi\rangle$ and $|\chi\rangle$:

$$A_\psi^{[\sigma_1]} = \begin{pmatrix} A_\phi^{[\sigma_1]} & A_\chi^{[\sigma_1]} \end{pmatrix}, \quad A_\psi^{[\sigma_k]} = \begin{pmatrix} A_\phi^{[\sigma_k]} & 0 \\ 0 & A_\chi^{[\sigma_k]} \end{pmatrix}, \quad A_\psi^{[\sigma_N]} = \begin{pmatrix} A_\phi^{[\sigma_N]} \\ A_\chi^{[\sigma_N]} \end{pmatrix}. \tag{2.30}$$

Any previous valid orthonormalization constraints will be invalidated and need to be reestablished after the addition is completed. The cost of having an exact addition is the increased dimension of the resulting state $D_\psi = D_\phi + D_\chi$. This is often undesirable and a truncation step can be applied to reduce D_ψ.

Alternatively, instead of a separate addition and truncation process the *fitting technique* (see Sec. 2.4.4) can generate an optimal approximation to $|\phi\rangle + |\chi\rangle$ in one step.

2.3 Matrix product operators

Any operator for a Hilbert space of N sites has the form

$$O = \sum_{\sigma'_1 \ldots \sigma'_N, \sigma_1 \ldots \sigma_N} O_{\sigma'_1 \ldots \sigma'_N, \sigma_1 \ldots \sigma_N} |\sigma'_1\rangle\langle\sigma_1| \ldots |\sigma'_N\rangle\langle\sigma_N| . \tag{2.31}$$

The same rationale as for MPS can be applied to operators leading to a matrix product representation for operators in analogy to Eq. (2.2) which was first recognized for density matrix operators [14, 77]

$$O = \sum_{\sigma'_1 \dots \sigma'_N, \sigma_1 \dots \sigma_N} B^{[\sigma'_1, \sigma_1]} \dots B^{[\sigma'_N, \sigma_N]} |\sigma'_1\rangle\langle\sigma_1| \dots |\sigma'_N\rangle\langle\sigma_N| \,, \tag{2.32}$$

where each $B^{[\sigma'_k, \sigma_k]}$ is a matrix so that B_k is a rank 4 object. It turns out, that almost all physically relevant operators (e. g. the Hamiltonian and its constituents) can be represented exactly as a matrix product operator (MPO) with very low dimension D_B (i. e. the dimension of $B^{[\sigma'_k, \sigma_k]}$) making the MPO formulation a useful tool in practice. Here, we will describe the basic usage of MPOs. For more details we refer to [45, 78–80] and the appendix of [47].

2.3.1 Graphical representation

MPOs are depicted graphically in complete analogy to MPS, each B is represented by a box with 4 (at the beginning and end of the system 3) links attached corresponding to the indices of B, where the up/ down links represent the physical basis and the left/ right links assemble the matrix product. Connected links denote a contraction over the respective indices (see Fig. 2.11). Multiplying a MPO and a MPS is straightforward. By

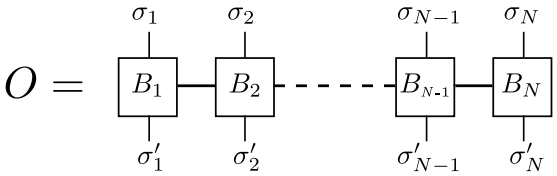

Figure 2.11: Graphical representation of an MPO

aligning the MPO to the bottom of the MPS and connecting the physical indices (thereby contracting) the product is carried out. From the graphical construction it is obvious that the MPS-form of the resulting state is retained.

2.3.2 Construction of MPOs

For operators acting on a single site and products thereof the corresponding MPO has bond dimension $D_B = 1$ and the individual B-matrices are just the operators at these sites. For the example of c_1, the annihilation operator for the first site, we have

$$B^{[\sigma'_1, \sigma_1]} = (c)_{\sigma'_1, \sigma_1} \,, \qquad B^{[\sigma'_k, \sigma_k]} = (\mathbb{1})_{\sigma'_1, \sigma_1} \quad \forall k > 1 \,. \tag{2.33}$$

We review the MPO-representations of operators consisting of a sum of local terms and of a sum of nearest-neighbor terms, which make out the most important building blocks

of common Hamilton operators and can be found e. g. in [45]. For the sum of local terms $H_l = \sum_{i=1}^{N} S_i^z$ we yield 2×2 B-matrices

$$B^{[\sigma_1',\sigma_1]} = \begin{pmatrix} S^z_{\sigma_1',\sigma_1} & \delta_{\sigma_1',\sigma_1} \end{pmatrix}, \quad B^{[\sigma_k',\sigma_k]} = \begin{pmatrix} \delta_{\sigma_k',\sigma_k} & 0 \\ S^z_{\sigma_k',\sigma_k} & \delta_{\sigma_k',\sigma_k} \end{pmatrix}, \quad B^{[\sigma_N',\sigma_N]} = \begin{pmatrix} \delta_{\sigma_N',\sigma_N} \\ S^z_{\sigma_N',\sigma_N} \end{pmatrix} \tag{2.34}$$

and for the nearest-neighbor operator $H_{\mathrm{nn}} = \sum_{i=1}^{N-1} S_i^x S_{i+1}^x$ we obtain 3×3 B-matrices

$$B_1 = \begin{pmatrix} 0 & S^x & \mathbb{1} \end{pmatrix}, \quad B_k = \begin{pmatrix} \mathbb{1} & 0 & 0 \\ S^x & 0 & 0 \\ 0 & S^x & \mathbb{1} \end{pmatrix}, \quad B_N = \begin{pmatrix} \mathbb{1} \\ S^x \\ 0 \end{pmatrix} \tag{2.35}$$

where we dropped the local indices.

2.3.3 Arithmetic with MPOs

A MPO can be formally mapped to a MPS by fusing the local σ and σ' indices of the B-matrices of the MPO. That way the whole toolbox of MPS operations is available for MPOs, too. Especially, the *scalar product* adapted this way for MPOs allows to define a numerically feasible measure for the distance [79] of two MPOs and thus makes the versatile *fitting* technique (see Sec. 2.4.4) also available for operators. Nevertheless, because of the often small MPO dimensions it may be desirable to perform simple arithmetic on MPO exactly.

Adding MPOs

The sum of two MPOs is calculated exactly as the sum of two MPSs. So for $Q = O + P$ the bulk B-matrices of Q are given by

$$B_Q^{[\sigma_k',\sigma_k]} = \begin{pmatrix} B_O^{[\sigma_k',\sigma_k]} & 0 \\ 0 & B_P^{[\sigma_k',\sigma_k]} \end{pmatrix}, \tag{2.36}$$

the B-matrices at the first and last site have row and column vector form as in Eq. (2.30).

Multiplying MPOs

The multiplication of two MPOs is very similar to the scalar product of MPS, the connecting local indices are being contracted only the result retains MPO form

$$O' \otimes O = \sum_{\substack{\sigma_1' \ldots \sigma_N' \\ \sigma_1 \ldots \sigma_N}} \sum_{s_1 \ldots s_N} \left(B'^{[\sigma_1',s_1]} B^{[s_1,\sigma_1]} \right) \ldots \left(B^{[\sigma_N',s_N]} B^{[s_N,\sigma_N]} \right) |\sigma_1'\rangle\langle\sigma_1| \ldots |\sigma_N'\rangle\langle\sigma_N|. \tag{2.37}$$

As a consequence immediately visible in Fig. 2.12 the dimension of the resulting MPO is given by the product of the dimensions of both factors since their indices are just fused into the new bond index. In most cases the new dimension will be too big and a separate truncation needs to be done, alternatively, the fitting technique can be used to calculate the operator product in one step.

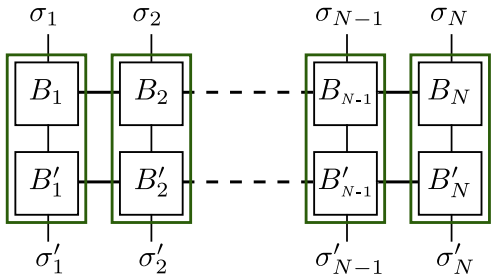

Figure 2.12: Multiplication of two MPOs. The green boxes indicate the resulting B-matrices after the contraction of the local indices. The bond indices become fused, yielding the product of the former dimensions as new dimension.

MPO acting on a MPS

Multiplying a MPO onto a MPS is a very common operation and works almost the same as multiplying two MPOs

$$O|\psi\rangle = \sum_{\sigma_1 \ldots \sigma_N} \sum_{s_1 \ldots s_N} \left(B^{[\sigma_1, s_1]} A^{[s_1]}\right) \ldots \left(B^{[\sigma_N, s_N]} A^{[s_N]}\right) |\sigma_1\rangle \ldots |\sigma_N\rangle. \tag{2.38}$$

For simple (low dimensional) operators this direct calculation (see Fig. 2.13) works fine. For more complicated MPOs a fitting approach (see Sec. 2.4.4) will be favorable as results

$O|\psi\rangle =$

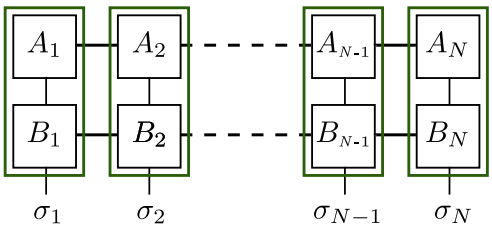

Figure 2.13: MPS multiplied by a MPO. The green boxes show the new A-matrices while the bond dimensions grow to the product of the former dimensions.

would require further truncation anyway.

Expectation values

While the calculation of expectation values can be thought of as two step process with first calculating the product $|\psi'\rangle = O|\psi\rangle$ and then the overlap $\langle O\rangle = \langle\psi|\psi'\rangle$, it is numerically recommendable to perform the calculation in a single step

$$\langle\psi|O|\psi\rangle = \sum_{\sigma'_1 \ldots \sigma'_N \ldots \sigma_1 \ldots \sigma_N} \left(A^{[\sigma_1]^*} B^{[\sigma'_1, \sigma_1]} A^{[\sigma_1]}\right) \ldots \left(A^{[\sigma_N]^*} B^{[\sigma'_N, \sigma_N]} A^{[\sigma_N]}\right). \tag{2.39}$$

The necessary contractions should be carried out in analogy to the scalar product discussed in Sec. 2.2.7 and also indicated in Fig. 2.14.

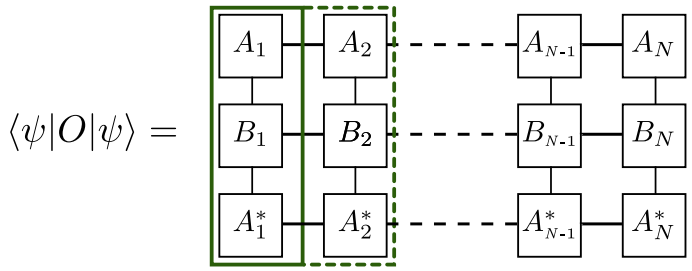

Figure 2.14: Expectation value of a MPO. The contractions are to be carried out recursively as indicated by the green boxes. First all indices inside the solid box are contracted out. Then the dashed box is contracted piecewise onto the already obtained object. This is repeated until all indices are contracted.

2.3.4 Operators in an effective basis

Above we described various manipulations on MPOs and MPS within the global picture. When performing local updates during sweeps (see Sec. 2.4), however, we operate in the center matrix view of a state and thus need to be able to perform the same manipulations also in the center matrix view. This is done using the basis transformation properties of the A-matrices discussed in Sec. 2.2.5.

Let k be the current site with the center matrix C and orthonormal effective basis sets $|l_c\rangle$ and $|r_c\rangle$, where one or both are expanded. What we now need is a (approximate) representation of any operator within this basis

$$O = O_{l'_c r'_c l_c r_c} |l'_c\rangle\langle l_c||r'_c\rangle\langle r_c| = E^{\alpha}_{l'_c l_c} F^{\alpha}_{r'_c r_c} |l'_c\rangle\langle l_c||r'_c\rangle\langle r_c|. \tag{2.40}$$

Taking the matrix product structure of the operator O into account O can be split into an *left* and *right* part E^{α} and F^{α} operating on the left and right part of the effective Hilbert space, respectively. The index α stems from the bond index of the MPO at bond k. The effective operator representation[5] E^{α} is obtained (assuming proper orthonormalization for the center view) by the following recursive prescription[6] (see Fig. 2.15 for an illustration)

$$E^{\alpha}_{l'_2 l_2} = \sum_{\sigma_1 \sigma'_1} A^{[\sigma'_1]^*}_{l'_2} B^{[\sigma'_1,\sigma_1]}_{\alpha} A^{[\sigma_1]}_{l_2} \tag{2.41a}$$

$$E^{\alpha}_{l'_{n+1} l_{n+1}} = \sum_{\substack{l'_n l_n \beta \\ \sigma_n \sigma'_n}} E^{\beta}_{l'_n l_n} A^{[\sigma'_n]^*}_{l'_n l'_{n+1}} B^{[\sigma'_n,\sigma_n]}_{\beta\alpha} A^{[\sigma_n]}_{l_n l_{n+1}} . \tag{2.41b}$$

The recursion step Eq. (2.41b) is iterated until the current effective basis $|l_c\rangle \equiv |l_n\rangle$ is reached. For the *right* part of the operator F^{α} exactly the same scheme is used iterating from site N down until the center matrix C is reached. As the center matrix moves through the system during a sweep this recursive prescription makes it easy to maintain a effective

[5] We drop the site index of E^{α} if it can be deduced from the basis state labels.

[6] The same terms also appear as intermediate results when calculating expectation values via Eq. (2.39).

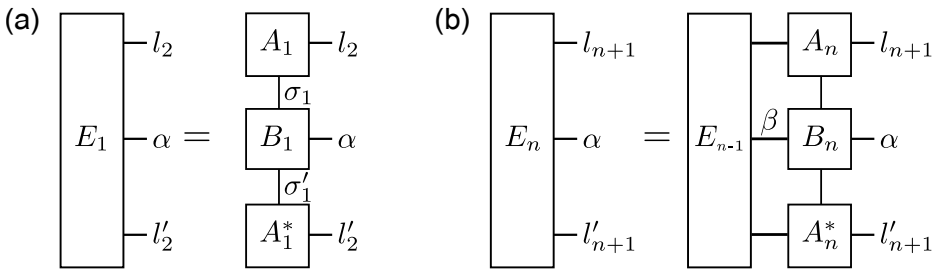

Figure 2.15: Calculation of the effective operator representation E^α. (a) Initial step at the beginning of the system. Iteration step (b) is repeated until the effective left basis of the center site is reached.

representation of any MPO within the current basis. E. g. when moving the right from k to $k+1$ only E_{k+1} needs to be calculated as F_{k+2} is already known from the previous left sweep or the initial calculation of the effective operator representation.

Having an effective description of the MPO O via Eq. (2.40) makes manipulations of a state $|\psi\rangle$ in the center matrix view of Eq. (2.5) straightforward (see Fig. 2.16 for illustration). The action of an operator on a state is given by

$$O|\psi\rangle = C'_{l_c r_c}|l_c\rangle|r_c\rangle = \sum_{\alpha l'_c r'_c} E^\alpha_{l_c l'_c} F^\alpha_{r_c r'_c} C_{l'_c r'_c}|l_c\rangle|r_c\rangle \tag{2.42}$$

and the scalar product is given by

$$\langle\psi|O|\psi\rangle = \sum_{\alpha l'_c r'_c l_c r_c} C^*_{l_c r_c} E^\alpha_{l_c l'_c} F^\alpha_{r_c r'_c} C_{l'_c r'_c}\,. \tag{2.43}$$

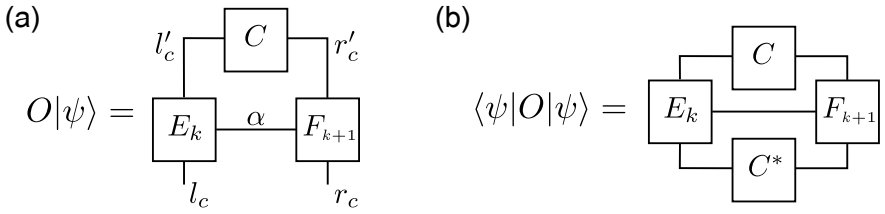

Figure 2.16: Using the effective operator representation. Once the center matrix view of the state $|\psi\rangle$ and the associated effective operator representation of O has been obtained acting with operator on states and calculating expectation values is straightforward in the center matrix picture.

For simple operators as e. g. the creation operator $c^\dagger$ of a single site the MPO formalism may seem exaggerated. However, for such operators the corresponding MPO takes an almost trivial form. All B-matrices are 1×1 and have as sole entry the identity operator for the local states space $|\sigma\rangle$ and only on one site $c^\dagger$ instead. While operating in the global picture the identity operators can be ignored from a numerical point of view. The same

is true in the center matrix view with proper orthonormalization guaranteed. So there is no real drawback caused by MPOs while the formulation and manipulation of complex operator expression is greatly simplified.

Above, we only presented an effective representation for MPOs using the center matrix view. In principle the same can be done using the local view of Eq. (2.1). The respective effective Hilbert spaces are equivalent span $(|l_c\rangle \otimes |r_c\rangle) \equiv$ span $(|l_k\rangle \otimes |\sigma_k\rangle \otimes |r_k\rangle)$ for one-site DMRG case, but in the center matrix it consists of only two parts instead of three simplifying all operations within the effective basis.

2.4 Variational optimization scheme

The basic techniques introduced in the previous sections are the building blocks for DMRG sweeps, an iterative scheme to determine an optimal approximation for a certain state. The most common use is finding the optimal MPS representation for the ground state of a given Hamiltonian operator. This scheme starts at some site as current site and optimized the state $|\psi\rangle$ with respect to the current center matrix. This optimization is done by performing a *local update* of the center matrix C within the current effective Hilbert space. Afterwards the center matrix is shifted by one site and the next local update is performed.[7] The process of shifting the center matrix through the whole system once[8] and optimizing at every site is called a *sweep* and is illustrated in Fig. 2.17. These sweeps are repeated until $|\psi\rangle$ converges.

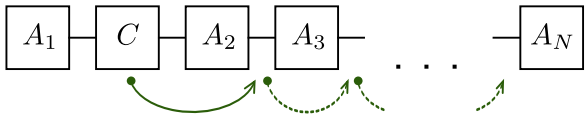

Figure 2.17: One rightward sweep. At each step the current center matrix C is optimized and then moved on step further to the right.

Although DMRG sweeps have first been used for groundstate calculations where the optimization goal at each step is to minimize the energy of $|\psi\rangle$, *sweeping* is a general concept for solving a high dimensional optimization problem within the space of MPS. Of course the nature of the local updates will be adapted for each optimization problem. Below we will first describe the local updates for groundstate calculations, followed by the correction-vector method for Greens functions in Sec. 2.4.3 and the fitting method used for truncation and general operator expressions in Sec. 2.4.4.

[7] Sites where no truncation takes places because of accordingly chosen dimensions may be skipped.

[8] For the more complex MPS geometry used in Chapter 3 we defined a sweep slightly different to have the current site at the same position before and after one sweep.

2.4.1 Convergence

At the end of each sweep the convergence of the state $|\psi\rangle$ needs to be checked. One criterion feasible for all types sweeps is the change of the state during a single sweep. If $|\psi\rangle$ already is a good approximation to the goal of the calculation then $|\psi\rangle$ will change only by a small amount during the next sweep. This can be tested by calculating the overlap of $|\psi\rangle$ before and after a sweep. If the normalized overlap differs from 1 only by a small number ϵ_1 (typically $\epsilon_1 \simeq 10^{-6} \dots 10^{-10}$ depending on the problem), the last sweep did not improve $|\psi\rangle$ and we can assume the sweeping has led to a converged state:

$$|1 - \langle\psi_{i-1}|\psi_i\rangle| \leq \epsilon_1 \,, \tag{2.44}$$

where the $|\psi_i\rangle$ denotes the state obtained after sweep number i. Additionally, one can check the relative change of the overlaps

$$\frac{|\langle\psi_{i-1}|\psi_i\rangle - \langle\psi_{i-2}|\psi_{i-1}\rangle|}{|\langle\psi_{i-1}|\psi_i\rangle|} \leq \epsilon_2 \,, \tag{2.45}$$

with ϵ_2 chosen similar to ϵ_1. When no good initial guess state $|\psi_0\rangle$ is known, we start with a random MPS. Especially in that case but also when we know the initial state is not good, it is favorable to start sweeping with a relatively small dimension $D \simeq 50$ and upon convergence gradually increase D until the desired dimension is reached. This narrows the risk of stopping the sweeping prematurely because the above criteria detect erroneous no relevant change to the state. It is also more efficient to obtain a good approximation with small D first and only then make the effort of sweeps with higher D as the costs of each step scale with D^3.

2.4.2 Ground state

In order to find the ground state of the system we have to minimize the energy $E = \langle\psi|H|\psi\rangle$ of the matrix product state $|\psi\rangle$ with the constraint that the norm of $|\psi\rangle$ must not change. Introducing λ as Lagrange multiplier to ensure proper normalization, we arrive at the problem of determining

$$\min_{|\psi\rangle} \left(\langle\psi|H|\psi\rangle - \lambda\langle\psi|\psi\rangle\right) . \tag{2.46}$$

In the sweeping procedure introduced above, the current site is changed from one site to the next and the energy is minimized in each local description. Thus, we need Eq. (2.46) in terms of the parameters of the current center matrix. Inserting Eq. (2.5) into Eq. (2.46) yields (see Fig. 2.18)

$$\min_{C} \left(\sum_{lrl'r'\alpha} C^*_{l'r'} E^\alpha_{l'l} F^\alpha_{r'r} C_{lr} - \lambda \sum_{lr} C^*_{lr} C_{lr} \right) , \tag{2.47}$$

where E and F are the representation of $H_{\text{eff}} = \sum_\alpha E^\alpha F^\alpha$ in the effective basis as introduced in Eq. (2.40).

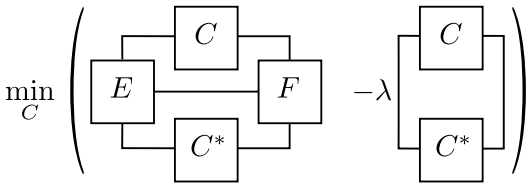

Figure 2.18: The minimization problem expressed in the current center matrix.

The multi-dimensional minimization problem Eq. (2.46) has been transformed to a local minimization problem of only one C-matrix while all A-matrices are kept constant. Such a procedure could, in principle, cause the system to get stuck in a local minimum in energy, but experience shows that the procedure works well [35], especially in the presence of a gap.

To obtain a solution for Eq. (2.47), we differentiate the equation with respect to $C^*_{l'r'}$ (this is possible because the Hilbert space has an hermitian scalar product) and obtain

$$0 = \sum_{lr} (H_{\text{eff}})_{l'r'lr} C_{lr} - \lambda C_{l'r'} \,. \tag{2.48}$$

The effective MPO representation of H $(H_{\text{eff}})_{l'r'lr} = E^{\alpha}_{l'l} F^{\alpha}_{r'r}$ may be calculated easily using the techniques introduced in Sec. 2.3.4. Changing to matrix notation and replacing λ with E_0 in anticipation of its interpretation as an energy, we obtain an eigenvalue equation:

$$H_{\text{eff}} C = E_0 C \,. \tag{2.49}$$

The minimization problem reduces to a local eigenvalue problem, which can be solved by standard techniques. The full Hilbert space of the current local problem has dimension $D^2 d$ for the one-site DMRG (or $D^2 d^2$ for the two-site DMRG, respectively) and may become large, but it is not necessary to determine the full spectrum of H_{eff}, since we are interested only in the ground state. The Lanczos [81] algorithm is an effective algorithm to achieve exactly that, the Arnoldi [82] and Davidson [83] methods are viable alternatives. The advantage of this algorithm is that we only have to compute $H|\psi\rangle$, which saves much effort. The Lanczos algorithm produces as output the ground state eigenvalue and eigenvector, the latter giving the desired optimized version of the matrix C_{lr}.

Details

Before the actual sweeping may be started we have to set up an initial state in the center matrix view. Usually, we start with the current site $k = 1$, placing the center matrix C at the first bond, with a proper expanded effective basis. In addition we prepare the effective representation of the Hamiltonian at this position $H_{\text{eff}} = E^{\alpha}_1 F^{\alpha}_2$. It is advisable to store all the $F^{\alpha}_n \; \forall \, n > 2$ needed to calculate F^{α}_2 as they can be used again when optimizing other sites. Now everything is in place to perform the optimization of the current C-matrix. Therefore we solve the eigenvalue problem Eq. (2.49) approximately by a Lanczos solver,

however limit the number of Lanczos iterations to $N_{\text{Lanczos}} \simeq 10$. This usually is sufficient to improve the state while not wasting too much effort as the basis $|l_c\rangle|r_c\rangle$ is only an approximation. After having replaced C by the output of the Lanczos we move the center matrix view one site to the right as described in Sec. 2.2.9. Also the effective Hamiltonian operator needs to be adapted to $H_{\text{eff}} = E_2^\alpha F_3^\alpha$, where only E_2^α needs to be calculated as shown in Eq. (2.41b) and F_3^α is already known. One may consider storing an updated[9] E_1^α for later use. With that everything is set up for the next optimization step of the current C-matrix.

This procedure is repeated until the end of the chain is reached and this sweep is completed. Then the convergence of $|\psi\rangle$ is checked as described in Sec. 2.4.1 and additionally the analog checks can be performed on the groundstate energy available also at every Lanczos optimization step. If $|\psi\rangle$ has not sufficiently converged another sweep this time from right to left is performed. the sweeps are repeated until $|\psi\rangle$ is converged.

As the ground state is an eigenstate to the Hamiltonian operator it is possible to measure the quality of $|\psi\rangle$ by evaluating the variance [21]

$$\sigma^2 = \langle\psi|H^2|\psi\rangle - \left(\langle\psi|H|\psi\rangle\right)^2 . \tag{2.50}$$

The variance is proportional to the squared difference of the MPS solution and the exact ground state (in first order) and as such a measure for the quality of the MPS ground state. For a converged state the truncation error τ from Eq. (2.28) is proportional to $\sqrt{\sigma^2}$ [45].

Numerical costs

The step with the most impact on the numerical costs of the algorithm is the calculation of $H|\psi\rangle$ in the Lanczos method. This method is an iterative scheme using several *Lanczos steps*, of which usually only ~ 10 are carried out at one step. Each Lanczos step calculates $H|\psi\rangle$ exactly once. This calculation basically consists of elementary matrix multiplications, see Sec. A.3 for details on the numerical costs of such calculations. The costs of the multiplication of the effective Hamiltonian operator with the C-matrix in Eq. (2.49) are of order $\mathcal{O}\left(D^3 d^2 D_B\right)$ for the one-site DMRG and $\mathcal{O}\left(D^3 d^3 D_B\right)$ for the two-site DMRG, where D_B denotes the dimension of the MPO H in both cases. The total numerical cost for the minimization process (two-site DMRG) is

$$C = N_{\text{Sweep}} \times N \times N_{\text{Lanczos}} \times \left(D^3 d^3 D_B\right) , \tag{2.51}$$

where N_{Sweep} is the number of sweeps, N the chain length and N_{Lanczos} the number of Lanczos steps. In practice the MPS cutoff dimension D is significantly higher than the both the local Hilbert space dimension d and the MPO dimension D_B of H and thus the dominating factor of Eq. (2.51) is $\mathcal{O}\left(D^3\right)$.

[9] E_1^α will change after the A_1 providing the expanded basis $|l_c\rangle$ is updated in the site-switching/ truncation step of Eq. (2.23) or Eq. (2.27).

2.4.3 Correction vector

Evaluating static quantities like expectation values or correlators is straightforward using the techniques described above once the ground state $|\psi\rangle$ has been obtained. Dynamic quantities like Greens functions, however, are much more challenging. A typical zero temperature Greens function has the form

$$\mathcal{G}_\eta^{\mathcal{AB}}(\omega) = \langle\psi_0|\mathcal{A}\frac{1}{E_0+\omega+i\eta-H}\mathcal{B}|\psi_0\rangle\,, \tag{2.52}$$

where $|\psi_0\rangle$ and E_0 denote the ground state and its energy of the Hamiltonian operator H and η is a positive infinitesimal. The corresponding spectral function would be given by $\mathcal{A}^{\mathcal{AB}}(\omega) = -\lim_{\eta\to 0}\frac{1}{\pi}\Im\mathcal{G}_\eta^{\mathcal{AB}}(\omega)$. Working in frequency space the underlying problem for evaluating Eq. (2.52) is an inversion problem within a very high dimensional Hilbert space and the effective basis provided by $|\psi_0\rangle$ to represent H is optimized for low-energy sector of the Hilbert space and thus is not adequate for H^{-1}. Switching to the time domain via a Fourier transform is possible [84, 85] but only shifts the problem to calculating a time evolution which is also challenging for long times.

Historically, the first approach for calculating Greens functions with DMRG has been the continued fraction or Lanczos approach [6] which uses the Lanczos algorithm to obtain a tridiagonal Hamiltonian operator which is in turn inverted by a continued fraction. This approach is numerically inexpensive yet turned out to work well only for simple systems where no excitation continuum exists. Recently the continued fraction technique has been ported to a MPS based scheme thereby improving the quality to some extent [86].

The DMRG standard approach to Eq. (2.52) in frequency space is the so-called *correction vector* approach [7, 87] which allows to calculate accurate Greens functions with, however, substantial numerical effort. In Sec. 4.1 we present a novel adaption of Chebyshev techniques [88] to DMRG while here we will outline the correction vector method.

Defining the correction vector [89] through

$$|\chi(\omega,\eta)\rangle = \frac{1}{E_0+\omega+i\eta-H}\mathcal{B}|\psi_0\rangle \tag{2.53}$$

the Greens function is given by a simple expectation value $\mathcal{G}_\eta^{\mathcal{AB}}(\omega) = \langle\psi_0|\mathcal{A}|\chi(\omega,\eta)\rangle$ while $|\chi\rangle$ is the solution of the linear system

$$(E_0+\omega+i\eta-H)\,|\chi\rangle = \mathcal{B}|\psi_0\rangle\,. \tag{2.54}$$

There exist several slightly different approaches for solving Eq. (2.54): solving the real and imaginary part separately [7], reformulation of Eq. (2.54) into a minimization problem [8] or a variational optimization of the correction vector [21]. Here we formulate a direct solution through local updates of the MPS $|\chi\rangle$. Therefore, we switch to the center matrix view of $|\chi\rangle$ and insert an approximate identity operator $\sum_{l_c r_c}|l_c\rangle\langle l_c||r_c\rangle\langle r_c|$ in the left hand side of Eq. (2.54) and multiply with $\langle l_c'|\langle r_c'|$ from the left, leading to

$$\sum_{l_c r_c}\langle l_c'|\langle r_c'|\,(E_0+\omega+i\eta-H)\,|l_c\rangle|r_c\rangle\langle l_c|\langle r_c||\chi\rangle = \langle l_c'|\langle r_c'|\mathcal{B}|\psi_0\rangle. \tag{2.55}$$

As the left/ right basis $|l_c\rangle$/ $|r_c\rangle$ is constructed from the A-matrices to the left/ right to the center matrix C, we recognize the left hand side of Eq. (2.55) as the product of a MPO with the state $|\chi\rangle$ in the center matrix view and the right hand side as the transformation of $\mathcal{B}|\psi_0\rangle$ into the effective current basis of $|\chi\rangle$. In a more compact notation we have (see Fig. 2.19 for a sketch)

$$E^{\alpha}_{l'l} F^{\alpha}_{r'r} C_{lr} = G_{l'r'} \,, \tag{2.56}$$

where $E^{\alpha}F^{\alpha}$ is the current effective representation of the MPO $E_0 + \omega + i\eta - H$ and $G = \langle l'_c|\langle r'_c|\mathcal{B}|\psi_o\rangle$ (graphical definition in Fig. 2.19).

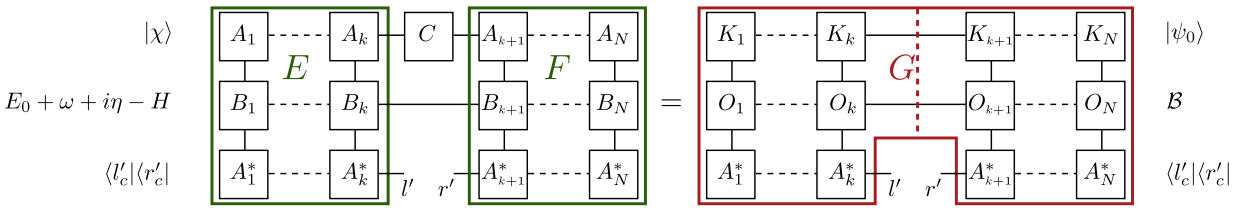

Figure 2.19: Linear system of Eq. (2.56) in the center matrix view with the matrices building up the effective representations E^{α}, F^{α} and G still shown as parts of the colored bigger blocks. The MPS $|\chi\rangle$ is represented by the matrices A and the center matrix C, the MPO $E_0 + \omega + i\eta - H$ by the matrices B, the MPS $|\psi_0\rangle$ by the matrices K and the MPO $\mathcal{B}$ by the matrices O as also indicated at the left and right side of the figure.

The local linear system Eq. (2.56) can be solved by the generalized minimal residual method (GMRES) [90], alternatively the stabilized biconjugate gradient method (BICG-STAB) [91] can also be used. Having the local update for the correction vector established the complete procedure for calculating $|\chi\rangle$ is as follows. Prepare for sweeping by providing the center matrix view of $|\chi\rangle$, the effective representation $E^{\alpha}F^{\alpha}$ and G, where with regard to G one might consider storing the partial overlaps for the left and right part similar to E^{α} and F^{α}. Then start sweeping using the solution of Eq. (2.56) for the local update until convergence. For the correction vector the only viable convergence measure is the overlap of $|\chi\rangle$ before and after the current sweep as outlined in Sec. 2.4.1. For good results the dimension D of $|\chi\rangle$ usually has to be increased compared to $|\psi_0\rangle$.

2.4.4 Fitting algorithm

Given a MPS $|\phi\rangle$ it may be useful to calculate an approximation $|\psi\rangle$ to $|\phi\rangle$ such that the squared norm

$$\mathcal{N}^2 = \| |\psi\rangle - |\phi\rangle \|^2 \tag{2.57}$$

is minimal [75]. Common examples for this are the truncation of $|\phi\rangle$ to a state $|\psi\rangle$ with smaller dimension $D_\psi < D_\phi$ or to approximate $|\phi\rangle = O|\varphi\rangle$ where O is a complicated (high dimensional) MPO. The scheme can be straightforwardly generalized to the case of $|\phi\rangle$ being a complicated expression of operator terms acting on several MPSs and we make heavy use of this in Chapter 4. Here however, we restrict ourselves to the simple case of an ordinary MPS $|\phi\rangle$ to keep the notation concise.

In order to minimize $\mathcal{N}^2$ we write $|\psi\rangle$ and $\langle\psi|$ in the center matrix form and set the derivative w. r. t. to C^* to zero

$$\begin{aligned} 0 &= \frac{\partial}{\partial C^*}\mathcal{N}^2 = \frac{\partial}{\partial C^*}\langle\psi|\psi\rangle - \frac{\partial}{\partial C^*}\langle\psi|\phi\rangle \\ &= \sum_{lr}\left(P^{[L_k]}_{\langle\psi|\psi\rangle}\right)_{l'l} C_{lr}\left(P^{[R_k]}_{\langle\psi|\psi\rangle}\right)_{r'r} - \sum_{m}\left(P^{[L_k]}_{\langle\psi|\phi\rangle}\right)_{l'm}\left(P^{[R_k]}_{\langle\psi|\phi\rangle}\right)_{r'm}, \end{aligned} \tag{2.58}$$

where $P^{[L_k]}$ and $P^{[R_k]}$ denote partial scalar products defined in Eqs. (2.15) and (2.16) with an extra subscript to indicate the corresponding scalar product. Due to the orthonormalization properties of the A-matrices to the left and right of C the first term simplifies through $\left(P^{[L_k]}_{\langle\psi|\psi\rangle}\right)_{l'l} = \delta_{l'l}$ and $\left(P^{[R_k]}_{\langle\psi|\psi\rangle}\right)_{r'r} = \delta_{r'r}$ leading to

$$C_{l'r'} = \sum_{m}\left(P^{[L_k]}_{\langle\psi|\phi\rangle}\right)_{l'm}\left(P^{[R_k]}_{\langle\psi|\phi\rangle}\right)_{r'm} \tag{2.59}$$

as a prescription for the local update also depicted in Fig. 2.20. The complete fitting

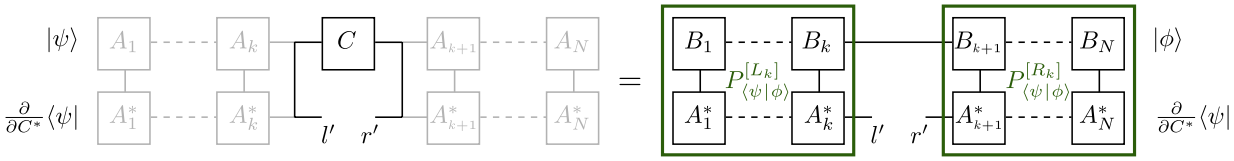

Figure 2.20: Local update for the fitting algorithm. The A-matrices together with the center matrix C represent the state $|\psi\rangle$ while $|\phi\rangle$ is represented by the matrices B. The partial scalar products reducing to $\delta_{l'l}$ and $\delta_{r'r}$ are displayed in gray.

procedure consists of sweeps on $|\psi\rangle$ using Eq. (2.59) for the local update of each center site using the convergence tests of Sec. 2.4.1. As a final check of the quality of the converged $|\psi\rangle$ we can check the value of $\langle\psi|\phi\rangle$ which should be very close to one. As the maximal value of $\langle\psi|\phi\rangle$ that is reachable depends on the dimension D_ψ of $|\psi\rangle$ it is difficult to employ as a sole convergence criterion without also checking the changes of $\langle\psi|\phi\rangle$ after each sweep.

2.5 Symmetries

Matrix product states can be easily adapted to properly account for conserved quantum numbers, representing the global symmetries of the Hamiltonian operator. Common examples include the particle number N and total spin $\boldsymbol{S}$ or its z-component S_z. We will limit ourselves to Abelian symmetries, meaning that the irreducible representation of the symmetry group is Abelian, as these are easily implemented, which is not necessarily the case for non-Abelian symmetries [92, 93].

An Abelian symmetry allows a quantum number Q to be attached to every state. The property that the symmetry is Abelian manifests itself in that this quantum number is

strictly additive. For two states $|Q_1\rangle$ and $|Q_2\rangle$, the quantum number of the direct product of these two states is given by $|Q_1\rangle \otimes |Q_2\rangle = |Q_1 + Q_2\rangle$. For example, if the Hamiltonian operator commutes with the number operator for the full system, the quantum number Q could represent particle number.

For matrix product states, the introduction of Abelian symmetries has the consequence that the A-matrix $A^{[\sigma]}_{lr}$ may be written as $(A^{Q_\sigma}_{Q_l Q_r})^{\gamma_\sigma}_{\alpha_l \beta_r}$. Here Q_σ, Q_l, Q_r are the quantum numbers attached to the local, left effective and right effective basis, respectively. The index α_l distinguishes different states $|Q_l, \alpha_l\rangle$ characterized by the same quantum number Q_l, and similarly for $|Q_r, \beta_r\rangle$ and $|Q_\sigma, \gamma_\sigma\rangle$. If A describes, for example, the mapping of the $|l\rangle$-basis of the left block together with the local basis to a combined (truncated) $|r\rangle$-basis, then the only non-zero blocks of the A-matrix are those for which $Q_\sigma + Q_l = Q_r$. For the current site, the total symmetry Q_{tot} of the full quantum many-body state manifests itself in that the corresponding A-matrix fulfills $Q_l + Q_r + Q_\sigma = Q_{\text{tot}}$.

For the handling of matrix product states quantum numbers imply a significant amount of bookkeeping, i.e. for every state we have to store its quantum number. The benefit is that we can deal with large effective state spaces at reasonable numerical cost. The Lanczos algorithm, in particular, takes advantage of the block structure.

Of course, the treatment of Abelian symmetries is generic and not limited to only one symmetry. We may incorporate as many symmetries as exist for a given Hamiltonian operator, by writing Q as a vector of the corresponding quantum numbers.

2.6 Time evolution

For the sake of simplicity of the following discussion, we restrict ourselves to time-independent Hamiltonian operators. This restriction is straight-forward to lift as all here presented approaches perform the time evolution for small time steps Δt at a time. For a time-dependent Hamiltonian operator $H(t)$, Δt is limited from above to a time interval ΔT such that $H(t)$ is approximately constant for the interval $[t, t + \Delta T]$, resulting in a time evolution of a piecewise constant Hamiltonian operator.

The central problem in calculating the time evolution of a certain quantum state is given by the time evolution operator

$$U(t) = e^{-iHt}\,, \tag{2.60}$$

requiring the exponentiation of H. The exponentiation of a big matrix alone poses a numerical challenge [94] which is even bigger in DMRG since the Hamiltonian operator has an accessible, yet approximate, matrix representation only in the effective basis at each site. We will illustrate two commonly used approaches for approximating the exponential of Eq. (2.60), the Trotter-Suzuki decomposition in Sec. 2.6.1 and the Krylov subspace method in Sec. 2.6.2.

In the first attempts of time evolution [95] the DMRG specific problem of not having an explicit representation of H was addressed by working with a fixed current site. Thereby essentially only the center matrix expressing the state is time-evolved while the left and

right effective basis states remain constant in time (static). The use of static effective basis states severely limits the accessible time scales. With the invention of *adaptive* time-dependent DMRG (tDMRG) [9–11, 13] the simulation of the time evolution for reasonable long time intervals became possible. The key idea to tDMRG is that not only the current center matrix but also all A-matrices are evolved in time leading to an evolution of the effective basis states as well.

2.6.1 Trotter-Suzuki decomposition

For the case of H containing only local and nearest-neighbor interactions we can split the Hamiltonian operator into "bond" terms h_j acting only on sites j and $j+1$

$$H = H_{\text{odd}} + H_{\text{even}} = \sum_{j=1}^{N-1} h_j \,, \qquad \text{with } H_{\text{odd}} = \sum_{j \text{ odd}} h_j \,, \quad H_{\text{even}} = \sum_{j \text{ even}} h_j \,. \tag{2.61}$$

With this separation into odd and even terms we apply the Trotter-Suzuki decomposition [96] in first order for a small time step Δt on the time evolution operator

$$U(\Delta t) = e^{-iH\Delta t} = e^{-iH_{\text{odd}}\Delta t} e^{-iH_{\text{even}}\Delta t} + \mathcal{O}(\Delta t^2) \,. \tag{2.62}$$

Higher order decompositions exist [97], especially the second and forth order expression are popular [36], which reduce the *Trotter error*, i. e. the error introduced in Eq. (2.62), but for simplicity we consider only the first order decomposition, here. Since all terms of H_{odd} and H_{even} commute with each other the remaining operator exponentials like $e^{-iH_{\text{odd}}\Delta t}$ factor into $e^{-iH_{\text{odd}}\Delta t} = \prod_{j \text{ odd}} e^{-ih_j\Delta t}$. Each of the factors $e^{-ih_j\Delta t}$ can be calculated directly as h_j has only size $d^2 \times d^2$.

It is now straight-forward to apply $U(\Delta t)$ of Eq. (2.62) onto a state $|\psi\rangle$. First, during one sweep through the system all e. g. odd bond terms $e^{-ih_j\Delta t}$ are multiplied one after each other onto $|\psi\rangle$ in the matching center matrix representation, typically immediately followed by a truncation to keep the dimensions manageable which would otherwise grow from D to d^2D. On the following sweep back, all even bond terms are applied in the same manner. After sweeping back and forth once the state $|\psi\rangle$ is propagated in time by Δt. This prescription is iterated until the designated total time is reached. For higher order Trotter-Suzuki decompositions in general more sweeps are necessary for a single time step, however, bigger time steps are possible due to their reduced Trotter error.

Alternatively, it is possible to convert each bond term $e^{-ih_j\Delta t}$ into MPO form by performing one SVD. So each term $e^{-iH_{\text{odd}}\Delta t}$ and $e^{-iH_{\text{even}}\Delta t}$ can be represented as a MPO and one Trotter-Suzuki time step is given by two MPOs as demonstrated in Fig. 2.21. The product $U(\Delta t)|\psi\rangle$ can be calculated via two MPO-MPS products which can even be performed in a variational way (see Sec. 2.4.4).

In practice, these differences in the evaluation of $U(\Delta t)|\psi\rangle$ play only a minor role as in both approaches the numerical errors are controllable. Writing the time evolution operator in MPO form, however, opens new possibilities. It is now possible to formally apply the

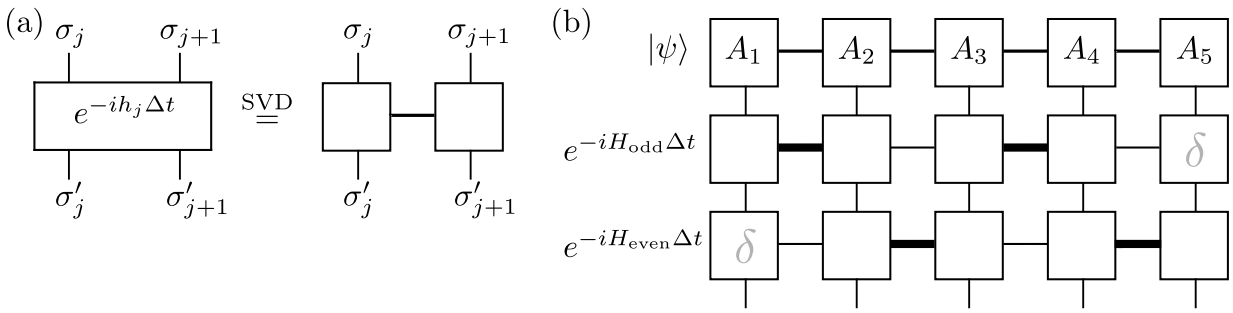

Figure 2.21: Trotter-Suzuki time evolution operator $U(\Delta t)$ in MPO form. (a) SVD to obtain the MPO form for a single bond term $e^{-ih_j\Delta t}$ of $U(\Delta t)$. (b) Complete MPO for one time step of a $N = 5$ system, thick lines indicate MPO dimension $D_B > 1$. MPO matrices consisting of identity operators are labeled by a gray δ.

time evolution operator repeatedly until the desired time is reached without explicitly calculating the states $|\psi(n\Delta t)\rangle$. Considering a time-dependent expectation value $\langle\psi|O(t)|\psi\rangle$ of an operator O, such a formal representation of the time evolved state $|\psi(t)\rangle$ leads to a two-dimensional tensor network which gives, once fully contracted, the value $\langle\psi|O(t)|\psi\rangle$ (see Fig. 2.22). So far this is only a reformulation of how time-dependent expectation values are typically evaluated. As we will shortly mention below in Sec. 2.6.3 a new technique generated by this novel view improves efficiency for time-dependent calculations.

2.6.2 Krylov subspace method

In contrast to the Trotter-Suzuki decomposition for $U(t)$ which is "ignorant" about the state $|\psi\rangle$ which is to be time evolved, the Krylov subspace method strives for an approximation of $U(t)$ tailored onto $|\psi\rangle$. Defining the Krylov subspace [98] of dimension d_K

$$\mathcal{K}_{d_K}(H, |\psi\rangle) = \text{span}\{|\psi\rangle, H|\psi\rangle, H^2|\psi\rangle, \ldots, H^{d_K-1}|\psi\rangle\} \tag{2.63}$$

and corresponding Krylov vectors $|k_l\rangle = H^l|\psi\rangle +$ orthonormalization, allows for an approximation of H within the Krylov space $\mathcal{K}_{d_K}(H, |\psi\rangle)$

$$(H_K)_{lm} = \langle k_l|H|k_m\rangle\,. \tag{2.64}$$

The time evolution of $|\psi\rangle$ is now given as

$$U(\Delta t')|\psi\rangle = \sum_l \left(e^{-iH_K\Delta t'}\right)_{l0} |k_l\rangle\,. \tag{2.65}$$

The use of the Krylov approximated H_K in the exponential of Eq. (2.65) is the main source of error, but it is well understood and can be controlled [99]. To implement this strategy with MPS every Krylov vector k_l is represented as a MPS of its own to avoid an overly increase on the MPS dimension. All steps of this calculation can be carried out using the techniques of Secs. 2.2 and 2.3.

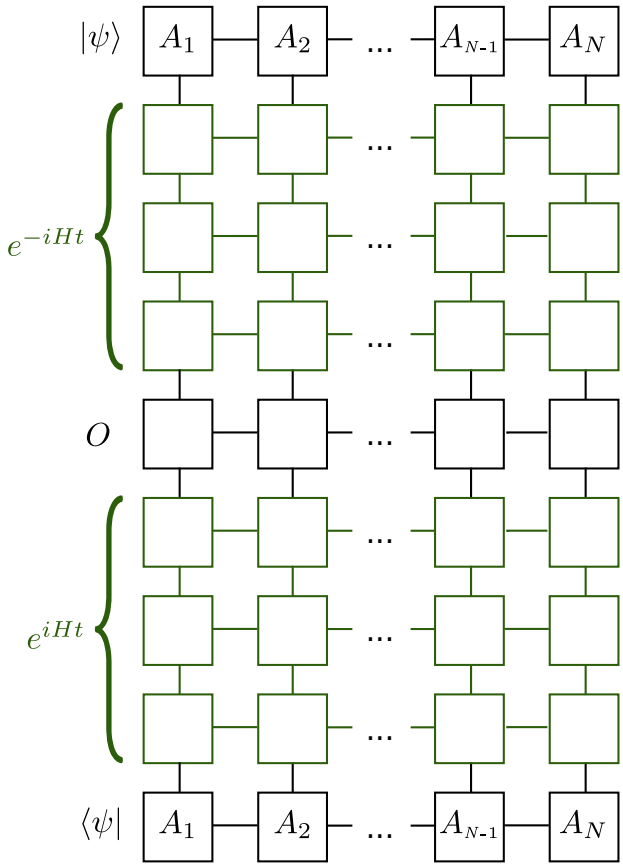

Figure 2.22: Two dimensional tensor network which encodes $\langle\psi|O(t)|\psi\rangle$. The time evolution operators are shown in green.

The time interval $\Delta t'$ used for a single time step for the Krylov subspace method differs from Δt for the Trotter-Suzuki decomposition and we typically have $\Delta t' > \Delta t$ with Krylov subspace dimensions of $d_K = \mathcal{O}(10)$.

The main advantage of the Krylov subspace method compared to the Trotter-Suzuki decomposition is that the Krylov method is applicable for an arbitrary Hamiltonian H including long range interaction terms. As a minor technical advantage the Krylov dimension d_K and time step $\Delta t'$ can be adapted dynamically according to a desired error bound often allowing $\Delta t' > \Delta t$. On the downside, there is no easy MPO representation for the Krylov time evolution operator in Eq. (2.65) as the Krylov subspace $\mathcal{K}(H, |\psi\rangle)$ depends on the state $|\psi\rangle$ to be time evolved.

2.6.3 Limitations

In both schemes the errors specific to the method can be controlled, nevertheless, for long times the error of the time evolution grows exponentially [100] due to the truncation error which is introduced to keep the MPS dimensions manageable. The physical reason for

the increasing difficulty to represent $|\psi(t)\rangle$ as an MPS lies in the at most linear growth of entanglement [65]. Trying to represent an MPS with linear growing entanglement would in turn require exponential resources [101] which strongly limits the time scales accessible via tDMRG and prohibits an extension of the reachable maximal time by simply increasing the MPS dimension.

As a potential way around this problem, a very promising new idea for contracting the tensor network for a time-dependent expectation value of Fig. 2.22 has been suggested recently [102]. By "folding" the tensor network of Fig. 2.22 in half and diverting from the standard order of contraction the usual buildup of entanglement gets reduced allowing for significantly longer time scales. This approach is assumed to allow for an extension of the reachable time scales by a factor of 2 to 5 [103] while using the same amount of resources as standard tDMRG.

As a different way of dealing with the entanglement growth in the time evolved state it has been already earlier been speculated [12] about representing $|\psi(t)\rangle$ as a linear combination of several states and thus dividing the entanglement over all these states. The Chebyshev expansion of the time evolution operator which we discuss in Sec. 4.2 has this property.

Chapter 3

Matrix product state approach for a two-lead, multi-level Anderson impurity model

In this chapter we investigate a two-lead Anderson model by modelling each lead as a seperate Wilson chain. The resulting MPS starlike geometry is quasi-1-dimensional and with a adaption of the sweeping sequence all DMRG techniques are accessible. We furthermore show that the representation of the leads can be improved by introducing an "optimal" chain basis. This "optimal" chain basis effectively decouples degrees of freedom on different Wilson chains further out the chains and turns out to also diagonalize the chain-to-chain scattering matrix of the model.

PHYSICAL REVIEW B **81**, 125126 (2010)

Matrix product state approach for a two-lead multilevel Anderson impurity model

Andreas Holzner,[1,2] Andreas Weichselbaum,[1] and Jan von Delft[1]
[1]*Physics Department, Arnold Sommerfeld Center for Theoretical Physics, and Center for NanoScience, Ludwig-Maximilians-Universität München, D-80333 München, Germany*
[2]*Institute for Theoretical Physics C, RWTH Aachen University, D-52056 Aachen, Germany*
(Received 10 December 2009; published 26 March 2010)

We exploit the common mathematical structure of the numerical renormalization group and the density-matrix renormalization group, namely, matrix product states, to implement an efficient numerical treatment of a two-lead multilevel Anderson impurity model. By adopting a starlike geometry, where each species (spin and lead) of conduction electrons is described by its own Wilson chain, instead of using a single Wilson chain for all species together, we achieve a very significant reduction in the numerical resources required to obtain reliable results. We illustrate the power of this approach by calculating ground-state properties of a four-level quantum dot coupled to two leads. The success of this proof-of-principle calculation suggests that the star geometry constitutes a promising strategy for future calculations the ground-state properties of multiband multilevel quantum impurity models. Moreover, we show that it is possible to find an "optimal" chain basis, obtained via a unitary transformation (acting only on the index distinguishing different Wilson chains), in which degrees of freedom on different Wilson chains become effectively decoupled from each other further out on the Wilson chains. This basis turns out to also diagonalize the model's chain-to-chain scattering matrix. We demonstrate this for a spinless two-lead model, presenting DMRG results for the mutual information between two sites located far apart on different Wilson chains, and NRG results with respect to the scattering matrix.

DOI: 10.1103/PhysRevB.81.125126 PACS number(s): 78.20.Bh, 02.70.−c, 72.15.Qm, 75.20.Hr

I. INTRODUCTION

A very successful method for solving quantum impurity models is Wilson's numerical renormalization group (NRG) (Refs. 1–3). Recently, it has been pointed out[4] that the approximate eigenstates of the Hamiltonian produced by NRG have the structure of matrix product states (MPSs).[5] This observation established a structural relation between NRG and the density-matrix renormalization group (DMRG) (Refs. 6–8) because the states produced by the latter likewise have the form of MPS.[9–13]

This structural relation between NRG and DMRG has opened up very interesting perspectives for combining advantageous features of both methods. In particular, the fact that DMRG, in essence, is a method for variationally optimizing MPSs (Refs. 9, 12, and 13) can be used to devise a corresponding variational treatment of quantum impurity models.[4,14] This has the advantage that MPSs with much richer more complex structures can be adopted than those produced by standard NRG, entailing a much more efficient use of numerical resources. Concretely, the dimension D of the matrices from which the MPS is constructed can be reduced very significantly, typically by several orders of magnitude. As a result, it becomes feasible to study complex quantum impurity problems that would be very challenging for standard NRG.

In this paper, we illustrate this idea by calculating ground-state properties of a multilevel quantum dot coupled to two spinful leads (Fig. 1). Standard NRG treats the latter as a single quantum chain with 2^4 states per site (to account for two spin and two lead degrees of freedom), for which one typically needs $D \gtrsim 4000$ to achieve satisfactory results. In contrast to the latter "single-chain geometry," we adopt here a MPS with a "star geometry," involving four separate chains, each with only two states per site, and variationally optimize one chain after the other. This enables us to obtain good results using matrices with D ranging between 16 and 36. This reduction in numerical memory resources relative to standard NRG illustrates the increased numerical efficiency alluded to above. Furthermore, we show that a numerically optimal basis, involving rotated Wilson chains, can be found by requiring that the new representation minimizes the mutual information between different chains. This optimal basis has an instructive physical interpretation: it is the basis in which the chain-to-chain scattering matrix is diagonal.

This paper is structured as follows. In Sec. II we briefly review why standard NRG produces MPSs with a single-chain geometry and advocate the adoption of MPSs with an alternative star geometry. In Sec. III, we describe how a star-MPS representation of the ground state can be determined by variationally minimizing its energy. In Sec. IV we present proof-of-principle calculations of some ground-state properties and comparisons thereof to NRG results. Finally, Sec. V illustrates how a numerically optimal basis for the chains can be obtained by effectively minimizing the mutual information between two sites of different chains.

II. MATRIX PRODUCT STATE ANSATZ

A. Model

We study a multilevel two-lead Anderson impurity model described by the following Hamiltonian:

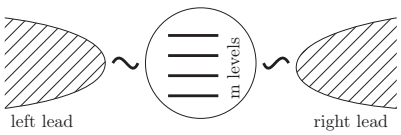

FIG. 1. Quantum dot coupled to two leads.

 ©2010 The American Physical Society

$$H = H_{\text{dot}} + H_{\text{int}} + H_{\text{leads}} + H_{\text{coupling}}, \tag{1}$$

where H_{dot} describes the eigenenergies of the m dot levels

$$H_{\text{dot}} = \sum_{i=1}^{m} \sum_{s=\uparrow,\downarrow} \epsilon_{is} d_{is}^{\dagger} d_{is}, \tag{2}$$

H_{int} is the Coulomb interaction on the dot

$$H_{\text{int}} = \frac{U}{2} \sum_{(i,s)\neq(j,s')} d_{is}^{\dagger} d_{is} d_{js'}^{\dagger} d_{js'}, \tag{3}$$

H_{leads} is the free lead Hamiltonian for N_{l} leads ($\alpha = 1, \ldots, N_{\text{l}}$)

$$H_{\text{leads}} = \sum_{\tilde{k}\alpha s} \epsilon_{\tilde{k}} c_{\tilde{k}\alpha s}^{\dagger} c_{\tilde{k}\alpha s}, \tag{4}$$

and H_{coupling} is the coupling between the dot levels and the leads

$$H_{\text{coupling}} = \sum_{i\tilde{k}\alpha s} V_{i\alpha} (d_{is}^{\dagger} c_{\tilde{k}\alpha s} + c_{\tilde{k}\alpha s}^{\dagger} d_{is}). \tag{5}$$

At a late stage of this work we became aware of work of Kashcheyevs *et al.*[15] suggesting to perform a singular value decomposition on H_{coupling} which has the merit of decoupling some levels from some leads. Applying this idea to our system should also give some improvement in numerical efficiency. In general, however, all the levels will remain to be coupled to all leads. As we will show later, a more general scheme than just a singular value decomposition is capable of generating a new basis for the leads that will minimize the coupling of the leads among themselves.

Following Wilson,[1] we adopt a logarithmic discretization of the conduction bands and tridiagonalize $H_{\text{leads}}+H_{\text{coupling}}$. As a result, the dot, represented by the "dot site," is coupled to the first sites of $2N_{\text{l}}$ separate "Wilson" chains, labeled by (α, s)

$$H_{\text{coupling}} = W \sum_{i\alpha s} \sqrt{\frac{2\Gamma_{i\alpha}}{\pi W}} (f_{0\alpha s}^{\dagger} d_{is} + d_{is}^{\dagger} f_{0\alpha s}), \tag{6}$$

$$H_{\text{leads}} = W \sum_{\alpha s} \frac{1}{2}(1+\Lambda^{-1}) \times \sum_{n=0}^{L-1} \Lambda^{-n/2} \xi_n (f_{n\alpha s}^{\dagger} f_{(n+1)\alpha s} + \text{H.c.}). \tag{7}$$

Here $\xi_n = (1-\Lambda^{-n-1})(1-\Lambda^{-2n-1})^{-1/2}(1-\Lambda^{-2n-3})^{-1/2}$ are coefficients of order 1, $\Gamma_{i\alpha} = \pi\rho V_{i\alpha}^2$ the hybridization, ρ is the density of states, and $2W$ is the bandwidth of the conduction bands of the leads centered at the Fermi edge. We set the NRG discretization parameter $\Lambda = 2$ throughout this paper.

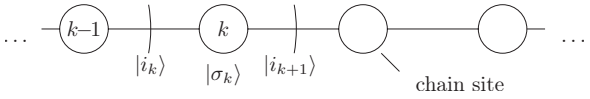

FIG. 2. Iterative generation of matrix product states for a chain.

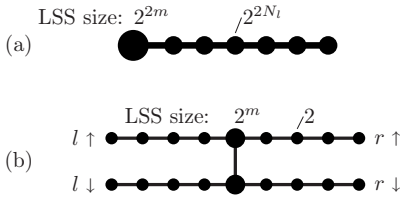

FIG. 3. (a) Single chain geometry: a single Wilson chain of local dimension $2^{2N_{\text{l}}}$ coupled to one dot site of local dimension 2^{2m}. (b) Star geometry: $2N_{\text{l}}$ Wilson chains (here $N_{\text{l}}=2$ and $\alpha=l,r$), each with local dimension 2, coupled to two dot sites of local dimension 2^m.

The length L of the Wilson chain determines the energy resolution with which the lowest-lying eigenstates of the chain are resolved. We typically choose $L=60$.

A standard NRG treatment of this model would combine all four Wilson chains into a single one, whose sites are labeled by a single site index $k=0,\ldots,L$ [see Fig. 3(a)]. Each site would represent a $2^{2N_{\text{l}}}$-dimensional local state space, consisting of the set of states $\{|\sigma_k\rangle\}$, where the state label σ_k takes on $2^{2N_{\text{l}}}$ different values. Then one proceeds to diagonalize the Hamiltonian iteratively, as follows: suppose a short Wilson chain up to and including site $k-1$ has been diagonalized exactly, yielding a set of eigenstates $|i_k\rangle \in \text{span}\{\{|\sigma_1\rangle\}\otimes\{|\sigma_2\rangle\}\otimes\cdots\otimes\{|\sigma_{k-1}\rangle\}\}$. Then one adds the next site, k, to the chain, thereby enlarging the Hilbert space by a factor of $2^{2N_{\text{l}}}$, diagonalizes the Hamiltonian in this enlarged space, and truncates by discarding all but the lowest D eigenstates of the Hamiltonian. The latter can in general be written as linear combinations of the following form (illustrated in Fig. 2):

$$|i_{k+1}\rangle = \sum_{i_k,\sigma_k} A_{i_k,i_{k+1}}^{[\sigma_k]} |i_k\rangle|\sigma_k\rangle. \tag{8}$$

Iterating this procedure up to and including site L produces eigenstates of the form

$$|i_{L+1}\rangle = A_{i_k,i_{k+1}}^{[\sigma_k]} \cdots A_{i_L,i_{L+1}}^{[\sigma_L]} |i_k\rangle|\sigma_k\rangle\cdots|\sigma_L\rangle, \tag{9}$$

where sums over repeated indices are implied. Since such states are completely characterized by sums over products of matrices, they have come to be known as matrix product states. The form of these MPS produced by NRG is analogous to the state for a chain as shown in Fig. 4.

B. Star geometry

One limiting factor for the accuracy of the NRG approach is that a certain amount of information is lost at each iteration step due to truncation. In general, for a system with N_{l} bands (in the two-lead case which we will investigate below,

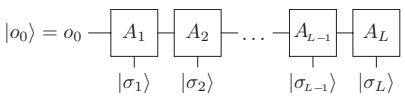

FIG. 4. Graphical representation of Eq. (10a).

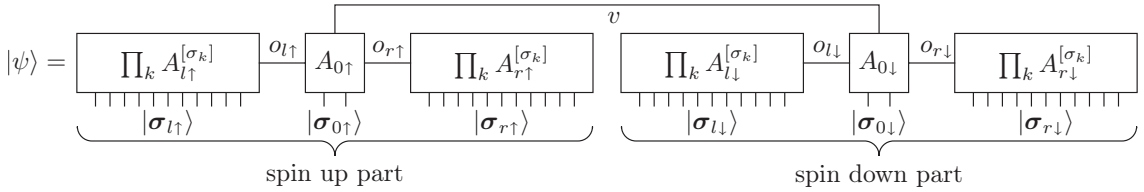

FIG. 5. MPS representation for a quantum dot coupled to two spinful leads. The lead chains are combined to big boxes for clarity. The indices of the dot matrices are labeled explicitly.

$N_l=2$), the dimension of the effective Hilbert space is enlarged from D to $D2^{2N_l}$ upon adding a new site to the Wilson chain. Thus, the larger N_l, the more information is lost during the subsequent truncation of the Hilbert space back to dimension D, and the less accurate the NRG treatment is expected to be.

The main goal of the present paper is to illustrate that a very significant improvement of efficiency can be obtained as follows: instead of combining all $2N_l$ chains into a single Wilson chain of local dimension 2^{2N_l} ("single-chain geometry"), we shall treat them as separate chains, each with local dimension 2 and each coupled to the same set of dot levels ["star geometry," see Fig. 3(b)]. Although the total number of sites thereby increases from $\mathcal{O}(L)$ to $\mathcal{O}(N_l L)$, the dimension of the local state space *per site* is reduced from 2^{2N_l} to 2. We find that, due to the latter fact, the dimension D of the constituent matrices in the star-MPS can be chosen to be significantly smaller than in the chain MPS.

The change from single-chain to star geometry, however, necessitates a change in truncation strategy for the following reason: in contrast to the single-chain geometry, where each site represents a definite energy scale, in the star geometry a given scale is represented by a set of $2N_l$ sites, one on each of the star's chains, i.e., at locations that are widely "separated" from each other on the star. Therefore, a truncation scheme based on energy scale separation, such as that used by standard NRG, can no longer be applied. Instead, we shall simply minimize[4] the expectation value of the Hamiltonian within the space of all MPSs with the same star structure. This can be done efficiently by optimizing the matrices in the star-MPS one site at a time, and sweeping through all sites until convergence.

To be explicit, we construct our star-MPS for the two-lead system as follows. In total $4=2N_l$ ($N_l=2$) Wilson chains are connected to the dot. Each of these chains is very similar to the NRG MPS from above, except that the local state space (LSS) is only of dimension 2. To simplify the notation we drop the labels α and s whenever possible and incorporate them into the site index k, which from now on will be taken to uniquely determine a site in the whole star structure. σ_k still labels the LSS at site k. With this every Wilson chain can be represented as (see Fig. 4)

$$|o_0\rangle = A^{[\sigma_1]}_{o_0 o_1} A^{[\sigma_2]}_{o_1 o_2} \cdots A^{[\sigma_L]}_{o_{L-1}} |\sigma_1\rangle|\sigma_2\rangle\cdots|\sigma_L\rangle \tag{10a}$$

$$= \left(\prod_{k=1}^{L} A^{[\sigma_k]}\right)|\vec{\sigma}\rangle, \tag{10b}$$

where $|\vec{\sigma}\rangle=|\sigma_1\rangle|\sigma_2\rangle\cdots|\sigma_L\rangle$. Here the label o stands for "outer," for reasons that will become clear below. We introduce an intuitive graphical representation for these MPS. Every A will be represented by a box and every index of A is depicted by a line attached to the box. For matrix products or other index summations the corresponding lines are connected. Using this representation, a single chain can be depicted as in Fig. 4.

The fact that the Hamiltonian does not contain terms that flip spin up to down or vice versa suggests representing the dot state space by two separate sites, representing all dot states having spin up or down, respectively [see Fig. 3(b)]. Correspondingly, we also introduce two types of dot matrices, $A^{[\sigma_{0\uparrow}]}$ and $A^{[\sigma_{0\downarrow}]}$, which carry an extra index v that is being summed over to link the spin up and down subsystems. So we arrive at the starlike structure of Fig. 5 with two linked dot matrices (one for each spin) and two leads (left and right) attached to each:

$$|\psi\rangle = \left(\prod_{k_{l\uparrow}} A^{[\sigma_{k_{l\uparrow}}]}\right)_{o_{l\uparrow}} A^{[\tilde{\sigma}_{0\uparrow}]}_{o_{l\uparrow} o_{r\uparrow} v} \left(\prod_{k_{r\uparrow}} A^{[\sigma_{k_{r\uparrow}}]}\right)_{o_{r\uparrow}} \left(\prod_{k_{l\downarrow}} A^{[\sigma_{k_{l\downarrow}}]}\right)_{o_{l\downarrow}} A^{[\tilde{\sigma}_{0\downarrow}]}_{o_{l\downarrow} o_{r\downarrow} v}$$
$$\times \left(\prod_{k_{r\downarrow}} A^{[\sigma_{k_{r\downarrow}}]}\right)_{o_{r\downarrow}} |\vec{\sigma}_{l\uparrow}\rangle|\vec{\sigma}_{0\uparrow}\rangle|\vec{\sigma}_{r\uparrow}\rangle|\vec{\sigma}_{l\downarrow}\rangle|\vec{\sigma}_{0\downarrow}\rangle|\vec{\sigma}_{r\downarrow}\rangle. \tag{11}$$

This starlike structure basically consists of two y-junctions, as discussed by Guo and White,[16] next to each other.

Hiding the explicit structure [Eq. (11)] of the MPS as illustrated in Fig. 5, we can write a state symbolically as

$$|\psi\rangle = \left(\prod_k A^{[\sigma_k]}\right)|\vec{\sigma}\rangle. \tag{12}$$

We call Eq. (12) the global representation of $|\psi\rangle$.

An important point to note is that this system is still effectively one dimensional, in the sense that if we cut out a given site, the system breaks apart into two (or three in case of a dot site) disjoint parts. We shall call the one containing the dot sites the "inner" part, the other one the outer part. As a consequence, it is possible to also give a "local" description of $|\psi\rangle$ of the form

$$|\psi\rangle = A^{[\sigma_k]}_{i_k,o_k} |i_k\rangle|\sigma_k\rangle|o_k\rangle, \tag{13}$$

where $\{|\sigma_k\rangle\}$ represents the LSS of the chosen site, $\{|i_k\rangle\}$ is an orthonormal set of states representing the inner state space (ISS), namely, the inner part of the star with respect to the chosen site k, and $\{|o_k\rangle\}$ is an orthonormal set of states representing the outer state space (OSS), namely, the outer part of the star.

III. VARIATIONAL SITE OPTIMIZATION SCHEME

We will use the MPS of Fig. 5 as an ansatz for the ground state of our system. In order to find the ground state we need to calculate the MPS $|\psi\rangle$ that minimizes the energy $E=\langle\psi|H|\psi\rangle$ with the constraint of keeping the norm of $|\psi\rangle$ constant.[4] Using λ as Langrange multiplier ensuring normalization we arrive at the following minimization problem:

$$\min_{|\psi\rangle}(\langle\psi|H|\psi\rangle-\lambda\langle\psi|\psi\rangle). \tag{14}$$

The key idea of the variational MPS optimization is to optimize every single A-matrix of $|\psi\rangle$ separately until the ground-state energy has converged. Therefore we insert the local MPS description from Eq. (13) into Eq. (14) and obtain

$$\min_{A_k}(A^{[\sigma_k']*}_{i'o'}H_{(i'\sigma_k'o'),(i\sigma_k o)}A^{[\sigma_k]}_{io}-\lambda A^{[\sigma_k]*}_{io}A^{[\sigma_k]}_{io}), \tag{15}$$

where $H_{(i'o'\sigma_k'),(io\sigma_k)}$ are the Hamilton matrix elements in the current effective bases

$$H_{(i'\sigma_k'o'),(i\sigma_k o)}=\langle o'|\langle\sigma_k'|\langle i'|H|i\rangle|\sigma_k\rangle|o\rangle. \tag{16}$$

By setting the derivative of Eq. (15) with respect to the matrix elements of A_k^* to zero and replacing λ by E_o, we obtain the following eigenvalue equation for A_k:

$$H_{(i'\sigma_k'o'),(i\sigma_k o)}A^{[\sigma_k]}_{io}=E_0A^{[\sigma_k']}_{i'o'}. \tag{17}$$

The eigenvector with the smallest eigenvalue is the solution to our minimization problem. So after having solved this eigenvalue problem for the current site k we replace A_k with the newly found eigenvector and move on to the next site in order to optimize that $A_{k'}$. We repeat the whole process (sweeping) until the ground-state energy has converged (see below).

By following this procedure we succeed to divide a very high dimensional minimization problem into manageable smaller units. For general problems this can be a very bad approach as one can get stuck in a local minimum during the optimization. However, it has proven to work reliably when the site-site coupling varies smoothly and monotonously. In our case the Hamiltonian has only nearest-neighbor interactions and there are no long-range correlations in the system. As a result, the system reliably converges without getting stuck in local minima.

A. Updating the A matrices and changing the effective basis states

When updating A matrices during sweeping, one must ensure that two conditions are satisfied. First, whenever we use the local description of Eq. (13), we rely on the basis states being orthonormal: $\langle o_k|\sigma_k'\rangle=\delta_{o_k,\sigma_k'}$. This condition translates to

$$\sum_{\sigma_{k'}}A^{[\sigma_{k'}]}A^{[\sigma_{k'}]\dagger}=\mathbb{1}\quad\text{for } k'>k, \tag{18}$$

for all outer matrices with respect to site k. We will focus here on the OSS basis, everything works completely analogously for the ISS basis.

Second, we also want to create an effective basis that spans a DMRG optimal Hilbert space, i.e., the states we keep for an effective basis are to be the ones having the largest weights in the density matrix of the current state (as described below).

For definiteness, we consider an inward sweep and focus on how to move the "current site" from k to $k-1$. We assume that a new set of A matrices for site k has been obtained by energy minimization. The question is how to ensure that both above mentioned conditions are satisfied. As all the inner A matrices of site $k-1$ have not changed since we optimized site $k-1$ the last time when moving outwards, we only need to create a new effective OSS basis $|o_{k-1}\rangle$ for site $k-1$.

Starting from the density matrix in the local description of site k,

$$\rho^{(k)}=|\psi\rangle\langle\psi|=A^{[\sigma_k]}_{io}A^{[\sigma_k']*}_{i'o'}|i\rangle\langle i'||\sigma_k\rangle\langle\sigma_k'||o\rangle\langle o'|, \tag{19}$$

suppose one traces out the inner part of this system to obtain reduced density matrix of the outer part and site k,

$$\rho^{(k)}_{\text{red}}=\text{tr}_i\,\rho^{(k)}=A^{[\sigma_k]}_{io}A^{[\sigma_k']*}_{io'}|\sigma_k\rangle\langle\sigma_k'||o\rangle\langle o'|, \tag{20}$$

which corresponds precisely to the outer part with respect to site $k-1$.

Now employ the singular value decomposition (SVD) $A=USV^\dagger$ which exists for every rectangular matrix A. S is a diagonal matrix containing the singular values ordered by magnitude; U and $V^\dagger$ are column and row unitary matrices, respectively, and obey $U^\dagger U=V^\dagger V=\mathbb{1}$. Combine $|\sigma_k\rangle$ and $|o_k\rangle$ to $|l_k\rangle=|\sigma_k\rangle|o_k\rangle$ and insert the SVD for $A_{il}=U_{im}S_{mj}(V^\dagger)_{jl}$

$$\rho^{(k)}_{\text{red}}=A_{il}A^*_{il'}|l_k\rangle\langle l_k'|=V_{j'l'}S_{l'm}S_{ml}V^\dagger_{jl}|l_k\rangle\langle l_k'|=\sum_j\rho_j^{(k)}|j_k\rangle\langle j_k|. \tag{21}$$

The second line follows since S^2 is diagonal, and we wrote $\rho_j^{(k)}=S^2_{jj}$ and $|j_k\rangle=V^\dagger_{jl}|l_k\rangle$. We see that the SVD automatically diagonalizes the reduced density matrix with the states ordered according to their weight.

So all we actually have to do for moving the actual site from k to $k-1$ is to calculate the SVD of the newly optimized $A_k=USV^\dagger$. We then replace $A_k\to\tilde{A}_k=V^\dagger$ and $A_{k-1}\to\tilde{A}_{k-1}=A_{k-1}US$ as illustrated by Fig. 6. By doing so we do not change the total state, since the product

$$A_{k-1}A_k=\tilde{A}_{k-1}\tilde{A}_k \tag{22}$$

remains unchanged. Thus we create an effective orthonormal OSS basis,

$$|o_{k-1}\rangle=\tilde{A}^{[\sigma_k]}_{o_{k-1}o_k}|\sigma_k\rangle|o_k\rangle, \tag{23}$$

which at the same time is DMRG optimal.

The so-called site optimization procedure outlined above, where we optimize the A matrices directly, is equivalent to one-site finite-size DMRG.

The relation between the singular values and the weights of the reduced density matrix can be used to optimize our choice for the dimensions of the respective effective Hilbert spaces: instead of using the same dimensions for *all* A ma-

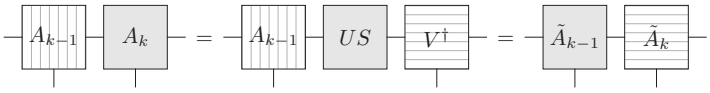

FIG. 6. Procedure for moving the actual site from k to $k-1$. The matrices that are not orthonormalized in any direction are printed with gray background. The gray lines within the boxes indicate whether the row or column vectors are orthonormal (with the local level associated with row or column, respectively).

trices in the system, which turns out to be inefficient for inhomogeneous ones like ours, we adopt as truncation criterion the demand that the minimum value of S^2 at a given site is to be smaller than some threshold $w_{\min}$ (in our case typically taken as 10^{-6}). After calculating the singular values, we choose the matrix dimensions D_k at the corresponding bond k (between site k and its neighbor in the direction of the dot) according to the following recipe. We choose D_k large enough to ensure that the minimal singular value $s_{\min}(k)$ fulfills $s^2_{\min}(k) < w_{\min}$, but subject to this constraint choose D_k to be as small as possible, in order to minimize computational resources.

It is instructive to also explore the relation between D_k and the bond entropy S_k of site k, which can be computed from the reduced density matrix $\rho^{(k)}_{\text{red}}$ at site k according to

$$S_k = -\operatorname{tr}(\rho^{(k)}_{\text{red}} \ln \rho^{(k)}_{\text{red}}). \tag{24}$$

The entropy S_k is a measure for the entanglement between the traced out part of the system and the part kept in the description of $\rho^{(k)}_{\text{red}}$. Thus, large S_k implies large D_k, which turns out to be roughly proportional to e^{S_k}. The dimensions D_k resulting from the above criterion for the singular values $s_{\min}(k)$ together with the exponentiated bond entropy e^{S_k} associated with the reduced density matrix at bond k are shown in Fig. 7. This figure shows, first, that a larger dimension is required near the dot and, second, that e^{S_k} (times a constant) is a rather good indicator of the required dimension D_k. For the limiting case of a reduced density matrix $\rho^{(k)}_{\text{red}}$ with uniform weights $\rho_j(k) = \frac{1}{D_k}$ $\forall$ $j \in [1, D_k]$, the exponentiated bond entropy then gives $e^{S_k} = D_k$. Thus, D_k is a upper bound to e^{S_k}.[17] The dip at $k=0$ for the bond between the two spin subsystems (dimension D_v) is due to the fact that there is only a density-density interaction along this bond but no particle exchange. For our system we found that it is sufficient to have dimensions of 36 or less near the dot.

B. Sweeping sequence

In principle the order in which we optimize the single matrices during a sweep is not important. However, it is both convenient and more efficient to move only to a neighboring site (and not further) for the next optimization step. In this way we need to change the actual site only by one in order to get the desired new local description. Having our MPS ansatz structure in mind, this requirement immediately suggests a particular order of sweeping, shown in Fig. 8. Starting from the far end of any chain we move in toward the dot matrix and then out again along another chain. We repeat this until we have covered the whole system. Sweeping that way (solid

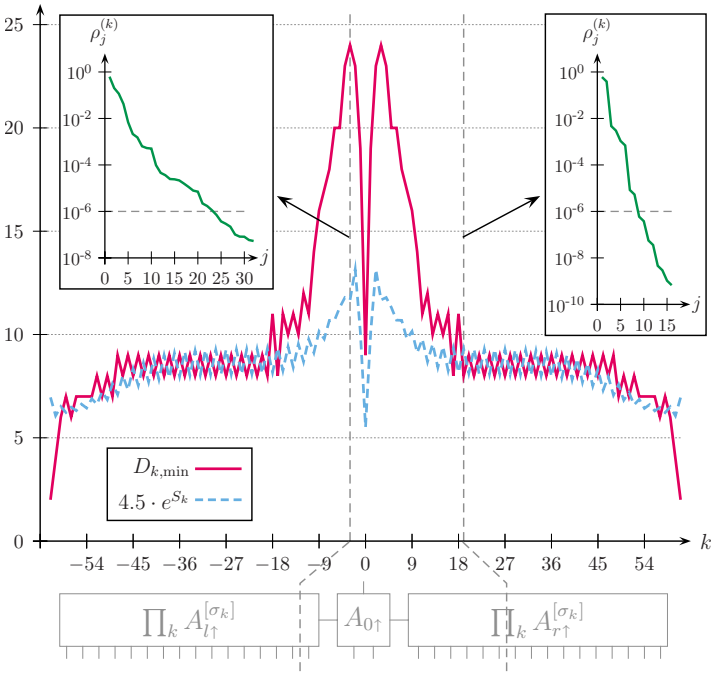

FIG. 7. (Color online) The solid line shows the dimension D_k needed at bond k of the spin up chain to satisfy $w_{\min} = 10^{-6}$ for the reduced density matrix at each bond (negative k correspond to the left chain). The dashed line displays the exponentiated bond entropy e^{S_k} multiplied by 4.5 to visually match the $D_{k,\min}$ curve for large k. Here $k=0$ corresponds to the "vertical" bond between the two spin subsystems. The two insets show spectra of reduced density matrices at different bonds k indicated by the vertical dashed lines of the main plot. The data shown in this figure has been obtained from the ground state of the four-level model shown in Fig. 10 with $\epsilon = -1.7U$. In general, the maximum dimension needed depends strongly on the model parameters.

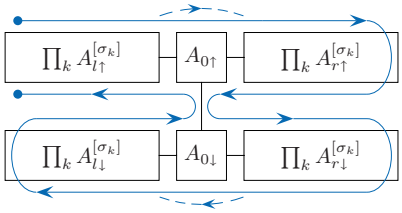

FIG. 8. (Color online) Sweeping sequence. For clarity we place the spin up and spin down parts on top of each other to emphasize the starlike structure. The solid blue line depicts the standard sweeping sequence.

blue line in Fig. 8) we optimize the two dot matrices three times but all the other sites only twice. If one wants to optimize all sites twice during a sweep one can once skip the optimization step at the dot sites as indicated by the dashed blue line.

As the dot matrices are by far the biggest in the system, optimizing them takes much longer than optimizing any of the chain matrices. Thus by skipping the dot optimization step once, we can reduce the computational time needed for a single sweep. However, since the dot optimization step also has the biggest effect for improving our MPS ansatz, skipping its optimization once has to be compensated by performing more sweeps to achieve as good convergence of the ground state as in the case where we perform three optimizations at the dot matrices. We compared both approaches for our model and found no significant differences in the overall performance.

We stop the sweeping when the MPS has converged. To probe the convergence we compare the MPSs before and after sweep N, $|\psi_{N-1}\rangle$, and $|\psi_N\rangle$. If the change in overlap,

$$1 - |\langle\psi_{N-1}|\psi_N\rangle| \leq \epsilon, \tag{25}$$

is smaller than a certain threshold, we stop the sweeping. We typically use $\epsilon = 10^{-3}$ and need 10–15 sweeps. This depends crucially on the system parameters, though, and in some cases we need to perform up to 25 sweeps.

C. Numerical costs

The most computational effort is needed for solving the eigenvalue problem [Eq. (17)] for the minimal eigenvector. We use the Lanczos method for solving Eq. (17), which is an iterative method and requires the calculation of $H|\psi\rangle$ in the local picture once for every iteration. As we cannot influence the number of Lanczos iterations in our implementation, we will only investigate the costs of calculating $H|\psi\rangle$, which are given by the costs of the matrix-matrix multiplication $\Sigma_{io\sigma_k} H_{(i'o'\sigma_k'),(io\sigma_k)} A_{io}^{[\sigma_k]}$. The costs of a matrix-matrix multiplication is given by the size of the outcome times the dimension of the index being summed over. $H_{(i'o'\sigma_k'),(io\sigma_k)}$ splits up into a sum of different terms, such as $(c_k^\dagger)_{\sigma_k'\sigma_k} \otimes (c_{k+1})_{o'o}$, each consisting of a direct tensor product of operators living in the ISS, OSS or LSS. Thus the product $H|\psi\rangle$ can be split up into smaller matrix products. By looking at the structure of the Hamiltonian (1), one recognizes that there will be no terms containing tensor products of operators from the ISS and OSS, since they would correspond to next-nearest-neighbor terms, but tensor products with one operator from the LSS and the other one from the ISS or OSS. These terms lead to multiplications over an index of length Dd, being the product of the dimensions of the ISS and LSS. If the current site is the dot site, the size of the resulting matrix is $D^2 D_v d^m$ and thus the costs for a single multiplication $H|\psi\rangle$ at a dot site is given by

$$C_{\text{dot}} = \mathcal{O}(D^2 D_v d^m D d) = \mathcal{O}(D^3 D_v d^{m+1}). \tag{26}$$

In case of a chain site instead of a dot site exactly the same reasoning applies and because of the smaller matrix size the costs reduce to $\mathcal{O}(D^3 d^2)$. From Eq. (26) we see that optimizing the dot sites is the most expensive step in the optimization and scales particularly unfavorably when the number of dot levels m is increased.

D. Bond optimization

As an alternative to the site optimization scheme discussed above, we can begin to move the current site as in Fig. 6 to obtain $A_{k-1}(US)V^\dagger$, where $A_k = USV^\dagger$. At this step we can represent the overall state as $|\psi\rangle = (US)_{i_k o_{k-1}} |i_k\rangle |o_{k-1}\rangle$. Now we perform the optimization on $B = US$ in complete analogy to the site optimization and obtain a new $\tilde{B}$. Then A_{k-1} is replaced by $\tilde{A}_{k-1} = A_{k-1}\tilde{B}$ which results in a state with the actual site $k-1$. We call this process "bond optimization" as the matrix we actually optimize is somehow located at the bond between two original sites.

One can easily see that the costs for calculating $H_{(i'o'),(io)} B_{io}$ are $\mathcal{O}(D^3)$ and thus independent of the number of dot levels. Considering only the costs for a single sweep the bond optimization scheme will be considerable faster than site optimization, which is especially expensive at the dot sites. This advantage, however, is compromised to some extent by the slower convergence of the bond optimization due to the optimization taking place within in a much smaller effective Hilbert space. This makes more sweeps necessary and also enforces a lower threshold in Eq. (25) as convergence criterion. It turned out to be very difficult to judge the convergence of the bond optimization scheme based on Eq. (25) especially if one starts from a state not too different from the actual ground state because in such cases the convergence can be really slow and one might wrongly consider the state already converged.

However, one might try to avoid unnecessary site optimizations at the beginning of the sweeping and use cheap bond optimizations instead and switch after several sweeps to the site optimization scheme to make use of the better convergence properties.

IV. RESULTS FOR LOCAL OCCUPATIONS

We used the approach described above to calculate the ground state and level occupancies of a spinful multilevel quantum dot coupled to two leads. Throughout this part we fix the Coulomb interaction $U = 0.2W$, $2W$ being the bandwidth, and use the convention $W = 1$.

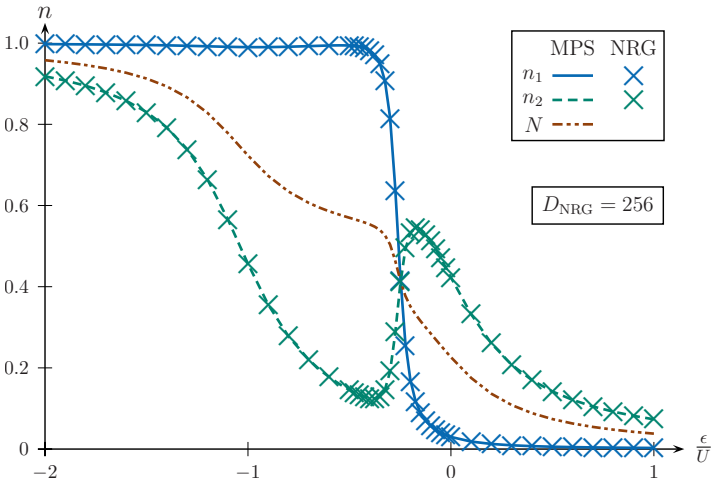

FIG. 9. (Color online) Dot level occupation for a spinless two-level system, with $\epsilon_{1,2}=\epsilon\pm\Delta/2$, level spacing $\Delta=0.1U$ and couplings $\Gamma_{1l}=\Gamma_{1r}=0.005U$, $\Gamma_{2l}=\Gamma_{2r}=30\Gamma_{1l}$. This parameter set was used in Sindel *et al.* (Ref. 20) $N=\frac{1}{2}(n_1+n_2)$ is half the total dot occupation. Note that the sign in $\Gamma_{i\alpha}$ just serves as an indication of the sign of the related hopping matrix element $V_{i\alpha}$ in the Hamiltonian.

The results shown below demonstrate that it is possible to calculate local ground-state quantities of a complex quantum dot efficiently using this approach. Already with calculating the occupation of the dot levels it is possible to investigate the stability diagram of small quantum dots.[18] Under certain conditions, local occupancies can be related to phase shifts, which in turn can be used to calculate the conductance through a quantum dot.[19]

First we consider the simpler case of a spinless two-level model with level positions $\epsilon_{1,2}=\epsilon\pm\Delta/2$, coupled symmetrically to two leads. NRG works very reliable for this kind of impurity model. The lower of the two levels is assumed to couple significantly stronger to the leads. We calculated the occupation, $n_i=\langle d_i^\dagger d_i\rangle$, of both levels as a function of ϵ, using both our MPS approach and NRG. In Fig. 9 we show the occupation of both levels as we sweep the gate potential by shifting the levels from below toward the Fermi edge of the leads and then further above. At the beginning of this process mainly the lower level starts to empty. This is due to the much bigger couplings Γ_2 of the lower level compared to the upper level and results in an occupation inversion situation where the energetically higher level has higher occupation than the lower level. A second consequence of the small couplings Γ_1 is the sharp transition of the occupation of the upper level from almost filled to almost empty. Once the upper level is almost empty the dot system may gain energy by increasing the occupation of the lower level without having to pay Coulomb energy. This leads to the nonmonotonic occupation of the lower level, known as charge oscillation. See Sindel *et al.*[20] for a more detailed discussion. The results for the level occupation of the simple spinless model as shown in Fig. 9, demonstrate excellent agreement between both NRG and DMRG calculations. The relative difference of the ground-state energies obtained by NRG and MPS was on average 10^{-5}.

We demonstrate the power of the MPS approach by considering a spinful four-level dot coupled asymmetrically to two leads, a system sufficiently complex that its treatment by NRG is a highly challenging task. We therefore have no NRG reference data for this system and present only DMRG results. For every dot level we calculate the occupation $n_{is}=\langle d_{is}^\dagger d_{is}\rangle$ as a function of gate voltage, as shown in Fig. 10. This calculation is solely performed within the site optimization scheme. We kept the effective dimensions for all A matrices describing the leads the same compared to the two-level plot, only the LSS size at the dot matrices was increased, thus demanding more computational time for the optimization at the dot.

For the four-level system we chose random values for the level couplings Γ varying over two orders of magnitude. Moreover, as the couplings have been chosen asymmetric, one *cannot* simplify the model by decoupling certain linear combinations of the leads, while keeping the remaining relevant degrees of freedom. The occupation of the individual levels shows very rich behavior. By sweeping the gate potential similar to the spinless case above, we find the sharpest transition for the second level $(n_{2\uparrow},n_{2\downarrow})$. The couplings of this level are one magnitude smaller than all other couplings causing this sharp transition and associated with it charge oscillations in all the other levels.

V. ROTATION TO OPTIMAL BASIS OF WILSON CHAINS

As described above the use of a star-shaped MPS works well for local quantities. However, one might ask the question whether introducing such a geometry causes a loss of longer-ranged correlations between different chains. To be able to assess this question we consider two sites in different chains $c\neq c'$, both at distance k from the dot. The mutual information[17] $I_\rho^{cc'}(k)$ contained between these two sites is given by

$$I_\rho^{cc'}(k)=S_{\rho_{\rm red}^{c}(k)}+S_{\rho_{\rm red}^{c'}(k)}-S_{\rho_{\rm red}^{cc'}(k)}, \tag{27}$$

with the entropy S

$$S_\rho=-\mathrm{tr}(\rho\ln\rho). \tag{28}$$

Here $\rho_{\rm red}^{c}(k)$ is the reduced one-site density matrix obtained by tracing out the entire system except for site k in chain c. Likewise $\rho_{\rm red}^{cc'}(k)$ is the reduced two-site density matrix, obtained by tracing out all sites except two, situated at a dis-

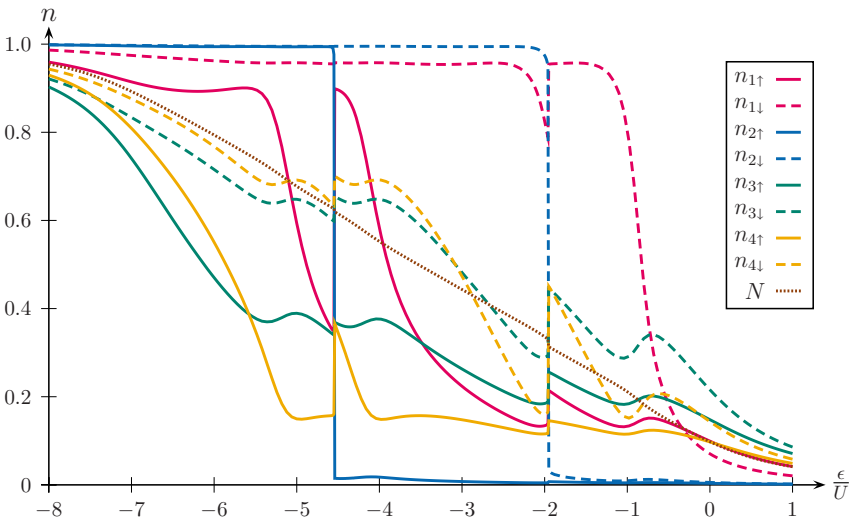

FIG. 10. (Color online) Dot level occupation for a spinful four-level system. We parametrize the dot level energies as $\epsilon_{is}=\epsilon+\epsilon_i \pm B/2$ for $s=\uparrow,\downarrow$, where B represents the applied magnetic field with $B=0.2U$ and ϵ a gate voltage, with $\epsilon_i=(-0.1,-0.03,0.07,0.1)U$. The coupling of the dot levels are chosen asymmetrically $\Gamma_{ir}=s_i\Gamma_{il}$ with $s_i=(1,-1,-1,1)$ and $\Gamma_{il}=(0.5,0.02,1,0.7)0.2U$.

tance k from the dot in two different chains, c and c'. $I_\rho^{cc'}(k)$ is a measure for how much information the sites contain about each other. As a consequence, a decaying $I_\rho^{cc'}(k)$ as a function of distance k indicates that chains c and c' effectively decouple.

For simplicity and to make a comparison with NRG feasible, we restrict ourselves to the spinless case, e.g., we only look at the spin-up part of the original four-level system, however with different couplings compared to the parameters used for Fig. 10. As NRG treats both the left and right lead in a combined single chain we can, nevertheless, study the effect of "unfolding" the two parts of the NRG chain.

If we calculate $I_\rho^{l,r}$ for this spinless two-lead Hamiltonian as it stands, the correlations between two sites on opposite sides of the dot but at equal distance from it are found to decay only very weekly with k [Fig. 11(a), dot-dashed line]. This illustrates, on the one hand, that our MPS ansatz does successfully capture correlations between sites representing comparable energy scales, in spite of the fact that in the star geometry they lie "far" from each other (namely on different chains). On the other hand, it also raises the question whether one can choose a (numerically) better suited basis for the leads that effectively does decouple different chains far from the dot. Since in that case the correlations would intrinsically decay with distance from the dot, less numerical resources would be required to capture all correlations accurately.

Indeed, we shall show that it is possible to choose such an optimal basis by making a suitably chosen unitary transformation which rotates the lead degrees of freedom into each other in an "optimal" way to be described below. When the leads are first rotated by a certain optimal angle of rotation θ_{opt} (defined precisely below) and $I_\rho^{l,r}$ is calculated in this rotated basis, then $I_\rho^{l,r}$ is found to decay rapidly with k, see solid line in Fig. 11(a).

We begin with the observation that the labeling of the unfolded chains with $\alpha=l,r$ is arbitrary. We can choose any linear combination of l and r as new basis, e.g., for symmetric couplings to the dot it is well known that with the symmetric and antisymmetric combination only the symmetric lead couples to the dot while the antisymmetric lead is completely decoupled. To be specific, we can introduce a unitary transformation acting on the original lead states specified in the Hamiltonian

$$\tilde{f}_{\beta n\sigma} = U_{\beta\alpha} f_{\alpha n\sigma} \tag{29}$$

independent of the site n and spin σ, acting only on the lead index α. For systems with time-reversal symmetry, the unitary matrix is always chosen real. So in our case, for $N_l=2$ $U=U(\theta)$ is a real two-dimensional matrix and can be thought of as a planar rotation parametrized by a single angle θ. The optimal basis for DMRG treatment would have minimal correlations between the rotated chains. The angle of rotation θ can be restricted to $\theta\in[0,\pi/2]$ as we choose to ignore the particular order and relative sign of the new basis vectors. In order to find the optimal angle it is sufficient to look at the reduced two-site density matrix $\rho_{\text{red}}^{l,r}(k)$. As the Hamiltonian (1) preserves particle number, this density matrix is a 4×4 matrix in block form: a 1×1 block for both the zero-particle and two-particle sectors and a 2×2 block for the one-particle sector.

Finite off-diagonal elements of this 2×2 block show that both sites are effectively correlated with each other. However, by diagonalizing this block of $\rho_{\text{red}}^{l,r}(k)$ via a real unitary matrix U we immediately obtain a rotated lead basis according to Eq. (29). So the angle of rotation θ_{opt} can be found by diagonalizing $\rho_{\text{red}}^{l,r}(k)$. It is most desirable to decouple the far ends of the chains best, so we choose $\theta=\theta(k=L)$, where $U[\theta(k=L)]$ diagonalizes $\rho_{\text{red}}^{l,r}(k=L)$.

By applying the transformation $U(\theta)$ to the Hamiltonian (1) only the tunneling elements to and from the dot levels are changed

$$\tilde{V}_{\beta i\sigma} = U(\theta_{\text{opt}})_{\beta\alpha} V_{\alpha i\sigma}. \tag{30}$$

This way, we have obtained a new lead basis for our Hamiltonian that is better suited for the DMRG calculations, as long ranging correlations are suppressed in this basis. As we

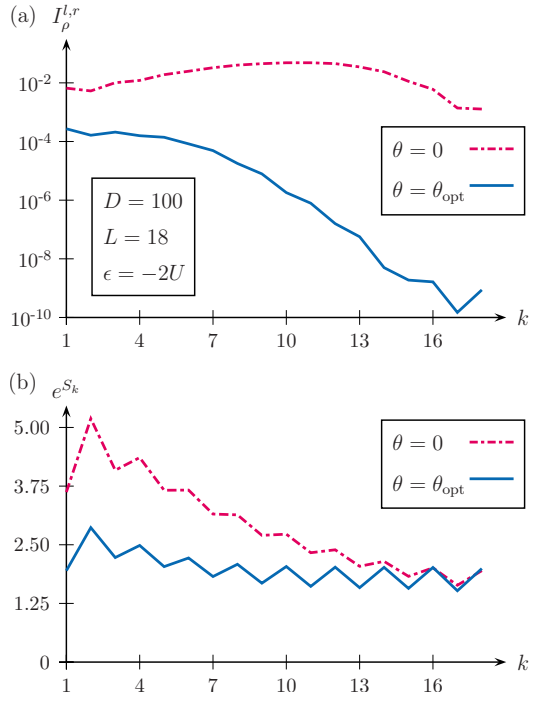

FIG. 11. (Color online) (a) Mutual information $I_\rho^{l,r}$ between two sites situated in different leads but at equal distances k from the dot, for a spinless four-level, two-lead model with dot levels $\epsilon_i/U = (-0.1, -0.03, 0.07, 0.1) + \epsilon$, $\epsilon = -2U$ fixed, couplings $\Gamma_{ir} = (0.3, -0.02, -1, 0.2)$ and $\Gamma_{il} = (0.5, 0.08, 1, 0.7)$ and $\Lambda = 3$. The dashed line shows $I_\rho^{l,r}$ for the system with the leads in the original basis of Eq. (1), whereas the solid line shows $I_\rho^{l,r}$ after the leads have been rotated by the (fixed k independent) optimal angle $\theta_{\rm opt}$ obtained from Fig. 12(a). (b) Exponentiated bond entropy e^{S_k} along the right chain of the system both prior (dashed line) and after (solid line) the rotation with $\theta_{\rm opt}$, indicating an effective reduction in the required matrix dimension D_k close to the impurity for the rotated system by about $\frac{1}{2}$ for the same numerical accuracy.

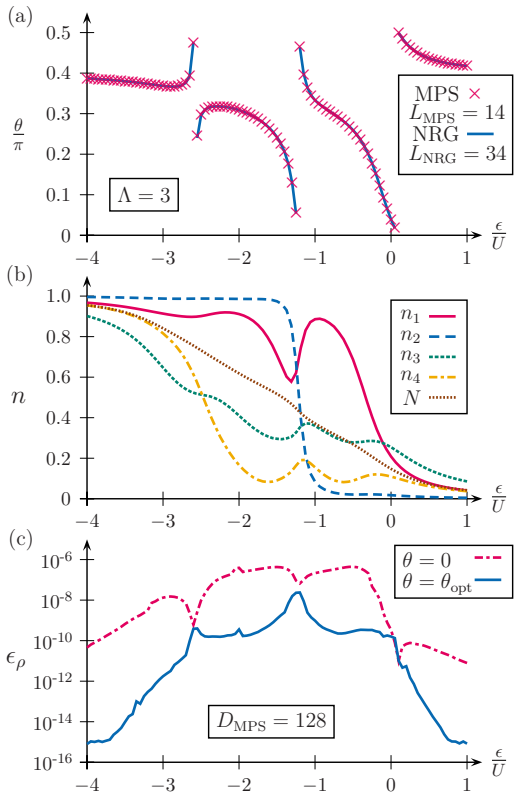

FIG. 12. (Color online) Optimal basis for the leads of a spinless four-level, two-lead system (same parameters as for Fig. 11, but with varying ϵ). (a) Optimal angle of rotation $\theta_{\rm opt}$ for the leads obtained by diagonalizing $\rho_{\rm red}^{l,r}(k=L)$ for the DMRG calculation (red symbols) in comparison with angle that diagonalizes the scattering matrix calculated with NRG (blue line). $\theta_{\rm opt}$ is defined mod $\pi/2$. (b) Dot level occupation. $N = \frac{1}{4}\Sigma_{i=1}^4 n_i$ is the rescaled total dot occupation. Rapid changes in the angle $\theta_{\rm opt}$ coincide with rapid shifting of dot-level occupations. (c) Truncation error (accumulated discarded density-matrix eigenvalues) of the DMRG calculation considering two neighboring sites at a time for a rotated and nonrotated system. We typically used 20 sweeps for the DMRG calculations. The truncation error is significantly reduced for the rotated system except for the points where $\theta_{\rm opt}$ actually shows rather rapid transitions through $\theta_{\rm opt} = 0$ itself. At these points the leads are already decoupled from the outset.

benefit already from a rotation in the leads even if the angle is only close (but not equal) to the optimal choice $\theta_{\rm opt}$, it is feasible to start with a small system (of only, say, 14 sites per Wilson chain) in order to obtain an approximate value for $\theta_{\rm opt}$; the latter can then be used to rotate the leads of a bigger system, from which a better determination of the optimal angle can be extracted.

In Fig. 12 we show the optimal angle of rotation $\theta_{\rm opt}$ for a spinless four-level system. We compare with NRG calculations where we diagonalize the T-matrix

$$T_{\alpha\beta} = \lim_{\omega \to 0^+} [\hat{V}^\dagger \hat{G}^{\rm dot}(\omega) \hat{V}]_{\alpha\beta}, \tag{31}$$

where $\hat{G}^{\rm dot}$ is the local retarded Green's-function matrix calculated by standard NRG techniques[21] and $\hat{V}$ is the tunneling matrix from the Hamiltonian. The angle extracted from the diagonalization of the T matrix [i.e., from requiring that $U(\theta)TU^\dagger(\theta)$ be diagonal] is shown as a solid line in panel (a). Remarkably, this line agrees quantitatively with the $\theta_{\rm opt}$ values found by DMRG. This shows that the angle of rotation that minimizes correlations between the two rotated leads has a clear physical interpretation: it also diagonalizes the scattering matrix, a result that is intuitively very reasonable. We note, though, that this fact cannot be used to determine $\theta_{\rm opt}$ *before* doing the DMRG calculation, as with the knowledge of the scattering matrix we would have already solved the system. Nevertheless, shorter systems can already give a clean indication of the angle that decouples the chains.

In Fig. 11 we demonstrate that by rotating the leads to the new optimal basis as suggested above it is possible, indeed, to ensure that lead degrees of freedom on different (rotated)

Wilson chains become effectively decoupled from each other further out on the chains. Also the bond entropy S_k is reduced. If the leads are rotated into the optimal basis the mutual information drops quickly along the chains [see Fig. 12(a)], and the truncation error is significantly smaller [see Fig. 12(c)], thus making numerical treatment less demanding. Note that rapid changes in the angle θ_{opt} coincide with rapid shifting of dot-level occupations [see Fig. 12(b)].

VI. SUMMARY

Using the DMRG approach gives us the possibility to choose a more flexible MPS geometry compared to NRG. While in NRG one is bound to a simultaneous treatment of a single combined Wilson chain due to the requirement of energy scale separation, this restriction can be lifted in a DMRG treatment. In our case of a two-lead Anderson model we modeled each spin and each lead by a Wilson chain on its own treated separately from each other. Thus we achieved a significant reduction in both the dimension of the LSS and the dimension D of the ISS and OSS at each site. The Hilbert space of one site in the single chain geometry is equivalent to the direct product of the Hilbert spaces of the $4=2N_l$ corresponding sites of each chain. So in order to map a star geometry description into an equivalent single chain description, in the sense that the effective Hilbert spaces at every site have the same dimension, the dimension D' of the single chain A matrices would scale exponentially with the number of leads, $D' \simeq D^{2N_l}$, as a consequence of the tensor product of the $2N_l$ smaller star geometry A matrices. Thus, adopting the star geometry reduces the numerical costs for treating the leads by $D \simeq D'^{1/2N_l}$. Although this strategy has the consequence that the cost of treating the dot site increases significantly [see Eq. (26)], for all cases studied in this paper the latter effect is far outweighed by the decrease in costs for treating the leads. Indeed we found that dimensions $D \leq 36$ suffice for getting an accurate description of the system (note that when translated into a single chain this would result in a huge effective dimension of $D' \simeq D^4 = 1.7 \times 10^6$).

Due to the fact that the Anderson Hamiltonian under consideration features only a density-density interaction term at the dot between electrons with different spin, the dot matrices can be conveniently split into two sets, one for each spin, yielding another gain in efficiency. As it turns out, the dimension D_v connecting to two sets of dot matrices can be chosen significantly smaller than D (cf. Fig. 7). In addition an optimal basis (in terms of numerical efficiency) for representing the leads has been determined, which minimizes correlations between different Wilson chains and in which, it turns out, the scattering matrix becomes diagonal. Moreover, the DMRG sweeping procedure allows the dimensions D of the MPS matrices in the system to be adjusted very flexibly. Indeed, in our case it was possible to reduce the matrix dimensions along the chain away from the dot considerably. The combination of all these resource-saving features makes it feasible to calculate the *ground-state* properties of generic complex quantum impurity models using only relatively moderate numerical resources.

The calculation of dynamical quantities like local spectral functions is, in principle, also possible for the star geometry, for example, by suitably modifying the approach of Ref. 4 to the present geometry. However, we expect that the increased computational costs of DMRG relative to NRG for calculating dynamical quantities would in this case likely offset the advantages of the star geometry.

In closing, we would like to make the following comment: while we expect that a rotation to an optimal basis as described above should be applicable to a large class of impurity models, there may be cases where it does not work. In particular, we suspect that this might be the case for some models showing non-Fermi-liquid behavior, such as the two-channel spin-$\frac{1}{2}$ Kondo model, where overscreening of the impurity is likely to lead to strong mutual correlations between all Wilson chains. A quantitative analysis of this problem using the present star geometry approach is beyond the scope of the present investigation but would be an interesting subject for future study.

ACKNOWLEDGMENTS

We gratefully acknowledge fruitful discussions with Frank Verstraete, Ulrich Schollwöck, Theresa Hecht, Hamed Saberi, and Ian McCulloch. This work was supported by DFG (SFB 631, De-730/3-2, SFB-TR12, SPP 1285, De-730/4-1). Financial support of the German Excellence Initiative via the "Nanosystems Initiative Munich (NIM)" is gratefully acknowledged.

[1] H. R. Krishna-murthy, J. W. Wilkins, and K. G. Wilson, Phys. Rev. B **21**, 1003 (1980).
[2] K. G. Wilson, Rev. Mod. Phys. **47**, 773 (1975).
[3] R. Bulla, T. A. Costi, and T. Pruschke, Rev. Mod. Phys. **80**, 395 (2008).
[4] A. Weichselbaum, F. Verstraete, U. Schollwöck, J. I. Cirac, and J. von Delft, Phys. Rev. B **80**, 165117 (2009).
[5] S. Östlund and S. Rommer, Phys. Rev. Lett. **75**, 3537 (1995).
[6] U. Schollwöck, Rev. Mod. Phys. **77**, 259 (2005).
[7] S. R. White, Phys. Rev. B **48**, 10345 (1993).
[8] S. R. White, Phys. Rev. Lett. **69**, 2863 (1992).
[9] J. Dukelsky, M. A. Martín-Delgado, T. Nishino, and G. Sierra, Europhys. Lett. **43**, 457 (1998).
[10] M. Fannes, B. Nachtergaele, and R. F. Werner, Commun. Math. Phys. **144n**, 443 (1992).
[11] F. Verstraete, M. A. Martin-Delgado, and J. I. Cirac, Phys. Rev. Lett. **92**, 087201 (2004).
[12] F. Verstraete, D. Porras, and J. I. Cirac, Phys. Rev. Lett. **93**, 227205 (2004).
[13] H. Takasaki, T. Hikihara, and T. Nishino, J. Phys. Soc. Jpn. **68**, 1537 (1999).
[14] H. Saberi, A. Weichselbaum, and J. von Delft, Phys. Rev. B **78**,

035124 (2008).
[15] V. Kashcheyevs, A. Schiller, A. Aharony, and O. Entin-Wohlman, Phys. Rev. B **75**, 115313 (2007).
[16] H. Guo and S. R. White, Phys. Rev. B **74**, 060401(R) (2006).
[17] M. A. Nielson and I. L. Chuang, *Quantum Computation and Quantum Information* (Cambridge University Press, Cambridge, 2000).
[18] L. Gaudreau, S. A. Studenikin, A. S. Sachrajda, P. Zawadzki, A. Kam, J. Lapointe, M. Korkusinski, and P. Hawrylak, Phys. Rev. Lett. **97**, 036807 (2006).
[19] C. Karrasch, T. Hecht, A. Weichselbaum, J. von Delft, Y. Oreg, and V. Meden, New J. Phys. **9**, 123 (2007).
[20] M. Sindel, A. Silva, Y. Oreg, and J. von Delft, Phys. Rev. B **72**, 125316 (2005).
[21] A. Weichselbaum and J. von Delft, Phys. Rev. Lett. **99**, 076402 (2007).

Chapter 4

Chebyshev matrix product state techniques

4.1 Chebyshev matrix product state approach for spectral functions

In this chapter, we present a novel approach for calculating spectral functions in DMRG by carrying known Chebyshev expansions for spectral functions [88] over into the domain of MPS. The resulting Chebyshev matrix product state approach (CheMPS) is capable of producing spectral functions with an accuracy competitive to the correction vector technique at significantly reduced numerical cost. The advantageous mathematical properties of Chebyshev polynomials carry over to CheMPS, mainly, a numerically stable recursion relation, almost uniform spectral resolution and a well-controlled broadening scheme.

We also introduce the time-dependent Chebyshev MPS method (tCheMPS) for which we add a more detailed discussion in Sec. 4.2.

PHYSICAL REVIEW B **83**, 195115 (2011)

Chebyshev matrix product state approach for spectral functions

Andreas Holzner,[1] Andreas Weichselbaum,[1] Ian P. McCulloch,[2] Ulrich Schollwöck,[1] and Jan von Delft[1]
[1]*Physics Department, Arnold Sommerfeld Center for Theoretical Physics, and Center for NanoScience, Ludwig-Maximilians-Universität München, D-80333 München, Germany*
[2]*School of Physical Sciences, University of Queensland, Brisbane, Queensland 4072, Australia*
(Received 29 January 2011; revised manuscript received 24 March 2011; published 10 May 2011)

We show that recursively generated Chebyshev expansions offer numerically efficient representations for calculating zero-temperature spectral functions of one-dimensional lattice models using matrix product state (MPS) methods. The main features of this Chebyshev matrix product state (CheMPS) approach are as follows: (i) it achieves *uniform* resolution over the spectral function's entire spectral width; (ii) it can exploit the fact that the latter can be much *smaller* than the model's many-body bandwidth; (iii) it offers a well-controlled *broadening* scheme that allows finite-size effects to be either resolved or smeared out, as desired; (iv) it is based on using MPS tools to *recursively* calculate a succession of Chebyshev vectors $|t_n\rangle$, (v) the *entanglement entropies* of which were found to remain bounded with increasing recursion order n for all cases analyzed here; and (vi) it *distributes* the *total entanglement entropy* that accumulates with increasing n over the set of Chebyshev vectors $|t_n\rangle$, which need not be combined into a single vector. In this way, the growth in entanglement entropy that usually limits density matrix renormalization group (DMRG) approaches is packaged into conveniently manageable units. We present zero-temperature CheMPS results for the structure factor of spin-$\frac{1}{2}$ antiferromagnetic Heisenberg chains and perform a detailed finite-size analysis. Making comparisons to three benchmark methods, we find that CheMPS (a) yields results comparable in quality to those of correction-vector DMRG, at dramatically reduced numerical cost; (b) agrees well with Bethe ansatz results for an infinite system, within the limitations expected for numerics on finite systems; and (c) can also be applied in the time domain, where it has potential to serve as a viable alternative to time-dependent DMRG (in particular, at finite temperatures). Finally, we present a detailed error analysis of CheMPS for the case of the noninteracting resonant level model.

DOI: 10.1103/PhysRevB.83.195115 PACS number(s): 02.70.−c, 75.10.Pq, 75.40.Mg, 78.20.Bh

I. INTRODUCTION

Consider a one-dimensional lattice model amenable to treatment by the density matrix renormalization group (DMRG),[1–4] with Hamiltonian $\hat{H}$, ground state $|0\rangle$, and ground-state energy E_0. This paper is concerned with zero-temperature spectral functions of the form

$$\mathcal{A}^{\mathcal{BC}}(\omega) = \langle 0|\hat{\mathcal{B}}\,\delta(\omega - \hat{H} + E_0)\,\hat{\mathcal{C}}|0\rangle, \tag{1}$$

which represents the Fourier transform $\int \frac{dt}{2\pi} e^{i\omega t} G^{\mathcal{BC}}(t)$ of the correlator

$$G^{\mathcal{BC}}(t) = \langle 0|\hat{\mathcal{B}}(t)\hat{\mathcal{C}}(0)|0\rangle. \tag{2}$$

One possible framework for calculating such spectral functions is to expand them in terms of Chebyshev polynomials, as advocated in Ref. 5. Such a Chebyshev expansion offers precise and convenient control of the accuracy and resolution with which a spectral function is to be computed. This is very useful, particularly when broadening the spectral function of a length-L system, which exhibits finite-size subpeaks with spacing $\omega_L \sim 1/L$, in order to mimic that of an infinite system. If the latter has structures (e.g., sharp or diverging peaks), which are not yet properly resolved at the scale ω_L, the broadened version of the finite-size spectral function inevitably bears L-dependent errors in the vicinity of these structures. Hence, when calculating the finite-size version of these structures for the length-L system, there is no need to achieve an accuracy beyond that of the expected L-dependent errors, and having convenient control of this accuracy can significantly reduce numerical costs.

In this paper, we show that Chebyshev expansions offer numerically efficient representations for calculating spectral functions using matrix product state (MPS) methods,[4,6–10] with numerical costs that compare favorably to those of other established DMRG-based approaches. In particular, the Chebyshev MPS approach presented here, to be called CheMPS, allows the above-mentioned control of accuracy and resolution to be imported into the DMRG and MPS arena.

The historically first approach for calculating spectral functions with DMRG is the continued-fraction expansion.[11] While this method requires only modest numerical resources, it is limited to low frequencies and it is difficult to produce reliable results with it in the case of continua (however, algorithmic improvements were reported recently[12]). At present, the most accurate, but also most time-consuming, approaches are (i) the correction-vector (CV) method[13–15] and (ii) time-dependent DMRG (tDMRG),[7,9,16–18] in particular, when combined with linear prediction techniques.[19–22] Since any new approach must measure up to their standards, let us briefly summarize their key ideas, advantages, and drawbacks.

(i) To calculate $\mathcal{A}^{\mathcal{BC}}(\omega)$ using the CV approach, it is expressed as

$$\mathcal{A}^{\mathcal{BC}}(\omega) = \langle 0|\hat{\mathcal{B}}|\mathcal{C}\rangle_\omega \tag{3a}$$

in terms of the so-called correction vector

$$|\mathcal{C}\rangle_\omega \equiv -\lim_{\eta\to 0}\frac{1}{\pi}\mathrm{Im}\left[\frac{1}{\omega - \hat{H} + E_0 + i\eta}\right]\hat{\mathcal{C}}|0\rangle. \tag{3b}$$

The correction vector can be calculated (for finite broadening parameter η) using either conventional DMRG (Refs. 13–15) or variational matrix product state (MPS) methods.[23] A major

 © 2011 American Physical Society

advantage of this approach is that arbitrarily high spectral resolution can be achieved by reducing η and sampling enough frequency points. However, this comes at considerable numerical costs: first, a separate calculation is required for every choice of ω (although, in doing so, results for $|\mathcal{C}\rangle_\omega$'s from previous frequencies can be incorporated); and second, the calculation of $|\mathcal{C}\rangle_\omega$ involves an operator inversion problem that is numerically poorly conditioned, ever more so the smaller η is.

(ii) An alternative possibility is to use tDMRG to calculate the time-domain correlator $G^{\mathcal{BC}}(t)$, Fourier transforming to the frequency domain only at the very end. To this end, one expresses

$$G^{\mathcal{BC}}(t) = e^{iE_0 t}\langle 0|\hat{\mathcal{B}}|\tilde{\mathcal{C}}\rangle_t \tag{4a}$$

in terms of the time-evolved state

$$|\tilde{\mathcal{C}}\rangle_t \equiv e^{-i\hat{H}t}\hat{\mathcal{C}}|0\rangle \tag{4b}$$

and uses tDMRG to calculate the latter. Two attractive features of this strategy are as follows: first, it builds on an extensive body of algorithmic knowledge for efficiently calculating time evolution,[7,16,17] and, second, a simple linear-prediction scheme[19–22] can be used to extrapolate the time dependence calculated for short and intermediate time scales to longer times, thereby improving the quality of results at low frequency at hardly any additional numerical cost. However, obtaining reliable results over a sufficiently large time interval can, in itself, be numerically very expensive, since the time evolution of the many-body state $|\tilde{\mathcal{C}}\rangle_t$ is accompanied by a strong growth in entanglement entropy. This unavoidably also implies a growth of tDMRG truncation errors.

Note that, in both of the schemes outlined above, significant (often heroic) amounts of numerical resources are devoted to calculating a single state $|\mathcal{C}\rangle_\omega$ for given ω or $|\tilde{\mathcal{C}}\rangle_t$ for given t, as accurately as possible; the overlaps or expectation values of interest, namely, $\langle 0|\hat{\mathcal{B}}|\mathcal{C}\rangle_\omega$ for $\langle 0|\hat{\mathcal{B}}|\tilde{\mathcal{C}}\rangle_t$, are only calculated *at the end*, in a single, final step after $|\mathcal{C}\rangle_\omega$ or $|\tilde{\mathcal{C}}\rangle_t$ have been fully determined. Actually, these states are calculated so accurately that they would have been equally suitable for calculating any other quantity (correlator or matrix element) involving that state. In a sense, DMRG is asked to work harder than necessary; it is used to calculate a single state with "general-purpose accuracy," whereas the accurate calculation of a particular expectation value involving that state would have been sufficient.

The main motivation for this paper is to attempt to reduce this calculational overhead by employing a representation of the spectral function that avoids the need for calculating a single state with such high accuracy and instead allows numerical resources to be focused directly on the calculation of the relevant expectation values. This can be achieved by representing the spectral function via a *Chebyshev expansion*,[5,24,25] the coefficients of which, the so-called Chebyshev moments, can be calculated recursively using MPS tools. Below, we briefly summarize the structure and main features of such an expansion, thereby providing both an introduction and an overview of the material developed in detail in the main part of this paper.

The Chebyshev polynomials $T_n(x)$ form an orthonormal set of polynomials on the interval $x \in [-1,1]$. They are very well studied mathematically,[26–28] and are widely used for function

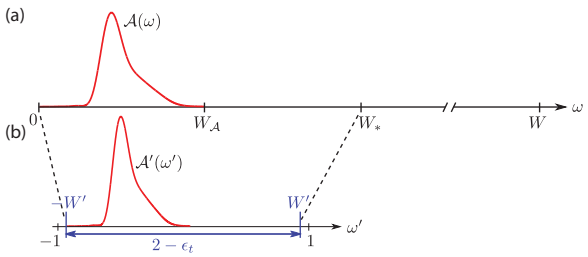

FIG. 1. (Color online) (a) Sketch of a spectral function, the spectral width $W_{\mathcal{A}}$ of which is much smaller than the many-body bandwidth W. Before making a Chebyshev expansion, we rescale the interval $\omega \in [0, W_*]$, with effective bandwidth $W_* = 2W_{\mathcal{A}}$, onto the interval $\omega' \in [-W', W']$, shown in (b), with rescaled half-bandwidth $W' = 1 - \frac{1}{2}\epsilon_t$ and a safety factor $\epsilon_t \simeq 0.025$.

expansions since they have very favorable convergence properties. As will be described in detail below, the spectral function can be represented approximately by a so-called Chebyshev expansion, which becomes exact for $N \to \infty$, of the following form:

$$\mathcal{A}_N^{\mathcal{BC}}(\omega) = \frac{2W'/W_*}{\pi\sqrt{1-\omega'^2}}\left[g_0\mu_0 + 2\sum_{n=1}^{N-1} g_n\mu_n T_n(\omega')\right]. \tag{5}$$

Here, the *Chebyshev moments* $\mu_n = \langle 0|\hat{\mathcal{B}}|t_n\rangle$ are obtained from the *Chebyshev vectors* $|t_n\rangle = T_n(\hat{H}')\hat{\mathcal{C}}|0\rangle$, and the g_n are known *damping factors* that influence broadening effects. The primes indicate that the Hamiltonian $\hat{H}$ and frequency ω were expressed in terms of rescaled and shifted versions $\hat{H}'$ and ω' in such a manner that an interval $\omega \in [0, W_*]$, which contains the entire spectral weight, is mapped onto a *rescaled band* $\omega' \in [-W', W']$ of half-width $W' < 1$.

This representation has several useful features:

(i) It resolves the interval $\omega \in [0, W_*]$ with a *uniform* resolution of $\mathcal{O}(W_*/N)$.

(ii) The range of frequencies over which the spectral function has nonzero weight, say $W_{\mathcal{A}}$ (to be called its *spectral width*), is often significantly smaller than the many-body bandwidth of the Hamiltonian, say W, as depicted in Fig 1. By choosing the effective bandwidth W_* to be of order $W_{\mathcal{A}}$ instead of W, huge gains in resolution are possible.

(iii) A well-controlled broadening scheme, encoded in the damping factors g_n, is available that allows finite-size effects to be either resolved or smeared out, as desired.

(iv) The Chebyshev vectors $|t_n\rangle$ are calculated using a (numerically stable) *recursion* scheme, which exploits Chebyshev recurrence relations to calculate $|t_n\rangle$ from $H'|t_{n-1}\rangle$ and $|t_{n-2}\rangle$ [see Eq. (30)]. Thus, the expectation values from which the spectral function is constructed are built up in a series of recursive steps [see Eq. (7) below] instead of being calculated at the end in one final step.

(v) The bond entropy of successive Chebyshev vectors $|t_n\rangle$ is found empirically to *remain bounded* with increasing recursion number n, thus, the complexity of these vectors remains manageable up to arbitrarily large n.

(vi) Finally, and from the perspective of numerical costs, most importantly, CheMPS *efficiently copes* with the *growth in bond entropy* with increasing iteration number that usually limits DMRG approaches. It does so by distributing this entropy over all $|t_n\rangle$, thereby packaging it into manageable units [see (v)]. In particular, when constructing and using the states $|t_n\rangle$, one never needs to know more than three at a time (and after use may delete them from memory). Hence, it is not necessary to combine all information contained in all $|t_n\rangle$ into a single MPS.

Let us contrast this with the CV or tDMRG approaches: imagine expanding the correction-vector or time-evolved state in terms of the Chebyshev vectors $|t_n\rangle$, i.e., expressing them as linear combinations of the form

$$|\mathcal{C}\rangle_\omega \simeq \sum_{n=0}^{N-1} C_\omega^n |t_n\rangle, \quad |\tilde{\mathcal{C}}\rangle_t \simeq \sum_{n=0}^{N-1} \tilde{C}_t^n |t_n\rangle, \tag{6}$$

respectively. (The coefficients C_ω^n and $\tilde{C}_t^n$ are related by Fourier transformation.) Now, the CV or tDMRG approaches, in effect, attempt to accurately represent the *entire linear combination* using a single MPS. This endeavor is numerically very costly since the entanglement entropy of this linear combination grows rapidly with N. The Chebyshev approach avoids this problem by taking expectation values *before* performing the sum on n:

$$\langle 0|\hat{\mathcal{B}}|\hat{\mathcal{C}}\rangle_\omega \simeq \sum_{n=0}^{N-1} C_\omega^n \mu_n, \quad \langle 0|\hat{\mathcal{B}}|\tilde{\mathcal{C}}\rangle_t \simeq \sum_{n=0}^{N-1} \tilde{C}_t^n \mu_n. \tag{7}$$

Thus, the Chebyshev expansion very conveniently organizes the calculation into many separate and, hence, numerically less costly, packages or subunits.

Our paper is organized as follows. We introduce the Chebyshev expansion for spectral functions in Sec. II and discuss its implementation using MPS, including an algorithm for performing a projection in energy, in Sec. III. In Sec. IV, we present CheMPS results for the structure factor of a spin-$\frac{1}{2}$ Heisenberg chain, perform a detailed analysis of finite-size effects (see Fig. 5), and compare our results to CV, Bethe ansatz, and tDMRG (see Figs. 4, 6, and 8, respectively). In Sec. V, we perform an extensive error analysis of the CheMPS approach using the quadratic resonant level model, and discuss some salient features of density matrix eigenspectra in Sec. VI. Section VII summarizes our main conclusions, and Sec. VIII presents a brief outlook toward possible future applications, involving time dependence or finite-temperature correlators. An appendix gives a detailed account of CheMPS results for the resonant level model used for the error analysis of Sec. V.

II. CHEBYSHEV EXPANSION OF $\mathcal{A}^{\mathcal{BC}}(\omega)$

A. Chebyshev basics

Let us start by briefly summarizing those properties of Chebyshev polynomials that will be needed below. We follow the notation of Ref. 5, which gives an excellent general discussion of Chebyshev expansion techniques (although without mentioning possible DMRG and MPS applications).

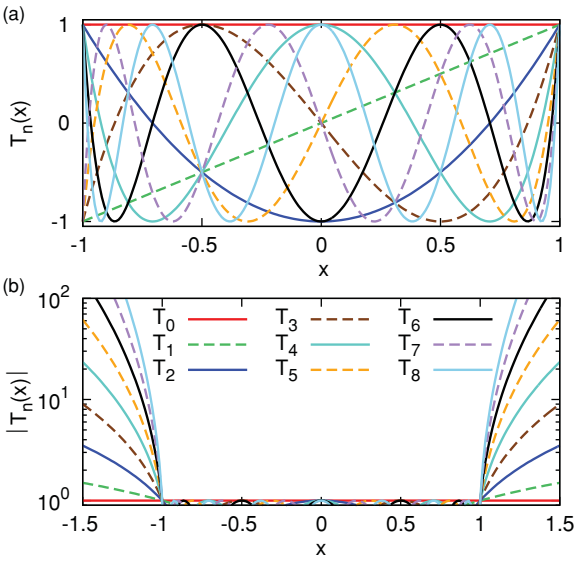

FIG. 2. (Color online) Chebyshev polynomials of the first kind, $T_n(x)$, for n up to 8. (a) All zeros and extrema of every $T_n(x)$ are located within the interval $I = [-1,1]$, and all extremal values equal 1 or -1. (b) Chebyshev polynomials $|T_n(x)|$ for $x \in [-1.5,1.5]$. The $|T_{n>0}(x)|$ grow rapidly when $|x|$ increases beyond 1.

Chebyshev polynomials of the first kind, $T_n(x)$, henceforth simply called Chebyshev polynomials, are defined by the recurrence relations

$$\begin{aligned} T_{n+1}(x) &= 2xT_n(x) - T_{n-1}(x), \\ T_0(x) &= 1, \qquad T_1(x) = x. \end{aligned} \tag{8}$$

They also satisfy the useful relation (for $n \geqslant n'$)

$$T_{n+n'}(x) = 2T_n(x)T_{n'}(x) - T_{n-n'}(x). \tag{9}$$

Two useful explicit representations are

$$T_n(x) = \cos[n \arccos(x)] = \cosh[n \operatorname{arccosh}(x)]. \tag{10}$$

On the interval $I = [-1,1]$, the Chebyshev polynomials constitute an orthogonal system of polynomials (over a weight function $(\pi\sqrt{1-x^2})^{-1}$), in terms of which any piecewise smooth and continuous function $f(x)|_{x\in I}$ can be expanded. In fact, the $T_n(x)$ are optimally suited for this purpose since they have the unique property (setting them apart from other systems of orthogonal polynomials) that on I their values are confined to $|T_n(x)| \leqslant 1$, with all extremal values equal to 1 or -1. This is evident from the first equality in Eq. (10); the second equality implies that, for $x \notin I$, $|T_n(x)|$ grows rapidly with increasing $|x|$. These properties are illustrated in Fig. 2.

There are several ways of constructing Chebyshev approximations for $f(x)|_{x\in I}$ (see Weisse *et al.*,[5] Sec. II A). The Chebyshev expansion that is practical for present purposes has the form

$$f(x) = \frac{1}{\pi\sqrt{1-x^2}}\left[\mu_0 + 2\sum_{n=1}^{\infty}\mu_n T_n(x)\right], \tag{11}$$

where the *Chebyshev moments* μ_n are given by

$$\mu_n = \int_{-1}^{1} dx f(x) T_n(x). \tag{12}$$

An approximate representation of order N is obtained for $f(x)$ if only the first N terms (i.e., $n \leqslant N-1$) are retained. However, such a truncation, in general, introduces artificial oscillations of period $\simeq 1/N$ called *Gibbs oscillations*. These can be smoothed by employing certain broadening kernels, which, in effect, rearrange the infinite series (11) before truncation. This leads to a *reconstructed* expansion of the form

$$f_N(x) = \frac{1}{\pi\sqrt{1-x^2}}\left[g_0\mu_0 + 2\sum_{n=1}^{N-1} g_n\mu_n T_n(x)\right], \tag{13}$$

which (for properly chosen kernels) converges *uniformly*:

$$\max_{-1<x<1} |f(x) - f_N(x)| \overset{N\to\infty}{\longrightarrow} 0. \tag{14}$$

The reconstructed series (13) contains the same Chebyshev moments μ_n as Eq. (12), but they are multiplied by *damping factors* g_n, real numbers with a form that is characteristic of the chosen kernel. Several choices have been proposed, which damp out Gibbs oscillations in somewhat different ways (see Ref. 5 for details). We will mostly employ *Jackson damping*, given by

$$g_n^J = \frac{(N-n+1)\cos\frac{\pi n}{N+1} + \sin\frac{\pi n}{N+1}\cot\frac{\pi}{N+1}}{N+1}. \tag{15}$$

This is usually the best choice since it guarantees an integrated error of $\mathcal{O}(\frac{1}{N})$ for $f_N(x)$. When used to approximate a δ function $\delta(x-\bar{x})$ sitting at $\bar{x} \in I$, Jackson damping yields a nearly Gaussian peak of width $\sqrt{1-\bar{x}^2}\,\pi/N$. On one occasion, we will also employ *Lorentz damping*

$$g_{n,\lambda}^L = \frac{\sinh\left[\lambda\left(1-\frac{n}{N}\right)\right]}{\sinh\lambda}, \tag{16}$$

where λ is a real parameter. Lorentz damping preserves analytical properties (causality) of Green's function and broadens a δ function $\delta(x-\bar{x})$ into a peak, the shape of which, for the choice $\lambda = 4$ used here (following Ref. 5), is nearly Lorentzian of width $\sqrt{1-\bar{x}^2}\,\lambda/N$.

To summarize: The order-N Chebyshev reconstruction $f_N(x)$ with Jackson or Lorentzian damping with $\lambda = 4$ yields a result that is very close to the broadened function

$$f_N^X(x) = \int_{-1}^{1} d\bar{x}\, K^X_{\eta'_{N,\bar{x}}}(x-\bar{x}) f(\bar{x}) \tag{17}$$

($X = J, L$) with broadening kernels and widths given by

$$K^J_{\eta'}(x) = \frac{e^{-x^2/(2\eta'^2)}}{\sqrt{2\pi}\eta'}, \quad \eta'_{N,\bar{x}} = \sqrt{1-\bar{x}^2}\,\frac{\pi}{N}, \tag{18a}$$

$$K^L_{\eta'}(x) = \frac{\eta'/\pi}{x^2+\eta'^2}, \quad \eta'_{N,\bar{x}} = \sqrt{1-\bar{x}^2}\,\frac{4}{N}, \tag{18b}$$

respectively. Thus, $f_N(x)$ resolves the shape of $f(x)$ with a resolution of $\mathcal{O}(1/N)$.

For purposes of illustration, Fig. 3(a) shows three Chebyshev reconstructions of a δ function at $\bar{x} = 0$: without damping, giving Gibbs oscillations; with Jackson damping, yielding a near-Gaussian peak; and with Lorentz damping, yielding a near-Lorentzian peak. Figure 3(b) shows a Jackson-damped Chebyshev reconstruction of a comb of Gaussian peaks $\sum_\alpha K^J_{\bar{\eta}'_\alpha}(x-\bar{x}_\alpha)$, the widths $\bar{\eta}'_\alpha$ of which are all equal. It illustrates how increasing N reduces the amount of broadening until the original peak form is recovered for sufficiently large N. It also shows that the broadened peak widths depend on the peak positions, reflecting the fact that convolving a Gaussian of width $\bar{\eta}'_\alpha$ with a near Gaussian of width $\eta'_{N,\bar{x}_\alpha}$ [Eq. (17)] produces a near Gaussian of width

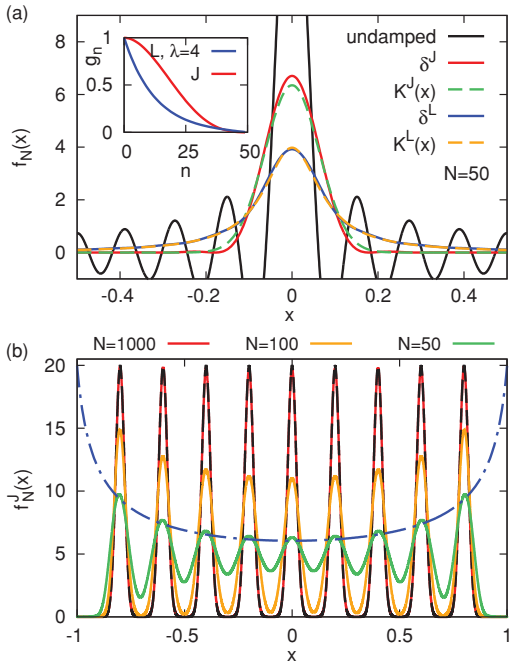

FIG. 3. (Color online) Three Chebyshev reconstructions of $\delta(x)$, with $N = 50$: The undamped case ($g_n = 1$) yields Gibbs oscillations [central peak has height $\delta_{50}(0) = 16.23$]; Jackson damping (δ^J) mimics a Gaussian peak $K^J(x)$ of width π/N; Lorentz damping (δ^L) for $\lambda = 4$ mimics a Lorentzian peak $K^L(x)$ of width λ/N. Inset: Jackson and Lorentz damping factors g_n^J and $g_{n,\lambda=4}^L$, respectively, plotted for $N = 50$. Both decrease monotonically from 1 to 0, but in somewhat different ways. (b) Jackson-damped reconstruction of a comb of normalized Gaussians (dashed line), all of width $\bar{\eta}' = 0.02$, for three values of N (solid lines). The x dependence of the peak heights is given by $[2\pi(\bar{\eta}'^2 + \eta'^2_{N,x})]^{-1/2}$ (dashed-dotted line) [see Eq. (19)].

$$\eta'_\alpha \simeq \sqrt{\bar{\eta}'^2_\alpha + \eta'^2_{N,\bar{x}_\alpha}}. \tag{19}$$

To evaluate the $T_n(x)$ that occur in Eq. (13), we use the first equality of Eq. (10). Although numerically more efficient methods exist for this purpose,[5] their use becomes advisable only for expansion orders much larger than the $N \lesssim \mathcal{O}(10^3)$ that we will need in this work.

B. Rescaling of ω and $\hat{H}$

To construct a Chebyshev expansion of the spectral function $\mathcal{A}^{\mathcal{BC}}(\omega)$ of Eq. (1), we need to rescale and shift[5] the Hamiltonian $\hat{H} \mapsto \hat{H}'$ and the frequency $\omega \mapsto \omega'$ in such a way that the spectral range of $\mathcal{A}(\omega)$, i.e., the interval $[0, W_{\mathcal{A}}]$ within which it has nonzero weight, is mapped *into* the interval $[-1,1]$. Rescaled, dimensionless energies and frequencies will always carry primes. As safeguards against "leakage" beyond $[-1,1]$ due to numerical inaccuracies, we choose the linear map (see Fig. 1)

$$\omega \in [0, W_*] \mapsto \omega' \in [-W', W'], \quad W' = 1 - \tfrac{1}{2}\epsilon_t, \tag{20}$$

which entails two precautionary measures. First, the ω interval is taken to be larger than the requisite $[0, W_{\mathcal{A}}]$ by choosing the *effective bandwidth* W_* to be larger than the spectral width $W_{\mathcal{A}}$; second, the ω' interval is taken to be slightly smaller than the requisite $[-1,1]$ by choosing the *rescaled half-bandwidth* W' to be smaller than 1, with a safety factor[5] of $\epsilon_t \simeq 0.025$. To be explicit, we define

$$\omega' = \frac{\omega}{a} - W', \quad a = \frac{W_*}{2W'}, \tag{21a}$$

$$\hat{H}' = \frac{\hat{H} - E_0}{a} - W', \tag{21b}$$

where $\hat{H}'$ has ground-state energy $E_0' = -W'$. Then, we express the spectral function (1) as

$$\mathcal{A}^{\mathcal{BC}}(\omega) = \frac{1}{a}\langle 0|\hat{\mathcal{B}}\,\delta(\omega' - \hat{H}')\,\hat{\mathcal{C}}|0\rangle \tag{22}$$

[with $\omega' = \omega'(\omega)$ and $\hat{H}'$ given by Eqs. (21)], which by construction has no weight for $\omega' \notin [-W', W']$.

One possible choice for W_* is to equate it to the width of the many-body spectrum of H, given by $W = E_{\max} - E_0$. When using DMRG, E_0 is usually already known from calculating the ground state $|0\rangle$ of H, and $E_{\max}$ can be found, e. g. , by calculating[29] the ground state of $-H$ (reduced DMRG accuracy relative to usual ground-state calculations is sufficient, since only $E_{\max}$ is of interest here.)

A disadvantage of the choice $W_* = W$ is that the many-body bandwidth W typically is large (it scales with system size), whereas optimal spectral resolution requires W_* to be as small as possible: since an Nth order Chebyshev expansion yields a resolution of $\mathcal{O}(1/N)$ on the interval $[-1,1]$, its resolution on the original interval $[0, W_*]$ will be $\mathcal{O}(W_*/N)$, which evidently becomes better the smaller W_*. If $\hat{\mathcal{B}}$ and $\hat{\mathcal{C}}$ are single-particle operators, the spectral width $W_{\mathcal{A}}$ of $\mathcal{A}^{\mathcal{BC}}(\omega)$ is independent of system size and, hence, much smaller than the many-body bandwidth W. In this case, it is advisable to choose W_* to be of similar order (though still larger) than $W_{\mathcal{A}}$. We will choose $W_* = 2W_{\mathcal{A}}$, which is typically $\ll W$, as illustrated in 1.

C. Chebyshev expansion in frequency domain

To expand the δ function in Eq. (22) in Chebyshev polynomials, we use $\hat{f}(x) = \delta(x - \hat{H}')$ with $x = \omega'$ in Eq. (12), and obtain from Eq. (13) a reconstructed Chebyshev operator expansion of the form

$$\delta_N(\omega' - \hat{H}') = \frac{1}{\pi\sqrt{1-\omega'^2}}\left[g_0 + 2\sum_{n=1}^{N-1} g_n T_n(\hat{H}')T_n(\omega')\right]. \tag{23}$$

Inserting this into Eq. (22) for $\mathcal{A}^{\mathcal{BC}}(\omega)$ yields the Chebyshev expansion (5), with Chebyshev moments given by

$$\mu_n = \langle 0|\hat{\mathcal{B}}T_n(\hat{H}')\hat{\mathcal{C}}|0\rangle. \tag{24}$$

Thus, μ_n is a ground-state expectation value of an nth-order polynomial in $\hat{H}'$, the construction of which might *a priori* appear to become increasingly daunting as n increases. Fortunately, this challenge can be dealt with *recursively* by expressing the moments as

$$\mu_n = \langle 0|\hat{\mathcal{B}}|t_n\rangle, \quad |t_n\rangle = T_n(\hat{H}')\hat{\mathcal{C}}|0\rangle, \tag{25}$$

and calculating the *Chebyshev vectors* $|t_n\rangle$ by exploiting the Chebyshev recurrence relations (8). The details of this recursive scheme will be discussed in Sec. III.

D. Chebyshev expansion in time domain

The Chebyshev expansion can also be employed for studying time evolution in general, and the correlator $G^{\mathcal{BC}}(t)$ in particular. To this end, we express the time-evolution operator as

$$\hat{U}(t) = e^{-i\hat{H}t} = \int_{-1}^{1} d\omega' e^{-i[a(\omega'+W')+E_0]t}\,\delta(\omega' - \hat{H}') \tag{26}$$

and insert Eq. (23) (without damping, $g_n = 1$) into the latter. This yields[30,31]

$$\hat{U}_N(t) = e^{-i(E_0+aW')t}\left[c_0(t) + 2\sum_{n=1}^{N-1} T_n(\hat{H}')c_n(t)\right], \tag{27a}$$

$$c_n(t) = \int_{-1}^{1} \frac{e^{-iat\omega'}T_n(\omega')}{\pi\sqrt{1-\omega'^2}}d\omega' = (-i)^n J_n(at). \tag{27b}$$

Here, $J_n(at)$ is the Bessel function of the first kind of order n. It decays very rapidly with n once $n > at$. Hence, an expansion of given order N gives an essentially exact representation of $\hat{U}(t)$ for times up to $t_{\max} \lesssim \frac{N}{a}$, while $c_{N-1}(t)$ provides an estimate of the error.

By inserting Eqs. (27) into Eqs. (4) for $G^{\mathcal{BC}}(t)$, we find

$$G_N^{\mathcal{BC}}(t) = e^{-iaW't}\left[\mu_0 J_0(at) + 2\sum_{n=1}^{N-1}(-i)^n \mu_n\, J_n(at)\right], \tag{28}$$

where the Chebyshev moments μ_n are again given by Eq. (25). Thus, the Chebyshev expansions of $G^{\mathcal{BC}}(t)$ and $\mathcal{A}^{\mathcal{BC}}(\omega)$ are governed by the *same* set of moments μ_n, as is to be expected for functions linked by Fourier transformation.

III. MPS EVALUATION OF THE CHEBYSHEV MOMENTS μ_n

We now present a recursive scheme for calculating the Chebyshev moments μ_n. The manipulations described below

were implemented using MPS-based methods,[4,6–10] which are very convenient for constructing the states of interest, while matrix product operators[10] (MPOs) simplify the implementation of the shift and rescaling transformation [Eq. (21b)] of the Hamiltonian.

A. Recurrence fitting

To initialize the Chebyshev expansion, we calculate ground state $|0\rangle$ and ground-state energy E_0 of $\hat{H}$, make a specific choice for W_* and W', and construct $\hat{H}'$ according to Eq. (21b). Then comes the main task, namely, the recursive calculation of the moments μ_n. This is done by starting from

$$|t_0\rangle = \hat{\mathcal{C}}|0\rangle, \quad |t_1\rangle = \hat{H}'|t_0\rangle \tag{29}$$

and using the recurrence relation [obtained from Eq. (8)]

$$|t_n\rangle = 2\hat{H}'|t_{n-1}\rangle - |t_{n-2}\rangle, \tag{30}$$

which can be implemented using the so-called compression or fitting procedure[32] (see Ref. 4, Sec. 4.5.2 for details). It finds an MPS representation for $|t_n\rangle$, at minimal loss of information for given MPS dimension m, by variationally minimizing the *fitting error*

$$\Delta_{\text{fit}} = \| |t_n\rangle - (2\hat{H}'|t_{n-1}\rangle - |t_{n-2}\rangle) \|^2. \tag{31}$$

We will call this procedure *recurrence fitting*. In practice, the variational minimization proceeds via a sequence of fitting sweeps back and forth along the chain. These are continued until the state being optimized becomes stationary, in the sense that the overlap

$$\Delta_{\text{c}} = \left| 1 - \frac{\langle t_n | t'_n \rangle}{\| |t_n\rangle \| \, \| |t'_n\rangle \|} \right| \tag{32}$$

between the states $|t_n\rangle$ and $|t'_n\rangle$ before and after one fitting sweep drops below a specified *fitting convergence threshold* (typically in the range 10^{-6} to 10^{-8}). The maximum expansion order for which $|t_n\rangle$ is obtained using recurrence fitting will be denoted by N_{max}.

The MPS dimension m needed to achieve accurate recurrence fitting turns out to be surprisingly small (see Sec. V for a detailed analysis). For example, $m = 32$ sufficed for the antiferromagnetic Heisenberg chain of length $L = 100$, discussed in Sec. IV. The reason for this remarkable and eminently useful feature lies in the fact that the Chebyshev recurrence relations (30) contain only two terms on the right-hand side, the addition of which requires only modest computational effort. In contrast, CV or tDMRG typically require much larger m since they attempt to represent the sum of many states [see Eq. (6)] in terms of a single MPS.

For the special but common case that $\hat{\mathcal{B}} = \hat{\mathcal{C}}^\dagger$, Eq. (9) yields a relation between different moments

$$\mu_{n+n'} = 2\langle t_n | t_{n'} \rangle - \mu_{n-n'}. \tag{33}$$

This can be used to effectively double the order of the expansion to $2N_{\text{max}}$ without calculating any additional Chebyshev vectors, by setting $n' = n - 1$ or n:

$$\begin{aligned} \tilde{\mu}_{2n-1} &= 2\langle t_n | t_{n-1} \rangle - \mu_1, \\ \tilde{\mu}_{2n} &= 2\langle t_n | t_n \rangle - \mu_0. \end{aligned} \tag{34}$$

We use tildes to distinguish $\tilde{\mu}_n$ moments calculated in this manner from the μ_n moments obtained via Eq. (25). Although they should nominally be identical, in numerical practice, $\tilde{\mu}_n$ moments are less accurate [by up to a factor of 5 in Fig. 9(c) below] since they depend on two Chebyshev vectors, whereas μ_n moments depend on only one. Our Chebyshev reconstructions thus generally employ the μ_n moments and, unless stated otherwise, $\tilde{\mu}_n$ moments are used only for results requiring $N_{\text{max}} \leqslant n < 2N_{\text{max}}$.

B. Energy truncation

We have argued above that, in order to optimize spectral resolution, it may be desirable to choose the effective bandwidth W_* to be smaller than the full many-body bandwidth W. If this is done, however, it is essential to include an additional *energy truncation* step into the recursion procedure to ensure that each $|t_n\rangle$ remains free from "high-energy" components, i.e., $\hat{H}'$ eigenstates with eigenenergies $E'_k > 1$, which fall outside the range $[-1,1]$ that is admissable for arguments of Chebyshev polynomials. If $W_* < W$, numerical noise causes the state $|t_n\rangle$ to contain such high-energy contributions in spite of the precautionary measures described after Eq. (20) because the application of $\hat{H}'$ to $|t_{n-1}\rangle$ in Eq. (30) entails a DMRG truncation step, which is not performed in the eigenbasis of $\hat{H}'$. If such high-energy components were fed into subsequent recursion steps, the norms $\|t_n\rangle\|$ of successive Chebyshev vectors would diverge rapidly (as would the resulting moments μ_n) because this effectively amounts to evaluating Chebyshev polynomials $T_n(x)$ for $|x| > 1$, where $|T_n| \gg 1$ [see Fig. 2(b)].

As a consequence, after obtaining a new state $|t_n\rangle$ from Eq. (30), we take the precautionary measure of projecting out any high-energy components that it might contain before proceeding to the next $|t_{n+1}\rangle$. This can be done by performing several *energy truncation sweeps*. During an energy truncation sweep, we focus on one site at a time, perform an energy truncation in a local Krylov basis constructed for that site, and then move on to the next site. Shifting the current site is accomplished by standard MPS means, without any truncation, as a DMRG truncation would counteract the energy truncation. (As a consequence, an energy truncation in terms of two-site sweeps has not been implemented.)

The truncation must take place in the energy eigenbasis of the Hamiltonian $\hat{H}'$. Of course, its complete eigenbasis is not accessible, thus, we build a Krylov subspace of dimension d_K within the effective Hilbert space at every site. Alternatively, energy truncation can also be performed in the bond representation $|\psi\rangle = B_{l_r}|l_k\rangle|r_k\rangle$. In this Krylov subspace, the effective Hamiltonian $\hat{H}'_K$ of dimension d_K can be fully diagonalized and so we can construct a projection operator to project out all eigenstates with energy bigger than some *energy truncation threshold* ε_P. The choice of this threshold depends on the choice of W_*. We have found the combination $W_* = 2W_A$ and $\varepsilon_P = 1.0$ to work well (but other choices, involving, e.g., smaller W_* and larger ε_P would be possible, too.)

In the following, we describe the procedure just outlined in more detail for a single site using standard MPS nomenclature. Let the effective local Hilbert space for this site be spanned

TABLE I. List of CheMPS parameters that control various algorithmic tasks, influencing their numerical costs and the quality of results. Since the tasks "recurrence fitting" and "energy truncation" are carried out at every recursion step, the importance of the corresponding parameters is self-evident. However, W_* and ϵ_t, which determine the rescaled Hamiltonian $\hat{H}'$, turn out to have a high impact on the results, too, as the quality of the energy truncation sweeps strongly depends on $\hat{H}'$. For $\varepsilon_P = 1$, the choice of taking W_* to be twice the spectral bandwidth $W_{\mathcal{A}}$ (or equal to the many-body bandwidth W) was found to work well with (or without) energy truncation, respectively. N and g_n do not affect the calculated moments of the expansion, but control the broadening of the reconstructed spectral function.

Parameter	Recommended value	Description	Task
W_*	$2W_{\mathcal{A}}$ (or W)	Effective bandwidth with (or without) energy truncation	Rescaling of H
ϵ_t	0.025	Safety offset in rescaled half-bandwidth: $W' = 1 - \frac{1}{2}\epsilon_t$	
m		MPS dimension	Recurrence fitting
Δ_c	$10^{-6}, \ldots, 10^{-8}$	Fitting convergence threshold	
d_K	30	Krylov subspace dimension	Energy truncation
n_S	10	Number of sweeps	
ε_P	1.0	Energy truncation threshold (in rescaled units)	
N	Depends on system size	Order of expansion, broadening	Spectral reconstruction
g_n	g_n^J	Choice of damping factors	

by the left, local, and right basis vectors $|l\rangle$, $|\sigma\rangle$, and $|r\rangle$, and expand the Chebyshev vector $|\psi\rangle = |t_n\rangle$ in this basis:

$$|\psi\rangle = \sum_{l\sigma r} A^{[\sigma]}_{lr} |l\rangle|\sigma\rangle|r\rangle. \tag{35}$$

To construct a projection operator P that projects out the high-energy components for this site $|\psi\rangle \mapsto P|\psi\rangle$, one may proceed as follows.

First, build a Krylov subspace of dimension d_K within $\mathrm{span}\{|l\rangle|\sigma\rangle|r\rangle\}$ and calculate the matrix elements of $\hat{H}'$ within it (no truncation necessary):

$$|\tilde{i}\rangle = (\hat{H}')^{i-1}|\psi\rangle, \quad i = 1, \ldots, d_K \tag{36a}$$

$$|\tilde{i}\rangle \mapsto |i\rangle \quad \text{orthonormalize via Gram-Schmidt,} \tag{36b}$$

$$(\hat{H}'_K)_{ij} = \langle i|\hat{H}'_K|j\rangle, \quad \hat{H}'_K \in \mathbb{C}^{d_K \times d_K}. \tag{36c}$$

Next, fully diagonalize $\hat{H}'_K$ to obtain all eigenenergies ε'_α and eigenvectors $|e_\alpha\rangle$:

$$\hat{U}^\dagger \hat{H}'_K \hat{U} = \sum_{\alpha=1}^{d_K} |e_\alpha\rangle \varepsilon'_\alpha \langle e_\alpha|. \tag{37}$$

Then, construct the projection operator

$$P = \mathbb{1} - \sum_{\alpha:\varepsilon'_\alpha \geqslant \varepsilon_P} |e_\alpha\rangle\langle e_\alpha| \tag{38}$$

for a certain energy threshold ε_P and apply it:

$$|\psi\rangle \mapsto P|\psi\rangle. \tag{39}$$

Performing this procedure once for every site of the chain constitutes a truncation sweep. The state obtained after several truncation sweeps, say $|t_n\rangle_{\mathrm{tr}}$, is stripped from the unwanted high-energy components of $|t_n\rangle$, as well as possible within a Krylov approximation. After fitting and truncation have been completed, the resulting (unnormalized) state $|t_n\rangle_{\mathrm{tr}}$ is renamed $|t_n\rangle$, used for calculating μ_n, and fed into the next recursion step.

To quantify the effects of energy truncation, we consider two measures of how much $|t_n\rangle$ changes during truncation. First, for a given truncation sweep, we define the *average truncated weight per site* (averaged over all sites) by

$$N_{\mathrm{tr}}^{\mathrm{sweep}} = \sqrt{\frac{1}{L}\sum_k \sum_{\alpha:\varepsilon'_\alpha \geqslant \varepsilon_P} \left|\langle e^k_\alpha | \psi\rangle\right|^2}, \tag{40}$$

where $|e^k_\alpha\rangle$ are the vectors constituting the projector of Eq. (38) at site k. Second, we define the *truncation-induced state change* by

$$\Delta_{\mathrm{tr}} = \| |t_n\rangle_{\mathrm{tr}} - |t_n\rangle \|^2. \tag{41}$$

It measures changes in the state due to the intended truncation of high-energy weight, but also due to unavoidable numerical errors. In our experience, neither of the truncation measures $N_{\mathrm{tr}}^{\mathrm{sweep}}$ and Δ_{tr} show clear signs of decay when increasing the number of truncation sweeps, say n_S [see Fig. 10(c) below]. This reflects the fact that energy truncation has the status of a precautionary measure, not a variational procedure, and implies that there is no dynamic criterion as to when to stop truncation sweeping. As a consequence, one has to analyze how the accuracy of the results depends on n_S and optimize the latter accordingly. This will be described in Sec. V B below.

The numerical costs for energy truncation are as follows: The cost for the steps in Eqs. (36) are $\mathcal{O}(d_K^2 m^3 d^2 D_H)$, where m is the MPS dimension, d is the size of the local site basis, and D_H is the matrix product operator dimension of $\hat{H}'$. The diagonalization of $\hat{H}'^K$ is of $\mathcal{O}(d_K^3)$, where d_K is theoretically bounded by $m^2 d$. In our experience, the purpose of the energy truncation, which is solely to eliminate high-energy contributions, is well accomplished already for a relatively small Krylov subspace dimension of $d_K = 30 \ll m^2 d$.

An overview of all the parameters relevant for CheMPS is given in Table I. Where applicable, it also lists the values that we found to be optimal. A detailed error analysis, tracing the effects of various choices for these parameters, will be presented in Sec. V.

IV. RESULTS: HEISENBERG ANTIFERROMAGNET

To illustrate the capabilities and power of the proposed CheMPS approach, this section presents results for the spin structure factor of a one-dimensional spin-$\frac{1}{2}$ Heisenberg antiferromagnet (HAFM) and compares them against results obtained from CV and tDMRG approaches.

A. Spin structure factor

We study the spin-$\frac{1}{2}$ HAFM for a lattice of length L:

$$\hat{H}_{\mathrm{HAFM}} = J \sum_{j=1}^{L-1} \hat{\boldsymbol{S}}_j \cdot \hat{\boldsymbol{S}}_{j+1}, \tag{42}$$

where $\hat{\boldsymbol{S}}_j$ denotes the spin operator at site j. We choose $J = 1$ as unit of energy throughout this section. This model exhibits SU(2) symmetry, which has been exploited[33] in our calculations; accordingly, all MPS dimensions noted for the HAFM are to be understood as the number of SU(2) (representative) states being kept. To account for the open boundary conditions, we define spin-wave operators as

$$\hat{\boldsymbol{S}}_k = \sqrt{\frac{2}{L+1}} \sum_{j=1}^{L} \sin(jk) \hat{\boldsymbol{S}}_j \tag{43}$$

with quasimomentum $k = l\pi/(L+1)$, $l = 1, \ldots, L$. [When displaying numerical results for "$k = \pi$" or $\pi/2$ below, we mean $k = \pi L/(L+1)$ or $\pi(L/2+1)/(L+1)$, respectively, choosing L even throughout.] The spin structure factor (spectral function) we are interested in is given by

$$S(k,\omega) = \mathcal{A}^{\boldsymbol{S}_k^\dagger \cdot \boldsymbol{S}_k}(\omega). \tag{44}$$

It is known from exact solutions[34–38] that the dominant part of the spin structure factor stems from two-spinon contributions, bounded from below and above by

$$\omega_1 = \frac{\pi}{2} |\sin k| \quad \text{and} \quad \omega_2 = \pi \left| \sin \frac{k}{2} \right|. \tag{45}$$

(For the exact solution of an infinite system, k refers to the true momentum, not quasimomentum.) Moreover, for an infinite system, $S(k,\omega)$ is known[37,38] to diverge as

$$S(k,\omega) \sim [\omega - \omega_1]^{-\frac{1}{2}} \sqrt{\ln[1/(\omega - \omega_1)]} \quad \text{for } k \neq \pi, \tag{46a}$$

$$S(\pi,\omega) \sim \omega^{-1} \sqrt{\ln(1/\omega)} \tag{46b}$$

as ω approaches the lower threshold ω_1 from above. This divergence reflects the tendency toward staggered spin order of the ground state of the Heisenberg antiferromagnet. It poses a severe challenge for numerics, which always deals with systems of finite size, and hence will never yield a true divergence. Instead, the divergence will be cut off at $\omega - \omega_1 \simeq 1/L$, yielding a peak of finite height

$$\max S(k,\omega) \sim [L \ln L]^{\frac{1}{2}} \quad \text{for} \quad k \neq \pi, \tag{47a}$$

$$\max S(\pi,\omega) \sim L[\ln L]^{\frac{1}{2}}. \tag{47b}$$

Thus, the best that one can hope to achieve with numerics is to capture the nature of the divergence as ω approaches ω_1 before it is cut off by finite size, or the scaling of the peak height with system size.

Equation (45) gives a good guide for choosing W_*. We found the choices $W_* = 6.3 \simeq 2\pi$ and $\epsilon_t = 0.025$ to work well for all k and have used them for all figures (4 to 6) of this section. As consistency checks, we verified that the resulting $S(k,\omega)$ is essentially independent of W_* and that it agrees with a calculation that included the full many-body bandwidth ($W_* = W$).

To have an accurate starting point for all calculations, we used throughout a ground state obtained by standard DMRG with MPS dimension $m = 512$. From expansion order $n = 1$ onward, it turned out to be sufficient to represent all Chebyshev vectors $|t_n\rangle$ using a surprisingly small MPS dimension of $m = 32$, or $m = 64$ for some results involving very large iteration number, as indicated in every figure. (In retrospect, this implies that, for the ground state too, a much smaller m would have sufficed.) We have verified that the structure factor $S(k,\omega)$ is well converged w.r.t. m nevertheless. Detailed evidence for this claim will be presented below. However, already at this stage it is worth remarking that *the ability of CheMPS to get good results with comparatively small m values is perhaps the single most striking conclusion of our work*. This will be discussed in detail below.

B. Comparison to CV

We begin our discussion of CheMPS results by comparing them to those of CV calculations, which are known to be very accurate, although also computationally expensive. The CV method involves a broadening parameter η and broadens δ functions into Lorentzian peaks of width η. This can be mimicked with CheMPS by using Lorentz damping (with $\lambda = 4.0$) since this also produces Lorentzian broadening, representing a δ function $\delta(\omega' - \bar{\omega}')$ by a near-Lorentzian peak, albeit with a frequency-dependent width $\eta'_{N,\bar{\omega}'} = \sqrt{1 - \bar{\omega}'^2}\, \lambda/N$ (see Sec. II A and 3). To compare CheMPS results with CV results at given η, we thus identify $\eta = a\eta'_{N,\bar{\omega}'}$, where a is the scaling factor from Eqs. (21) and $\bar{\omega}'$ is taken to be the rescaled and shifted version of the frequency $\omega_{\max}$ at which the peak reaches its maximum. Thus, we set the expansion order used for reconstruction to

$$N = \frac{4a}{\eta} \sqrt{1 - (\omega_{\max}/a - W')^2}. \tag{48}$$

Figure 4 shows such a comparison for the structure factor $S(\pi/2,\omega)$ of a $L = 100$ Heisenberg chain. We used two choices of η that are large enough to avoid finite-size effects, namely, $\eta = 0.1$ and 0.05, and set $\omega_{\max} = \pi/2$ [cf. ω_1 of Eq. (45)]. We used MPS dimensions of $m_{\mathrm{CV}} = 1000$ or $m_{\mathrm{Ch}} = 32$ for CV or CheMPS calculations, respectively. (Our choice for m_{CV} aimed for achieving highly accurate CV results; for $\eta = 0.05$, this required $m_{\mathrm{CV}} = 1000$, but for $\eta = 0.1$, a slightly smaller value for m_{CV} would have sufficed.) We find excellent agreement between the two approaches without adjusting any free parameter since N is fixed by (48). For example, for $\eta = 0.05$, $N = 255$, the relative error is less than 3% for all ω.

Since this level of agreement is obtained using $m_{\mathrm{Ch}} \ll m_{\mathrm{CV}}$, we conclude that CheMPS with Lorentz damping gives results,

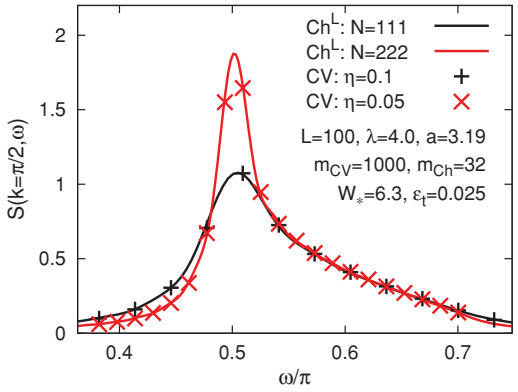

FIG. 4. (Color online) Comparison of CheMPS vs correction-vector (CV) calculations of $S(k=\pi/2,\omega)$ for a Heisenberg chain: Lines show Chebyshev results reconstructed for $N=118$ and 236 using Lorentz damping [(16)] with $\lambda=4.0$; symbols show CV results, obtained using broadening parameters of $\eta=0.1$ and 0.05. We expect and indeed find good agreement between lines and symbols since both Lorentz damping and the correction-vector method, in effect, broaden the spectral function by Lorentzians, the widths of which we equated by choosing $a\lambda/N=\eta$ (with $a=3.19$) [see Eq. (48) and also Fig. 3]. Since $m_{\rm Ch}\ll m_{\rm CV}$, the numerical cost of obtaining an *entire* curve via Chebyshev is dramatically cheaper than calculating a *single* point via CV, as discussed in the text.

the accuracy of which is comparable to those of CV, *at dramatically reduced numerical cost*. Indeed, for $\eta=0.05$, the calculation of the entire CheMPS spectral function was 25 times faster than that of a single CV data point and took up 21 hours on a 2.6-GHz single-core Opteron CPU.

C. Finite-size effects

Let us now analyze the role of finite system size. To this end, it is, of course, important to understand broadening effects in detail. The fact that CheMPS offers simple and systematic control of broadening via the choice of the expansion order (and damping factors), as will be illustrated below, is very convenient and may be regarded as one of its main advantages.

Figure 5(a) shows CheMPS results for the spin structure factors $S(k,\omega)$ of four different momenta k, calculated for $L=100$ using Jackson damping. They were reconstructed using the largest expansion order, say N_L, that does not yet resolve finite-size effects, a choice that will be called *optimal broadening*. Each curve shows a dominant peak, and we are interested in finding its intrinsic shape $S^\infty(k,\omega)$ in the continuum limit of an infinitely long chain ($L\to\infty$). Thus, the following general question arises: Under which conditions will a spectrum calculated for finite system size L and reconstructed with finite expansion order N, say, $S^L_N(\omega)$, correctly reproduce the desired continuum spectrum $S^\infty(\omega)$? The general answer, of course, is that the optimally broadened spectrum should have converged as a function of L, i.e., the shape of $S^L_{N_L}(\omega)$ should not change upon increasing L. However, for a spectrum with an intrinsic divergence, such as Eq. (46), the peak's height will never saturate with L; at best, one can hope to observe L convergence of the shape of its tail and the proper scaling of its height Eq. (47).

To illustrate the nature of finite-size effects and the role of N in revealing or hiding them, Fig. 5(b) shows $S(\pi,\omega)$ for $L=100$ and several values of N, both smaller and larger than N_L. As N is increased and the effective broadening $\eta_N\simeq\mathcal{O}(W_*/N)$ decreases, the main peak of the initially very broad and smooth spectral function becomes sharper. Optimal broadening in Fig. 5(b) corresponds to $N_L\simeq 70$, beyond which additional "wiggles" emerge. These develop, with beautifully uniform resolution, into *dominant subpeaks* as N is increased further. The discrete subpeaks reflect the quantized energies of spin-wave excitations in a finite system. With sufficiently high resolution [$N=999$ in Fig. 5(b)], numerous additional minor subpeaks emerge, but their weight is very small compared to that of the dominant subpeaks. This fact is important since it implies that the structure factor of a finite-size system is exhausted almost fully by the set of dominant subpeaks, with very small intrinsic widths.

We have checked that there are $\mathcal{O}(L)$ dominant subpeaks within the spectral bandwidth of $S(k,\omega)$. Correspondingly, the average spacing between dominant subpeaks, to be called the *finite-size energy scale* ω_L, is proportional to $\frac{1}{L}$ [Figs. 5(c) and 5(d)]. The weight of each subpeak decreases similarly, ensuring that the total weight in a given frequency interval converges as $L\to\infty$. The inverse subpeak spacing $\hbar/\omega_L$ corresponds to the Heisenberg time, i.e., the time within which a spin-wave packet propagates the length of the system.

Figures 5(e) and 5(f) illustrate two slightly different broadening strategies. In Fig. 5(e), L is increased for fixed N: the distinct subpeaks increasingly overlap, resulting in a smooth spectral function once ω_L drops below η_N. In Fig. 5(f), optimal broadening is used (η_N just larger than ω_L: now, no subpeaks are visible and the L evolution of the main peak is revealed with better resolution).

In both Figs. 5(e) and 5(f), the peak height shows no indications of converging with increasing L. [The same is true for the data of Fig. 5(a).] This reflects the intrinsic divergence of the peak height expected from Eq. (46). Figures 6(a) and 6(b) contain a quantitative analysis of this divergence for $S(\pi,\omega)$ and $S(\pi/2,\omega)$, respectively. The shape of the divergences for an infinite system are shown by the thick solid lines, representing exact Bethe ansatz results from Ref. 38. Thin dashed lines show results from tDMRG from Ref. 22 for $L=100$, and thin solid lines show CheMPS results for several system sizes between $L=50$ and 300. For CheMPS spectral reconstruction, we determined the expansion order N_{300} that ensures optimal broadening for $L=300$, and used a fixed ratio of $N/L=N_{300}/300$ for all curves [namely, 0.42 or 0.67 for Figs. 4(a) and 4(b), respectively]. CheMPS (for $L=300$) and tDMRG reproduce the peak's tail and flank well, but clearly and expectedly are unable to produce a true divergence at the lower threshold frequency. Nevertheless, the insets show that the manner in which the CheMPS peak heights increase with L is indeed consistent with Eq. (46). {For the limited range of available system sizes, however, a reliable distinction between $L[\ln(L)]^{1/2}$, $[L\ln(L)]^{1/2}$, or L behavior is not possible.}

It is also possible to determine the lower threshold frequency ω_1 rather accurately from the CheMPS results by doing an $1/L$ extrapolation. We illustrate this in 6(b) by extrapolating

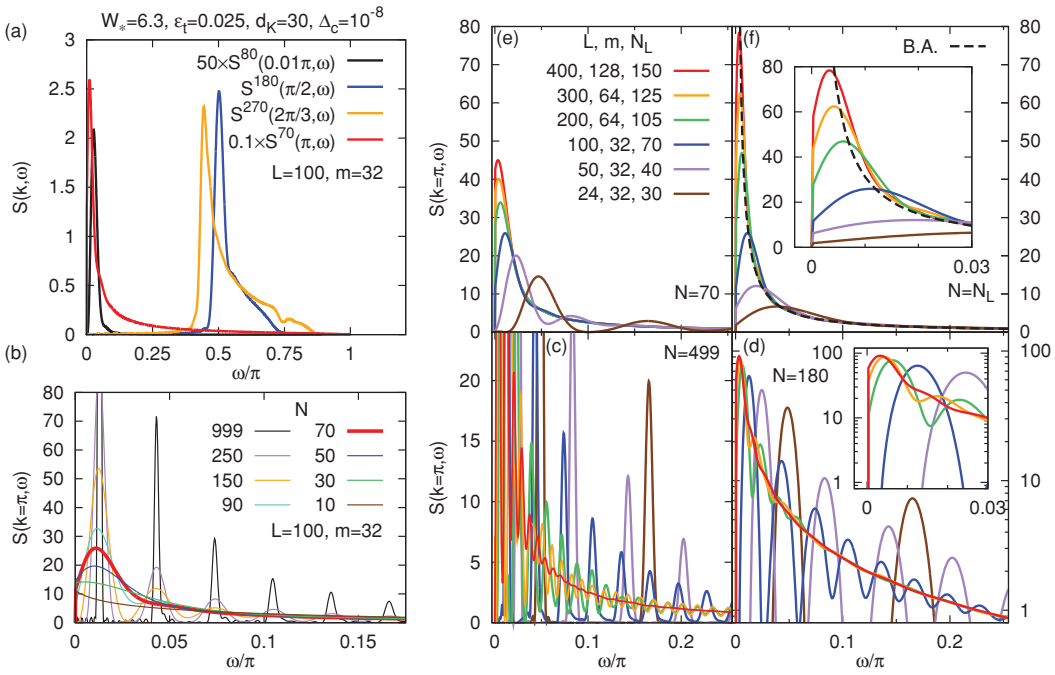

FIG. 5. (Color online) Spin structure factors for a Heisenberg chain, reconstructed using Jackson damping. (a) $S(k,\omega)$ for four choices of momentum k, for a chain of length $L = 100$. Each spectrum was reconstructed using optimal broadening, i.e., by choosing the largest expansion order, say, N_L (indicated by superscripts), that does not yet resolve finite-size effects. (b)–(f) Finite-size analysis of $S(\pi,\omega)$. (b) To determine N_L for given L (here 100), several different expansion orders N are considered. Increasing N reduces the effective broadening $\eta_N \simeq \mathcal{O}(W_*/N)$ until finite-size subpeaks appear for $N > N_L$ (here, $N_L = 70$, bold red curve). (c) Evolution of the finite-size structure with L, revealed by fixing N large enough (here $= 499$) to resolve the first few dominant subpeaks of all curves. There are L dominant subpeaks (not all shown here) within the spectral bandwidth, with average spacing $\omega_L \sim 1/L$. (d) Same as (c), but plotted on a semilog scale, and with somewhat smaller N (here $= 180$), chosen to be somewhat larger than the optimal broadening N_L for the largest L (here $N_{300} = 125$). As L increases and ω_L decreases, the subpeaks coalesce toward the intrinsic lineshape $S^\infty(k,\omega)$. (e) When L is increased at *fixed* N (here 70), finite-size effects disappear once ω_L drops below the effective broadening η_N, resulting in a smooth spectral function. (f) In contrast, when L is increased while using *optimal broadening*, $N = N_L$ (i.e., η_N just above ω_L), none of the curves show finite-size effects, and the resulting main peak is sharper than in (e). In both (e) and (f), the peak height shows no indications of converging with L, reflecting the fact that the true peak shape involves an $\omega^{-1}[\ln\omega]^{-1/2}$ divergence. Moreover, the CheMPS curves in (f) show signs of overbroadening when compared to the exact Bethe ansatz result (dashed lines) from Ref. 38.

the frequencies at which $S(\pi/2,\omega) = 0.1$ (triangles). Since the data exhibit a slight curvature when plotted against $1/L$ [see lower inset of 6(b)], they were fitted using a second-order polynomial in $1/L$. Extrapolating the fit to $1/L = 0$ yields $\omega_1 = 0.496\pi$ (marked by a square), in good agreement with the prediction $\omega_1 = \pi/2$ from Eq. (45).

D. Discrete representation of spectral function

In both Figs. 5(f) and 6, the right flank of the peak still bears signatures of overbroadening: the curve for a given L lies above those for larger L (before bending over toward its peak), and all curves lie significantly above the exact Bethe ansatz curve (dashed line). One way of reducing this broadening would be to simply increase L, but this is numerically costly. Clearly, alternative strategies for reducing finite-size effects would be desirable. One such scheme, involving linear prediction in the time domain, will be discussed in the next subsection. Here, we present another scheme, which exploits the ability of CheMPS to accurately resolve finite-size peaks.

The origin of overbroadening is clear: When neighboring subpeaks are broadened enough to overlap, weight is inevitably transferred from large peaks to smaller peaks. This effect is negligible only in the limit $L \to \infty$, where the subpeak spacing becomes negligible. To avoid overbroadening for a finite-L system, one thus has to analyze spectra for which N is large enough that subpeaks do *not* overlap significantly, such as that shown in Fig. 5(b).

To be concrete, let us represent the true, discrete spectrum of a system of size L by a sum of peaks, enumerated by a counting index α, with position Ω_α, width $\bar{\eta}_\alpha$, weight W_α, and Gaussian shape K^J [cf. Eq. (18a)]:

$$S^L(k,\omega) \simeq \sum_\alpha W_\alpha K^J_{\bar{\eta}_\alpha}(\omega - \Omega_\alpha). \tag{49}$$

Its Chebyshev reconstruction with Jackson damping, say, $S^L_N(k,\omega)$, will have the same form, except that the peaks will be broadened to have widths $\eta_\alpha = (\bar{\eta}_\alpha^2 + \eta_{N,\alpha}^2)^{1/2}$ as explained before Eq. (19). If N is large enough, the broadened peaks will

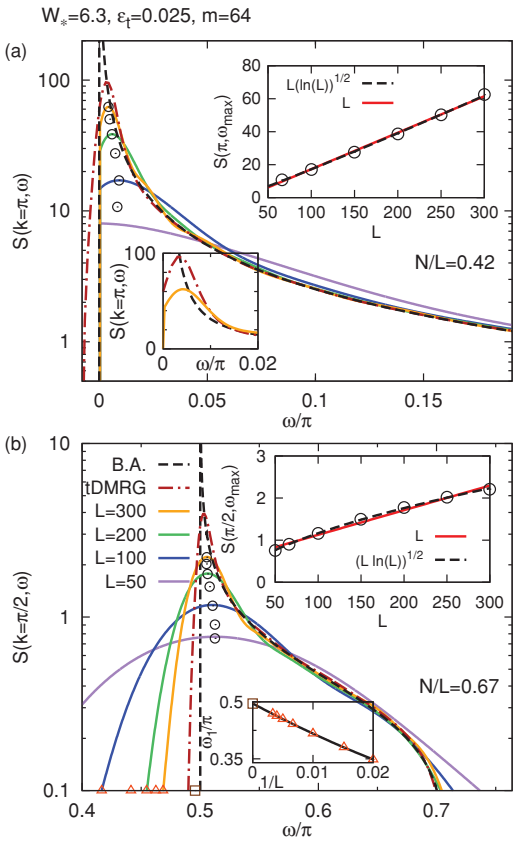

FIG. 6. (Color online) Comparison of CheMPS, Bethe ansatz, and tDMRG + prediction for HAFM structure factors with (a) $k = \pi$ and (b) $k = \pi/2$. Dashed lines: Bethe ansatz results for $L = \infty$, from Ref. 38. Dashed-dotted lines: tDMRG results, from Ref. 22. Other lines show CheMPS results for $L = 50$, 100, 200, and 300, reconstructed using a fixed ratio of N/L, namely, 0.42 for (a) and 0.67 for (b). Circles mark Chebyshev peak maxima, also for $L = 66$, 150, and 250, for which no curves are shown. The lower inset in (a) zooms into the peak region using a linear scale, illustrating overbroadening. The upper insets of (a) and (b) show the peak heights vs L (circles), together with a fit to the Bethe ansatz expectation from Eq. (46) (dashed line) or to a straight line (solid line). In (b), triangles mark the lower threshold frequencies for which $S(\pi/2,\omega)$ equals a fixed, small value, arbitrarily chosen as 0.1. Their $1/L \to 0$ extrapolation, shown in the lower inset, gives an estimate for the lower threshold frequency, namely, $\omega_1/\pi = 0.496$ (marked by a square); the exact value is 1/2.

still be clearly separated (as for $N = 999$ or 250 in Fig. 5). By fitting each peak (separately, one by one) to a Gaussian, one can determine its position Ω_α, weight W_α, and effective width η_α and deduce the intrinsic width via $\bar{\eta}_\alpha = (\eta_\alpha^2 - \eta_{N,\alpha}^2)^{1/2}$. We find (not shown) that the intrinsic width grows with increasing frequency Ω_α. This implies, not unexpectedly, that higher-lying spin-wave excitations have shorter lifetimes. However, it also implies that higher-lying peaks eventually start to overlap, so that the analysis to be described below is feasible only for a limited number of low-lying peaks.

The discrete peaks suggest a natural partitioning of the frequency spectrum into intervals I_α: Each contains one peak of weight W_α at position Ω_α, extends halfway to the next peaks at $\Omega_{\alpha\pm1}$ on either side, and has width $\Delta_\alpha = (\Omega_{\alpha+1} - \Omega_{\alpha-1})/2$. The first interval above the lower spectral threshold (ω_1) is defined slightly differently: I_1 has lower bound ω_1 and width $\Delta_1 = (\Omega_1 + \Omega_2)/2 - \omega_1$.

Now, to produce a smooth curve devoid of finite-size effects, the subpeaks must be broadened until they overlap substantially. However, if the weights in two neighboring intervals differ, say, $W_\alpha > W_{\alpha+1}$, such broadening inevitably transfers weight from interval I_α to $I_{\alpha+1}$, resulting in overbroadening.

Such overbroadening can be avoided by constructing a *discrete* representation of the spectral function $S_{\rm dis}(k,\Omega_\alpha)$, defined by the set of coordinates

$$\{(\Omega_\alpha, S_\alpha)\} \quad \text{with} \quad S_\alpha = S_{\rm dis}(k,\Omega_\alpha) = W_\alpha/\Delta_\alpha. \qquad (50)$$

The identification of S_α with W_α/Δ_α follows from applying the definition of a spectral function, namely, spectral weight per unit frequency interval, to the interval I_α.

Figure 7 shows the resulting discrete data points for four different system sizes. Remarkably, they all fall onto the same curve, which agrees well with the Bethe ansatz result (dashed line). In particular, the first two or three data points for each L lie right on top of the Bethe ansatz curve [(dashed line), see Fig. 7, left inset], beautifully mapping out the true shape of the spectral function down to the lowest discrete excitation frequency Ω_α that exists for that L. Evidently, the discrete spectral function is completely *free from broadening artifacts*, in marked contrast to the optimally

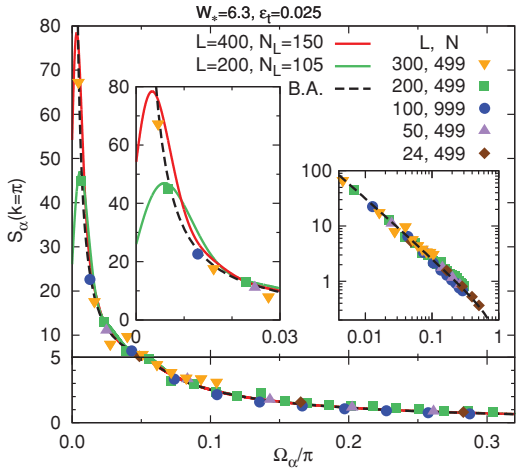

FIG. 7. (Color online) Discrete representation [Eq. (50)] of the structure factor $S_\alpha = S_{\rm dis}(\pi,\Omega_\alpha)$ (symbols) for five different system sizes. (The lower panel uses an enlarged vertical scale to zoom in on the tail region.) For comparison, the Bethe ansatz result (dashed line) and two optimally broadened spectra, for $L = 400$ and 200 (solid lines), are also shown. Left inset: Zoom to low frequencies, showing that the discrete data completely avoid overbroadening, in contrast to the optimally broadened spectra. Right inset: The log-log version of main plot. The frequency range does not extend low enough to be able to uncover the pure asymptotic predicted by Eq. (46b).

broadened curves shown for $L = 200$ and 400 (solid lines) [compare also Fig. 5(f)]. This advantage comes at the price of specifying the spectral function only at discrete points, not via a continuous curve. However, for a system of finite size, such discreteness is fundamentally unavoidable. The good news is that the continuum curve $S_N^\infty(k,\omega)$ is evidently well mimicked by the discrete representation $\{(\Omega_\alpha, S_\alpha)\}$, and that CheMPS allows the latter to be determined in a straightforward fashion for system sizes well beyond what can be done with exact diagonalization. We are not aware of any other numerical many-body method capable of doing so for system sizes as large as those considered here.

For larger frequencies, the scatter of the discrete data w.r.t. the Bethe ansatz curve increases, reflecting the fact that subpeaks begin to overlap there, making the extraction of discrete data increasingly difficult. However, this is not a serious concern since, in this frequency regime, optimal broadening is able to produce smooth spectra in good agreement with Bethe ansatz anyway.

To conclude this subsection, let us summarize the two main results of our finite-size analysis. The first concerns physics: For a chain of finite chain of L sites, the structure factor is dominated by a set of $\mathcal{O}(L)$ sharp subpeaks, the spacing and weight of which scale as $1/L$. The second concerns methodology: CheMPS very conveniently allows this structure to be revealed or hidden by simply choosing N appropriately. Moreover, it can exploit information on the positions and weights of the discrete subpeaks to largely eliminate broadening artifacts.

E. Comparison of tCheMPS to tDMRG

Another possible scheme for reducing finite-size effects is to work in the *time domain* using linear prediction, as shown in Ref. 22 for the HAFM. The idea is to calculate the Fourier transform of $S(k,\omega)$, namely,

$$S(k,t) = \sum_{x=1}^{L} e^{ik(x-x')} \langle \hat{\boldsymbol{S}}_x(t) \hat{\boldsymbol{S}}_{x'}(0) \rangle, \tag{51}$$

with x' chosen near the middle of the chain and t chosen small enough that the spin excitation created at x' does not reach the edge of the system within t. The function $S(k,t)$ thus obtained will contain only weak finite-size effects. It is then extrapolated to larger times via linear prediction techniques,[19–22] exploiting the fact that momentum excitations typically exhibit damped harmonic dynamics, the time dependence of which can be extrapolated quite accurately. Since the extrapolated function extends to very large times, its Fourier transform yields good spectral resolution at low frequencies[19] (with an accuracy that depends on that achieved during linear prediction).

In Ref. 22, the input correlator needed for linear prediction, $S(k,t)$, was calculated using tDMRG. (Two examples of the resulting spectra are included in our Fig. 6.) We note that $S(k,t)$ can also be calculated using CheMPS in the time domain, to be called tCheMPS. Indeed, the numerical cost for calculating $S(k,t)$ by evaluating the requisite correlators $\langle \hat{\boldsymbol{S}}_x(t) \hat{\boldsymbol{S}}_{x'}(0) \rangle$ via Eq. (28) is essentially the same as calculating its Fourier transform $S(k,\omega)$ via Eq. (23) since the corresponding Chebyshev moments μ_n can be calculated using the same recursion scheme. In fact, if one defines $\hat{\boldsymbol{S}}_k$ in Eq. (43) using a pure exponential e^{ikj} instead of a sin function, the Chebyshev moments needed for $S(k,t)$ are simply linear combinations of those of $S(k,\omega)$.

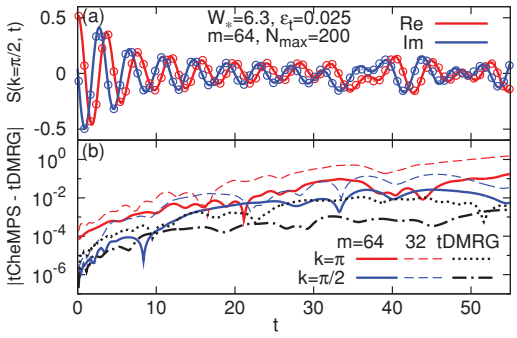

FIG. 8. (Color online) (a) Time dependence of $S(\pi/2,t)$, calculated with tCheMPS (lines) and tDMRG (symbols). Solid and dashed lines show, respectively, the real and imaginary parts of S. (b) The differences between tCheMPS and tDMRG (with a specified truncation error of 10^{-6}) of $S(k,t)$ for two values of k and two values of m (dashed/solid lines). To estimate the accuracy of tDMRG, we also show (dashed-dotted lines) the differences between two tDMRG calculations performed with different truncation error thresholds, namely, 10^{-5} and 10^{-6}, requiring up to $m = 75$ or 125 states, respectively.

To gauge the accuracy of tCheMPS, we have calculated $S(\pi/2,t)$ using both tCheMPS and tDMRG. Figure 8(a) compares the results, and 8(b) characterizes the differences. We view the tDMRG results as benchmark because, for the times of interest, we have checked them to be well converged [with errors $\lesssim 10^{-3}$ for $t < 50$, see 8(b), dashed-dotted line]. As expected, the agreement between tCheMPS and tDMRG is better for larger m. The differences are very small, but grow with time, from being (for $m = 64$) below 10^{-3} for $t \lesssim 10$ to around 10^{-2} for $t \simeq 30$, beyond which finite-size effects start to appear.

More generally, the results of Fig. 8 illustrate that CheMPS offers a viable route to time evolution for situations where extreme accuracy is not required. Further comments on this prospect are included in the outlook, Sec. VII.

V. ERROR ANALYSIS

The convergence properties of a Chebyshev expansion are mathematically well controlled and understood [see Eq. (14)], provided that the Chebyshev moments μ_n are known precisely. Their evaluation via CheMPS, however, introduces various sources of numerical errors. This section is devoted to an analysis of these errors. In particular, we seek to determine appropriate choices for the control parameters associated with the various CheMPS tasks listed in Table I. We perform this analysis mostly for a resonant level model (RLM), describing three local levels coupled to a fermionic bath. This model is introduced and discussed in the Appendix, which, for the sake of completeness, also includes CheMPS expansions of the corresponding spectral functions. However, the details presented there are not needed for the following discussion.

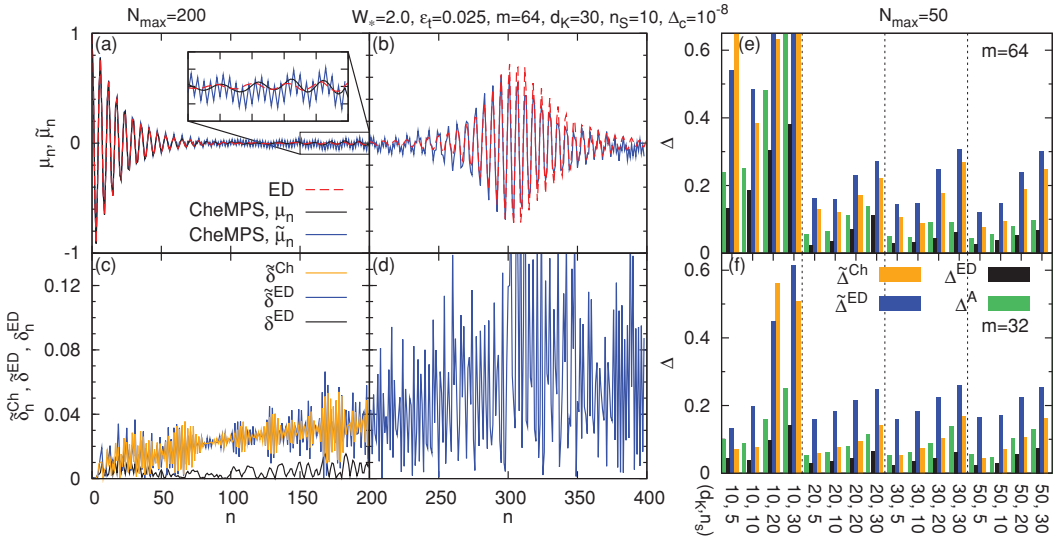

FIG. 9. (Color online) Comparison of CheMPS and ED results for Chebyshev moments of the RLM spectral function A^{-}_{11}. (a), (b) show μ_n and $\tilde{\mu}_n$ moments [Eqs. (25) and (34)] and (c), (d) show the n-dependent error measures δ^{ED}_n, $\tilde{\delta}^{\mathrm{ED}}_n$, and $\tilde{\delta}^{\mathrm{Ch}}_n$ [Eqs. (52)], plotted in (a), (c) for $n < N_{\max} = 200$ and in (b), (d) for $N_{\max} \leqslant n < 2N_{\max}$. In (b), the increase in moment magnitude starting around $n \simeq 250$ marks the onset of resolving finite-size structure in the spectral function. (e), (f) show the cumulative error measures Δ^{ED}, $\tilde{\Delta}^{\mathrm{ED}}$, $\tilde{\Delta}^{\mathrm{Ch}}$ [Eqs. (53)], and Δ^{A} [Eq. (54)] for various combinations of the MPS dimension m, the number of energy truncation sweeps n_S, and the Krylov subspace dimension d_K.

For the RLM, on the one hand, the CheMPS evaluation of the μ_n is feasible to arbitrarily high orders, and on the other, exact diagonalization (to be denoted by subscript or superscript ED) of the single-particle Hamiltonian allows both the spectral function and the Chebyshev moments μ_n to be found exactly. We use the RLM parameters specified in the Appendix throughout and focus mainly on the properties of one of its correlators $\mathcal{A}^{-}_{11}$ (without displaying corresponding subscripts and superscripts), which is defined in Eq. (A2) and the behavior of which is representative for that of $\mathcal{A}^{\pm}_{ij}$.

A. Definition of error measures

We will analyze both μ_n and $\tilde{\mu}_n$ moments, calculated from Eqs. (25) and (34), respectively. The differences between CheMPS and ED can be quantified by the error measures

$$\delta^{\mathrm{ED}}_n = \left|\mu^{\mathrm{CheMPS}}_n - \mu^{\mathrm{ED}}_n\right|, \quad n < N_{\max} \tag{52a}$$

$$\tilde{\delta}^{\mathrm{ED}}_n = \left|\tilde{\mu}^{\mathrm{CheMPS}}_n - \mu^{\mathrm{ED}}_n\right|, \quad n < 2N_{\max}. \tag{52b}$$

Moreover, to characterize the accuracy of CheMPS moments without referring to exact results, we also consider

$$\tilde{\delta}^{\mathrm{Ch}}_n = \left|\tilde{\mu}^{\mathrm{CheMPS}}_n - \mu^{\mathrm{CheMPS}}_n\right|, \quad n < N_{\max}. \tag{52c}$$

We will also use cumulative versions of these, namely,

$$\Delta^{\mathrm{ED}} = \sqrt{\sum_{n=0}^{N_{\max}-1} \left(\delta^{\mathrm{ED}}_n\right)^2}, \tag{53a}$$

$$\tilde{\Delta}^{\mathrm{ED}} = \sqrt{\Delta^{\mathrm{ED}2} + \sum_{n=N_{\max}}^{2N_{\max}-1} \left(\tilde{\delta}^{\mathrm{ED}}_n\right)^2}, \tag{53b}$$

$$\tilde{\Delta}^{\mathrm{Ch}} = \sqrt{\sum_{n=0}^{N_{\max}-1} \left(\tilde{\delta}^{\mathrm{Ch}}_n\right)^2}. \tag{53c}$$

Furthermore, we also introduce an integrated error measure for undamped spectral functions (using Jackson damping would yield qualitatively similar error measures):

$$\Delta^{\mathrm{A}} = \sqrt{\int_0^{W_*} d\omega |\mathcal{A}^{2N_{\max}}(\pm\omega) - \mathcal{A}^{\infty}(\pm\omega)|^2}. \tag{54}$$

Here we use $\pm$ for $\mathcal{A}^{\pm}(\omega)$ spectra proportional to $\theta(\pm\omega)$ [see Eq. (A2)] and employ μ_n moments for $n < N_{\max}$ and $\tilde{\mu}_n$ moments for $N_{\max} \leqslant n < 2N_{\max}$ during spectral reconstruction. [Note that $\tilde{\Delta}^{\mathrm{ED}}$ of Eq. (53b) was constructed to reflect this combination of μ_n and $\tilde{\mu}_n$.]

B. Comparison of CheMPS and ED moments

Figure 9 contains the results of our comparison of CheMPS and ED moments for a fixed set of CheMPS parameters, stated in the figure legend. Figures 9(a) and 9(b) show Chebyshev moments μ_n and $\tilde{\mu}_n$ and Figs. 9(c) and 9(d) show the n-dependent error measures δ^{ED}_n, $\tilde{\delta}^{\mathrm{ED}}_n$, and $\tilde{\delta}^{\mathrm{Ch}}_n$. From Fig. 9(c), we note several points: (i) For $n \leqslant N_{\max}$, the μ_n moments from CheMPS and ED agree to within about 1%; this illustrates that CheMPS is able to generate rather accurate results for several hundred moments at modest computational costs. (ii) μ_n moments are more accurate than $\tilde{\mu}_n$ moments; the reason is that each μ_n moment depends on only one Chebyshev vector, whereas each $\tilde{\mu}_n$ moment depends on two.

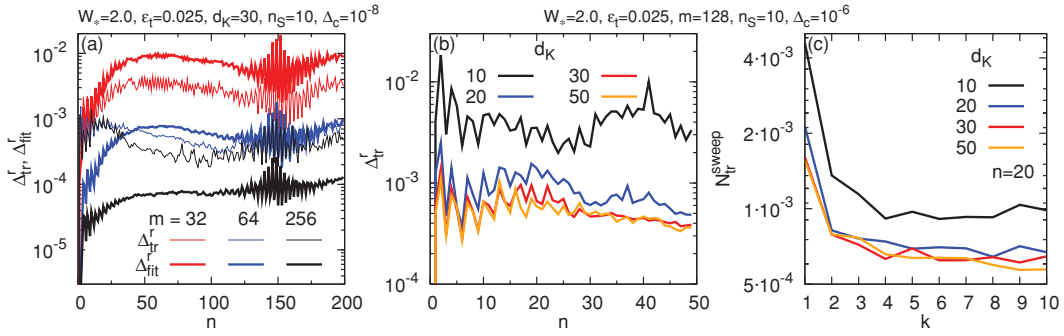

FIG. 10. (Color online) (a) Relative fitting error $\Delta^{\mathrm{r}}_{\mathrm{fit}} = \Delta_{\mathrm{fit}}/\,\||t_n\rangle\|^2$ [Eq. (31)] and relative truncation-induced state change $\Delta^{\mathrm{r}}_{\mathrm{tr}} = \Delta_{\mathrm{tr}}/\,\||t_n\rangle\|^2$ [Eq. (41)], as functions of recursion number n, for three different choices of MPS dimension m. Both quantities decrease with increasing m, but $\Delta^{\mathrm{r}}_{\mathrm{fit}}$ more strongly so since recurrence fitting is a strictly variational procedure, whereas energy truncation is not. (b) $\Delta^{\mathrm{r}}_{\mathrm{tr}}$ as function of n and (c) the average truncated weight per site $N^{\mathrm{sweep}}_{\mathrm{tr}}$ (for $n = 20$) as function of truncation sweep number k. Both (b) and (c) show results for four choices of Krylov subspace dimension d_K, the d_K dependence of which saturates beyond $d_K = 30$.

[Note, though, that if spectral reconstruction is performed by employing both μ_n moments for $n \leqslant N_{\max}$ and $\tilde{\mu}_n$ moments for $n > N_{\max}$ (as done, e.g., for Figs. 5 and 13), the reduced accuracy of the $\tilde{\mu}_n$ moments is offset to some extent if damping factors g_n are employed since these decay to 0 as n approaches N (see inset of Fig. 3).] (iii) The error measures $\tilde{\delta}^{\mathrm{Ch}}_n$ and $\tilde{\delta}^{\mathrm{ED}}_n$ are of comparable magnitude; this implies that $\tilde{\delta}^{\mathrm{Ch}}_n$ is a useful error quantifier if exact results are not available.

The way in which these errors depend on the various CheMPS control parameters can conveniently be analyzed using the cumulative error measures Δ^{ED}, $\tilde{\Delta}^{\mathrm{ED}}$, $\tilde{\Delta}^{\mathrm{Ch}}$, and Δ^{A}. These are shown in Figs. 9(e) and 9(f) for various combinations of m, n_S, and d_K. Several more observations can be made: (iv) When increasing the Krylov subspace dimension d_K, all cumulative errors decrease from $d_K = 20$ to 30, but the decrease saturates beyond $d_K = 30$. (v) Increasing the number of energy truncation sweeps beyond $n_S = 10$ does not necessarily reduce the cumulative errors; on the contrary, most actually increase, implying that energy truncation sweeping should not be overdone. (vi) The cumulative errors depend only weakly on the MPS dimension m (except for $d_K = 10$, which is unreliable anyway) and tend to be smaller(!) for $m = 32$ than 64 [compare Figs. 9(e) and 9(f)]. This trend suggests that the errors introduced by energy truncation grow if the mismatch between m and d_K grows. Points (iv) to (vi) indicate that energy truncation is the limiting factor for reducing CheMPS errors, a fact that will be elaborated on in Sec. V C below.

To identify an optimal combination of CheMPS control parameters, we have collected error data such as those shown in Figs. 9(e) and 9(f) for each possible combination of $W_* = (1.1,1.5,2.0)$, $\epsilon_{\mathrm{t}} = (0.1,0.01,0.025)$, $d_K = (10,20,30,50)$, $n_S = (5,10,20)$, and several m values for fixed maximum recursion number $N_{\max} = 50$ and convergence threshold $\Delta_{\mathrm{c}} = 10^{-8}$. We concluded that the choices $d_K = 30$, $n_S = 10$, $W_* = 2W_A$, and $\epsilon_{\mathrm{t}} = 0.025$ robustly yield good results (also for the HAFM) and, hence, list these as recommended values in Table I. Actually, the precise choice of ϵ_{t} has only small effects on the error, as long as W_* is chosen big enough. If W_* is too small, however, the resulting spectral function will lose some weight at high frequencies because numerical errors may cause energy truncation to effectively also project out some contributions with energies smaller than the energy truncation threshold ε_P.

C. Errors induced by recursion fitting and energy truncation

To better understand the error dependence on m, d_K, and n_S observed in points (iv) to (vi) of Sec. V B above, let us analyze in more detail the errors generated during recurrence fitting (Sec. III A) and energy truncation (Sec. III B). The error incurred when constructing $|t_n\rangle$ from $|t_{n-1}\rangle$ and $|t_{n-2}\rangle$ using recurrence fitting is characterized by the relative fitting error $\Delta^{\mathrm{r}}_{\mathrm{fit}} = \Delta_{\mathrm{fit}}/\,\||t_n\rangle\|^2$ [Eq. (31)]. The effect of projecting out high-energy states using energy truncation $|t_n\rangle \mapsto P_{\mathrm{tr}}|t_n\rangle$ can be characterized by the average truncated weight per site during one truncation sweep $N^{\mathrm{sweep}}_{\mathrm{tr}}$ [Eq. (40)], and by the relative truncation-induced state change $\Delta^{\mathrm{r}}_{\mathrm{tr}} = \Delta_{\mathrm{tr}}/\,\||t_n\rangle\|^2$ [Eq. (41)]. The latter measures intended changes in the state due to the truncation of high-energy weight, but also incorporates the effects of unavoidable numerical errors.

These quantities are analyzed in Fig. 10 in dependence on m, d_K, and n_S. Continuing our list of observations from the previous subsection, we note the following additional features: (vii) Both $\Delta^{\mathrm{r}}_{\mathrm{fit}}$ and $\Delta^{\mathrm{r}}_{\mathrm{tr}}$ are smaller than 1% already for $m = 32$ [Fig. 10(a)], in accord with similar error margins for δ^{ED}_n in Fig. 9(c). (viii) Both $\Delta^{\mathrm{r}}_{\mathrm{fit}}$ and $\Delta^{\mathrm{r}}_{\mathrm{tr}}$ decrease with increasing m, but $\Delta^{\mathrm{r}}_{\mathrm{tr}}$ does so more slowly, and its decrease seems to saturate beyond $m = 64$. This implies that *energy truncation is the main limiting factor* for CheMPS. The reason is that the intended purpose of energy truncation, namely, to strip $|t_n\rangle$ from its high-energy components, modifies it in a way so that the errors can not be reduced to arbitrarily small values. Indeed, this is illustrated by the following two points: (ix) While both Δ_{tr} and $N^{\mathrm{sweep}}_{\mathrm{tr}}$ initially decrease with increasing Krylov subspace dimension d_K, the decrease saturates for $d_K \gtrsim 30$ [Figs. 10(b) and 10(c)]. (x) While $N^{\mathrm{sweep}}_{\mathrm{tr}}$ initially decreases with the number of sweeps n_S, the decrease saturates already for $n_S \lesssim 10$ [Fig. 10(c)]. Qualitatively, the behavior shown in Fig. 10(c) is robust. (However, the choices of other CheMPS control parameters do influence its quantitative

details, such as the d_K beyond which $N_{\rm tr}^{\rm sweep}$ becomes d_K independent.) The lack of saturation of $N_{\rm tr}^{\rm sweep}$ with n_S implies that there is no automatic stopping criterion for truncation sweeps. Instead, the choice of n_S can be optimized as described in Sec. V B, where we already concluded that taking n_S much larger than 10 actually deteriorates the results.

When no exact results are available for comparison, the only relevant error measures among all those listed in Eqs. (52) and (53) are $\tilde{\delta}^{\rm Ch}$ and $\tilde{\Delta}^{\rm Ch}$. Nevertheless, Figs. 9(a)–9(d) show that these measures provide a reasonable estimate of the actual errors compared to the exact solution since the magnitudes of $\tilde{\delta}^{\rm Ch}$ and $\tilde{\delta}^{\rm ED}$ are comparable. Moreover, Figs. 9(e) and 9(f) show that the cumulative error measures $\tilde{\Delta}^{\rm Ch}$ and $\tilde{\Delta}^{\rm ED}$ reveal the same trends for their dependence on CheMPS parameters such as d_K and n_S. Hence, $\tilde{\delta}^{\rm Ch}$ and $\tilde{\Delta}^{\rm Ch}$ may be used as measures for optimizing CheMPS parameters and estimating the errors of the final results.

Of course, truncation-induced errors can be avoided by simply using the full bandwidth $W_* = W$, for which no truncation is necessary. However, in our experience, the gain in resolution obtained by using, instead, an effective bandwidth $W_* \ll W$ outweighs the small loss in accuracy incurred by the necessity to then perform energy truncation.

VI. DENSITY MATRIX SPECTRA

The effects of energy truncation can be understood in more detail by considering the reduced density matrix

$$\hat{\rho}_n = {\rm Tr}_{\rm half} |t_n\rangle\langle t_n|, \tag{55}$$

where the trace is over one half of the chain. Let us analyze the n dependence of the spectrum of its eigenvalues, say, $\rho_n(i)$. It can be used to quantify the entanglement encoded in $|t_n\rangle$ via the associated *entanglement* or *bond entropy*

$$S_n^{\rm bond} = -\sum_i \rho_n(i) \ln[\rho_n(i)]. \tag{56}$$

Figure 11 shows such density matrix spectra for both the RLM [panels (a) and (b)] and the HAFM [panels (c) and (d)] calculated using both the full many-body bandwidth $W_* = W$ [panels (a) and (c)] and a smaller effective bandwidth W_* [panels (b) and (d)]. The $n = 0$ line in all panels shows the eigenvalue spectrum $\rho_0(i)$, which reflects the entanglement encoded in $|t_0\rangle = \hat{\mathcal{C}}|0\rangle$ at the start of the recursion procedure. In principle, one would expect the entire spectrum of density matrix eigenvalues $\rho_n(i)$ to shift or rise to higher values as n increases since multiplying $|t_{n-1}\rangle$ by $\hat{H}'$ when calculating $|t_n\rangle$ [cf. Eq. (30)] generates entanglement entropy. Such a *spectral rise* with increasing n is indeed observed in all four panels of Fig. 11, but the rise eventually saturates for sufficiently large n. The speed of the initial stages of the rise differs from panel to panel. For the density matrix spectra calculated *without* energy truncation [Figs. 11(a) and 11(c)], the initial rise is rather slow, in particular for the RLM [11(a), where the rise is preceded by a slight initial decrease], reflecting the lack of strong correlations of this model. In contrast, for density matrix spectra calculated *with* energy truncation [Figs. 11(b) and 11(d)], the initial rise is very rapid, and its subsequent saturation sets in at quite small n (of order 20 to 30). Thus, energy truncation evidently has the effect of increasing entanglement entropy. The reason is

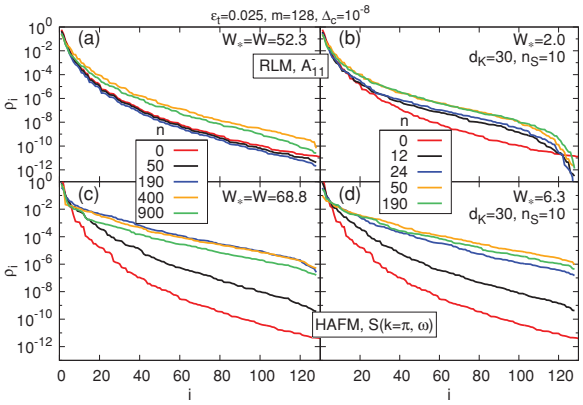

FIG. 11. (Color online) Eigenvalue spectra $\rho_n(i)$ of the reduced density matrix at the center of the system for several expansion vectors $|t_n\rangle$ of (a), (b) the RLM with $L_b = 101$, and (c), (d) the HAFM with $L = 100$. In (a), (c), we used the full many-body bandwidth $W_* = W$ without energy truncation, and in (b), (d) a reduced effective bandwidth with energy truncation.

that the latter is calculated in a different basis (the eigenbasis of $\hat{\rho}_n$) than that used to perform energy truncation (the local eigenbasis of $\hat{H}'$).

According to 11(d), the small MPS dimension of $m = 32$ used for the HAFM in Fig. 5(a) in effect amounts to discarding the contributions to the reduced density matrix of all states with weight below a threshold of around 10^{-3}. This threshold is rather large compared to typical DMRG calculations, where characteristic truncation errors lie in the range 10^{-6} to 10^{-8}. It is remarkable that CheMPS is nevertheless able to give rather accurate results (such as reproducing CV results obtained using $m_{\rm CV} = 1500$).

This efficiency appears to be an intrinsic feature of CheMPS, arising from the recursive manner in which the Chebyshev vectors $|t_n\rangle$ are constructed. Evidence for this conclusion is presented in Fig. 12(a), which shows the bond entropy $S_n^{\rm bond}$ associated with $|t_n\rangle$ as a function of recursion number n. Remarkably, the bond entropy shows no tendencies toward unbounded growth, even up to values as large as $n = 2000$. Quite to the contrary, although the bond entropy increases somewhat when increasing m from 32 to 128 (with $W_* = 6.3$), for either case it tends to *decrease* with recursion number n, and similarly for the choice $W_* = W$ without energy truncation. All of this is very encouraging since it indicates that n can be increased, apparently at will, *without incurring any runaway growth of DMRG truncation errors*. The reasons for this fact will be recapitulated in the summary below.

For comparison, Fig. 12(b) shows the bond entropy $S_t^{\rm bond}$ of a tDMRG calculation of the time evolution of $|\psi(t)\rangle = e^{-i\hat{H}t}\hat{\mathbf{S}}_{x=50}|0\rangle$. This entropy is, overall, smaller than the $S_n^{\rm bond}$ of the Chebyshev vectors because the initial state for the time evolution involves an excitation at only one site, whereas the starting state for the CheMPS recursion involved a linear combination of local excitations $\hat{\mathbf{S}}_k|0\rangle$ [see Eq. (43)]. The most striking difference between $S_n^{\rm bond}$ and $S_t^{\rm bond}$, however, is that the former shows no trend to increase with n, whereas

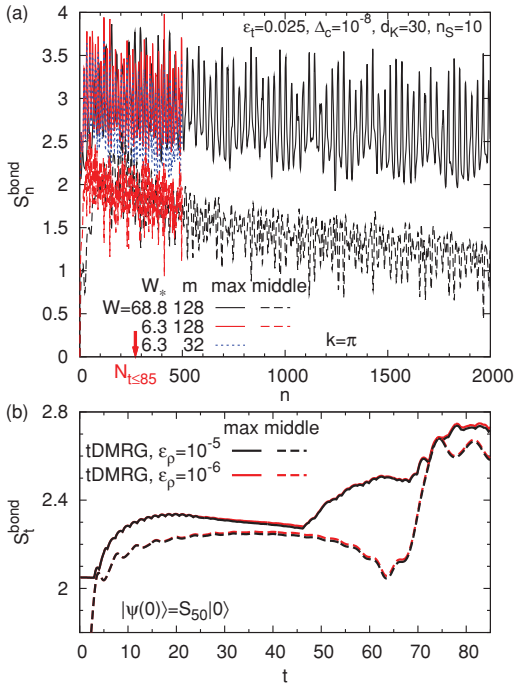

FIG. 12. (Color online) Entanglement or bond entropy S^{bond} for the $k = \pi$ spectral function of the HAFM. (a) S_n^{bond} for the Chebyshev vectors $|t_n\rangle$ and (b) S_t^{bond} during the tDMRG time evolution of $e^{-i\hat{H}t}\hat{\mathbf{S}}_{x=50}|0\rangle$. In both (a) and (b), solid and dashed lines show the maximum bond entropy and the bond entropy at the middle of the system, respectively. (a) S_n^{bond} is shown for two choices of W_*; the dotted line is from a calculation with a reduced $m = 32$ and some entropy is lost due to truncation. The red arrow marks the expansion order roughly necessary to reach the time $t = 85$ using the tCheMPS technique for $W_* = 6.3$; here $N_{t\leqslant 85} = 271$. To reach the same time using $W_* = W = 68.8$, an order of expansion of $N_{t\leqslant 85} = 2961$ would be necessary. (b) S_t^{bond} is shown for two choices of the truncation error ϵ_ρ.

the latter does with t. The increase in S_t^{bond} occurs in spurts, which happen each time a spin wave gets reflected from one of the ends of the system, at which point more numerical resources are required to keep track of the superposition of incident and reflected spin waves. For the present problem, the increase in S_t^{bond} was not severe and remained completely under control (staying below S_n^{bond} throughout). Nevertheless, we do believe that the contrast between Figs. 12(a) and 12(b), showing a nonincreasing trend for S_n^{bond} versus an increasing trend for S_t^{bond}, is striking and significant. It suggests that, for situations that feature strong entanglement growth with time, tCheMPS might be a promising alternative to tDMRG.

VII. SUMMARY

In this paper, we have described CheMPS as a method for calculating zero-temperature spectral functions of one-dimensional quantum lattice models using a combination of a Chebyshev expansion and MPS technology. To summarize our analysis, we would like to highlight what we believe to be the two most important features of CheMPS, namely, its efficiency and its control of spectral resolution.

Efficiency. The first main feature is that CheMPS provides an *attractive compromise between accuracy and efficiency*. It is capable of reproducing correction-vector results in the frequency domain and tDMRG results in the time domain with comparably modest numerical resources. In particular, surprisingly small values for the MPS dimension of m are sufficient, even for obtaining spectral resolution high enough to resolve finite-size effects in great detail. (For example, $m = 32$ sufficed for the spin-$\frac{1}{2}$ antiferromagnetic Heisenberg model.) This remarkable efficiency, which we had not anticipated when commencing this study, appears to be a consequence of several factors: (i) CheMPS does not suffer from a runaway growth of DMRG truncation error with increasing n because the information needed to construct the spectral function with a specified accuracy, say $\mathcal{O}(1/N)$, is not encoded in a single state, but uniformly distributed over N distinct Chebyshev vectors $|t_n\rangle$. (ii) These can be determined from Chebyshev recurrence relations involving only three terms, so that it is never necessary to accurately represent the sum of more than two MPS. (iii) Moreover, these recurrence relations are numerically stable, i.e., the inaccuracies in the calculation of Chebyshev vectors $|t_n\rangle$ do not cause the Chebyshev expansion to diverge. (iv) Finally, the accuracy needed for each $|t_n\rangle$ is set by that needed for $\mu_n = \langle 0|\mathcal{B}|t_n\rangle$ [(25)], which does not need to be better than the specified accuracy, namely, $\mathcal{O}(1/N)$.

For spectral functions with a finite spectral width $W_{\mathcal{A}}$ (which is typically much smaller than the many-body bandwidth W), CheMPS offers a further attractive feature for enhancing efficiency: one may use an "effective bandwidth" W_* of order $W_{\mathcal{A}}$ (we typically take $W_* = 2W_{\mathcal{A}}$), which enhances spectral resolution by a factor W/W_*, at the cost of requiring additional energy truncation sweeps. The latter are not necessary if one takes $W_* = W$, but then considerably higher expansion orders are necessary to achieve comparable resolution. In our experience, the benefits of enhanced resolution offered by the choice $W_* = 2W_{\mathcal{A}}$ outweigh the costs of energy truncation.

Control of spectral resolution. The second main feature of CheMPS is that it offers *very convenient control of the accuracy and resolution* of the resulting spectral function by simply adjusting the expansion order N. This is particularly useful for studying finite-size effects, as exemplified in Fig. 5. On the one hand, Fig. 5(b) shows very strikingly that the structure factor of an HAFM chain of finite length is dominated by a set of discrete subpeaks, which may be associated with the quantized eigenenergies of spin-wave excitations in a finite system. CheMPS allows the energies and weights of these excitations, and their dependence on L, to be determined with unprecedented accuracy and ease by simply increasing N until the peaks are well resolved. On the other hand, Fig. 5(f) shows that the limit $L \to \infty$ may be mimicked by choosing N just small enough that the finite-size subpeaks are smeared out. Although the peak shape thus obtained is slightly overbroadened [see inset of Fig. 5(f)], this overbroadening can be eliminated completely (see Fig. 7) by using a discrete representation of the spectral function that uses the energies

and weights of the discrete subpeaks as input. The ability to fully eliminate overbroadening effects even for very large many-body systems is, to the best of our knowledge, a unique feature of CheMPS.

On a technical level, the implementation of CheMPS requires only standard MPS techniques, such as the addition of different states and the multiplication of operators. For energy truncation, single-site sweeping needs to be set up with a new kind of local update, as described in III B. However, this procedure is not too different from other known local update prescriptions and can be implemented with modest programming effort.

VIII. OUTLOOK

Regarding future applications of CheMPS, two directions for further methodological development appear particularly promising, namely, time dependence and finite temperature. A few comments are due about each.

Time dependence. While the good agreement between tCheMPS and tDMRG reported in 8 is encouraging, a detailed analysis of tCheMPS should be performed to understand the nature of its error growth with time, and to explore under which conditions, if any, tCheMPS offers competitive advantages relative to tDMRG. On the one hand, tDMRG has the advantage that highly efficient Krylov methods can be used to optimize the evaluation of $e^{-i\hat{H}\Delta t}|\psi(t)\rangle$ w.r.t. the state $|\psi(t)\rangle$ being propagated; however, its numerical costs increase rapidly if $|\psi(t)\rangle$ contains a broad spectrum of excited states. On the other hand, CheMPS has the advantage (i) that the Chebyshev expansion of the operator $e^{-i\hat{H}t}$ can be applied with equal accuracy to every state in the Hilbert space, in particular, also highly excited ones. Moreover, (ii) very large evolution times might be achieved more easily with tCheMPS than tDMRG since the former represents $|\psi(t)\rangle$ as a sum over many Chebyshev vectors [see Eq. (6)], thereby being potentially less susceptible than tDMRG to the growth of truncation errors (as discussed in the Introduction, and exemplified in 12). We expect that, for some applications, (i) and/or (ii) may offer advantages for tCheMPS over tDMRG, e.g., for calculating quantum quenches starting from strongly nonequilibrium initial states, but leave a detailed investigation to the future.

Finite temperature. The fact that CheMPS uniformly resolves the entire energy spectrum of $\hat{H}$ suggests that it should be particularly suited for calculating the spectral functions $\mathcal{A}_T^{\mathcal{BC}}(\omega) = \int \frac{dt}{2\pi} e^{i\omega t} G_T^{\mathcal{BC}}(t)$ of finite-temperature correlators such as

$$G_T^{\mathcal{BC}}(t) = \mathrm{Tr}[\hat{\rho}_T \hat{\mathcal{B}}(t)\hat{\mathcal{C}}(0)], \quad \hat{\rho}_T = \frac{e^{-\beta\hat{H}}}{Z}. \tag{57}$$

According to Ref. 5, such a spectral function can be evaluated using Chebyshev expansions by proceeding as follows: Express the partition function as

$$Z = \int d\omega\, e^{-\beta\omega}\rho(\omega) \tag{58a}$$

by introducing the density of states

$$\rho(\omega) = \mathrm{Tr}[\delta(\omega - \hat{H})], \tag{58b}$$

and the spectral function as

$$\mathcal{A}_T^{\mathcal{BC}}(\omega) = \frac{1}{Z}\int d\bar{\omega}\, e^{-\beta\bar{\omega}}\rho^{\mathcal{BC}}(\bar{\omega},\omega+\bar{\omega}) \tag{59a}$$

by introducing the *density of matrix elements*[39,40]

$$\rho^{\mathcal{BC}}(\bar{\omega},\omega) = \mathrm{Tr}[\delta(\bar{\omega} - \hat{H})\,\hat{\mathcal{B}}\,\delta(\omega - \hat{H})\,\hat{\mathcal{C}}]. \tag{59b}$$

Then, Chebyshev expand the δ functions in Eqs. (58b) and (59b) using Eq. (23) (after suitably rescaling Hamiltonian and frequencies). The resulting Chebyshev expansions will contain moments of the form

$$\mu_n^{\rho} = \mathrm{Tr}[T_n(\hat{H}')], \tag{60a}$$

$$\mu_{nn'}^{\mathcal{BC}} = \mathrm{Tr}[T_n(\hat{H}')\,\hat{\mathcal{B}}\,T_{n'}(\hat{H}')\,\hat{\mathcal{C}}]. \tag{60b}$$

We now note that this framework is very well suited for an MPO implementation, which would consist of three steps: (i) Using Chebyshev recurrence relations, recursively construct and store MPO representations for each operator $T_n(\hat{H}')$; we expect (based on our experience with the Chebyshev vectors $|t_n\rangle$) that this should be possible without runaway costs in numerical resources since the construction of $T_n(\hat{H}')$ requires only $\hat{H}'T_{n-1}(\hat{H}')$ and $T_{n-2}(\hat{H}')$. (ii) Calculate the moments in Eqs. (VIII) by evaluating the traces, which is straightforward in the context of MPS and MPO. (iii) Insert the resulting moments into the reconstructed Chebyshev expansions for $\rho(\omega)$ and $\rho^{\mathcal{BC}}(\bar{\omega},\omega)$, and finally evaluate the integrals Eqs. (58a) and (59a). Note the economy of this scheme: After once constructing the MPO for each $T_n(\hat{H}')$, and once evaluating the trace for each moment μ_n^{ρ} and $\mu_{nn'}^{\mathcal{BC}}$, the spectral function $\mathcal{A}_T^{\mathcal{BC}}(\omega)$ can be calculated for arbitrary combinations of ω and T. The implementation of this strategy is left for future studies.

We conclude by remarking that the idea of using Chebyshev expansions in the context of many-body numerics, advocated in inspiring fashion in Ref. 5, can be implemented in combination with any method that is able to efficiently apply a Hamiltonian $\hat{H}$ to a state $|\psi\rangle$. Chebyshev expansions optimize the resolution that can be extracted from a limited number of applications of $\hat{H}$. While CheMPS is based on doing this using MPS methods for one-dimensional lattice models, similar developments have been pursued within the context of exact diagonalization[41,42] and Monte Carlo[43] methods, and Chebyshev expansions should also be useful in combination with tensor network methods for two-dimensional quantum lattice models.

ACKNOWLEDGMENTS

We thank A. Weiße for an inspiring talk on kernel polynomial methods, which motivated us to implement the ideas of Ref. 5 using MPS technology; T. Barthel and J.-S. Caux for providing the tDMRG and Bethe ansatz data, respectively, that are shown in Figs. 5–7; and J. Halimeh for help with extracting the discrete data shown in Fig. 7 from large-N CheMPS spectra. We gratefully acknowledge helpful discussions with P. Schmitteckert, who independently pursued ideas similar to those presented here, A. Alvermann, T. Barthel, H. Fehske, and M. Vojta. This work was supported by DFG (SFB 631, De-730/3-2, SFB-TR12, SPP 1285, and De-730/4-1).

Financial support by the Excellence Cluster "Nanosystems Initiative Munich (NIM)" is gratefully acknowledged.

APPENDIX: RESONANT LEVEL MODEL

This appendix introduces the fermionic resonant level model that was used for the error analysis of Sec. V and presents CheMPS results for its spectral functions. The RLM is defined by the following Hamiltonian:

$$\hat{H}_{\mathrm{RLM}} = \sum_{i=1}^{n_d} \varepsilon_i \hat{d}_i^\dagger \hat{d}_i + \sum_{i=1}^{n_d} V_i \sum_{k=1}^{L_b} (\hat{d}_i^\dagger \hat{c}_k + \mathrm{H.c.}) + \sum_{k=1}^{L_b} \varepsilon_k \hat{c}_k^\dagger \hat{c}_k. \tag{A1}$$

It describes a set of n_d discrete, "local" noninteracting fermion levels with energies ε_i that hybridize with strengths V_i with a band of L_b ($\gg$) fermion levels with energies ε_k, assumed uniformly spaced within the interval $[-W_b, W_b]$. We choose $W_b = 1$ as unit of energy throughout this section. We will parametrize the hybridization strengths V_i in terms of the associated level widths $\Gamma_i = \pi \frac{L_b}{2} V_i^2$.

The spectral function $A_{ij}(\omega) \equiv A_{ij}^+(\omega) + A_{ij}^-(\omega)$ has two contributions,

$$A_{ij}^+(\omega) \equiv \mathcal{A}^{d_i\, d_j^\dagger}(\omega), \quad A_{ij}^-(\omega) \equiv \mathcal{A}^{d_j^\dagger d_i}(-\omega), \tag{A2}$$

describing particle and hole excitations, which, at $T = 0$, are proportional to step functions $\theta(\pm\omega)$ that vanish for $\omega <$ or > 0, respectively. Since the RLM Hamiltonian is quadratic, the problem can be solved by diagonalizing the single-particle problem. In the continuum limit $L_b \to \infty$, this yields the following exact expression for the spectral function[44] for $|\omega| < D_b = 1$:

$$A_{ij}^\infty(\omega) = \lim_{\eta \to 0^+} -\frac{1}{\pi} \Im \left([\omega + i\eta - \Upsilon - \Delta(\omega)]^{-1} \right)_{ij},$$
$$\Upsilon_{ij} = \varepsilon_i \delta_{ij}, \quad \Delta_{ij}(\omega) = \frac{1}{\pi} \sqrt{\Gamma_i \Gamma_j} \left(\ln \left| \frac{\omega - D_b}{\omega + D_b} \right| - i\pi \right), \tag{A3}$$

where Υ and Δ are matrices of dimension $n_d \times n_d$. The Chebyshev moments μ_n for the finite system of length L can also be found exactly by evaluating the expectation values [Eq. (24)], using the (numerically determined) exact single-particle eigenstates of $\hat{H}$.

The Hamiltonian (A1) corresponds to a "star geometry" since each local level couples to every band level. For the purposes of using CheMPS, however, it needs to be transformed to a "chain geometry" of the form

$$\hat{H}_{\mathrm{RLM}} = \sum_{i=1}^{n_d} \varepsilon_i \hat{d}_i^\dagger \hat{d}_i + \sum_{i=1}^{n_d} \sqrt{\frac{2\Gamma_i}{\pi}} (\hat{d}_i^\dagger \hat{f}_1 + \mathrm{H.c.}) + \sum_{\ell=1}^{L_b - 1} \lambda_\ell (\hat{f}_\ell^\dagger \hat{f}_{\ell+1} + \mathrm{H.c.}). \tag{A4}$$

This can be achieved[45] by using Lanczos tridiagonalization of the band part of the Hamiltonian, thereby determining the hopping coefficients λ_ℓ.

Starting from Eq. (A4), we have used CheMPS to calculate the diagonal components $\mathcal{A}_{jj}$ of the RLM spectral function for a model with $n_d = 3$ local levels. In contrast to Sec. IV C, our interest here is not in analyzing finite-size effects, but in determining how the CheMPS parameters need to be adjusted to recover the exact continuum function $\mathcal{A}_{jj}^\infty$ of Eq. (A3). Thus, we purposefully chose a set of model parameters leading to three well-separated peaks of slightly different widths, taking $\varepsilon_j \in \{-0.5, 0.1, 0.6\}$ and $\Gamma_j \in \{0.04, 0.06, 0.03\}$, and chose the number of band levels $L_b = 101$ large enough so that the finite-size spacing $\omega_L \simeq 1/L_b = 0.01$ is somewhat smaller than the smallest peak width Γ_3. By choosing the expansion order for each curve such that the effective broadening lies in the window between the finite-size spacing and the intrinsic peak width $\omega_L < \eta_N < \Gamma_j$, it should be possible to reveal the shape of $\mathcal{A}_{jj}^\infty$ quite accurately without yet resolving finite-size subpeaks (although traces of the latter might show up for $\mathcal{A}_{33}$, for which this window is small). To this end, we used the following criterion for choosing N when reconstructing $\mathcal{A}_{jj}^N$: the effective broadening η_N was taken as large as possible without lowering the peak height significantly below that of A_{jj}^∞ (this corresponds to choosing $\eta_N \lesssim \Gamma_j$).

The results of these calculations are summarized in Fig. 13; all spectra shown there were obtained by performing separate expansions for the positive and negative branches $A_{jj}^\pm(\omega)$ (with one exception, noted below).

Figures 13(a1)–13(g1) were calculated using an effective bandwidth of $W_* = 2.0$ (with $\varepsilon_t = 0.025$) for each branch, corresponding to roughly twice the spectral width of each branch, which is of order of the single-particle bandwidth $W_A \simeq W_b = 1$. For this choice, an MPS dimension of merely $m = 32$ was found to suffice for accurate recurrence fitting. Figure 13(a1) illustrates a number of points: (i) By choosing η_N according to the above criterion of recovering the correct peak height, excellent agreement with the continuum limit A^∞ of Eq. (A3) is obtained over most of the frequency range. (ii) This is the case both with and without Jackson damping (thin black or blue lines, respectively), but, with Jackson damping, higher expansion orders are needed to obtain the correct peak heights since Jackson damping induces some artificial broadening [by a factor of π, see Eq. (18a)]. (iii) Small oscillations remain in some frequency ranges [see Figs. 13(b1)–13(g1) for zooms]. These stem from three sources: finite-size subpeaks, numerical inaccuracies, and step-function artifacts near $\omega = 0$ [cf. points (iv), (vi), and (viii) below, respectively]. (iv) For the spectrum with the narrowest peak $\mathcal{A}_{33}$, the window between ω_L and Γ_{33} is so small that the criterion of reproducing the continuum peak height implies that small finite-size subpeak remain visible [see Figs. 13(e1)–13(g1) for zooms]. (v) In contrast, such oscillations are almost entirely absent for the broadest peak $\mathcal{A}_{22}$ [see Figs. 13(d1) and 13(e1)] since its width Γ_2 is somewhat larger than ω_L.

To illustrate the effect of energy truncation, Figs. 13(a2)–13(g2) show the same spectral functions as Figs. 13(a1)–13(g1), but now setting $W_* = W$, the full many-body bandwidth (here $= 52.3$), so that no energy truncation is needed. This allows us to make some additional instructive observations: (vi) Using the full bandwidth yields results of higher quality, in that numerical artifacts are significantly weaker (except near $\omega = 0$) [compare Figs. 13(d2)–13(g2)

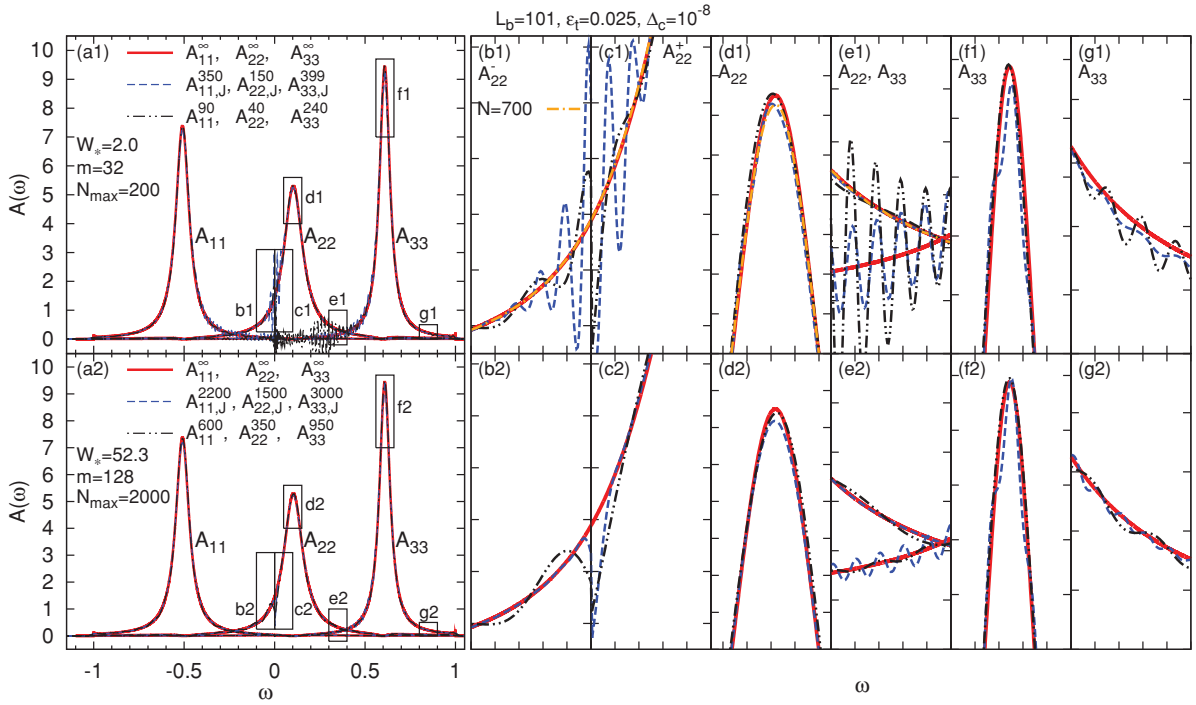

FIG. 13. (Color online) Diagonal spectral functions $\mathcal{A}_{jj}(\omega)$ of a three-level RLM. Thick solid lines show the continuum limit $A^{\infty}_{jj}(\omega)$ from (A3). Dashed and dashed–double-dotted lines show CheMPS results $\mathcal{A}^{N}_{jj,J}$ or $\mathcal{A}^{N}_{jj}$, with or without Jackson broadening, respectively, calculated for $L_b = 101$ band levels. For each spectrum, the effective broadening η_N was taken as large as possible without lowering the peak height significantly below that of A^{∞}_{jj}. In (a1)–(g1), we used an effective bandwidth of $W_* = 2.0$ and, in (a2)–(g2), the full many-body bandwidth $W_* = 52.3$. The latter requires significantly larger expansion orders, but exhibits less numerical inaccuracies [compare (b1)–(g1) and (b2)–(g2)], which represent zooms of the rectangles indicated in (a1) and (a2), respectively. (b), (c): Gibbs oscillations arise if $\mathcal{A}^{\pm}(\omega)$ are expanded separately, so that CheMPS attempts to resolve their $\theta(\pm\omega)$ steps. Expanding instead their sum $\mathcal{A}^{+}(\omega) + \mathcal{A}^{-}(-\omega)$, and performing a Jackson-damped reconstruction, we obtain the smooth dashed-dotted line in (b1)–(e1) (calculated using ED moments). (d), (e) $\mathcal{A}^{N}_{22}$ nicely reproduces $\mathcal{A}^{\infty}_{22}$ because the peak is somewhat broader than ω_L. (e)–(g) $\mathcal{A}^{N}_{33}$ shows small but distinct finite-size wiggles because the main peak is so sharp and narrow that recovering its height fully requires an η_N so small that it is comparable to ω_L.

and 13(d1)–13(g1)]. The reason is that energy truncation constitutes CheMPS's dominant source of error (as shown in Sec. V below); its avoidance thus yields more precise Chebyshev moments μ_n, especially for $n > N_{\max}$. (vii) However, this improvement is numerically expensive: the increased effective bandwidth necessitates larger expansion orders N, which in turn require a higher MPS dimension (here $m = 128$). (viii) For the present model, it was possible to calculate several thousand moments without encountering numerical instabilities; this illustrates the fact that the Chebyshev recurrence relations are *numerically stable*.

Finally, let us address (ix) the wiggly artifacts near $\omega = 0$. They reflect the fact that CheMPS was *separately* applied to the positive and negative branches of the spectral function $A^{\pm}(\omega)$, shown in zooms in Figs. 13(b) and 13(c), respectively. These are proportional to step functions $\theta(\pm\omega)$, and hence abruptly dip to zero for $\omega < 0$ or > 0, respectively. The wiggly artifacts correspond to Gibbs oscillations decorating these sharps dips. This problem can be avoided by performing a single Chebyshev expansion of the *sum* $\mathcal{A}^{+}(\omega) + \mathcal{A}^{-}(-\omega)$, which is a smooth function and leads to the perfectly smooth long-dashed line in Figs. 13(b) and 13(c). This improvement comes at roughly twice the numerical cost since it requires a doubling of the spectral range to $\omega \in [-W_A, W_A]$. This implies a slight but obvious modification of the transformations from ω to ω' and from H to $\hat{H}'$ to account for the shifted range of ω; a doubling of W_* and, hence of the expansion order N, required to achieve a specified resolution.

The main conclusions from our CheMPS calculations for the RLM are as follows: The strategy of using twice the spectral width as effective bandwidth ($W_* = 2W_A$) and performing energy truncation [Fig. 13(a)] is a satisfactory compromise between efficiency (only a few hundred Chebyshev moments are needed) and accuracy (for which energy truncation is the main limiting factor). If desired, better results can be obtained by using the full bandwidth ($W_* = W$) and thus avoiding energy truncation, albeit at the cost of significantly increasing the required expansion order by the factor $W/2W_A$. Nevertheless, the calculation of Chebyshev moments μ_n with very large n is feasible due to the remarkably numerical stability of Chebyshev recurrence relations.

[1] S. R. White, Phys. Rev. Lett. **69**, 2863 (1992).
[2] S. R. White, Phys. Rev. B **48**, 10345 (1993).
[3] U. Schollwöck, Rev. Mod. Phys. **77**, 259 (2005).
[4] U. Schollwöck, Ann. Phys. **326**, 96 (2010).
[5] A. Weiße, G. Wellein, A. Alvermann, and H. Fehske, Rev. Mod. Phys. **78**, 275 (2006).
[6] J. Dukelsky, M. A. Martín-Delgado, T. Nishino, and G. Sierra, Europhys. Lett. **43**, 457 (1998).
[7] G. Vidal, Phys. Rev. Lett. **93**, 040502 (2004).
[8] F. Verstraete, D. Porras, and J. I. Cirac, Phys. Rev. Lett. **93**, 227205 (2004).
[9] F. Verstraete, J. J. Garcia-Ripoll, and J. I. Cirac, Phys. Rev. Lett. **93**, 207204 (2004).
[10] I. P. McCulloch, J. Stat. Mech.: Theory Exp. (2007) P10014.
[11] K. A. Hallberg, Phys. Rev. B **52**, 9827(R) (1995).
[12] It was shown very recently (Ref. 46) that the performance of the continued-fraction approach can be substantially improved by iteratively calculating its expansion coefficients using an adaptive Lanczos-vector method.
[13] S. Ramasesha, S. K. Pati, H. Krishnamurthy, Z. Shuai, and J. Brèdas, Synth. Met. **85**, 1019 (1997).
[14] T. D. Kühner and S. R. White, Phys. Rev. B **60**, 335 (1999).
[15] E. Jeckelmann, Phys. Rev. B **66**, 045114 (2002).
[16] S. R. White and A. E. Feiguin, Phys. Rev. Lett. **93**, 076401 (2004).
[17] A. J. Daley, C. Kollath, U. Schollwöck, and G. Vidal, J. Stat. Mech.: Theory Exp. **2004**, P04005 (2004).
[18] P. Schmitteckert, Phys. Rev. B **70**, 121302 (2004).
[19] W. H. Press, S. A. Teukolsky, W. T. Vetterling, and B. P. Flannery, *Numerical Recipes*, 3rd ed. (Cambridge University, Cambridge, UK, 2007).
[20] R. G. Pereira, S. R. White, and I. Affleck, Phys. Rev. Lett. **100**, 027206 (2008).
[21] S. R. White and I. Affleck, Phys. Rev. B **77**, 134437 (2008).
[22] T. Barthel, U. Schollwöck, and S. R. White, Phys. Rev. B **79**, 245101 (2009).
[23] A. Weichselbaum, F. Verstraete, U. Schollwöck, J. I. Cirac, and J. von Delft, Phys. Rev. B **80**, 165117 (2009).
[24] J. C. Wheeler, Phys. Rev. A **9**, 825 (1974).
[25] R. N. Silver and H. Röder, Int. J. Mod. Phys. C **5**, 935 (1994).
[26] *Handbook of Mathematical Functions with Formulas, Graphs, and Mathematical Tables*, edited by M. Abramowitz and I. A. Stegun (Dover, New York, 1970).
[27] J. P. Boyd, Lect. Notes Eng. **49**, (1989).
[28] T. J. Rivlin, *Chebyshev Polynomials: From Approximation Theory to Algebra and Number Theory, Pure and Applied Mathematics* (Wiley, New York, 1990).
[29] In principle, the Lanczos algorithm also provides the maximal eigenvalue. However, in DMRG, the Lanczos gets restarted at every site with the currently known ground state and, thus, the return maximal energy will no longer approach $E_{\max}$ as the ground state converges.
[30] H. Tal-Ezer and R. Kosloff, J. Chem. Phys. **81**, 3967 (1984).
[31] C. Leforestier, R. H. Bisseling, C. Cerjan, M. D. Feit, R. Friesner, A. Guldberg, A. Hammerich, G. Jolicard, W. Karrlein, and H. D. Meyer, J. Comput. Phys. **94**, 59 (1991).
[32] F. Verstraete and J. I. Cirac, e-print arXiv:cond-mat/0407066.
[33] I. P. McCulloch and M. Gulácsi, Europhys. Lett. **57**, 852 (2002).
[34] J. des Cloizeaux and J. J. Pearson, Phys. Rev. **128**, 2131 (1962).
[35] L. D. Faddeev and L. A. Takhtajan, Phys. Lett. A **85**, 375 (1981).
[36] G. Müller, H. Beck, and J. C. Bonner, Phys. Rev. Lett. **43**, 75 (1979).
[37] M. Karbach, G. Müller, A. H. Bougourzi, A. Fledderjohann, and K.-H. Mütter, Phys. Rev. B **55**, 12510 (1997).
[38] J.-S. Caux and R. Hagemans, J. Stat. Mech.: Theory Exp. (2006) P12013.
[39] L.-W. Wang and A. Zunger, Phys. Rev. Lett. **73**, 1039 (1994).
[40] L.-W. Wang, Phys. Rev. B **49**, 10154 (1994).
[41] A. Alvermann and H. Fehske, Phys. Rev. B **77**, 045125 (2008).
[42] A. Alvermann and H. Fehske, Phys. Rev. Lett. **102**, 150601 (2009).
[43] A. Weiße, Phys. Rev. Lett. **102**, 150604 (2009).
[44] A. C. Hewson, *The Kondo Problem to Heavy Fermions* (Cambridge University, Cambridge, UK, 1997).
[45] R. Bulla, T. A. Costi, and T. Pruschke, Rev. Mod. Phys. **80**, 395 (2008).
[46] P. Dargel, A. Honecker, R. Peters, R. M. Noack, and T. Pruschke, Phys. Rev. B **83**, 161104(R) (2011).

4.2 Chebyshev matrix product state approach for time dependence

As a start of a deepened discussion of tCheMPS, we repeat the central equation for the Chebyshev expansion [104, 105] of the time evolution operator $U(t) = e^{-iHt}$ from the previous section

$$U_N(t) = e^{-i(E_0+aW')t}\left[c_0(t) + 2\sum_{n=1}^{N-1} c_n(t)T_n(H')\right], \tag{4.1a}$$

$$c_n(t) = (-i)^n J_n(at), \tag{4.1b}$$

where E_0 is the ground state energy of H, H' the rescaled Hamiltonian operator and a and W' the rescaling parameters as defined in Sec. 4.1. To get some insight into what types of error may occur, we first study Eq. (4.1) by switching from the MPS/ MPO context to a scalar or a small random matrix instead of the MPO H.

4.2.1 Expansion of the scalar e^{ixt}

The expansion coefficients c_n of Eq. (4.1b) do not depend on H and are essentially given by the Bessel functions of the first kind $J_k(x)$. Let's assume we are interested in the expansion of $U(t)$ for times up to T. Since $J_k(at)$ decays rapidly with k for $k > at$ [see Fig. 4.1(a)], we can determine the necessary order of expansion N by demanding $|J_N(at)| < \delta_T$ for $t \leq T$ [see Fig. 4.1(b)] with a chosen error bond δ_T, e. g. $\delta_T = 10^{-4}$.

Using the scalar x instead of H we obtain the Chebyshev expansion of e^{-ixt}

$$e^{-ixt} \simeq c_0(t) + 2\sum_{n=1}^{N-1} c_n(t)T_n(x)\,, \qquad c_n(t) = (-i)^n J_n(t). \tag{4.2}$$

The deviation from the exact exponential at a fixed time t as a function of the "energy" x is given by

$$\Delta_{\mathrm{Ch}}^{N,t}(x) = \left|c_0(t) + 2\sum_{n=1}^{N-1} c_n(t)T_n(x) - e^{-ixt}\right|. \tag{4.3}$$

Comparing $\Delta_{\mathrm{Ch}}^{N,t}(x)$ for different N at $t = 15$ in Fig. 4.2, we see that the error $\Delta_{\mathrm{Ch}}^{N,t}$ is independent of x and decreases fast with increased N. While $\Delta_{\mathrm{Ch}}^{N,t}$ shows some wiggles, the upper envelope is constant. These wiggles, occurring $\mathcal{O}(N)$ times, are typical for the Chebyshev expansion[1].

So the Chebyshev expansion of Eq. (4.1a) provides equally good results independent of x, a property that should also hold for tCheMPS with x being replaced by the energy of the

[1] The sharp pronounced local minima of the error of a Chebyshev expansion correspond to the roots of the used polynomial.

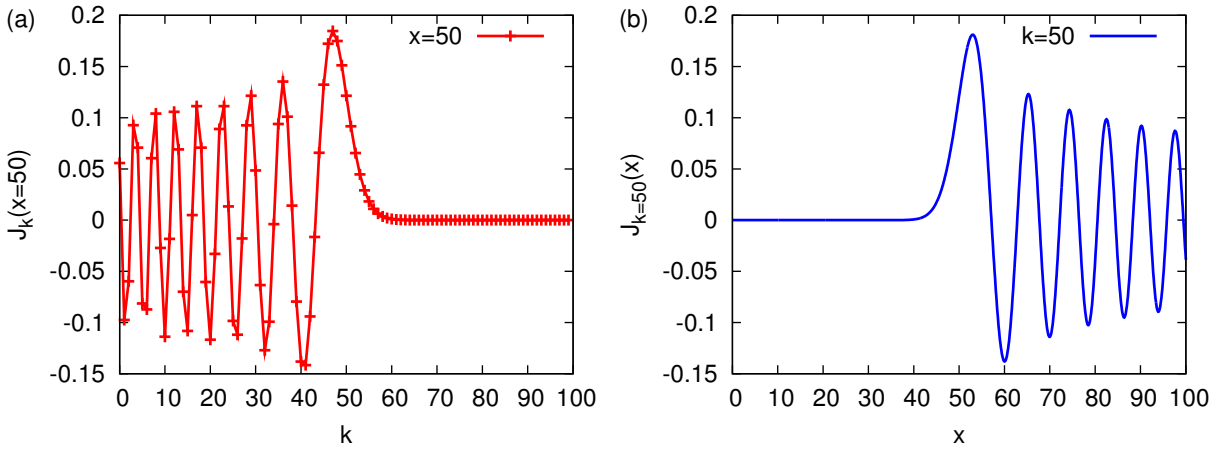

Figure 4.1: Bessel function of the first kind $J_k(x)$ for (a) fixed $x = 50$ as a function of k and (b) for fixed $k = 50$ as a function of x. For $k < x$ the Bessel function is highly oscillating and decays rapidly for $k > x$. So all coefficients up to $k \sim x$ contribute to the expansion, and increasing the order of expansion beyond that point does not increase the accuracy but increases the maximum time $T = N/a$ accessible by the expansion.

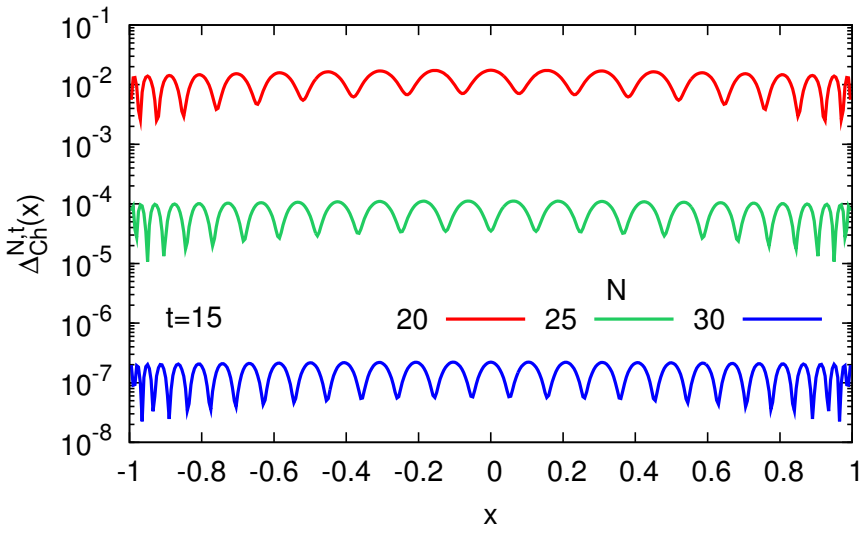

Figure 4.2: Errors $\Delta^{N,t}_{\mathrm{Ch}}(x)$ of the Chebyshev expansion of e^{-ixt} for different orders of expansion N at a fixed time $t = 15$. For each N the error is bounded from above independently of x.

state to be time evolved. This is slightly different[2] to the CheMPS expansion in frequency domain where broadening has a small frequency dependence of the form $\sqrt{1-\bar{x}^2}$. Since the coefficients c_n become negligible once the necessary order of expansion N is reached for a given time t, Gibbs oscillations do not occur and damping factors g_n need not be used.

[2]For tCheMPS the expansion is derived using Chebyshev polynomials of the first kind only as opposed to the Chebyshev polynomials of the second kind used for CheMPS (see [88] for details).

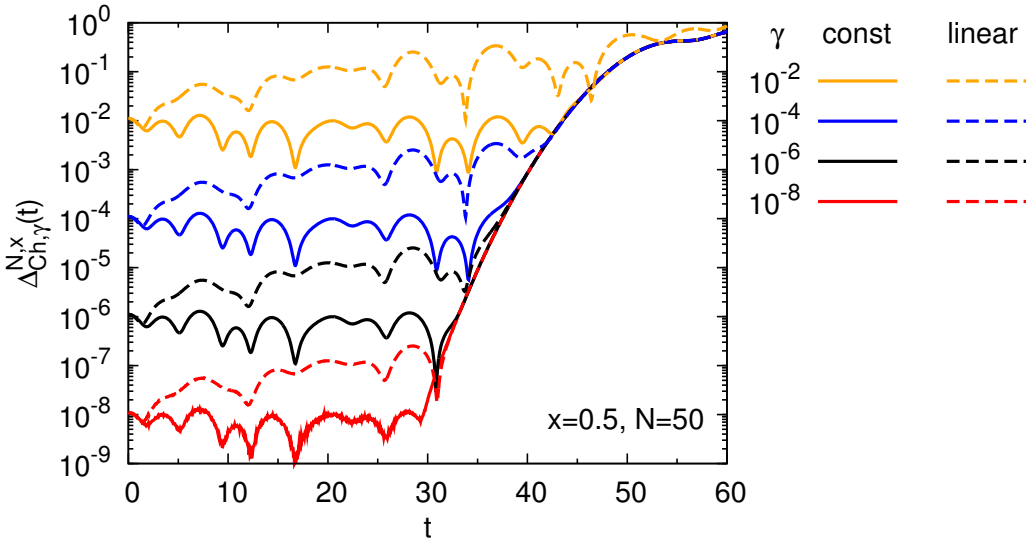

Figure 4.3: Errors $\Delta^{N,x}_{\mathrm{Ch},\gamma}(t)$ of the Chebyshev expansion of order $N = 50$ of e^{-ixt} with $x = 0.5$ under the influence of random noise with amplitude γ. The solid and dashed lines implement the constant amplitude protocol of Eq. (4.4a) and the linear amplitude protocol of Eq. (4.4b), respectively. For the constant noise the errors are given by γ and for the case of linearly increasing noise the error shows a corresponding increase with time until the error increases due to the finite order of expansion N.

4.2.2 Influence of noise

When applying the above expansion Eq. (4.1) to MPS we need to cope with the truncation error of DMRG as an additional source of error. In order to estimate the influence of the truncation error on the Chebyshev expansion we investigate the behavior of the scalar Chebyshev expansion of Eq. (4.2) under the presence of random noise being added to the coefficients $c_n(t)$. We consider two noise protocols: standard normal distributed noise with (a) constant amplitude at every iteration and (b) linearly increasing amplitude with the order of expansion to better simulate the DMRG errors occurring at every iteration. These protocols are implemented via

$$c_n(t) \mapsto c_n^\gamma(t) = (1 + \gamma\mathcal{N})\, c_n(t) \tag{4.4a}$$

$$c_n(t) \mapsto c_n^\gamma(t) = (1 + n\gamma\mathcal{N})\, c_n(t)\,, \tag{4.4b}$$

where $\mathcal{N}$ is a standard normal distributed random variable and γ the noise amplitude. For both noise protocols, we show in Fig. 4.3 for various noise amplitudes γ the deviation from the exact result

$$\Delta^{N,x}_{\mathrm{Ch},\gamma}(t) = \left| c_0^\gamma(t) + 2\sum_{n=1}^{N-1} c_n^\gamma(t) T_n(x) - e^{-ixt} \right| . \tag{4.5}$$

Thanks to the numerical stability of the Chebyshev polynomials the error introduced by the noise of Eq. (4.4) is well behaved. For the constant amplitude noise the error is of order

$\mathcal{O}(\gamma)$ and does not increase with time. With the linearly increasing noise amplitude we find a roughly-exponentially increasing error of approximately 1.5 orders of magnitude for times $t < 35$. Starting at $t = 30$ (for $\gamma = 10^{-8}$, red lines), independent of the noise-induced errors, the overall error increases because of the limited order of expansion N. For bigger noise amplitudes γ the error caused by finite N is masked by the error due to noise until the error due to N becomes dominant for bigger times.

While the applied noise in Eq. (4.4) can only be a crude approximation to the noise present in a MPS-based calculation, we nevertheless see that the Chebyshev expansion shows remarkable stability in the presence of noise. The tCheMPS algorithm constructs a large linear combination for a time evolved state instead of one huge MPS and we thus expect the truncation error of each Chebyshev expansion vector in principle to be manageable. Combined, this suggests that the resulting errors of the Chebyshev expansion should be dominated by the truncation errors of the individual expansion vectors.

4.2.3 Expansion of e^{-iHt} for random H

As a next step we investigate the time evolution with a random 64×64 Hamiltonian operator matrix and compare Chebyshev and Krylov expansions. For comparison we use the deviation of a time evolved state from the exact result

$$\Delta_{\mathrm{X}}^{N,|\psi\rangle}(t) = \left\| U_{\mathrm{X},N}(t)|\psi\rangle - e^{-iHt}|\psi\rangle \right\| , \tag{4.6}$$

where X=Ch denotes the Chebyshev expansion of order N and X=K the Krylov expansion of Eq. (2.65) with a Krylov subspace dimension of $d_K = N$. The Chebyshev time evolution operator of Eq. (4.1a) is independent of the state to be time evolved and thus can be applied iteratively. In Fig. 4.4 we compare the various approaches using a random state as initial state except where noted otherwise. We find that for random initial states and corresponding order of expansion and Krylov subspace dimension both methods give virtually identical results. The Chebyshev expansion is completely independent of the initial state as already argued above. However, the Krylov expansion may achieve longer reachable time scales for some states as demonstrated with the yellow lines in Fig. 4.4. The state $|\alpha\rangle$ is composed of two close eigenstates of equal weight with an additional random contribution of 10% weight. For this state the time T where the error starts to increase significantly is increased by 20% compared to the random state. The raised "background" noise for smaller times is due to numerical difficulties during the Gram-Schmidt orthonormalization and is of no practical relevance. If the Chebyshev time evolution operator is directly accessible it can be applied iteratively[3]

$$U(t) = [U_N(T')]^{\lfloor t/T' \rfloor} U_N\left(t - \lfloor t/T' \rfloor T'\right) , \tag{4.7}$$

where T' is the maximal reachable time with a single application of $U_N(t)$. Using this iterated Chebyshev expansion the reachable time scale T is significantly improved (black lines).

[3] Eq. (4.7) is in this form only valid for positive times t; however, it can be rewritten easily for negative times t.

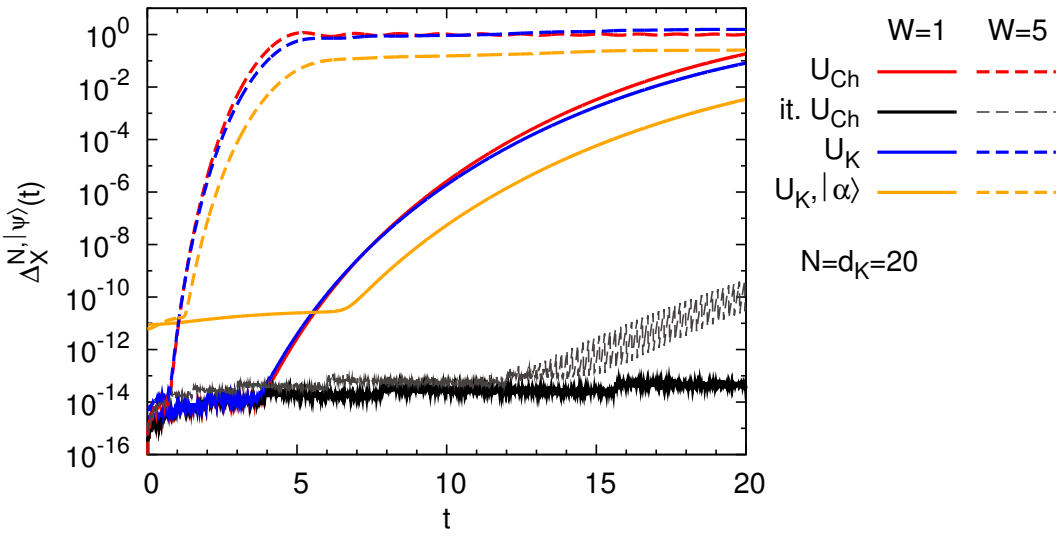

Figure 4.4: Time evolution of a random 64×64 Hamiltonian operator. The error $\Delta_{\mathrm{X}}^{N,|\psi\rangle}(t)$ as a function of time t is shown using Chebyshev (X=Ch) with $N = 20$ and Krylov expansions (X=K) with $d_K = 20$ for a bandwidth of H of $W = 1$ and $W = 5$. U_{Ch} denotes the standard Chebyshev expansion of Eq. (4.1), it. U_{Ch} the iterated application of $U_N(T)$ with small enough T; U_{K} denotes the Krylov expansion of Eq. (2.65) and additional label $|\alpha\rangle$ marks the use of an initial state composed of two eigenstates of H and a random contribution of weight 0.1 while all other lines are calculated from a complete random initial state.

Using a bandwidth W of H bigger than 1 reduces the reachable time scales by a factor of W for all approaches. This is obvious for the Chebyshev expansion as there the rescaled H' is used and the rescaling factor a enters the argument of the Bessel function in Eq. (4.1b). For the Krylov expansion the approximation of using only a low-dimensional Krylov subspace within which the exponential is calculated becomes worse for bigger arguments of the exponential. As a consequence the reachable time scale decreases as the bandwidth of H grows.

So far, we see that both the standard Chebyshev and Krylov approaches provide an accurate time evolution up to almost identical times T. In general, however, for certain states the Krylov approach can increase the time scale T. The Chebyshev expansion does not depend on the time evolved state and the corresponding time evolution operator can be applied iteratively with very high accuracy. Also the Chebyshev recursion is numerically stable in contrast to the Gram-Schmidt orthonormalization[4] so arbitrarily high orders of expansion are only possible for the Chebyshev expansion.

[4]There exist schemes to improve the numerical stability of the Gram-Schmidt orthonormalization [106]; however, the problem of invariant subspaces remains.

4.2.4 Comparison of tCheMPS with tDMRG

Up to now, the method-intrinsic sources of error have been analyzed. While it is important to fully understand these intrinsic errors of the methods being used, in practice, the most relevant source of error for DMRG that limits the maximal reachable time is given by the truncation error (see also the discussion in Sec. 2.6.3). We therefore switch to a MPS-based implementation of the time evolution schemes and study the time evolution $|\zeta(t)\rangle$ of the inhomogeneous initial state[5] $|\zeta\rangle = |\downarrow \ldots \downarrow\uparrow \ldots \uparrow\rangle$ under the spin-1/2 Heisenberg antiferromagnet Hamiltonian

$$H = \sum_{j=1}^{L-1} \boldsymbol{S}_j \boldsymbol{S}_{j+1} \tag{4.8}$$

for a system size of $L = 64$. The initial state with the domain wall at the middle of the system

$$|\zeta(t=0)\rangle = |\downarrow \ldots \downarrow\uparrow \ldots \uparrow\rangle = \bigotimes_{j=1}^{L/2} |\downarrow\rangle \otimes \bigotimes_{j=L/2+1}^{L} |\uparrow\rangle \tag{4.9}$$

is a product state and thus has an MPS representation with bond dimension 1.

For this setup, we calculated the time evolution of $|\zeta(t)\rangle$ both with tDMRG and tCheMPS. In Fig. 4.5 we show the time-dependent expectation value $\langle S_j^z(t)\rangle = \langle\zeta(t)|S_j^z|\zeta(t)\rangle$ for the exemplary sites $j = 33$ and $j = 50$ as well as the difference of the time evolved states

$$\Delta_{\mathrm{X}}(t) = \left\| |\zeta(t)\rangle_{\mathrm{X}} - |\zeta(t)\rangle_{\mathrm{tDMRG}}^{\tau=10^{-6}} \right\| , \tag{4.10}$$

where X stands for "tCheMPS, ϵ_ρ" or "tDMRG, τ", respectively. The tDMRG calculations were carried out using the Krylov time evolution, as described in Sec. 2.6.2, with a specified truncation error per time step τ up to $\tau = 10^{-6}$. Comparing results for $\tau = 10^{-5}$ and $\tau = 10^{-6}$, we found agreement of the expectation values $\langle S_j^z(t)\rangle$ within the line width in Fig. 4.5(a) and thus show only the data for $\tau = 10^{-6}$ which we consider as reference for the tCheMPS calculations.

For the tCheMPS time evolution calculations, we took the full many-body bandwidth of the Hamiltonian operator of $W = 43.9$ into account, leading to a rescaling factor of $a = 22.5$. This is necessary since the initial state is a highly excited state and it also avoids the energy truncation at every iteration. We fixed the safety parameter to $\epsilon_t = 0.05$ and the fitting convergence threshold to $\Delta_{\mathrm{c}} = 10^{-8}$ while the truncation cutoff for the reduced density matrix eigenvalues of the Chebyshev expansion vectors was varied from $\epsilon_\rho = 10^{-4}$ to $\epsilon_\rho = 10^{-7}$. In addition to the truncation cutoff ϵ_ρ we also specified a minimal DMRG dimension of $D = 32$ which effectively suppresses truncation errors completely for roughly the first 50 iterations (see Fig. 4.6) since $|\zeta(0)\rangle$ has $D = 1$. The tCheMPS expansion vectors $|t_n\rangle$ are calculated as described in Sec. 4.1 (For further details on how to obtain $\langle S_j^z(t)\rangle$ and $\Delta_{\mathrm{tCheMPS}}(t)$ see App. A.4). As we see in Fig. 4.5(b) the errors of the tCheMPS

[5] This setup was also used to study the properties of adaptive tDMRG using the Trotter time evolution very precisely [100].

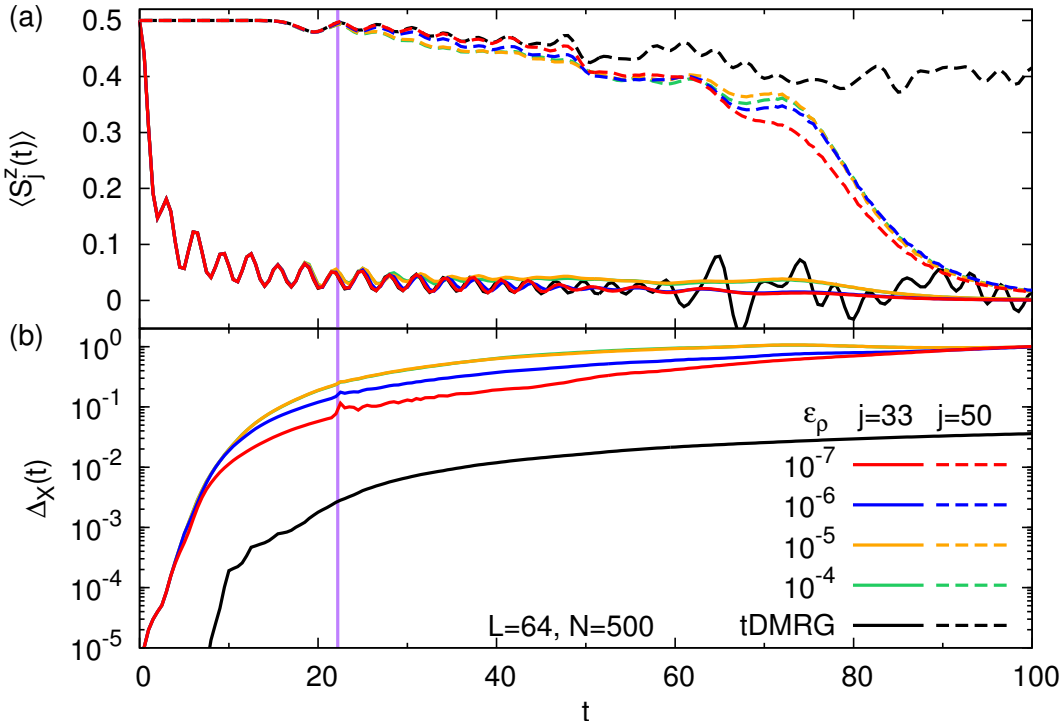

Figure 4.5: (a) Time-dependent S^z_j expectation values for sites next to the initial domain wall $j = 33$ and further away from the middle of the system $j = 50$ (dashed lines). We compare tCheMPS results for various truncation cutoff criteria ϵ_ρ with the tDMRG result with a truncation error of $\tau = 10^{-6}$ (black). (b) Error $\Delta^{\epsilon_\rho}_{\text{tCheMPS}}(t)$ from Eq. (4.10) of the tCheMPS result compared to the tDMRG result. The black line shows the difference $\Delta^{\tau=10^{-5}}_{\text{tDMRG}}$ between two tDMRG calculations with truncation errors $\tau = 10^{-5}$ and $\tau = 10^{-6}$. The vertical purple line indicates that for $N = 500$, estimated time reachable by tCheMPS is $T = 22.2$.

calculations grow rapidly and independently of ϵ_ρ for small times $t < 10$ followed by a less steep growth dependent on ϵ_ρ. At time $T = N/a = 22.2$ only a small kink is visible in contrast to Figs. 4.3 and 4.4 where another sharp step in the error is observable. This is due to the fact that the tCheMPS evolution of $|\zeta(t)\rangle$ at time $t = T$ already contains a rather high error level of roughly $\Delta_{\text{tCheMPS}}(t) = 0.05$ or bigger.

As energy truncation is not necessary, the fitting error Δ_{fit}, as shown in Fig. 4.6, is a precise measure of the numerical errors at each Chebyshev iteration. We find the fitting error to be consistent with the truncation cutoff ϵ_ρ after the first iterations when DMRG truncation is actually taking place. Since Δ_{fit} is defined as the squared fitting error (see Sec. 4.1) this explains the relatively high error levels of Fig. 4.5 and also indicates a straight-forward way to improve the errors, namely, significantly smaller ϵ_ρ. As even for the calculation at hand with $\epsilon_\rho = 10^{-7}$ the dimension never exceeds $D = 150$, it should well be possible to choose a smaller ϵ_ρ. That way it should be possible to achieve errors for tCheMPS at the level of tDMRG for times $t < T$. However, already for $\epsilon_\rho = 10^{-7}$ the tCheMPS dimension exceeds the tDMRG dimension which lies below 75. To better

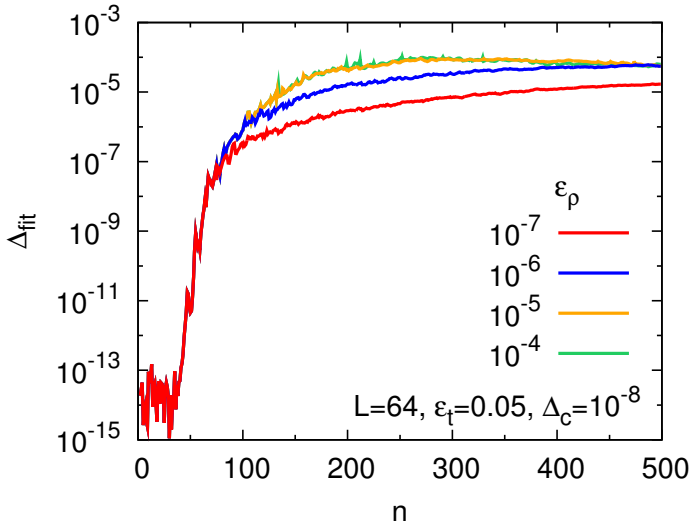

Figure 4.6: Fitting errors Δ_{fit} during the Chebyshev expansion calculations with various truncation cutoffs ϵ_ρ of every iteration vector $|t_n\rangle$. In addition to ϵ_ρ we also specified a minimal DMRG dimension of $D = 32$ during the recurrence fitting. This effectively suppresses truncation errors completely for the first 50 iterations and Δ_{fit} shows a steep increase at $n = 50$.

understand this need for bigger dimensions using tCheMPS we consider the bond entropy

$$S^{\text{bond}} = -\sum_i \rho_i \ln \rho_i \,, \tag{4.11}$$

where ρ_i is the eigenvalue spectrum of the reduced density matrix at a certain bond. Here we will choose the bond such that S^{bond} is maximal. The maximal bond entropy for each Chebyshev expansion vector $|t_n\rangle$ is shown in Fig. 4.7(a) and for the tDMRG time evolved states in Fig. 4.7(b). The bond entropy of the Chebyshev expansion vectors significantly exceeds the bond entropy of the tDMRG time evolved states, which is the reason for the bigger dimensions D needed for tCheMPS. The reason for this increased bond entropy is the fact that the tCheMPS time evolution operator of Eq. (4.1a) is capable of evolving every possible state in time with equal precision as opposed to the Krylov approach of tDMRG that is tailor-made for one specific state. This powerful property is reflected in the fast production of entropy during the Chebyshev iteration.

As a consequence, for cases where one is interested in the time evolution of only one or very few states (which is typically the case) tDMRG will be more efficient than tCheMPS if the desired maximal time can be reached with reasonable numerical effort. For such a case the properties of tDMRG (Krylov and Trotter likewise) fit exactly the problem, whereas the properties of tCheMPS provide potential benefits that are not needed, hence leading to an unnecessarily increased numerical effort. Specifically, the uniform precision for all initial states, which has been very advantageous in the frequency domain by yielding (almost) uniform spectral resolution, is usually not needed and renders the tCheMPS approach less efficient. This disadvantage is not compensated by producing the time evolved state in

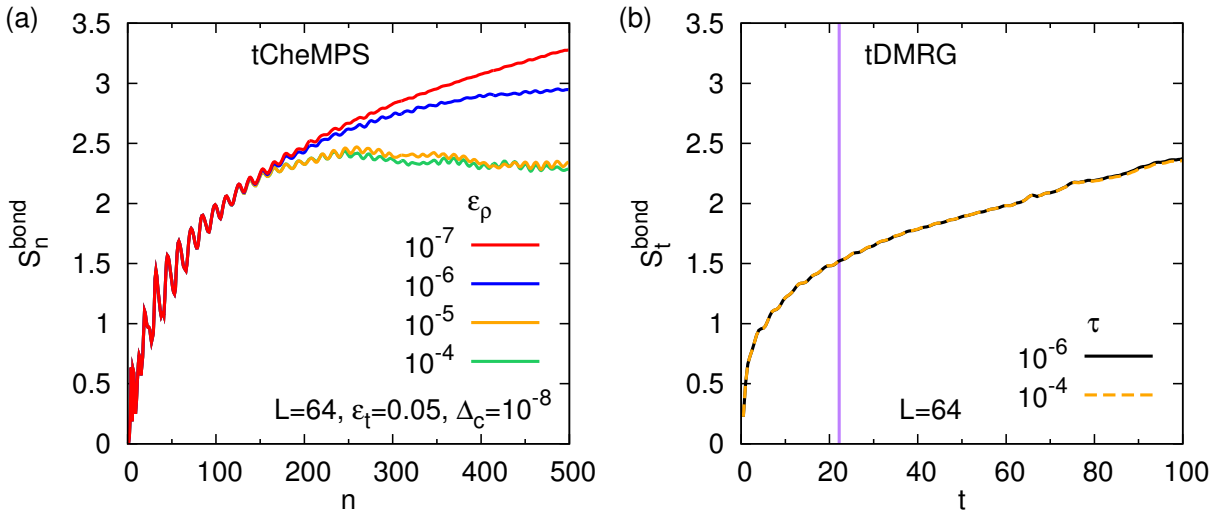

Figure 4.7: Maximal bond entropy S^{bond} (a) for every iteration n and (b) for every time t. The vertical purple line indicates the time T reachable by tCheMPS of order N. (a) The growth of S_n^{bond} is suppressed truncation effects for smaller ϵ_ρ starting at $n = 200$. For the case of tDMRG (b) the bond entropy is not affected by the truncation error τ. Also, the value of S^{bond} is smaller than the bond entropy for the Chebyshev vectors even for times $t > T$.

terms of a linear superposition (at least for not too high bond entropies). In situations where the time reached by tDMRG with acceptable effort is not sufficient, an MPO-based implementation of tCheMPS could extend the accessible time. Here, the feature of providing a linear superposition[6] for the time evolution translates the problem of states with high entropy and thus big DMRG dimensions into many states with less entropy each. After an initial time evolution using tDMRG, a tCheMPS MPO operator could be applied to evolve to bigger times. For this scenario, further studies are necessary in order to assess the potential benefit of this approach.

[6]It has already been speculated [12] about using superposition to lessen the buildup of entropy in the time evolved state, but up to now we are not aware of a successful implementation of this idea.

Chapter 5

Kondo screening cloud in the single-impurity Anderson model: A DMRG study

The Kondo effect [26] is a well-known hallmark of magnetic impurity systems caused by the interaction of an impurity spin with itinerant electrons and is characterized by the Kondo temperature T_{K}. The Kondo effect also manifests itself through spatially extended spin-spin correlations – the Kondo screening cloud – with an associated length scale, the Kondo screening length ξ_{K}.

There exist extensive theoretical studies of the Kondo screening cloud [34, 107–115] and the numerical renormalization group (NRG) [2, 116], the standard numerical method for impurity systems, has been extended to resolve spatial correlations [34]. In contrast to NRG, the DMRG on a real-space model provides direct access to spatial spin-spin correlations, however, at the cost of increased difficulty of reaching very small Kondo temperatures, as this would require very large system sizes. We study for the single-impurity Anderson model (SIAM) how the Kondo screening length ξ_{K} can be extracted from spin-spin correlations and how an applied gate voltage and magnetic field impairs the Kondo screening cloud.

PHYSICAL REVIEW B **80**, 205114 (2009)

Kondo screening cloud in the single-impurity Anderson model: A density matrix renormalization group study

Andreas Holzner,[1,2] Ian P. McCulloch,[3] Ulrich Schollwöck,[1] Jan von Delft,[1,4] and Fabian Heidrich-Meisner[2,4]
[1]*Physics Department, Arnold Sommerfeld Center for Theoretical Physics, and Center for NanoScience, Ludwig-Maximilians-Universität München, D-80333 München, Germany*
[2]*Institute for Theoretical Physics C, RWTH Aachen University, D-52056 Aachen, Germany*
[3]*School of Physical Sciences, University of Queensland, Brisbane, Queensland 4072, Australia*
[4]*Kavli Institute for Theoretical Physics, Kohn Hall, University of California, Santa Barbara, California 93106, USA*
(Received 19 June 2009; published 13 November 2009)

A magnetic moment in a metal or in a quantum dot is, at low temperatures, screened by the conduction electrons through the mechanism of the Kondo effect. This gives rise to spin-spin correlations between the magnetic moment and the conduction electrons, which can have a substantial spatial extension. We study this phenomenon, the so-called Kondo cloud, by means of the density matrix renormalization group method for the case of the single-impurity Anderson model. We focus on the question whether the Kondo screening length, typically assumed to be proportional to the inverse Kondo temperature, can be extracted from the spin-spin correlations. For several mechanisms—the gate potential and a magnetic field—which destroy the Kondo effect, we investigate the behavior of the screening cloud induced by these perturbations.

DOI: 10.1103/PhysRevB.80.205114 PACS number(s): 78.20.Bh, 02.70.−c, 72.15.Qm, 75.20.Hr

I. INTRODUCTION

The Kondo effect,[1] a well-known feature of magnetic impurity systems, has seen a tremendous renewed interest due to the realization of quantum dots and nanoscale systems.[2] The existence of Kondo correlations at low temperatures T has been firmly established in numerous experiments on quantum dots,[3] molecules,[4] and carbon nanotubes.[5] The interaction of an impurity spin with itinerant electrons, causing the Kondo effect, manifests itself in spatially extended spin-spin correlations—the Kondo screening cloud. These correlations have been extensively studied in theory[6–15] and many proposals for experimentally measuring the Kondo screening cloud have been put forward.[9,11,14,15] Also, several studies have emphasized the emergence of mesoscopic fluctuations on finite systems, and the existence of even-odd effects in the Kondo cloud when computed from a lattice model.[8,9,11,16,17] While there has been experimental progress toward the measurement of the Kondo cloud,[18,19] the detection of the spin-spin correlations has proven to be highly challenging and has not been accomplished so far. Depending on the Kondo temperature T_K, the Kondo cloud can have a significant extension of ~ 1 μm.[13]

In our work, we examine the spin-spin correlations in a real-space model, the single-impurity Anderson model (SIAM) that includes charge fluctuations, using the density matrix renormalization group method (DMRG).[20–22] We address two main questions: first, we compute the spin-spin correlations between the impurity spin and the conduction electrons at particle-hole symmetry and discuss how the Kondo screening length ξ_K can be directly extracted from such data. To that end, we discuss several ways of collapsing spin-spin correlations calculated for different Kondo temperatures onto a universal curve. In this analysis, we employ ideas suggested by Gubernatis *et al.*[6] that have also been used in previous DMRG studies of the Kondo cloud problem.[11,12] We find that from chains of about $L=500$ sites, suitable measures for the $L=\infty$ screening length can be extracted for Kondo temperatures of $k_B T_K/\Gamma \sim 1 \cdot 10^{-3}$ (Γ is the tunneling rate). Knowledge of the universal curve further allows us to estimate ξ_K even for Kondo temperatures for which the accessible system sizes are too small to host the full Kondo cloud. As a main result of our analysis, we find that our measures of ξ_K extracted from the spin-spin correlations have the same functional dependence on model parameters as ξ_K^0

$$\xi_K^0 = \hbar v_F / T_K, \tag{1}$$

at particle-hole symmetry (v_F is the Fermi velocity in the leads, we adopt $k_B=1$ throughout the rest of this work). The screening length ξ_K^0 governs the finite-size scaling of local quantities such as the polarization or the magnetic moment.[8]

Second, we consider several mechanisms that destroy Kondo correlations, namely, a gate voltage and a magnetic field applied to the quantum dot. We study the changes in the screening length induced by a variation in these parameters. We argue that computing the magnetic-field dependence of the screening length provides a means of extracting the Kondo temperature.

The emergence of an exponentially small energy scale in the Kondo problem, namely, T_K, restricts any real-space approach with respect to the Kondo temperatures that can be accessed. A powerful framework was introduced by Wilson[23] in the form of the numerical renormalization group (NRG) method,[23,24] which is explicitly tailored toward the Kondo problem. This is achieved through the introduction of a logarithmic energy discretization that allows the Kondo scale to be resolved but loses real-space information. Recently, an NRG method has been developed to access spatially resolved quantities,[13,14,25] extending some older NRG calculations for spatially dependent correlation functions.[26] Using the more recent NRG approach,[13] the spin correlations between the impurity and the sites in the leads have been computed for

 ©2009 The American Physical Society

the Kondo model, and it has been shown that at the Kondo screening length ξ_K^0, the envelope of the correlations crosses over from a $1/x$ decay at distances $x<\xi_K^0$ to a $1/x^2$ decay at distances $x>\xi_K^0$, where x denotes the distance between the impurity and a site in the leads.

Comparing NRG and DMRG, first, there are technical differences between DMRG and NRG with respect to how the spin-spin correlations $\langle \vec{S}_i \cdot \vec{S}_j \rangle$ ($\vec{S}_i$ denotes a spin-1/2 operator at site i) are obtained. NRG requires a separate run for each pair of indices, (i,j), whereas DMRG operates directly on real-space leads. That way, after calculating the ground state for a system of a given length, all correlations can be evaluated in a single run. While the use of real-space chains is restricted to one dimension, which is the case of interest in our work, NRG in principle works for higher dimensions too. Second, using DMRG, we can gain direct and easy information on the finite-size scaling of spin-spin correlations, which we heavily exploit in our analysis. Most importantly, DMRG can also be applied to quantum-impurity problems with interacting leads[12] that NRG is not designed for.

DMRG has previously been used to study the Kondo cloud in several papers, for both the single-impurity Anderson model[11] and the Kondo model.[8,10] In Ref. 11 by Hand *et al.*, in particular, an interesting relation between the screening length as extracted from the spin correlations and the weight of the Kondo resonance has been discussed. Our study extends the DMRG literature as we consider the mixed-valence regime, the effect of a magnetic field, and we discuss and demonstrate the universal scaling of spin-spin correlations for a wide range of parameters. Moreover, in the absence of a magnetic field, we exploit the SU(2) symmetry of the model in the spin sector in the DMRG simulations, which we find is crucial for efficiently obtaining reliable numerical results.

Besides the conceptual interest in understanding the scaling properties of the Kondo screening length with both system size and Kondo temperature, our results are relevant to gauge the range of validity of numerical approaches for calculating the conductance of nanostructures that employ a real-space representation of the leads such as time-dependent DMRG simulations of transport in the single-impurity Anderson model.[27–29] Moreover, the approaches discussed here to extract the screening length could be applicable to more complex geometries in a straightforward way, for instance, to multichannel and/or multidot problems.

Our work is organized as follows. In Sec. II, we introduce our model and define the quantities of interest. In Sec. III, the spin-spin correlations constituting the Kondo cloud are investigated and we demonstrate how to extract the value of the Kondo screening length ξ_K from the spin-correlation data, making use of the universal finite-size scaling behavior of ξ_K. We proceed with a discussion of the behavior of the screening length upon driving the system away from the Kondo point via a gate potential, presented in Sec. IV, and then turn to the case of a magnetic field in Sec. V. We conclude with a summary, Sec. VI, while technical detail on the method and computations are given in the Appendix.

II. MODEL

We model a quantum dot coupled to a lead by the single-impurity Anderson model, describing the lead by a tight-binding noninteracting chain. This constitutes a one-channel problem

$$H = \sum_{\sigma=\uparrow,\downarrow} \epsilon_d n_{d\sigma} + BS_d^z + U n_{d\uparrow} n_{d\downarrow} - t \sum_{\sigma} \sum_{i=1}^{L-1} (c_{i\sigma}^\dagger c_{(i+1)\sigma} + \text{h.c.}) - \sum_{\sigma} \sqrt{2} t' (c_{1\sigma}^\dagger d_\sigma + \text{h.c.}). \quad (2)$$

$c_{i\sigma}$ annihilates an electron with spin $\sigma=\uparrow,\downarrow$ on site i, d_σ annihilates an electron with spin σ on the dot, and $n_{d\sigma}=d_\sigma^\dagger d_\sigma$. The spin operators at any site are given by $S_i^a = c_{is}^\dagger \sigma_{ss'}^a c_{is'}/2$, where σ^a are the Pauli matrices ($a=x,y,z$). ϵ_d denotes the gate potential and B denotes the magnetic field applied to the dot, U denotes the strength of the Coulomb interaction on the quantum dot, t' denotes the hopping of the dot levels to the first site in the lead, t denotes the hopping within the lead. The width of the dot level due to the hybridization with the lead is given by $\Gamma = 2t'^2/t$.

In the absence of a magnetic field, this model has a spin SU(2) symmetry. In our analysis, we calculate the ground state of this system via DMRG using an implementation[30] exploiting the SU(2) symmetry, which greatly improves the efficiency[31,32] (see the Appendix for more detail). A typical run for $L=500$ sites with $m=1500$ states took about 60 h on a 2.6 GHz Opteron CPU.

All simulations, irrespective of ϵ_d, are performed at half-filling of the full system. As the Kondo scale depends exponentially on U/Γ, while in a real-space representation of the leads, the energy resolution is proportional to $1/L$, we restrict our analysis to the intermediate values of U/Γ. The trade-off for these limitations is that it is straightforward to calculate spin correlators, as outlined below [see Eq. (3)].

Throughout this work, we use chains with an overall *even* number of sites. It is well known that there are significant even-odd effects in impurity problem of this kind.[8,9,11,16,17] Earlier work (see, e.g., Ref. 33), suggests that the convergence with system size toward a Kondo state is much faster on chains with an even number of sites. We thus work in singlet subspaces.

III. SPIN-SPIN CORRELATIONS AND KONDO SCREENING LENGTH AT $\epsilon_d = -U/2$

In this section, we present our results for the spin-spin-correlation function at particle-hole symmetry and we discuss two ways of collapsing the data, allowing for a determination of the Kondo screening length. In order to investigate the behavior of the Kondo screening length, we shall study the following integrated spin-correlation function

$$\Sigma(x) = 1 + \sum_{i=1}^{x} \frac{\langle \vec{S}_d \cdot \vec{S}_i \rangle}{\langle \vec{S}_d \cdot \vec{S}_d \rangle}, \quad (3)$$

to be evaluated in the singlet subspace of the total spin $\vec{S}_{\text{tot}} = \vec{S}_d + \Sigma_{i=1}^{L-1} \vec{S}_i$, and under the assumption that $\langle \vec{S}_d^2 \rangle \neq 0$ (x is given in units of the lattice constant). This definition is mo-

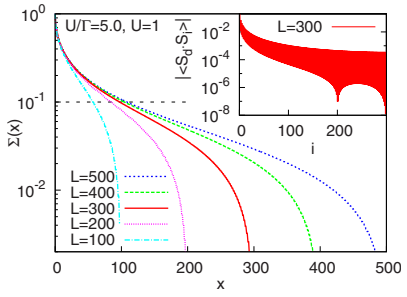

FIG. 1. (Color online) Integrated spin-spin correlations $\Sigma(x)$ [from Eq. (3)] for systems of different sizes at $U=1, \Gamma=0.20$ and $\epsilon_d=-U/2$. As an example, the threshold of 0.1 that we use in Eq. (5) to extract $\xi_{0.9}$ is indicated by the dashed horizontal line. As an illustration of the typical raw data, we show the absolute value of the spin-spin correlations $|\langle \vec{S}_d \cdot \vec{S}_i \rangle|$ for $L=300$ in the inset.

tivated by the following convenient properties: (i) the decay of $\Sigma(x)$ with x characterizes the extent to which the total spin of chain sites one to x is able to screen the spin on the impurity level, i.e., the extent to which $\Sigma_{i=1}^{x} \vec{S}_i$ has, crudely speaking, "become equal and opposite" to $\vec{S}_d$. (ii) When the sum includes the entire chain, we always have $\Sigma(L-1)=0$. This follows by noting that in the subspace with zero total spin, where $\langle \vec{S}_{\rm tot}^2 \rangle = 0$, we have $\langle \vec{S}_d^2 \rangle = \langle (\Sigma_{i=1}^{L-1} \vec{S}_i)^2 \rangle$, and hence also $\langle \vec{S}_{\rm tot}^2 \rangle = 2\langle \vec{S}_d \cdot \vec{S}_d \rangle \Sigma(L-1)$. (iii) The correlator is normalized to $\Sigma(0)=1$. (iv) In the absence of a magnetic field, $\Sigma(x)$ is SU(2) invariant, such that this symmetry can be exploited in our numerics. In the presence of a magnetic field, we shall use a symmetry-broken version, replacing $\langle \vec{S}_d \cdot \vec{S}_i \rangle / \langle \vec{S}_d \cdot \vec{S}_d \rangle$ by $(\langle S_d^z S_i^z \rangle - \langle S_d^z \rangle \langle S_i^z \rangle) / (\langle S_d^z S_d^z \rangle - \langle S_d^z \rangle^2)$.

As an example, the inset of Fig. 1 shows a DMRG result for the absolute value of the bare spin-spin correlator $\langle \vec{S}_d \cdot \vec{S}_i \rangle$. The feature at $i \sim 200$ is a simple effect of the open boundary conditions. The spin correlations for i smaller than a certain value (here roughly $i \sim 200$) oscillate between negative and positive, while beyond a certain point, all $\langle \vec{S}_d \cdot \vec{S}_i \rangle$ become positive. This feature at $i \sim 200$ precisely appears at the site where this happens, i.e., where $\langle \vec{S}_d \cdot \vec{S}_i \rangle$ with i even changes its sign and, as a consequence, the correlator passes arbitrarily close through zero. Summing up the correlator according to Eq. (3) yields $\Sigma(x)$, plotted in the main panel.

The notion of a screening length is based on the premise that the decay of $\Sigma(x)$ follows a universal form characterized by a single length scale, ξ_K, as long as this scale is significantly shorter than the system size, $\xi_K \ll L$. (According to the expectation that $\xi_K \propto \hbar v_F / T_K$, this condition is equivalent to the following statement: perfect spin screening in a system of finite size L can only be achieved if the level spacing, which scales like $\hbar v_F / L$, is smaller than T_K.) Whenever this condition is not met, the shape of the decay of $\Sigma(x)$ with x deviates from its universal form once x becomes large enough such that the finite system size makes itself felt [via the boundary condition $\Sigma(L-1)=0$]. To extract ξ_K from DMRG data obtained for finite-sized systems, we thus need a strategy for dealing with this complication. Below, we shall describe two different approaches that accomplish this, both involving a scaling analysis.

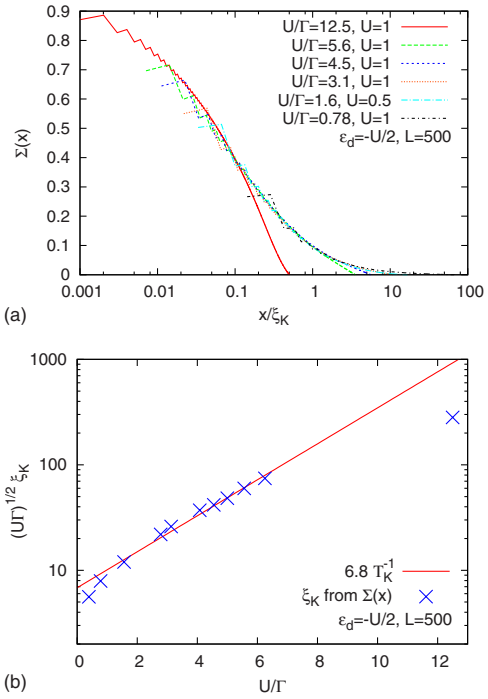

FIG. 2. (Color online) (a) Rescaled integrated spin-spin correlations $\Sigma(x)$, collapsed onto a universal curve via suitable choices of ξ_K. (b) Comparison of the U and Γ dependence of ξ_K and ξ_K^0 [from Eq. (4)]: $\sqrt{U\Gamma}\xi_K$ (symbols) and $\sqrt{U\Gamma} p T_K^{-1}$ (lines) plotted vs U/Γ, using p as the fitting parameter (resulting in $p=6.8$).

To check whether the screening length obtained using either of the two scaling strategies conforms to the theoretical expectations, we shall check whether its dependence on the parameters U, Γ, and ϵ_d agrees with that of the length scale $\xi_K^0 = \frac{\hbar v_F}{T_K}$ [Eq. (1)]. Using the known form of the Kondo temperature T_K for the Anderson model,[34,35] this dependence is given by

$$\xi_K^0 \equiv \frac{\hbar v_F}{\sqrt{U\Gamma}} \exp\left[\frac{\pi |\epsilon_d| |\epsilon_d + U|}{2U\Gamma} \right]. \tag{4}$$

We shall indeed find a proportionality of the form $\xi_K = p\xi_K^0$, where the numerical prefactor p reflects the fact that the definition of T_K involves an arbitrary choice of a prefactor on the order of one. We emphasize, however, that our determination of ξ_K will be carried out without invoking Eq. (4); rather, our results for ξ_K will turn out to confirm Eq. (4) *a posteriori*. In the present section we shall focus on the symmetric Anderson model ($\epsilon_d=-U/2$) at zero magnetic field, considering more general cases in Sec. IV.

A. Scaling collapse of $\Sigma(x)$

The first way of extracting the screening length is to plot $\Sigma(x)$ versus x/ξ_K, where ξ_K is treated as a fitting parameter, to be chosen such that all the curves collapse onto the same scaling curve [see Fig. 2]. When attempting to collapse the

$\Sigma(x)$ data, one faces two issues. First, the $\Sigma(x)$ data are nonmonotonic in L, due to the fact that the sign of $\langle \vec{S}_d \cdot \vec{S}_i \rangle$ oscillates, and for curves scaled by different values of ξ_K, the oscillations are stretched by different amounts on a semilog plot. This introduces some "noise" to the $\Sigma(x)$ curves, making it somewhat difficult to decide when the scaling collapse is optimal. Second, for some parameter combinations, the condition $\xi_K \ll L$ is not met, and, therefore, perfect scaling cannot be expected for all the curves.

These issues can be dealt with by a two-step strategy: (i) we start with the curves, which collapse the best, namely, those with the smallest U/Γ ratios. These yield the smallest ξ_K values and hence satisfy the condition $\xi_K < L$ required for good scaling well enough such that the shape of the universal scaling curve can be established unambiguously (to the extent allowed by the aforementioned noise). (ii) We then proceed to larger ratios of U/Γ, which yield larger ξ_K, and adjust ξ_K such that a good collapse of $\Sigma(x)$ vs x/ξ_K onto the universal curve is achieved in the regime of small x/ξ_K, where finite-size effects are not yet felt. Thus, knowledge of the universal scaling curve allows ξ_K to be extracted even when the condition $\xi_K \ll L$ is not fully met.

The result of such a scaling analysis is shown in Fig. 2(a). A universal scaling curve can clearly be discerned, with deviations from scaling evident in the curves with large U/Γ, as expected. Moreover, Fig. 2(b) shows that the results for ξ_K extracted from $\Sigma(x)$ scaling agree rather well with the parameter dependence expected from Eq. (4) for $p/(\hbar v_F) \cdot \xi_K^0$ (with a prefactor of $p=6.8$), provided that $U/\Gamma \gtrsim 2$. For smaller U/Γ, no well-defined local moment will form and the premise for Eq. (4) no longer holds.

B. Scaling collapse of $\xi_a(L)$

A second strategy for extracting the screening length, following Refs. 6, 11, and 12, is to determine the length, say ξ_a, on which the integrated spin-correlation function $\Sigma(x)$ has dropped by a factor of a of its $x=0$ value (for instance, $a=0.9$ would signify a 90% screening of the local spin). Thus, we define

$$\xi_a(L) = \min\{x; \Sigma(x) \leq 1 - a\}. \tag{5}$$

The argument of $\xi_a(L)$ serves as a reminder that this length depends on L, since the boundary condition $\Sigma(L-1)=0$ always enforces perfect screening for $x=L$. However, once the system size becomes sufficiently large ($L > \xi_K$) to accommodate the full screening cloud, $\xi_a(L)$ approaches a limiting value, to be denoted by ξ_a [shorthand for $\xi_a(\infty)$], which may be taken as a measure of the true screening length ξ_K. This is illustrated in the main panel of Fig. 1 for $a=0.9$: as L increases, the x values, where the $\Sigma(x)$ curves cross the threshold $1-a=0.1$ (horizontal dashed line), tend to a limiting value. This limiting value, reached in Fig. 1 for $L > 300$, defines $\xi_{0.9}$.

Figure 3 shows the L dependence of $\xi_{0.9}(L)$ for several values of U/Γ ranging from 0.4 to 12.5, and system sizes up to $L=500$. We observe that $\xi_{0.9}(L)$ reaches its limiting value for small ratios of U/Γ, which produce $\xi_{0.9}$ values smaller than $L=500$. For larger values of U/Γ, however, $\xi_{0.9}(L)$ does not saturate, implying that for these parameters, the true screening length is too large to fit into the finite system size.[36]

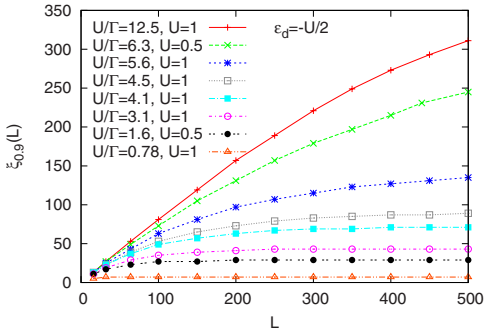

FIG. 3. (Color online) System size dependence of $\xi_{0.9}(L)$ for $\epsilon_d = -U/2$. Points represent numerical data; lines serve as guides to the eyes.

Nevertheless, it is possible to extract the true screening length in the latter cases as well, by performing a two-step finite-size scaling analysis: (i) for those parameters U/Γ for which $\xi_a(L)$ has already saturated on a finite system, we set $\xi_a = \xi_a(L=500)$, and plot $\xi_a(L)/\xi_a$ vs L/ξ_a. This collapses all such curves onto a universal scaling curve. For larger U/Γ, we rescale the $\xi_a(L)$ curves in a similar fashion, but now using ξ_a as a fit parameter, chosen such that the rescaled curves collapse onto the universal curve determined in step (i). As shown in Fig. 4(a) for $a=0.9$, this strategy produces an excellent scaling collapse for all combinations of U and Γ studied here.

The above procedure requires the threshold parameter a to be fixed arbitrarily. Qualitatively, one needs a large a to capture most of the correlations, i.e., $\xi_a(L \to \infty) \sim \xi_K$, yet a ought not to be too close to one to avoid boundary effects in the results. Technically, the calculation of ξ_a is much easier the smaller a is, as less correlators $\langle \vec{S}_i \cdot \vec{S}_d \rangle$ that are of a small numerical value need to be computed to high accuracy (see also the discussion in the Appendix). For instance, at $U/\Gamma = 5$ and $L=500$, $\xi_{0.9} \approx 112$ sites, while $\xi_{0.75} \approx 29$ sites.

We have carefully analyzed the qualitative dependence of our analysis on the threshold a. First, the universal scaling behavior in $\xi_a(L)/\xi_a$ is seen for $a > 0.6$. Using too small a value for a ignores the long-range behavior of $\Sigma(x)$. Qualitatively, ξ_a needs to be close to the point, where the decay of the envelope of spin-spin correlations changes from a power law with $1/x$ to $1/x^2$ (see Fig. 2 in Ref. 13). Second, it turns out that different choices of a produce values of ξ_a that differ only by a (U-independent and Γ-independent) prefactor $p(a)$, as illustrated in Fig. 4(b) (symbols). In particular, for $U/\Gamma \gtrsim 2$, all ξ_a follow the same functional dependence on the parameters U and Γ, satisfying the relation

$$\xi_a = \frac{p(a)}{\hbar v_F} \xi_K^0 \tag{6}$$

expected from Eq. (4) (lines in Fig. 4). It is obvious that ξ_a yields an *upper* bound to ξ_K^0 since $p(a) > 1$ for all choices of a.

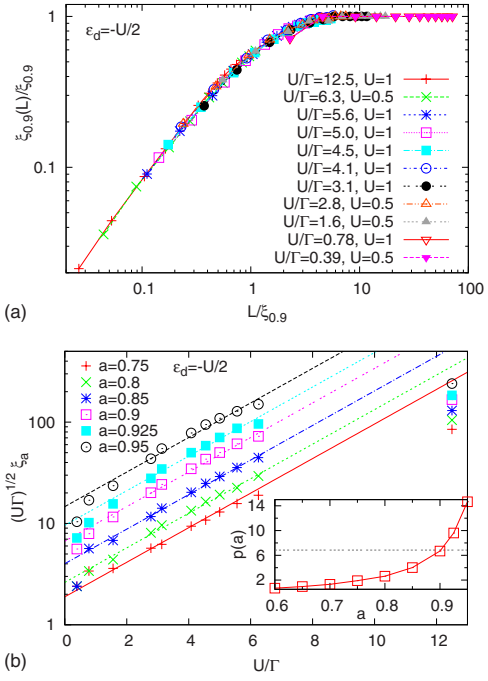

FIG. 4. (Color online) Results of a $\xi_a(L)$ scaling analysis for $\epsilon_d=-U/2$. (a) Scaling collapse of $\xi_{0.9}(L)/\xi_{0.9}$ vs $L/\xi_{0.9}$, obtained by the two-step scaling strategy described in the text in Sec. III B. (b) Comparison of the U and Γ dependence of ξ_a and ξ_K^0 [from Eq. (4)] for several values of a: $\sqrt{U\Gamma}\xi_a$ (symbols) and $\sqrt{U\Gamma}p(a)T_K^{-1}$ (lines) plotted vs U/Γ, using the fit parameters $p(a)$ shown in the inset (squares). The dotted line in the inset indicates the prefactor $p=6.8$ obtained from the $\Sigma(x)$ scaling analysis of Fig. 2(b).

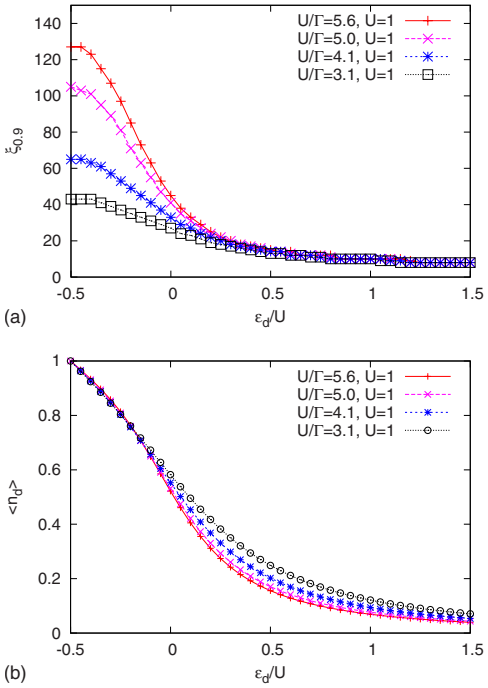

FIG. 5. (Color online) (a) Kondo screening length $\xi_{0.9}$ vs gate potential ϵ_d/U for several U/Γ and $L=500$. (b) Dot occupation $\langle n_d\rangle$ vs gate potential.

The only exceptions are the data points at $U/\Gamma=12.5$, for which ξ_a is too large in comparison to $L=500$ to yield reliable results. The latter are thus excluded when fitting the ξ_a data to determine the best values for $p(a)$, shown in the inset of Fig. 4.

The inset includes the prefactor $p=6.8$ (horizontal dotted line) obtained in Sec. III A, from Fig. 2, via a scaling analysis of $\Sigma(x)$ (which has the advantage of not involving any arbitrarily chosen threshold). Evidently, $p=6.8$ is rather well matched by $p(0.9)\simeq 6.7$, implying that the two alternative scaling strategies explored above, based on $\Sigma(x)$ and $\xi_a(L)$, yield essentially identical screening lengths for $a=0.9$. For the remainder of this paper, where we consider $\epsilon_d\neq -U/2$ or $B\neq 0$, we shall thus determine the screening length by employing $\xi_{0.9}(L)$ scaling, which is somewhat more straightforward to implement than $\Sigma(x)$ scaling.

IV. GATE POTENTIAL

We next investigate the behavior of the Kondo screening length while sweeping the gate potential applied to the dot. Qualitatively, one expects the Kondo temperature to increase upon gating the dot away from particle-hole symmetry and eventually, as the dot's charge starts to deviate substantially from one, the Kondo effect will be fully suppressed.[37] Consequently, we expect the Kondo cloud to shrink upon varying ϵ_d. To elucidate this behavior, we focus on values of $U/\Gamma \lesssim 5.6$ for which $\xi_{0.9}(L=500)$ yields a good estimate of the true ξ_K, as demonstrated in Sec. III.

Our results for $\xi_{0.9}$ are presented in Fig. 5(a). In addition, and as an illustration, we plot the dot level occupation $\langle n_d\rangle = \langle 0|n_{d\uparrow}+n_{d\downarrow}|0\rangle$ in Fig. 5(b), where $|0\rangle$ is the ground state of the system, obtained via DMRG. As we shift the dot level away from the particle-hole symmetric point at $\epsilon_d=-U/2$ and thus leave the Kondo regime, $\xi_{0.9}$ falls off rapidly. This is symmetric in the direction of the deviation from the Kondo point. In the regime $\epsilon_d \lesssim -\Gamma$ one would expect Eq. (4) to hold roughly. Indeed, for $\epsilon_d=-U/4$, Eq. (4) still applies,[38] while for, e.g., $\epsilon_d=0$ this is not the case anymore. The reason is that Eq. (4) is only valid in the Kondo regime with $\langle n_d\rangle \approx 1$. From Fig. 5(b) we see that the dot occupation starts to decrease quickly as we increase ϵ_d from $-U/2$, implying that the magnetic moment decreases as well. In the mixed-valence regime, $\epsilon_d \gtrsim -\Gamma$, $\xi_{0.9}$ measures the strength of the spin-spin correlations not originating from Kondo physics.

V. MAGNETIC FIELD

The application of a magnetic field is known to destroy the Kondo effect and its influence on the density of states (DOS) and the conductance has been widely studied.[39,40] Here, we investigate how the screening cloud collapses as the magnetic moment is squeezed by the magnetic field. In

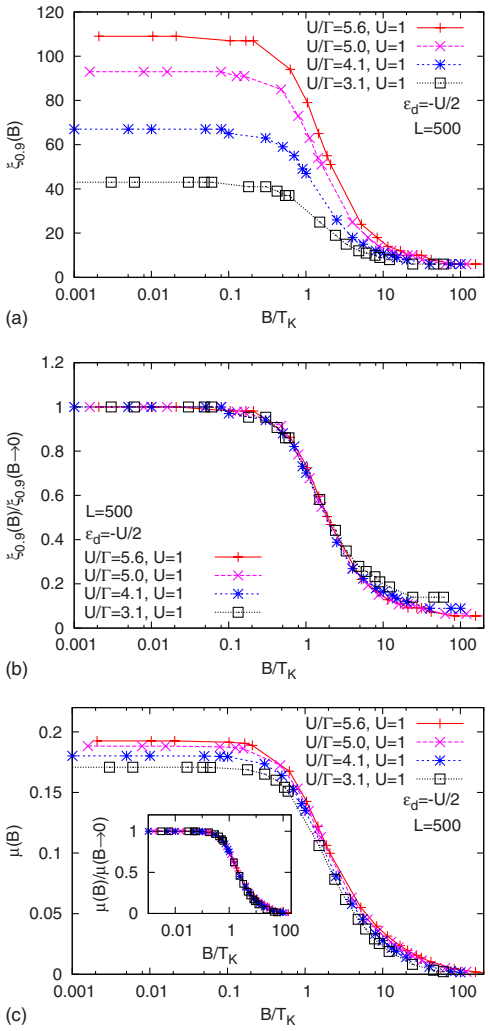

FIG. 6. (Color online) (a) Kondo screening length $\xi_{0.9}$ as a function of the magnetic field applied to the dot for $L=500$. In all panels, T_K is given by $T_K=\hbar v_F/\xi_K^0$ with ξ_K^0 from Eq. (4). (b) Scaling collapse of $\xi_{0.9}(B)/\xi_{0.9}(B\to 0)$ vs B/T_K (c) Magnetic moment $\mu=\langle(S_d^z)^2\rangle-\langle S_d^z\rangle^2$ vs B/T_K. The inset shows the rescaled data $\mu(B)/\mu(B\to 0)$.

the presence of a finite magnetic field the total spin $\vec{S}$ is no longer conserved but only S^z is conserved. Thus we are left with a U(1) symmetry for S^z instead of the SU(2) symmetry for $\vec{S}$. As a consequence, much more computational effort is needed in order to achieve an accuracy similar to the zero-field case (see the Appendix for detail).

Our results for (i) the screening length $\xi_{0.9}(L=500)$ and (ii) the magnetic moment of the dot $\mu=\langle(S_d^z)^2\rangle-\langle S_d^z\rangle^2$ are displayed in Figs. 6(a) and 6(c), respectively. As the magnetic field is increased but still smaller than T_K, there are almost no visible effects in $\xi_{0.9}$ (note the logarithmic scale in the figure). Once the magnetic field B reaches the order of the Kondo temperature T_K, the Kondo effect gets suppressed and the extent of the Kondo cloud shrinks rapidly. More precisely, a pronounced decay of the screening length sets in at $B\simeq 0.5T_K$, in agreement with findings for the field-induced splitting of the central peak in the impurity spectral function.[41] Qualitatively, both the screening length and the magnetic moment μ exhibit the same behavior. Note that for small U/Γ, charge fluctuations reduce the magnetic moment to lie below the value $\mu=1/4$ applicable for the Kondo model, which presupposes $U/\Gamma\gg 1$.

To identify the point at which the Kondo effect breaks down, we again study the collapse of results from Fig. 6 onto a universal curve. This is shown in Fig. 6(b), and as a main result we find

$$\frac{\xi_{0.9}(B)}{\xi_{0.9}(B\to 0)}\propto f(B/T_K), \tag{7}$$

where $f(x)$ describes the universal dependence on B/T_K. We note that due to higher numerical effort for calculations with a finite magnetic field (as further discussed in the Appendix) our numerical results slightly underestimate $\xi_{0.9}(B)$ at $U/\Gamma\gtrsim 5$, in particular, at small B. This, however, has no qualitative influence on the scaling collapse described by Eq. (7). We suggest that an analysis analogous to the one presented in Fig. 6 could be used to extract T_K for models in which the dependence of T_K on model parameters is not known. In such an analysis, T_K would be the only fitting parameter, since $\xi_{0.9}(B,L\to\infty)$ can be determined along the lines of Sec. III and one would obtain T_K up to an unknown prefactor, which is independent of U/Γ.

By rescaling the magnetic moment data to $\mu(B)/\mu(B\to 0)$ as shown in the inset of Fig. 6(c) we again find a universal curve very similar to the collapse of $\xi_{0.9}(B)/\xi_{0.9}(B\to 0)$ in Fig. 6(b). We thus confirm that a collapse of local quantities can be used to extract T_K, as previously shown using DMRG.[8] In principle, both a scaling analysis of $\xi_{0.9}(B)$ and $\mu(B)$ can be used to extract T_K. Using the analysis of the screening length data (ξ_K) offers the possibility of a scaling analysis as outlined in Sec. III to reach parameter regimes, where a convergence of the data in L has not yet been reached. Moreover, the analysis of ξ_K directly unveils the relevant length scales.

VI. SUMMARY

In this work, we studied the spin-spin correlations in the single-impurity Anderson impurity model using a state-of-the-art implementation of the density matrix renormalization group method. We first considered the particle-hole symmetric point and discussed two ways of collapsing the system-size-dependent data onto universal scaling curves to extract a measure of the Kondo cloud's extension, the screening length ξ_K, as a function of U/Γ, or T_K, respectively. The first analysis is based on a scaling collapse of the integrated correlations, while the second one employs a finite-size scaling analysis of the distance $\xi_a(L)$ from the impurity at which a certain fraction a of the impurity's magnetic moment is screened. $\xi_a(L)/\xi_a(\infty)$ exhibits a universal dependence on $L/\xi_a(\infty)$, independently of the parameter U/Γ. We further showed that for an appropriately chosen value of the parameter a, both approaches yield quantitatively similar estimates

of the screening length. Our results for ξ_K, obtained from either of the scaling analyses, nicely follow the expected dependence on U/Γ.

As DMRG works in real space, the scaling regime could only be reached for $U/\Gamma=4$ and system sizes of $L\lesssim 500$, but even for larger $U/\Gamma\lesssim 6$, a collapse onto the universal behavior could be achieved. Note that $U/\Gamma\sim 4$ is the regime, in which time-dependent DMRG is able to capture Kondo correlations in real-time simulations of transport[27] on comparable system sizes, consistent with our observations.

While NRG is better suited to access the regime of very small Kondo temperatures T_K, DMRG efficiently gives access to the full correlation function $\langle \vec{S}_d \cdot \vec{S}_i \rangle$ in a single run. As an outlook onto future applications, we emphasize that DMRG allows for the calculation of the spin-spin correlations in the case of interacting leads[12] or out-of-equilibrium, which is challenging if not impossible for other numerical approaches with current numerical resources.

While the first part of our study focused on the particle-hole symmetric point where Kondo physics is dominant, we have further analyzed how the screening cloud is affected (i) by varying the gate voltage and tuning the system into the mixed-valence regime, and (ii) by applying a magnetic field at particle-hole symmetry. The latter provides an independent measure of the Kondo temperature, through the universal dependence of the screening length on T_K/B.

Note added: while finalizing this work, we became aware of a related effort on the Kondo cloud, Ref. 42, using the so-called embedded-cluster approximation, slave bosons, and NRG. Their analysis is based on calculating the local density of states in the leads, as a function of the distance from the impurity.

ACKNOWLEDGMENTS

We gratefully acknowledge fruitful discussions with E. Anda, L. Borda, C. Büsser, E. Dagotto, G. B. Martins, J. Riera, and E. Vernek. This work was supported by DFG (SFB 631, De-730/3-2, SFB-TR12, SPP 1285, and De-730/4-1). Financial support by the Excellence Cluster "Nanosystems Initiative Munich (NIM)" is gratefully acknowledged. J.v.D and F.H.M. thank the KITP at UCSB, where this work was completed, for its hospitality. This research was supported in part by the National Science Foundation under Grant No. NSF PHY05-51164.

APPENDIX: NUMERICAL DETAIL

In this Appendix we provide detail on our numerical method. The DMRG calculations presented in this work are challenging for two reasons. First, we model the conduction band with a chain of length L that provides an energy resolution of $1/L$, whereas the Kondo temperature becomes exponentially small with increasing U/Γ [c.f. Eq. (4)]. Second, the spin-spin correlators are long-ranged quantities making very accurate calculations of quantities necessary that are small compared to the unit of energy, t. The parameter controlling the accuracy of our calculations is the number of states m used to approximate the ground state during the DMRG sweeps. Typically, we choose $m=1500$ (3000 at most) for the calculation of the ground state. This results in a residual norm per site,[43] a measure for the quality of the convergence of the calculated ground state toward an eigenstate of the Hamiltonian, $\delta r=\langle\psi_0|(\hat{H}-E)^2|\psi_0\rangle$, on the order of $\frac{\delta r}{L}=\mathcal{O}(10^{-7})$.

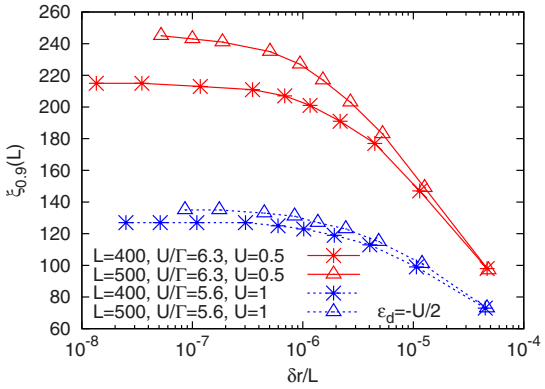

FIG. 7. (Color online) Convergence of $\xi_{0.9}$ vs the residual norm per site $\delta r/L$ for $\epsilon_d=-U/2$, extracted from ground-state calculations using the SU(2) symmetry. For each combination of U/Γ and L, the number of states kept increases for data points from right to left as $m=200,400,600,800,1000,1200,1500,2000,2500,3000$, except for the case $U/\Gamma=5.6$, $L=500$, where no point with $m=3000$ is shown.

Figure 7 illustrates the m dependence of $\xi_{0.9}$ for two values of U/Γ and two values of L at $\epsilon_d=-U/2$, obtained from simulations using the SU(2) symmetry. The larger the ratio U/Γ and the bigger the system size L, the higher the number of states m, needed to be kept to obtain a well-converged ground state, see Fig. 7. This can be understood as follows: higher U/Γ implies a smaller Kondo temperature, i.e., a

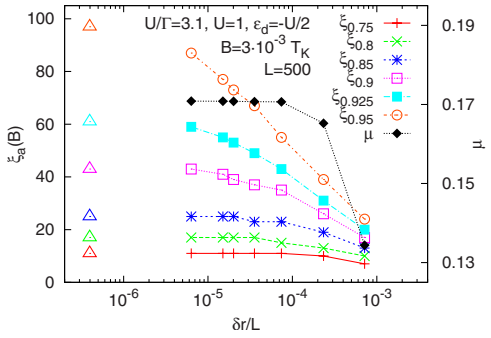

FIG. 8. (Color online) Convergence of $\xi_a(B)$ and the magnetic moment μ vs the residual norm per site $\delta r/L$ for a finite magnetic field of $B/T_K=3\cdot 10^{-3}$ and $\epsilon_d=-U/2$. For comparison, we add the $B=0$ data, represented by the open triangles, from calculations exploiting the SU(2) symmetry ($m=1500$ states kept). The calculation with a magnetic field (symbols connected with lines) uses the U(1) symmetry only ($m=100,200,400,600,800,1000,1500$ states kept from right to left). The results for the dot's magnetic moment μ are also included for comparison (solid diamonds).

larger screening length $\xi_{0.9}$ and longer-ranged spin-spin correlators $\langle \vec{S}_d \cdot \vec{S}_i \rangle$. A well-converged ground state requires these to be evaluated accurately over the entire range $i \lesssim \xi_{0.9}$, and hence more states need to be kept during the DMRG sweeps. For the scaling analysis presented in Sec. III (see Figs. 2 and 4), we only used data points that are converged with respect to the number of states kept.

In Fig. 8, we illustrate that the convergence with the number of states is greatly accelerated whenever the SU(2) symmetry can be exploited. We compare this preferable case to the calculations with a magnetic field, where the SU(2) symmetry is reduced to a U(1) symmetry. In the figure, we use a small magnetic field of $B/T_K = 3 \cdot 10^{-3}$, such that the results for $\xi_a(B, L=500)$ coincide with the results for $B=0$, previously obtained from the SU(2) calculation. For instance, at $L=500$ by keeping $m=1500$ states, $\delta r \simeq 3 \cdot 10^{-3}$ is reached in the U(1) case as compared to $\delta r \simeq 2 \cdot 10^{-4}$ for the SU(2) case. For $U=1$, $\Gamma=0.32$, we show that this residual norm ensures accurate data for ξ_a up to $a=0.9$, while for larger a, our U(1) results are well below the corresponding SU(2) ones computed with the same m.

Pragmatically, in the case of broken SU(2) symmetry, one may resort to using a smaller threshold a (instead of $a=0.9$), for which the convergence with m is faster. As we have shown in Fig. 4, ξ_K can be extracted from ξ_a with $0.6 \leq a \leq 0.95$ up to a nonuniversal prefactor using the schemes discussed in Sec. III.

In contrast to the screening length, the calculation of the magnetic moment μ, a local quantity, is much better behaved. Thus μ does not suffer much from the slower convergence of the U(1) calculation and converges quickly to a high precision (displayed as diamonds in Fig. 8).

[1] J. Kondo, Prog. Theor. Phys. **32**, 37 (1964).
[2] W. G. van der Wiel, S. De Franceschi, J. M. Elzerman, T. Fujisawa, S. Tarucha, and L. P. Kouwenhoven, Rev. Mod. Phys. **75**, 1 (2002).
[3] D. Goldhaber-Gordon, H. Shtrikman, D. Mahalu, D. Abusch-Magder, U. Meirav, and M. A. Kastner, Nature (London) **391**, 156 (1998).
[4] W. Liang, M. P. Shores, M. Bockrath, J. R. Long, and H. Park, Nature (London) **417**, 725 (2002).
[5] B. Zheng, C. Lu, G. Gu, A. Makarovski, G. Finkelstein, and J. Liu, Nano Lett. **2**, 895 (2002).
[6] J. E. Gubernatis, J. E. Hirsch, and D. J. Scalapino, Phys. Rev. B **35**, 8478 (1987).
[7] V. Barzykin and I. Affleck, Phys. Rev. Lett. **76**, 4959 (1996).
[8] E. S. Sørensen and I. Affleck, Phys. Rev. B **53**, 9153 (1996).
[9] I. Affleck and P. Simon, Phys. Rev. Lett. **86**, 2854 (2001).
[10] E. S. Sørensen and I. Affleck, Phys. Rev. Lett. **94**, 086601 (2005).
[11] T. Hand, J. Kroha, and H. Monien, Phys. Rev. Lett. **97**, 136604 (2006).
[12] S. Costamagna, C. J. Gazza, M. E. Torio, and J. A. Riera, Phys. Rev. B **74**, 195103 (2006).
[13] L. Borda, Phys. Rev. B **75**, 041307(R) (2007).
[14] I. Affleck, L. Borda, and H. Saleur, Phys. Rev. B **77**, 180404(R) (2008).
[15] R. G. Pereira, N. Laflorencie, I. Affleck, and B. I. Halperin, Phys. Rev. B **77**, 125327 (2008).
[16] P. Simon and I. Affleck, Phys. Rev. B **68**, 115304 (2003).
[17] W. B. Thimm, J. Kroha, and J. von Delft, Phys. Rev. Lett. **82**, 2143 (1999).
[18] V. Madhavan, W. Chen, T. Jamneala, M. F. Crommie, and N. S. Wingreen, Science **280**, 567 (1998).
[19] H. C. Manoharan, C. P. Lutz, and D. M. Eigler, Nature (London) **403**, 512 (2000).
[20] S. R. White, Phys. Rev. Lett. **69**, 2863 (1992).
[21] S. R. White, Phys. Rev. B **48**, 10345 (1993).
[22] U. Schollwöck, Rev. Mod. Phys. **77**, 259 (2005).
[23] K. G. Wilson, Rev. Mod. Phys. **47**, 773 (1975).
[24] R. Bulla, T. A. Costi, and T. Pruschke, Rev. Mod. Phys. **80**, 395 (2008).
[25] L. Borda, M. Garst, and J. Kroha, Phys. Rev. B **79**, 100408(R) (2009).
[26] K. Chen, C. Jayaprakash, and H. R. Krishnamurthy, Phys. Rev. B **45**, 5368 (1992).
[27] K. A. Al-Hassanieh, A. E. Feiguin, J. A. Riera, C. A. Büsser, and E. Dagotto, Phys. Rev. B **73**, 195304 (2006).
[28] S. Kirino, T. Fujii, J. Zhao, and K. Ueda, J. Phys. Soc. Jpn. **77**, 084704 (2008).
[29] F. Heidrich-Meisner, A. E. Feiguin, and E. Dagotto, Phys. Rev. B **79**, 235336 (2009).
[30] While we use a matrix-product-states-based implementation of DMRG,[32] for the problem studied here, equivalently good results can be obtained with standard DMRG codes that exploit sufficiently many good quantum numbers.
[31] I. P. McCulloch and M. Gulácsi, EPL **57**, 852 (2002).
[32] I. P. McCulloch, J. Stat. Mech. (2007), P10014.
[33] F. Heidrich-Meisner, G. B. Martins, C. A. Büsser, K. A. Al-Hassanieh, A. E. Feiguin, G. Chiappe, E. V. Anda, and E. Dagotto, Eur. Phys. J. B **67**, 527 (2009).
[34] F. D. M. Haldane, J. Phys. C **11**, 5015 (1978).
[35] R. Zitko, J. Bonca, A. Ramsak, and T. Rejec, Phys. Rev. B **73**, 153307 (2006).
[36] We note that by definition $\xi_a(L)$ is only accurate up to one lattice constant. As a consequence, very small changes in $\langle \vec{S}_d \cdot \vec{S}_i \rangle$ may cause a change in $\xi_a(L)$ by one. This can be seen in, *e.g.*, the data for $U=1$, $\Gamma=0.22$ from Fig. 3 (open squares), where $\xi_{0.9}(L)$ is very close to convergence in L but still increases between $L=450$ and $L=500$ by one.
[37] A. C. Hewson, *The Kondo Problem to Heavy Fermions* (Cambridge University, Cambridge, England, 1997).
[38] Note that the prefactor p depends on the gate potential, *i.e.*, $p = p(\epsilon_d)$.
[39] T. A. Costi, Phys. Rev. B **64**, 241310(R) (2001).
[40] A. Rosch, T. A. Costi, J. Paaske, and P. Wölfle, Phys. Rev. B **68**, 014430 (2003).
[41] T. A. Costi, Phys. Rev. Lett. **85**, 1504 (2000).
[42] C. A. Büsser, G. B. Martins, L. C. Ribeiro, E. Vernek, E. V. Anda, and E. Dagotto, arXiv:0906.2951 (unpublished).
[43] A. Weichselbaum, F. Verstraete, U. Schollwöck, J. I. Cirac, and J. von Delft, Phys. Rev. B **80**, 165117 (2009).

Chapter 6

Stroboscopic observation of quantum many-body dynamics

In the study presented in this chapter we apply tDMRG to a system of ultracold atoms. Such gases of ultracold atoms can be loaded in optical lattices [117] and serve as an excellent playground for low-dimensional quantum many-body physics [118, 119] since virtually every parameter of these systems can be controlled experimentally. Interactions play a particularly important role in one dimensional systems and can be controlled experimentally via Feshback resonances [120]. The experimental access to such strongly interacting one dimensional systems provided the ideal field of application for tDMRG and added to the big success of tDMRG. Here we discuss the effects of repeated (stroboscopic) observations of a many-particle system. We find a variant of the quantum Zeno effect [121–124] leading to inhibited or accelerated break-up of certain many-body configurations. The lifetime of such clusters depends in a non-monotonous fashion of the time interval between the observations.

arXiv:1102.1605v1 [cond-mat.quant-gas] 8 Feb 2011

Stroboscopic observation of quantum many-body dynamics

Stefan Keßler,[1] Andreas Holzner,[2] Ian P. McCulloch,[3] Jan von Delft,[2] and Florian Marquardt[1,4]
[1]*Institute for Theoretical Physics, Universität Erlangen-Nürnberg, Staudtstr. 7, 91058 Erlangen, Germany*
[2]*Physics Department, Arnold Sommerfeld Center for Theoretical Physics, and Center for NanoScience, Ludwig-Maximilians-Universität München, D-80333 München, Germany*
[3]*School of Physical Sciences, The University of Queensland, Brisbane, QLD 4072, Australia*
[4]*Max Planck Institute for the Science of Light, Günter-Scharowsky-Straße 1/Bau 24, 91058 Erlangen, Germany*

Recent experiments have demonstrated single-site resolved observation of cold atoms in optical lattices. Thus, in the future it may be possible to take repeated snapshots of an interacting quantum many-body system during the course of its evolution. Here we address the impact of the resulting Quantum (anti-)Zeno physics on the many-body dynamics. We use time-dependent DMRG to obtain the time evolution of the full many-body wave function that is then periodically projected in order to simulate realizations of stroboscopic measurements. For the example of a 1-D lattice of spin-polarized fermions with nearest-neighbor interactions, we find regimes for which many-particle configurations are stabilized and destabilized depending on the interaction strength and the time between observations.

Introduction.— In the last years ultracold atoms in optical lattices have proven to be a versatile tool to study various quantum many-body phenomena [1, 2]. Recently, tremendous progress has been achieved by implementing single-site resolved detection [3, 4] and addressing [5] of atoms. This opens the path for investigating the evolution of non-equilibrium quantum many-body states by taking snapshots revealing the position of each single atom. For simpler systems, the effect of frequent observations on the decay of an unstable state (or the dynamics of a coherently driven transition) has already been discussed and observed, leading to the notion of the Quantum (anti-)Zeno effect [6–9]. Zeno physics has also been seen in cold-atom experiments with atomic loss channels [10] and was theoretically addressed in [11–13]. Experiments with single-site detection, however, would allow to explore the effect of observations on the dynamics of a truly interacting quantum many-body system. Here we exploit a numerically efficient approach to simulate the repeated observation of many-particle configurations in interacting lattice models. This represents an idealized version of the dynamics that may be realized in future experiments. We illustrate the main features of this "stroboscopic" many-body dynamics in the case of a 1-D lattice of spin-polarized fermions with nearest-neighbor interactions. We find a variant of the Quantum Zeno Effect and discuss its tendency to inhibit or accelerate the break-up of certain many-particle configurations. Interestingly, the lifetime of such particle clusters depends in a non-monotonous fashion on the time interval between observations. These features may be seen, for example, in the expansion dynamics of interacting atomic clouds in a lattice.

Technique.— Ideally, each observation is a projective measurement in the basis of many-particle configurations (occupation number states in real space). However, due to the exponentially large number of states, we need a numerically efficient way to sample such outcomes. We start by drawing the position of the first particle from a random distribution given by the one-particle density. Afterwards, we draw the position of the second particle, *conditioned* on the location of the first one, and proceed iteratively. In doing so, we build on the fact that the n-particle density ρ_n factorizes into conditional probabilities,

$$\rho_n(s_1,\ldots,s_n) = \rho_1(s_1)\cdot\prod_{i=2}^{n}\rho_i(s_i|s_{i-1},\ldots,s_1), \qquad (1)$$

where s_i denotes the position of the ith particle and $\rho_i(s_i|s_{i-1},\ldots,s_1)$ is the conditional probability of finding the ith particle at site s_i given that there are $i-1$ particles at the sites $s_1,\ldots,s_{i-1}$. Using this approach, only $n\cdot N_s$ values of joint probability densities have to be calculated, in comparison to the full number $\binom{N_s}{n}$ of possible many-body configurations. This approach relies on being able to calculate efficiently both the pure time evolution between observations and the i-particle densities ($1\le i\le n$). For the present work, we use the time-dependent DMRG [14–17], which is an extremely powerful method for interacting 1-D systems. For the fermionic model considered below, it is numerically even more efficient to draw the position of the first particle as before and then project the state onto those configurations where a particle is present at the selected site. After rescaling the resulting state, the new one-particle density is calculated. From this distribution we draw the position of the second fermion, excluding all sites already occupied by a fermion, and iterate the steps for the remaining fermions.

Model.— In this paper, we study spin-polarized fermions in a 1-D lattice governed by the Hamiltonian

$$\hat{\mathcal{H}} = -J\sum_i\left(\hat{c}_i^\dagger\hat{c}_{i+1}+h.c.\right)+V\sum_i\hat{n}_i\hat{n}_{i+1}\,. \qquad (2)$$

Here, $\hat{c}_i(\hat{c}_i^\dagger)$ denote fermionic destruction (creation) operators on lattice site i, and $\hat{n}_i$ is the particle number. The

first term describes hopping with amplitude J between neighboring sites, the second encodes the interaction between fermions at neighboring sites. The Hamiltonian displays a dynamical $V \mapsto -V$ symmetry which shows up in expansion experiments [18]. Following analogous steps as in [18], we can conclude: If both the initial state and the experimentally measured quantity $\hat{\mathcal{O}}$ are invariant under both time reversal and π–boost, the observed time evolution $\langle \hat{\mathcal{O}}(t) \rangle$ is identical for repulsive and attractive interaction of the same strength. Here, a π–boost refers to a translation of all momenta by π. The initial occupation number states and the n-particle density observables in our case fall within the scope of this theorem. Thus, the only relevant dimensionless parameters in our scenario are $|\frac{V}{J}|$ and the rescaled time between observations, $J\Delta t$.

Single particle.—We first briefly turn to the single-particle case, with $V = 0$ in Eq. (2). This leads to a tight-binding band $E(k) = -2J\cos(k)$. A particle located initially at a single site is in a superposition of all plane wave momenta $k = -\pi \ldots \pi$. After a time t, the probability of detecting it at a distance l from the initial site is $\rho(l,t) = \mathcal{J}^2_{|l|}(2Jt)$, where $\mathcal{J}$ is the Bessel function of the first kind. This is shown in Fig. 1(a). The particle moves ballistically, with $\langle l^2 \rangle = 2(Jt)^2$. When the particle is observed stroboscopically, at intervals Δt, the ballistic motion turns into diffusion. In this case, after m time steps of duration $\Delta t = t/m$, we have $\langle l^2 \rangle = 2J^2 t\, \Delta t$. Thus the motion slows down, and in the limit of an infinite observation rate ($\Delta t \to 0$), the particle is frozen, which is known as the Quantum Zeno effect.

Dynamics of non-interaction fermions.— After each observation, the many-particle wave function is a Slater determinant of single particle wave functions, and for non-interacting fermions this remains true even during the subsequent evolution. Using Wick's theorem, the n-particle density of these N fermions can be written as (see also [19]):

$$\rho_n(s_1, \ldots, s_n; t) = \frac{(N-n)!}{N!} \begin{vmatrix} M_{s_1 s_1} & \ldots & M_{s_1 s_n} \\ \ldots & & \ldots \\ M_{s_r s_n} & \ldots & M_{s_n s_n} \end{vmatrix}. \quad (3)$$

Here, $M_{s_k s_l} = \sum_{j=1}^{N} T_{s_k m_j}(t) T^*_{s_l m_j}(t)$, where $T_{kl}(t) = i^{(k-l)} \mathcal{J}_{k-l}(2Jt)$ is the propagator for one fermion, and the sum is taken over all sites m_j that were occupied at the initial time. The normalization is chosen such that $\sum_{s_1,\ldots,s_n} \rho_n(s_1, \ldots, s_n; t) = 1$. Note that the one-particle density ρ_1 is just the sum of the individual densities (Fig. 1b). Motion in arbitrary potentials would be captured by different propagators T_{kl}.

Numerical details.— For the interacting case to be discussed now, we use a tDMRG simulation, with time steps of $J\delta t = 0.1$, a lattice of typically 115 sites, and keeping up to approximately 1000 states, at a truncation error of 10^{-6}. The n-particle densities are evaluated by calculating expectation values of the tDMRG wave functions. For the non-interacting case we checked the tDMRG density against the exact formula (3) for times $Jt \leq 20$. Note that tDMRG has been employed for dissipative dynamics of cold atoms recently [20].

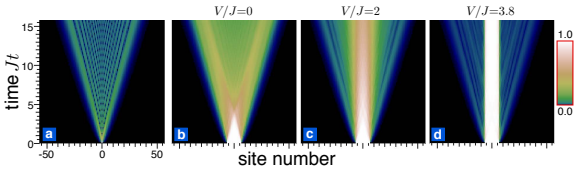

Fig. 1. Time evolution of the density profile of fermions expanding in a lattice without observation. (a) Single fermion for comparison. (b-d) Expansion of 13 fermions initially located at adjacent lattice sites for increasing interaction strength.

Stroboscopic many-body dynamics.— We will focus on an experimentally interesting scenario, namely the expansion of an interacting cloud from an initially confined state. Such an expansion in 2D was observed in an experiment with 2-species fermions in [18]. We will first briefly address the evaporation itself and then discuss qualitatively the resulting stroboscopic dynamics, with a more refined analysis presented further below. Fig. 1(b-d) shows the effect of the interaction on the free (unmeasured) time evolution of the density profile. For increasing interaction the fermions tend to remain localized near their initial positions. For large interaction strengths $|V/J| \gtrsim 3$ and the times shown here, $tJ < 16$, a more detailed analysis reveals that evaporation proceeds via the rare event of a single fermion dissociating from the cluster. This particle then moves away ballistically. The evaporation of particles off the edge of the confined cloud is hindered by the formation of bound states. This is a crucial phenomenon we will also encounter in the context of repeated measurements. For smaller interaction strengths ($|V/J| \lesssim 2$), the fermions split gradually into a larger and larger number of clusters as time increases. The parameter regimes in which the model described by Eq. (2) exhibits diffusive or ballistic transport was addressed using tDMRG in [21]. The effects of stroboscopic observation are shown in Fig. 2, for typical realizations of this stochastic process. For non-interacting fermions we find the behavior expected from the single particle case. The spread (and thus, the diffusion constant) increases with larger observation time intervals Δt. For very small $J\Delta t$ (strong Zeno effect), the motion is diffusive with a small diffusion constant that becomes independent of $|V/J|$. In general, it is useful to discuss the "lifetime" of the initial inner cluster that evaporates via expansion. For the interacting case, the lifetime is shortest at some intermediate observation time interval Δt, while it is enhanced again for large Δt. Apparently, at very large $|V/J|$, the lifetime may have yet another local

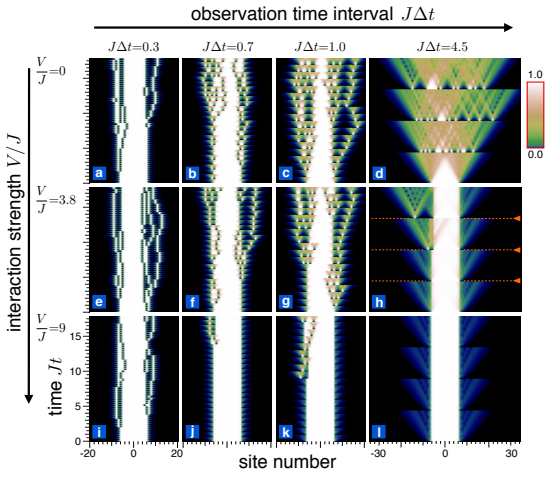

Fig. 2. Density plot of specific realizations for the expansion of 13 fermions with site-resolved detection during the evolution. We show the full evolution of density even between observations, which collapse the many-body wavefunction at regular time intervals $J\Delta t$ (as indicated by the dashed lines in panel h). Without interaction (a-d) the lifetime of the initial configuration decreases for larger $J\Delta t$, while for large interaction the lifetime is shortest for intermediate observation times $J\Delta t$ (h,l). For small $J\Delta t$ the dynamics becomes independent of $|V/J|$, see (a,e,i).

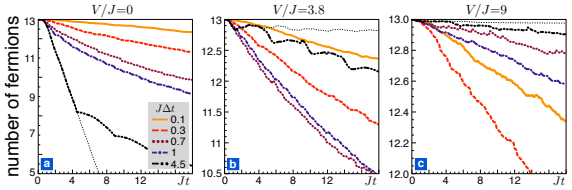

Fig. 3. For the parameters of Fig. 2, each panel shows the average number of fermions remaining at the 15 central lattice sites as a function of evolution time t for different values of $J\Delta t$. The thin dotted line corresponds to an evolution without observation. (a) Without interactions, the lifetime decreases monotonically with increasing $J\Delta t$. (b) At $V/J = 3.8$, the lifetime increases again for large $J\Delta t$. (c) At large interactions, $V/J = 9$, the lifetime is non-monotonous even for intermediate $J\Delta t$; compare $J\Delta t = 0.3, 0.7, 1.0$. Note that the lifetimes in (a-c) are almost identical for $J\Delta t = 0.1$.

maximum for intermediate Δt, see Fig. 2(j). We confirm this striking non-monotonous behavior of the lifetime by simulating 400 realizations for each panel shown in Fig. 2 and plot the average number of fermions at the central 15 lattice sites as a function of time, in Fig. 3. For sufficiently large $J\Delta t$ and $|V/J|$, this number decays roughly linearly at a rate that sets the inverse lifetime.

We will now see that the features observed here can be mainly attributed to two ingredients: a bound state and the two-level dynamics between the initial state and the state with a fermion detached from the others.

Doublets and the role of interactions.— The effect of interactions can be discussed already for the stroboscopic dynamics of two fermions. We focus on the decay of a doublet, i.e. two fermions sitting at neighboring sites.

In the quantum Zeno limit, $J\Delta t \ll 1$ (or $J\Delta t \ll |2J/V|$ for large $|V|$, see below) only single hopping events occur during Δt. The probability for a fermion hopping left or right during Δt is $2(J\Delta t)^2$. This leads to a rate equation for the probabilities p_l to find the two fermions l sites away from each other:

$$\frac{d}{dt}\,p_l = 2J^2\Delta t\,[p_{l+1} - p_l + (1-\delta_{l,1})(p_{l-1} - p_l)]\,. \quad (4)$$

In this limit, the average decay time for a doublet is $\langle Jt\rangle = 1/2J\Delta t$, independent of V, compare with Fig. 2 (a,e,i).

For larger $J\Delta t$, the interaction will become important. It gives rise to a bound state when the particles come close to each other (this effect also exists for clusters of more particles [22]). It is convenient to separate the dynamics of the 2-particle states into relative and center-of-mass (c.o.m.) motion. Considering the basis $|l, K\rangle = \frac{1}{\sqrt{N}}\sum_j \exp\{iK[j+l/2]\}c_j^\dagger c_{j+l}^\dagger|vac\rangle$ of the 2-particle sector with relative coordinate l, center of mass coordinate $j+l/2$, and total wavenumber $K = k_1 + k_2$, the action of the Hamiltonian (2) is $\mathcal{H}|l, K\rangle = |K\rangle \otimes \mathcal{H}_K|l\rangle$. The first part describes a plane wave with c.o.m. wavenumber K, the second the relative motion, which is described by an effective Hamiltonian

$$\mathcal{H}_K|l\rangle = -2J_K\big[|l+1\rangle + (1-\delta_{l,1})|l-1\rangle\big] + V\delta_{l,1}|l\rangle, \quad (5)$$

with a hopping amplitude $J_K = J\cos(K/2)$ depending on K. We now discuss the decay of a doublet (see Fig. 4(a)) with the help of the doublet survival probability $P_D(t) = \sum_{L'}|\langle l = 1, L'|e^{-iHt}|l = 1, L\rangle|^2$, where L and L' are c.o.m coordinates. A bound state exists if $|V| \geq |2J_K|$. It is given by $|\psi_K\rangle \propto \sum_{l=1}^{\infty}(-J_K/V)^{l-1}|l\rangle$. In the absence of observations the doublet survival probability is for $t \to \infty$ given by $P_D(\infty) = \frac{1}{2\pi}\int_{-\pi}^{\pi} dK\,|\langle\psi_K|l = 1\rangle|^4$. Specifically, in the more interesting case of large $|V/2J| \geq 1$, we have

$$P_D(\infty) = 1 - (2J/V)^2 + \frac{3}{8}(2J/V)^4\,. \quad (6)$$

While $P_D(\infty)$ is determined by the bound state, the evolution for times $Jt < 1$ is mostly determined by the two-level dynamics connecting $|l = 1\rangle$ and $|l = 2\rangle$. In this short-time limit, we find

$$P_D(t) = 1 - \frac{1}{\pi}\int_0^{\pi} dK\,\frac{\cos^2(K/2)}{\xi_K^2}\sin^2(2J\xi_K t), \quad (7)$$

with $\xi_K = \sqrt{(\frac{V}{4J})^2 + \cos^2(K/2)}$ (note the integral over K). In the strongly interacting regime we find three

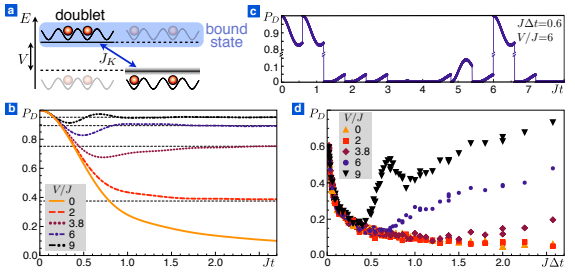

Fig. 4. (a) Doublet decay level scheme. The doublet is separated from the continuum of unbound states by an energy gap V. (b) Probability P_D of finding the doublet intact after an evolution time Jt. Dashed black lines correspond to $P_D(\infty)$ found in Eq. 6. (c) Single trajectory of P_D for a time evolution subject to observations, with $J\Delta t = 0.6$ and $V/J = 6$. (d) Doublet survival probability P_D as function of the observation time interval $J\Delta t \geq 0.02$ for a fixed total evolution time $Jt = 18$. Note the non-monotonous dependence on $J\Delta t$ for finite interactions.

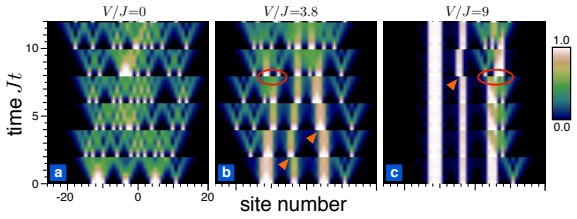

Fig. 5. Density plot for the time evolution of an initial state with clusters of different numbers of fermions and observations with time steps $J\Delta t = 2$. (b,c) For large interaction strength we find clusters moving as a whole (indicated by triangles). Also processes with single fermions being exchanged between clusters or attached to a new cluster are observed, indicated by loops.

regions for the doublet survival probability: for times $Jt \ll \xi_{K=0}^{-1}$ the probability is independent of the interaction strength, $P_D(t) = 1 - 2(Jt)^2$, for times $\xi_{K=0}^{-1} < Jt < 1$ one expects an oscillating behavior of $P_D(t)$ given by Eq. (7) with a period approximately $\frac{2\pi}{V}$ for $|V/4J| \gg 1$, and for $Jt \gg 1$ the probability approaches $P_D(\infty)$.

The full evolution of $P_D(t)$ using exact diagonalization is shown in Fig. 4. Without observations (Fig. 4(b)), $P_D(t)$ is interaction-independent at small times $Jt \lesssim 0.2$. Temporal oscillations in P_D develop for higher interaction strengths ($V/J \gtrsim 3.5$). The non-monotonic behavior at small times suggests that a change of the observation time interval in the stroboscopic dynamics may have a drastic effect on the survival probability. This effect is confirmed in Fig. 4(d). In that figure, the observation time interval $J\Delta t$ is varied, while keeping the total evolution time constant, $Jt = 18$ (with a corresponding number of observations $t/\Delta t$). The stroboscopic evolution is interaction-independent up to times $J\Delta t = \frac{\pi}{V/J}$. For larger $J\Delta t$ there is a drastic recovery of P_D, which can show oscillations as a function of Δt. The qualitative behavior matches well the expectations from Fig. 4(b) and does not depend in detail on the total time t. Thus we have explained the most prominent features of the stroboscopic many-body dynamics, shown in Fig. 2 and Fig. 3, through our the discussion of the doublet.

Other features that can be observed in the stroboscopic dynamics are the motion of whole clusters of fermions through the lattice and the exchange of fermions between clusters, as shown in Fig. 5. As expected, clusters are very stable for high interaction strengths. The hopping amplitude for a cluster of n fermions is of order $J^n/|V|^{n-1}$, decreasing strongly for larger clusters, as can be perceived in Fig. 5(c).

Experimental realization and outlook.— Our choice of Hamiltonian was primarily dictated by simplicity, as a one-species fermionic model in 1D. This Hamiltonian is related to the Heisenberg XXZ model by Wigner-Jordan transformation. The stroboscopic dynamics is identical for both models as the outcome of observations depends only on spatial density-density correlations. These Hamiltonians can be experimentally realized in optical lattices with fermionic polar molecules [23] or 2-species fermions in the insulating phase [24]. For both realizations single-site detection has not yet been implemented, but ideas exists and experimental progress is being made towards this goal. The generic features discussed in this paper should be found as well in other model, e.g. the Bose-Hubbard model (where a double occupancy would correspond to the doublet state). Experimentally, the most challenging step needed to observe the interplay of many-body dynamics and measurements discussed here would be to make the observations non-destructive, whereas currently atoms are heated into higher site orbitals. Beyond the scenarios discussed here, one may also be interested in the influence of external driving or measurements that are either weak or target only specific sites.

Acknowledgments.— Financial support by the DFG through NIM, SFB/TR 12, and the Emmy-Noether program is gratefully acknowledged.

[1] I. Bloch, J. Dalibard, and W. Zwerger, Rev. Mod. Phys. **80**, 885 (2008).
[2] M. Lewenstein *et al.*, Adv. Phys. **56**, 243 (2007).
[3] W. S. Bakr *et al.*, Nature Physics **462**, 74 (2009).
[4] J. F. Sherson *et al.*, Nature **467**, 68 (2010).
[5] C. Weitenberg *et al.*, arXiv:1101.2076v1.
[6] B. Misra and E. C. G. Sudarshan, J. Math. Phys. (N.Y.) **18**, 756 (1977).
[7] W. M. Itano *et al.*, Phys. Rev. A **41**, 2295 (1990).
[8] M. C. Fischer, B. Gutiérrez-Medina, and M. G. Raizen, Phys. Rev. Lett. **87**, 040402 (2001).

[9] P. Facchi and S. Pascazio, J. Phys. A: Math. Theor. **41**, 493001 (2008), and references therein.
[10] N. Syassen *et al.*, Science **320**, 1329 (2008).
[11] J. J. García-Ripoll *et al.*, New J. Phys. **11**, 013053 (2009).
[12] A. J. Daley *et al.*, Phys. Rev. Lett. **102**, 040402 (2009).
[13] R. Schützhold and G. Gnanapragasam, Phys. Rev. A **82**, 022120 (2010).
[14] G. Vidal, Phys. Rev. Lett. **93**, 040502 (2004).
[15] A. J. Daley *et al.*, J. Stat. Mech. (2004) P04005.
[16] S. R. White and A. E. Feiguin, Phys. Rev. Lett. **93**, 076401 (2004).
[17] P. Schmitteckert, Phys. Rev. B **70**, 121302(R) (2004).
[18] U. Schneider *et al.*, arXiv:1005.3545v1.
[19] G. Rickayzen, *Green's Functions and Condensed Matter* (Academic Press, New York, 1980).
[20] H. Pichler, A. J. Daley, and P. Zoller, Phys. Rev. A **82**, 063605 (2010).
[21] S. Langer *et al.*, Phys. Rev. B **79**, 214409 (2009).
[22] B. Sutherland, *Beautiful Models* (World Scientific, 2004).
[23] H. P. Büchler, A. Micheli, and P. Zoller, Nature Physics **3**, 726 (2007).
[24] L.-M. Duan, E. Demler, and M. D. Lukin, Phys. Rev. Lett. **91**, 090402 (2003).

Appendix A

Numerical details

A.1 Derivation of the orthonormality condition

The orthonormality condition Eq. (2.10) is easily derived by induction. The starting point is condition Eq. (2.9) and we limit to the derivation for the left basis. The derivation for the right basis is analogous.

The induction argument can be initialized with site $k = 1$ because its effective left basis is already orthonormal as it consists only of the vacuum state. Now, consider the case that site k has an orthonormal effective left basis and construct the condition for site $k+1$ to have an orthonormal effective left basis:

$$\begin{aligned}
\langle l'_{k+1}|l_{k+1}\rangle &= \left(\sum_{l'_k\sigma'_k}\langle l'_k|\langle\sigma'_k|A^{[\sigma'_k]}_{l'_k l'_{k+1}}{}^*\right)\left(\sum_{l_k\sigma_k} A^{[\sigma_k]}_{l_k l_{k+1}}|l_k\rangle|\sigma_k\rangle\right) \\
&= \sum_{l'_k l_k \sigma'_k \sigma_k} A^{[\sigma'_k]}_{l'_k l'_{k+1}}{}^* A^{[\sigma_k]}_{l_k l_{k+1}} \underbrace{\langle l'_k|l_k\rangle}_{\delta_{l'_k l_k}} \underbrace{\langle\sigma'_k|\sigma_k\rangle}_{\delta_{\sigma'_k\sigma_k}} = \sum_{l_k\sigma_k} A^{[\sigma_k]}_{l_k l'_{k+1}}{}^* A^{[\sigma_k]}_{l_k l_{k+1}} \\
&= \left(\sum_{\sigma_k} A^{[\sigma_k]\dagger} A^{[\sigma_k]}\right)_{l'_{k+1} l_{k+1}} .
\end{aligned} \tag{A.1}$$

Condition Eq. (2.10) follows with $\langle l'_{k+1}|l_{k+1}\rangle \stackrel{!}{=} \delta_{l'_{k+1}l_{k+1}}$.

A.2 Singular value decomposition

The singular value decomposition can be seen as a generalization of the spectral theorem, i.e. of the eigenvalue decomposition. It is valid for any real or complex $m \times n$ rectangular matrix. Let M be such a matrix, then it can be written in a singular value decomposition

$$M = USV^\dagger , \tag{A.2}$$

where U is a $m \times m$ unitary matrix, S a $m \times n$ matrix with real, nonnegative entries on the diagonal and zeros off the diagonal, and V a $n \times n$ unitary matrix. The numbers on the diagonal of S are called *singular values*, and there are $p = \min(n, m)$ of them. The singular values are unique, but U and V are not, in general. It is convenient to truncate and reorder these matrices in such a fashion that their dimension are $m \times p$ for U, $p \times p$ for S (with the singular values ordered in a non-increasing fashion) and $n \times p$ for V (i.e. $p \times n$ for $V^\dagger$). A consequence of this truncation is that U or V is no longer quadratic and unitarity is not defined for such matrices. This property is replaced by *column unitarity* (orthonormal columns) of U and *row unitarity* (orthonormal rows) for $V^\dagger$ - no matter which one is no longer quadratic. In this article all singular value decompositions are understood to be ordered in this fashion.

In cases where the actual singular values are of no interest, e. g. during the orthonormalization of an MPS without any truncation a thin QR decomposition [125] can be used instead of a SVD.

A.3 Numerical costs of index contractions

The numerical costs of matrix multiplications and index contractions of multi-index objects depend on the dimension of both the resulting object and of the contracted indices. In the case of matrix multiplications this is quite simple. Consider a $n \times m$ matrix M_1 multiplied by a $m \times p$ matrix M_2. The result is a $n \times p$ matrix M:

$$M_{ij} = \sum_{k=1}^{m} (M_1)_{ik} (M_2)_{kj} \ . \tag{A.3}$$

Evidently, each of the $n * p$ matrix elements M_{ij} requires a sum over m products of the form $(M_1)_{ik} (M_2)_{kj}$. Thus the process for calculating $M_1 M_2$ is of order $\mathcal{O}(nmp)$.

The numerical costs of multi-index objects are obtained analogously. Consider two multi-index objects, M_1 with indices $i_1, \ldots, i_n$ and dimensions $p_1 \times \cdots \times p_n$ and M_2 with indices $j_1, \ldots, j_m$ and dimensions $q_1 \times \cdots \times q_m$. If we contract the indices i_1 and i_2 of M_1 with the indices j_1 and j_2 of M_2 (assuming that $p_1 = q_1$ and $p_2 = q_2$), we obtain the multi-index object M:

$$M_{i_3 \ldots i_n j_3 \ldots j_m} = \sum_{k=1}^{p_1} \sum_{l=1}^{p_2} (M_1)_{kli_3 \ldots i_n} (M_2)_{klj_3 \ldots j_m} \ . \tag{A.4}$$

Thus for every entry of M, p_1 times p_2 multiplications have to be done, so that the process is of order $\mathcal{O}((p_3 \ldots p_n)(p_1 p_2)(q_3 \ldots q_m))$.

A.4 tCheMPS details

While the principles of the tCheMPS method are outlined in Cha. 4, here, we provide explicit expressions for the evaluation of time-dependent expectation values and error mea-

sures using a MPS-based implementation. Starting with the initial state $|\psi_0\rangle$ the time evolution of $|\psi_0\rangle$ is given by

$$|\psi(t)\rangle = U_N(t)|\psi_0\rangle = \pi(t)\sum_{n=0}^{N-1}\tilde{c}_n(t)|t_n\rangle \tag{A.5}$$

with $|t_n\rangle = T_n(H')|\psi_0\rangle$ and the convenience notations $\pi(t) = e^{-i(E_0+aW*)t}$ and $\tilde{c}_n(t) = (2-\delta_{n0})\,c_n(t)$, where with $U_n(t)$ and $c_n(t)$ are given by Eq. (4.1). The numerical focus lies on the calculation of the expansion vectors $|t_n\rangle$ while the coefficients $\tilde{c}_n(t)$ can be obtained using standard libraries for mathematical functions. In the following we provide explicit formulas in terms of $|t_n\rangle$ and $\tilde{c}_n(t)$ that can be evaluated directly.

Expecation values

A time-dependent expectation value is then given by

$$\langle O(t)\rangle = \langle\psi(t)|O|\psi(t)\rangle = \sum_{n=0}^{N-1}\sum_{m=0}^{N-1}\tilde{c}_n^*(t)\tilde{c}_m(t)\langle t_n|O|t_m\rangle\,. \tag{A.6}$$

This requires the calculation of $\mathcal{O}(N^2)$ expectation values of the type $\langle t_n|O|t_m\rangle$, of which a single evaluation is typically very cheap numerically, however, even for moderate N the numerical effort for total calculation can easily match the effort for calculating the vectors $|t_n\rangle$. Fortunately, the expression $\langle t_n|O|t_m\rangle$ does not depend on the time t and needs to be calculated only once for all times.

Norm

Theoretically, the norm of $|\psi(t)\rangle$ should stay constant, however, in the reality it does not and its deviation gives a estimate for the error during the time evolution.

$$\||\psi(t)\rangle\|^2 = \sum_{n=0}^{N-1}|\tilde{c}_n(t)|^2\,\||t_n\rangle\|^2 + 2\sum_{n<m}\Re\left(\tilde{c}_n^*\tilde{c}_m\langle t_n|t_m\rangle\right)\,. \tag{A.7}$$

The computational complexity is again $\mathcal{O}(N^2)$.

Scalar product

The scalar product of $|\psi(t)\rangle$ with an arbitrary state $|\varphi\rangle$ is straight-forward to calculate using the following $\mathcal{O}(N)$ expression

$$\langle\varphi|\psi(t)\rangle = \pi(t)\sum_{n=0}^{N-1}c_n(t)\langle\varphi|t_n\rangle\,. \tag{A.8}$$

Difference

The norm of the difference of the two states $|\psi(t)\rangle$ and $|\varphi\rangle$ as in Eq. (4.10) is given by a $\mathcal{O}(N^2)$ expression, making use of Eqs. (A.7) and (A.8),

$$\| |\psi(t)\rangle - |\varphi\rangle \| = \sqrt{\| |\varphi\rangle \|^2 + \| |\psi(t)\rangle \|^2 - 2\Re\langle\psi(t)|\varphi\rangle} \,. \tag{A.9}$$

For a comparison between tCheMPS and tDMRG the difference between $|\psi(t)\rangle$ and, say, M states $|\varphi(t)\rangle$ given by tDMRG only $\mathcal{O}(MN + N^2)$ MPS operations are necessary as the quadratic contribution in N stems only from the squared norm $\| |\psi(t)\rangle \|^2$.

List of Figures

Bibliography

[1] M. Troyer and U.-J. Wiese, Phys. Rev. Lett. **94**, 170201 (2005).

[2] K. G. Wilson, Rev. Mod. Phys. **47**, 773 (1975).

[3] S. R. White and R. M. Noack, Phys. Rev. Lett. **68**, 3487 (1992).

[4] S. R. White, Phys. Rev. Lett. **69**, 2863 (1992).

[5] S. R. White, Phys. Rev. B **48**, 10345 (1993).

[6] K. A. Hallberg, Phys. Rev. B **52**, 9827(R) (1995).

[7] T. D. Kühner and S. R. White, Phys. Rev. B **60**, 335 (1999).

[8] E. Jeckelmann, Phys. Rev. B **66**, 045114 (2002).

[9] G. Vidal, Phys. Rev. Lett. **93**, 040502 (2004).

[10] S. R. White and A. E. Feiguin, Phys. Rev. Lett. **93**, 076401 (2004).

[11] A. J. Daley, C. Kollath, U. Schollwöck and G. Vidal, J. Stat. Mech. **2004**, P04005 (2004).

[12] J. J. García-Ripoll, New J. Phys. **8**, 305 (2006).

[13] P. Schmitteckert, Phys. Rev. B **70**, 121302 (2004).

[14] F. Verstraete, J. J. Garcia-Ripoll and J. I. Cirac, Phys. Rev. Lett. **93**, 207204 (2004).

[15] A. E. Feiguin and S. R. White, Phys. Rev. B **72**, 220401 (2005).

[16] L. Amico, R. Fazio, A. Osterloh and V. Vedral, Rev. Mod. Phys. **80**, 517 (2008).

[17] S. Östlund and S. Rommer, Phys. Rev. Lett. **75**, 3537 (1995).

[18] J. Dukelsky, M. A. Martín-Delgado, T. Nishino and G. Sierra, Europhys. Lett. **43**, 457 (1998).

[19] I. Affleck, T. Kennedy, E. H. Lieb and H. Tasaki, Phys. Rev. Lett. **59**, 799 (1987).

[20] M. Fannes, B. Nachtergaele and R. F. Werner, Europhys. Lett. **10**, 633 (1989).

[21] A. Weichselbaum, F. Verstraete, U. Schollwöck, J. I. Cirac and J. von Delft, Phys. Rev. B **80**, 165117 (2009).

[22] L. P. Kouwenhoven and C. M. Marcus, Physics World **11**, 35 (1998).

[23] M. Greiner, O. Mandel, T. Esslinger, T. W. Hänsch and I. Bloch, Nature **415**, 39 (2002).

[24] W. G. van der Wiel, S. De Franceschi, J. M. Elzerman, T. Fujisawa, S. Tarucha and L. P. Kouwenhoven, Rev. Mod. Phys. **75**, 1 (2002).

[25] W. J. de Haas, J. H. de Boer and G. J. van de Berg, Physica (Utrecht) **1**, 1115 (1934).

[26] J. Kondo, Prog. of Theo. Phys. **32**, 37 (1964).

[27] D. Goldhaber-Gordon, H. Shtrikman, D. Mahalu, D. Abusch-Magder, U. Meirav and M. A. Kastner, Nature **391**, 156 (1998).

[28] L. Kouwenhoven and L. Glazman, Physics World **14**, 33 (2001).

[29] M. H. Anderson, J. R. Ensher, M. R. Matthews, C. E. Wieman and E. A. Cornell, Science **269**, 198 (1995).

[30] K. B. Davis, M. O. Mewes, M. R. Andrews, N. J. van Druten, D. S. Durfee, D. M. Kurn and W. Ketterle, Phys. Rev. Lett. **75**, 3969 (1995).

[31] C. C. Bradley, C. A. Sackett, J. J. Tollett and R. G. Hulet, Phys. Rev. Lett. **75**, 1687 (1995).

[32] B. P. Lanyon, C. Hempel, D. Nigg, M. Müller, R. Gerritsma, F. Zähringer, P. Schindler, J. T. Barreiro, M. Rambach, G. Kirchmair, M. Hennrich, P. Zoller, R. Blatt and C. F. Roos, Science **334**, 57 (2011).

[33] R. Feynman, International Journal of Theoretical Physics **21**, 467 (1982).

[34] L. Borda, Phys. Rev. B **75**, 041307(R) (2007).

[35] U. Schollwöck, Rev. Mod. Phys. **77**, 259 (2005).

[36] U. Schollwöck, Ann. Phys. **326**, 96 (2010).

[37] A. Klümper, A. Schadschneider and J. Zittartz, J. Phys. A **24**, L955 (1991).

[38] M. Fannes, B. Nachtergaele and R. F.Werner, Comm. Math. Phys. **144n**, 443 (1992).

[39] A. Klümper, A. Schadschneider and J. Zittartz, Z. Phys. B **87**, 281 (1992).

[40] B. Derrida, M. R. Evans, V. Hakim and V. Pasquier, J. Phys. A **26**, 1493 (1993).

[41] F. Verstraete, D. Porras and J. I. Cirac, Phys. Rev. Lett. **93**, 227205 (2004).

[42] S. Rommer and S. Östlund, Phys. Rev. B **55**, 2164 (1997).

[43] M. A. Martín-Delgado and G. Sierra, Int. J. Mod. Phys. A **11**, 3145 (1996).

[44] H. Takasaki, T. Hikihara and T. Nishino, J. Phys. Soc. Jpn. **68**, 1537 (1999).

[45] I. P. McCulloch, J. Stat. Mech. **2007**, P10014 (2007).

[46] S. R. White, Phys. Rev. Lett. **102**, 190601 (2009).

[47] E. M. Stoudenmire and S. R. White, New J. Phys. **12**, 055026 (2010).

[48] P. Jordan and E. Wigner, Z. Phys. **47**, 631 (1928).

[49] F. Verstraete and J. I. Cirac, Phys. Rev. B **73**, 094423 (2006).

[50] M.-C. Chung and I. Peschel, Phys. Rev. B **64**, 064412 (2001).

[51] I. Peschel, J. Stat. Mech. **2004**, P12005 (2004).

[52] L. Tagliacozzo, T. R. de Oliveira, S. Iblisdir and J. I. Latorre, Phys. Rev. B **78**, 024410 (2008).

[53] N. Schuch, M. M. Wolf, F. Verstraete and J. I. Cirac, Phys. Rev. Lett. **100**, 030504 (2008).

[54] J. Eisert and T. J. Osborne, Phys. Rev. Lett. **97**, 150404 (2006).

[55] J. I. Latorre and V. Picó, J. Phys. A **42**, 265302 (2008).

[56] J. Eisert, M. Cramer and M. B. Plenio, Rev. Mod. Phys. **82**, 277 (2010).

[57] M. Srednicki, Phys. Rev. Lett. **71**, 666 (1993).

[58] D. Gioev and I. Klich, Phys. Rev. Lett. **96**, 100503 (2006).

[59] C. Callan and F. Wilczek, Phys. Lett. B **333**, 55 (1994).

[60] M. B. Plenio, J. Eisert, J. Dreißig and M. Cramer, Phys. Rev. Lett. **94**, 060503 (2005).

[61] M. B. Hastings, J. Stat. Mech. **2007**, P08024 (2007).

[62] G. Vidal, J. I. Latorre, E. Rico and A. Kitaev, Phys. Rev. Lett. **90**, 227902 (2003).

[63] V. E. Korepin, Phys. Rev. Lett. **92**, 096402 (2004).

[64] M. Cramer, J. Eisert, M. B. Plenio and J. Dreißig, Phys. Rev. A **73**, 012309 (2006).

[65] P. Calabrese and J. Cardy, J. Stat. Mech. **2005**, P04010 (2005).

[66] S. Bravyi, M. B. Hastings and F. Verstraete, Phys. Rev. Lett. **97**, 050401 (2006).

[67] S. Liang and H. Pang, Phys. Rev. B **49**, 9214 (1994).

[68] S. R. White, Phys. Rev. Lett. **77**, 3633 (1996).

[69] T. Barthel, M.-C. Chung and U. Schollwöck, Phys. Rev. A **74**, 022329 (2006).

[70] H. Niggemann, A. Klümper and J. Zittartz, Z. Phys. B **104**, 103 (1997).

[71] T. Nishino, K. Okunishi, Y. Hieida, N. Maeshima and Y. Akutsu, Nucl. Phys. B **575**, 504 (2000).

[72] M. A. Martín-Delgado, M. Roncaglia and G. Sierra, Phys. Rev. B **64**, 075117 (2001).

[73] N. Schuch, M. M. Wolf, F. Verstraete and J. I. Cirac, Phys. Rev. Lett. **100**, 040501 (2008).

[74] G. Vidal, Phys. Rev. Lett. **99**, 220405 (2007).

[75] F. Verstraete and J. I. Cirac, *Renormalization algorithms for Quantum-Many Body Systems in two and higher dimensions* (2004).

[76] S. R. White, Phys. Rev. B **72**, 180403 (2005).

[77] M. Zwolak and G. Vidal, Phys. Rev. Lett. **93**, 207205 (2004).

[78] G. M. Crosswhite and D. Bacon, Phys. Rev. A **78**, 012356 (2008).

[79] F. Fröwis, V. Nebendahl and W. Dür, Phys. Rev. A **81**, 062337 (2010).

[80] B. Pirvu, V. Murg, J. I. Cirac and F. Verstraete, New J. Phys. **12**, 025012 (2010).

[81] J. K. Cullum and R. A. Willoughby, *Lanczos Algorithms for Large Symmetric Eigenvalue Computations*, volume 1, Birkhauser, Boston (1985).

[82] W. E. Arnoldi, Quarterly Appl. Math. **9**, 17 (1951).

[83] E. R. Davidson, Journal of Computational Physics **17**, 87 (1975).

[84] R. G. Pereira, S. R. White and I. Affleck, Phys. Rev. B **79**, 165113 (2009).

[85] S. R. White and I. Affleck, Phys. Rev. B **77**, 134437 (2008).

[86] P. Dargel, A. Honecker, R. Peters, R. M. Noack and T. Pruschke, Phys. Rev. B **83**, 161104(R) (2011).

[87] S. Ramasesha, S. K. Pati, H. Krishnamurthy, Z. Shuai and J. Brèdas, Synth. Met. **85**, 1019 (1997).

[88] A. Weiße, G. Wellein, A. Alvermann and H. Fehske, Rev. Mod. Phys. **78**, 275 (2006).

[89] Z. G. Soos and S. Ramasesha, J. Chem. Phys. **90**, 1067 (1989).

[90] Y. Saad and M. H. Schultz, SIAM J. Sci. and Stat. Comput. **7**, 856 (1986).

[91] H. A. van der Vorst, SIAM J. Sci. and Stat. Comput. **13**, 631 (1992).

[92] I. P. McCulloch and M. Gulácsi, Europhys. Lett. **57**, 852 (2002).

[93] A. Alex, M. Kalus, A. Huckleberry and J. von Delft, *A numerical algorithm for the explicit calculation of SU(N) and SL(N,C) Clebsch-Gordan coefficients* (2010).

[94] C. Moler and C. Van Loan, SIAM Rev. **45**, 3 (2003).

[95] M. A. Cazalilla and J. B. Marston, Phys. Rev. Lett. **88**, 256403 (2002).

[96] M. Suzuki, Phys. Lett. A **146**, 319 (1990).

[97] A. T. Sornborger and E. D. Stewart, Phys. Rev. A **60**, 1956 (1999).

[98] A. N. Krylov, Otdel. mat. i estest. nauk **4**, 491 (1931).

[99] M. Hochbruck and C. Lubich, SIAM Journal on Numerical Analysis **34**, 1911 (1997).

[100] D. Gobert, C. Kollath, U. Schollwöck and G. Schütz, Phys. Rev. E **71**, 036102 (2005).

[101] T. J. Osborne, Phys. Rev. Lett. **97**, 157202 (2006).

[102] M. C. Bañuls, M. B. Hastings, F. Verstraete and J. I. Cirac, Phys. Rev. Lett. **102**, 240603 (2009).

[103] S. Smerat, *priv. comm.* (2010).

[104] H. Tal-Ezer and R. Kosloff, J. Chem. Phys. **81**, 3967 (1984).

[105] C. Leforestier, R. H. Bisseling, C. Cerjan, M. D. Feit, R. Friesner, A. Guldberg, A. Hammerich, G. Jolicard, W. Karrlein and H. D. Meyer, Journal of Computational Physics **94**, 59 (1991).

[106] J. W. Daniel, W. B. Gragg, L. Kaufman and G. W. Stewart, Mathematics of Computation **30**, 772 (1976).

[107] J. E. Gubernatis, J. E. Hirsch and D. J. Scalapino, Phys. Rev. B **35**, 8478 (1987).

[108] V. Barzykin and I. Affleck, Phys. Rev. Lett. **76**, 4959 (1996).

[109] E. S. Sørensen and I. Affleck, Phys. Rev. B **53**, 9153 (1996).

[110] I. Affleck and P. Simon, Phys. Rev. Lett. **86**, 2854 (2001).

[111] E. S. Sørensen and I. Affleck, Phys. Rev. Lett. **94**, 086601 (2005).

[112] T. Hand, J. Kroha and H. Monien, Phys. Rev. Lett. **97**, 136604 (2006).

[113] S. Costamagna, C. J. Gazza, M. E. Torio and J. A. Riera, Phys. Rev. B **74**, 195103 (2006).

[114] I. Affleck, L. Borda and H. Saleur, Phys. Rev. B **77**, 180404(R) (2008).

[115] R. G. Pereira, N. Laflorencie, I. Affleck and B. I. Halperin, Phys. Rev. B **77**, 125327 (2008).

[116] R. Bulla, T. A. Costi and T. Pruschke, Rev. Mod. Phys. **80**, 395 (2008).

[117] M. Greiner, I. Bloch, O. Mandel, T. W. Hänsch and T. Esslinger, Phys. Rev. Lett. **87**, 160405 (2001).

[118] I. Bloch, J. Dalibard and W. Zwerger, Rev. Mod. Phys. **80**, 885 (2008).

[119] M. Lewenstein, A. Sanpera, V. Ahufinger, B. Damski, A. Sen and U. Sen, Adv. Phys. **56**, 243 (2007).

[120] P. Courteille, R. S. Freeland, D. J. Heinzen, F. A. van Abeelen and B. J. Verhaar, Phys. Rev. Lett. **81**, 69 (1998).

[121] B. Misra and E. C. G. Sudarshan, J. Math. Phys. **18**, 756 (1977).

[122] C. B. Chiu, E. C. G. Sudarshan and B. Misra, Phys. Rev. D **16**, 520 (1977).

[123] W. M. Itano, D. J. Heinzen, J. J. Bollinger and D. J. Wineland, Phys. Rev. A **41**, 2295 (1990).

[124] M. C. Fischer, B. Gutiérrez-Medina and M. G. Raizen, Phys. Rev. Lett. **87**, 040402 (2001).

[125] G. H. Golub and C. F. Van Loan, *Matrix Computations*, The Johns Hopkins University Press, 3rd edition (1996).

Acknowledgements

First and foremost I would like to thank my primary advisor Jan von Delft for all the encouragement and guidance for the research on this thesis and for giving me the opportunity of spending 2 years in Aachen. I am grateful to my co-advisor Ulrich Schollwöck for inviting me as a fellow Bavarian to his group in Aachen and for joining me on my way back to Munich (though this might be a mere coincidence). I appreciate their support and teaching of condensed matter physics, numerics and how to write scientific articles. I am also very grateful for the opportunity to visit various summer schools and conferences.

Big thanks go also to Andreas Weichselbaum for introducing me into the world of MPS and all the fruitful discussions from which I learned a lot. I am thankful to Ian McCulloch who was the no. 1 expert on numerics in Aachen for sharing his knowledge with me and his DMRG code which I used for most calculations in this thesis. I thank Fabian Heidrich-Meissner for the collaboration on the Kondo cloud project which turned out become the numerically most demanding calculations I performed.

I owe deep thanks to my roommates Thomas, Andreas, Christian, Stefan, Cheng, Constantin, Annika and Ferdinand both in Munich and Aachen for all the fun and despair we shared and for the discussions on physics and life in general we had.

For all the nice time during coffee breaks and barbecue parties I thank all the other group members Adrian, Severin, Frank, Stefan, Stephan, Theresa, Michael, Wolfgang, David, Georg, Karl, Alexei, Andrej, Guillaume, Hai-Bo, Florian, Oleg, Max, Clemens, Georg, Björn, Florian, Vitaly, Sebastian, Jan, Arne, Markus, Markus, Oliver, Alex, Peter, Ireneusz, Alexandre, Jiang, Alois, Wael, Philipp, Martin, Nicolai, Christoph. I thank Sebastian, Wolfgang and Jad for proofreading parts of this thesis.

I thank our computer administrators Uwe Kahlert and Ralph Simmler and their teams Michael, Alex, Umut, Veronika, Stefanie and Martin for keeping all computers operational and ordering enough fan replacements. I thank the LRZ for supporting my computer usage pattern. I also thank the secretaries Gaby Kramp-Salecker, Stéphane Schoonover and Sylvia Kaiser for helping me with the administrative stuff.

I am grateful to the Aachen climbing group and especially Beke for the introduction into sport climbing and the nice time we spent together.

My deepest thanks go to my family for their love and support during all these years.